Aeroacustic and Vibroacoustic Advancement in Aerospace and Automotive Systems

Edited by
Roberto Citarella, Luigi Federico and Mattia Barbarino

MDPI

Aeroacustic and Vibroacoustic Advancement in Aerospace and Automotive Systems

Aeroacustic and Vibroacoustic Advancement in Aerospace and Automotive Systems

Special Issue Editors

Roberto Citarella
Luigi Federico
Mattia Barbarino

MDPI

Special Issue Editors

Roberto Citarella
University of Salerno
Italy

Luigi Federico
Italian Aerospace Research
Center (CIRA)
Italy

Mattia Barbarino
Italian Aerospace Research
Center (CIRA)
Italy

This is a reprint of articles from the Special Issue published online in the open access journal *Applied Sciences* (ISSN 2076-3417) (available at: https://www.mdpi.com/journal/applsci/special_issues/aeroacustic_vibroacoustic).

For citation purposes, cite each article independently as indicated on the article page online and as indicated below:

LastName, A.A.; LastName, B.B.; LastName, C.C. Article Title. *Journal Name* **Year**, *Article Number*, Page Range.

Contents

About the Special Issue Editors

Roberto Citarella obtained his Doctor's degree and Ph.D. in Mechanical Engineering in 1994 and 1999, respectively, both at the University of Naples, Italy. In 1996, he received his Master of Business Administration (MBA) diploma at the school "Stoà" in Naples. Since March 2015, he has been Associate Professor of Machine Design in the Department of Industrial Engineering (DIIN) at the University of Salerno. He was Visiting Researcher at the Wessex Institute of Technology in Southampton (UK) in 1996 and the Queen Mary and Westfield College in London (UK) in 1998 and 2000. He was a member of the referee group for the first European call of FP7 Transport and Aeronautics. He is involved, as a main investigator and member, in several national research activities. He also collaborates with international research centers such as the Max Planck Institute of Greiswald, Germany, and the Kazan Scientific Center Russian Academy of Sciences, Kazan, Russia. He is Fellow of Wessex Institute of Technology. His main topics of research include the boundary element method, vibrational acoustics, bioengineering, fracture mechanics, and thermomechanical fatigue. He has published nearly 150 technical papers in international peer-reviewed journals and conference proceedings. He serves as a reviewer for many international journals and is a member of the editorial board of *Advances in Engineering Software, Applied Sciences*, and *The Open Mechanical Engineering Journal.*

Luigi Federico, Ph.D., is Head of the Environmental Impact of Air Transport System Unit at the Italian Aerospace Research Center (CIRA). His research activities include experimental and computational acoustics of fixed- and rotary-wing aircraft, vibrational acoustics, boundary and finite element methods, statistical energy analysis, and multibody and air transport system sustainability. His research unit is accredited by ENAC for noise certification according to ICAO Annex 16. Since 2018, has been Contract Professor of Computational Vibroacoustics at the University of Salerno.

Mattia Barbarino, Ph.D., is responsible for the Computational Acoustics Lab at CIRA. He has been working at CIRA since 2007 in aeroacoustics, CAA software development, and numerical simulation. He has developed a multidisciplinary view of the aircraft/rotorcraft noise prediction and reduction problem, leading activities in several EU and national funded projects (e.g., Clean Sky and Clean Sky 2, H2020) and in GARTEUR collaborative research groups. He is a member of the CEAS Aeroacoustics Specialists Committee and is the point of contact of the IFAR working group on NOISE.

Editorial

Aeroacustic and Vibroacoustic Advancement in Aerospace and Automotive Systems

Roberto Citarella [1],*, Luigi Federico [2] and Mattia Barbarino [2]

[1] Department of Industrial Engineering, University of Salerno, 84084 Fisciano, Italy
[2] Italian Aerospace Research Centre (C.I.R.A), via Maiorise snc, 81043 Capua, Italy;
    l.federico@cira.it (L.F.); m.barbarino@cira.it (M.B.)
* Correspondence: rcitarella@unisa.it

Abstract: This Special Issue highlights the latest enhancements in the abatement of noise and vibrations of aerospace and automotive systems. The reduction of acoustic emissions and the improvement of cabin interior comfort are on the path of all major transportation industries, having a direct impact on customer satisfaction and, consequently, the commercial success of new products. Topics covered in this Special Issue deal with computational, instrumentation and data analysis of noise and vibrations of fixed wing aircrafts, satellites, spacecrafts, automotives and trains, ranging from aerodynamically generated noise to engine noise, sound absorption, cabin acoustic treatments, duct acoustics and vibroacoustic properties of materials. The focus of this Special Issue is also related to industrial aspects, e.g.,: numerical and experimental studies have been performed for an existing and commercialized engine to enable design improvements aimed at reducing noise and vibrations; moreover, an optimization is provided for the design of low vibroacoustic volute centrifugal compressors and fans whose fluids should be strictly kept in the system without any leakage. Existing procedures and algorithms useful to reach the abovementioned objectives in the most efficient way are illustrated in the collected papers.

Keywords: vibroacoustics; aeroacoustics; acoustics; noise; vibration; aeronautics; automotive

1. Introduction

This Special Issue follows a previous one [1] on a similar topic, with the aim to keep on providing updates on state of the art research with reference to aeroacoustics and vibroacoustics in aerospace and automotive systems.

In the following, a brief summary on the content of the papers included in this special issue, clustered based on a thematic criterion, starting with the spacecraft vehicles and satellites, then moving to the automotive field, followed by the aeronautic field, the industry components for conditioning and, finally, the railway transport system.

In the section on spacecraft vehicles and satellites, the first paper is concerned with the vibration attenuation of meteorological satellites in the presence of periodic disturbances, leveraging on an optimal design of constant compensations against known-law periodic disturbances [2]. The methodology proposed is applied to a flexible spacecraft actuated by constant control torque in the presence of sustained periodic disturbances. The effectiveness of the optimal compensation torque is provided and compared with results of other selections in the frequency and amplitude ratio domain. Numerical simulation results and experimental results clearly demonstrate the good performance of proposed criteria. In a second paper [3], a frequency weighting matrix beamforming algorithm is proposed to localize air leakages caused by clashes between space debris and spacecraft in orbit. The elastic Lamb waves that are caused by leakages are acquired by an 'L' shaped sensor array consisting of eight

acoustic emission sensors. The angle of a leak can be obtained through the superposition of different time delays, and the intersection of two angles can be used to find the location of the leak.

Moving to the automotive field, again a couple of papers can be retrieved. The first analyses the influence of crankshaft torsional frequencies on its rotational speed behavior [4], with the aim to reduce the vibrations at the engine supports. In particular, a multibody calculation methodology has been applied to the vibration analysis of a 4-cylinder, 4-stroke, turbocharged diesel engine, with a simulation-driven study of the angular speed variation of a crankshaft. Time-dependent simulation results, evaluated at the engine supports, are condensed to a vibration index and compared with experimental results, obtaining satisfactory outcomes. The modal analysis also considers the damping aspects and has been conducted using a multibody model created with the software AVL/EXCITE. A second one is concerned with the vibration behavior of a 4-cylinder, 4-stroke, petrol engine as simulated by the finite element method (FEM) [5]. A reduced modelling strategy based on the component mode synthesis (CMS) is adopted to reduce the size of the full FEM model of the engine. Frequency response function (FRF) analyses are used to identify the resonant frequencies and corresponding modes of the different FEM models and the obtained results are compared with experimental data to get the model validation. Subsequently, modal-based frequency forced response analyses have been performed to consider the loads acting during the real operating conditions of the engine. Finally, the impact on vibrations at the mounts, produced by an additional bracket connecting the engine block and gearbox, is investigated. Both the full and reduced FEM model reproduce with high accuracy the vibration response at the engine mounts, but the reduced modelling strategy requires significantly shorter runtimes.

Considering then the aeronautic field, three papers are included in the Special Issue. In one of them, an analytical model to predict the performance of the plasma synthetic jet actuator (PSJA) array, coupled with the multichannel discharge model and PSJA aerodynamic model, is put forward [6]. Such a model can be used to improve the aeroacoustic performances of turbofans by active flow control. In another one [7], the effects of both steady and periodic tangential slot blowing are investigated with the aim to delay buffet onset and alleviate the buffet load. The results show that steady tangential blowing on the airfoil upper surface can postpone the buffet onset margin and evidently increase the lift coefficient at incidence angles near and above the buffet onset case of the clean airfoil. Under buffeting conditions of the clean airfoil, unsteady aerodynamic loads can be greatly suppressed by both steady and periodic blowing. Finally, a novel optimization framework, based on a multi-disciplinary optimization (MDO) procedure, applied to the vibroacoustic finite element method (FEM) model of an aircraft fuselage mock-up, is proposed in [8]. The MDO procedure, based on an efficient global optimization (EGO)-like approach, is implemented to characterize acoustic sources that replicate the sound pressure field generated by the engines on the fuselage. The proposed FEM-MDO framework enables us to set up ground experimental tests on aircraft components, which is useful to replicate their vibro-acoustic performances as if tested in flight. More generally, such a procedure can also be used as a reference tool to design simplified tests starting from more complex ones.

A component adopted for the air conditioning of industrial environments is studied in [9], where a numerical optimization to reduce the vibrational noise of a centrifugal fan volute is presented. Minimal vibrational radiated sound power is considered as the aim of the optimization, and the influence of vibroacoustic coupling is taken into account. The fan's aerodynamic performance, volute casing surface fluctuations, and vibration response have been validated by experiments, showing good agreement. The optimization results show that the vibrational noise optimization method proposed in this study can effectively reduce the vibrational noise of the fan.

The last subsection of this Special Issue is related to railway transport, with particular reference to the aerodynamic noise characteristics of a high-speed train [10]. Considering a pantograph installed on different configurations of the roof base, i.e., flush and sunken surfaces, the large eddy simulation (LES) is coupled with the acoustic finite element method (FEM) to analyze its noise impact. Numerical results are presented in terms of acoustic pressure spectra and distributions of aerodynamic noise in near-field

and far-field regions. The results show that the pantograph with the sunken base configuration provides better aerodynamic noise performances when compared to that with the flush base configuration.

References

1. Citarella, R.; Federico, L. Advances in Vibroacoustics and Aeroacustics of Aerospace and Automotive Systems. *Appl. Sci.* **2018**, *8*, 366. [CrossRef]
2. Xu, S.; Cui, N.; Fan, Y.; Guan, Y. A Study on Optimal Compensation Design for Meteorological Satellites in the Presence of Periodic Disturbance. *Appl. Sci.* **2018**, *8*, 1190. [CrossRef]
3. Qi, L.; Zeng, Z.; Zhang, Y.; Sun, L.; Rui, X.; Li, X.; Wang, L.; Liu, T.; Yue, G. Research on Leakage Location of Spacecraft in Orbit Based on Frequency Weighting Matrix Beamforming Algorithm by Lamb Waves. *Appl. Sci.* **2020**, *10*, 1201. [CrossRef]
4. Armentani, E.; Caputo, F.; Esposito, L.; Giannella, V.; Citarella, R. Multibody Simulation for the Vibration Analysis of a Turbocharged Diesel Engine. *Appl. Sci.* **2018**, *8*, 1192. [CrossRef]
5. Armentani, E.; Giannella, V.; Citarella, R.; Parente, A.; Pirelli, M. Substructuring of a Petrol Engine: Dynamic Characterization and Experimental Validation. *Appl. Sci.* **2019**, *9*, 4969. [CrossRef]
6. Huang, S.; Zhang, Z.; Song, H.; Wu, Y.; Sun, Z.; Li, Y. Analytic Model and the Influence of Actuator Number on the Performance of Plasma Synthetic Jet Actuator Array. *Appl. Sci.* **2018**, *8*, 1534. [CrossRef]
7. Dang, H.; Zhao, J.; Yang, Z.; Dang, H. Postponing the Onset and Alleviating the Load of Transonic Buffet by Using Steady and Periodic Tangential Slot Blowing. *Appl. Sci.* **2019**, *9*, 4132. [CrossRef]
8. Giannella, V.; Lombardi, R.; Pisani, M.; Federico, L.; Barbarino, M.; Citarella, R. A Novel Optimization Framework to Replicate the Vibro-Acoustics Response of an Aircraft Fuselage. *Appl. Sci.* **2020**, *10*, 2473. [CrossRef]
9. Chu, W.; Zhang, J.; Lv, Y. Vibroacoustic Optimization Study for the Volute Casing of a Centrifugal Fan. *Appl. Sci.* **2019**, *9*, 859. [CrossRef]
10. Yao, Y.; Sun, Z.; Yang, G.; Liu, W.; Prapamonthon, P. Analysis of Aerodynamic Noise Characteristics of High-Speed Train Pantograph with Different Installation Bases. *Appl. Sci.* **2019**, *9*, 2332. [CrossRef]

A Novel Optimization Framework to Replicate the Vibro-Acoustics Response of an Aircraft Fuselage

Venanzio Giannella [1,*], Riccardo Lombardi [2], Matteo Maria Pisani [1], Luigi Federico [3], Mattia Barbarino [3] and Roberto Citarella [1]

[1]   Department of Industrial Engineering, University of Salerno, via Giovanni Paolo II, 84084 Fisciano (SA), Italy; m.pisani18@studenti.unisa.it (M.M.P.); rcitarella@unisa.it (R.C.)
[2]   Noesis Solutions, Gaston Geenslaan, 3001 Leuven, Belgium; riccardo.lombardi@noesissolutions.com
[3]   Italian Aerospace Research Centre (C.I.R.A), via Maiorise snc, 81043 Capua (CE), Italy; l.federico@cira.it (L.F.); m.barbarino@cira.it (M.B.)
*   Correspondence: vgiannella@unisa.it; Tel.: +39-089-964111

Abstract: In this work, a novel optimization framework, based on a Multi-Disciplinary Optimization (MDO) procedure, applied to the vibro-acoustic Finite Element Method (FEM) model of an aircraft fuselage mock-up, is proposed. The MDO procedure, based on an Efficient Global Optimization (EGO)-like approach, is implemented to characterize acoustic sources that replicate the sound pressure field generated by the engines on the fuselage. A realistic sound pressure field, evaluated by aeroacoustic simulations, was considered as the reference acoustic load, whereas two equivalent sound fields, displayed by two different arrays of microphones and generated by the same configuration of monopoles, were calculated by the proposed vibro-acoustic FEM-MDO procedure. The proposed FEM-MDO framework enables to set up ground experimental tests on aircraft components, useful to replicate their vibro-acoustic performances as if tested in flight. More in general, such a procedure can also be used as a reference tool to design simplified tests starting from more complex ones.

Keywords: vibro-acoustics; FEM; MDO; aircraft fuselage

1. Introduction

Nowadays, an accurate evaluation of noise generation and propagation has become a key concern, especially in the areas in which the comfort for end users has become a turning point. An increasing interest of aerospace and automotive industries for the passengers' comfort has been providing the framework in which these issues have acquired a prominent role. The typical topics to be tackled for investigations of noise and vibrations of vehicles, aircraft, space launchers, etc. deal with aerodynamically generated noise, engine noise, Passive Noise Control (PNC), Active Noise Control (ANC) and assessment of acoustic properties of innovative materials [1]. The reduction of acoustic emissions and the improvement of interior comfort are on the path of all major industries of the transport system, having a direct impact on customer satisfaction and, consequently, on the commercial success of new products.

Nowadays, the aeronautics industry requires several experimental tests during the designing processes that, very often, present huge costs and generally are not simple to carry out with a reasonable accuracy.

In this work, a Finite Element Method-Multi-Disciplinary Optimization (FEM-MDO) framework has been proposed to characterize sets of acoustic sources that replicate the sound field produced by the real engines on an aircraft fuselage mock-up. This procedure would enable to set up ground experimental tests on aircraft components, useful to replicate their vibro-acoustic performances as if

tested in flight. More in general, it can also be used as a reference tool to design simplified tests for complex problems.

Similar approaches in which simplified acoustic sources were used to simulate more complex acoustic fields can be found in literature, e.g., the noise generated by rocket engines in [2–5]. In fact, in these works a semi-empirical jet noise model has been exploited and adapted for reconstructing the experimental acoustic near field on the external surface of a space launcher, allowing an affordable vibro-acoustic assessment based on the achieved pressure excitation. The reference theory to predict the noise radiated by rotors can be found in [6,7], in which Lighthill originally developed the first aeroacoustics analogy that, in the last decades, has been extensively applied in numerical aeroacoustics to reduce the complex sound sources to simple emitter types. In general, aeroacoustic analogies were derived from the compressible Navier–Stokes equations, rearranged into forms of the inhomogeneous acoustic wave equation. Some approximations were introduced to make the source terms independent of the acoustic variables and, in this way, linearized equations were derived to describe the propagation of the acoustic waves in a homogeneous resting medium.

The original formulation of Lighthill was extended by Ffowcs Williams [8] to take into account vibrating solid surfaces, by rearranging the Navier–Stokes equations with introduction of source terms composed by:

- quadrupole sources, generated by the turbulence of the fluid;
- dipole sources, caused by fluctuations of the fluid-structural interaction forces;
- monopole sources, generated by mass fluctuations.

These theories do not provide any indication about the positioning of sources that commonly are characterized by means of Computational Fluid Dynamics (CFD) simulations and located in correspondence of the geometrical central axis of the engine rotors. These theories are also still inefficient under near field conditions. Thus, it is commonly necessary to proceed numerically to determine type, number and position of the acoustic sources in the most complicated cases. Such numerical procedures allow to approximately replicate the real acoustic pressure fields generated by the engines via ordinary acoustic sources. In this way, the experimental testing could be carried out either in anechoic or semi anechoic environments with the emulated acoustic field imposed by loudspeakers.

If successful, this procedure would provide a preliminary step to go further in the prediction of cabin noise: the next step could be the monitoring of cabin noise as produced by the engine rotors, by adding microphones in a realistic mock-up placed in an equipped laboratory.

2. Problem Description

This work can be split in three main parts.

The first part comprises the CAD/FEM modeling of an aircraft fuselage mock-up in order to build up a simplified vibro-acoustic FEM model. Such a model was used to perform the vibro-acoustic analyses of the fuselage when loaded either with the sound pressure emitted by the engines, or with the sound pressure emulated by different sets of simple acoustic sources (monopoles).

The second part comprises the set-up of the MDO procedure, with the aim of characterizing the previously given sets of acoustic sources in order to reproduce, in a simplified manner, the reference pressure field. Moreover, such a procedure was performed two times in order to calculate, for a given configuration of acoustic sources, the results of two different configurations of microphones (two separate sets of simulations were run).

The last part comprises the presentation of results for the two simulated cases and their comparisons with the reference data. A discussion on such results is also provided and recommendations for further improvements are added.

3. CAD/FEM Modeling

3.1. FEM Mesh

The FEM model was built up by the commercial code Siemens NX Nastran 12.0 [9].

Starting from a CAD model of a fuselage barrel (Figure 1), an FEM model was generated comprising 2D/1D structural parts and 3D internal and external fluid volumes.
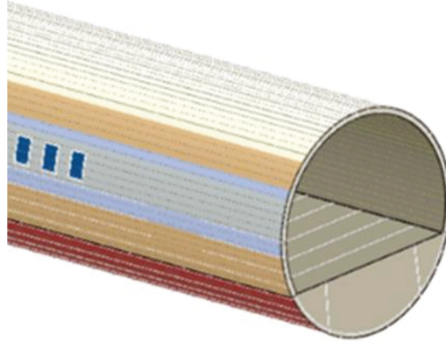
Figure 1. CAD model of the aircraft fuselage.

The 2D structural part represented the key contributor to the vibration response of the model, and comprised four main surfaces made out of different materials (Figure 2a):

- the external surface on which the external acoustic pressure directly impacts;
- the lining panel, realized by a sandwich suitable to reduce noise and vibration, to improve the comfort inside the cabin;
- the floor on which seats are located (seats were not modeled in this work);
- the window glasses.

(**a**)

(**b**)

Figure 2. *Cont.*

(**c**)
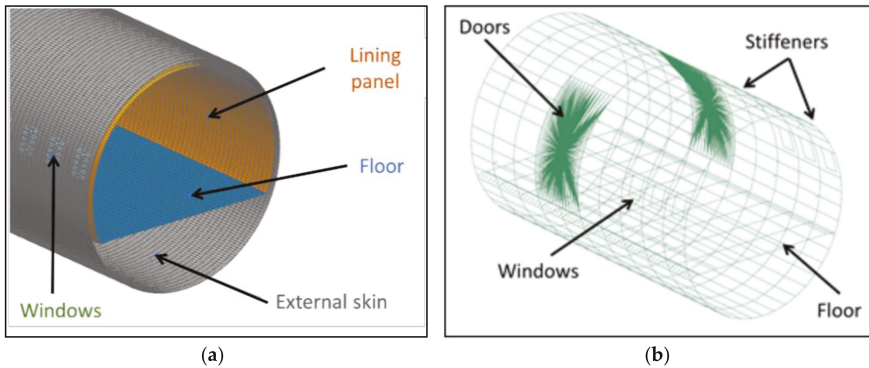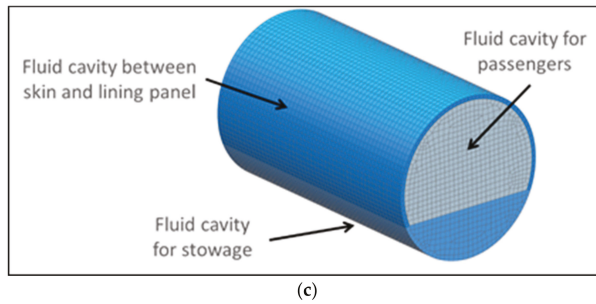
Figure 2. Finite Element Method (FEM) model subdivision: 2D (**a**) and 1D (**b**) structural elements; (**c**) internal fluid cavities.

The 1D structural elements (Figure 2b) were divided in: longerons and circumferential beams to stiffen the structure, transversal and axial floor support, formed by beams with different sections, windows frameworks and doors. Furthermore, the sandwich was linked to axial and circumferential beams by elastic and rigid constraints.

The internal fluid cavities (Figure 2c) were: the cabin occupied by passengers, the stowage under the floor, the volume displaced between the external surface and the internal lining panels.

The external air was modeled to let the sound waves propagate from the monopole sources, representative of the MDO inputs, to the structure. The external fluid modeling was also essential to measure the Acoustic Intensities (AIs), representative of the MDO outputs, in the 30 microphone locations on the external fuselage surface. Such external fluid was modeled as a cube of solid elements with a cavity in the center to accommodate the fuselage barrel. Such cube was modeled with a size large enough to comprise at least 2 wavelengths at the frequency of interest. This was required in order to prevent boundary effects since the condition of non-reflecting boundary condition was applied at the boundaries to simulate the infinite radiation [9]. The mesh comprised tetrahedral solid linear elements with variable size having at least 6 nodes per wavelength, in order to have an acceptable accuracy for fluid field calculation in the fluid-structure interface zone (close to the structure); larger elements were adopted far from the structure in order to reduce the computational burden (Figure 3b). Even if the accuracy could turn out to be not so high with 6 nodes per wavelength, it is not a problem for this work where the aim is to show that the proposed procedure is a viable approach for reducing the experimental effort, based on an acceptable agreement between the reproduced and the reference sound pressure distribution on the fuselage. More info about the level of approximation inherent the mesh density adopted could be retrieved in [10,11].

(**a**)   (**b**)

Figure 3. (**a**) External fluid mesh, (**b**) with close up to the mesh grading at the fluid-structure interface surfaces.

In [10], two numerical examples, a long duct and a sedan cabin compartment have been analyzed. In the first example, the analytical solution of the corresponding one-dimensional boundary value problem has been used for comparison. Numerical investigations limited to the frequency range of 0 < kl <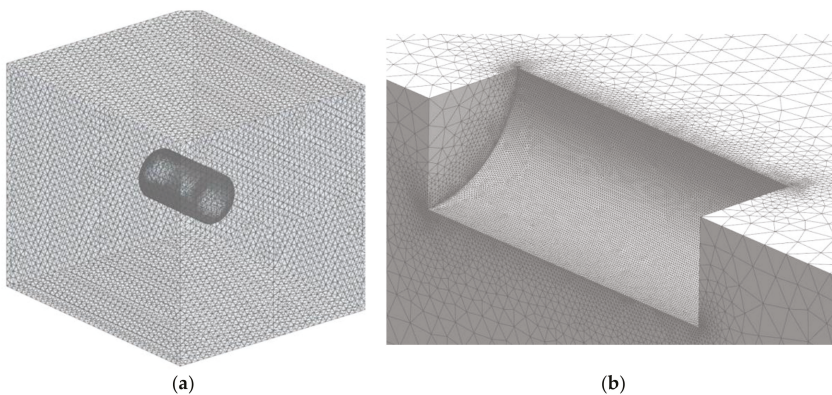 80 *Pi essentially confirmed the common rules of modeling that six constant or bilinear elements per wavelength are sufficient to obtain a solution of about 10 to 15% error. The common rule of six linear elements per wavelength, provide an error inferior than 10% in the Euclidean norm and inferior than 20% in the maximum norm. The second example confirmed most of these conclusions.

In [11], Zaleski investigated discretization requirements for sound radiation at complicated structures. He confirmed the rule of six linear boundary elements per wavelength to achieve an acceptable accuracy in the sound pressure for lower wave numbers, whereas the rule of a fixed number of elements per wavelength may be invalid for high wave numbers.

3.2. Reference Case (RC) and Simplified Cases (SC)

The so obtained vibro-acoustic FEM model was preliminary solved by considering as acoustic load the pressure on the external skin calculated by aeroacoustic calculations (Figure 4). This simulation was termed as Reference Case (RC) because it provided the benchmark to assess the Simplified Cases (SCs). Such pressure distribution outside the fuselage was obtained by aeroacoustic simulations, based on the integral formulation of Ffowcs Williams and Hawkings [8], and considered the rotating engine rotors, at the first Blade Passage Frequency (1BPF), as the only noise contributor providing periodic low frequency loads on the structure. It was considered just the 1BPF because it was the most relevant under cruise flight condition.

| (a) | (b) | (c) |
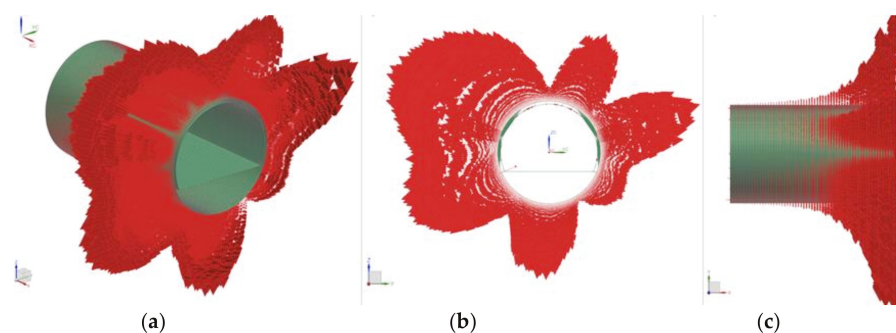
Figure 4. Sound pressure field on the fuselage considered as boundary condition for the Reference Case (RC) (the engine is located on the right side of Figure 4c). (**a**) isometric view; (**b**) front view; (**c**) lateral view.

From Figure 4, it can be qualitatively noticed that the acoustic pressure load shape was caused by the phase shift of the engine rotors (an arbitrary non-null value was selected in this case), and the increment of the load amplitude in the axial direction, as a consequence of the distance reduction from the rotors position. The circumferential distribution of pressure loads presents a complex pattern, clearly variable as a function of the imposed phase shift.

More in general, given the model being available, the calculation of additional frequencies or noise contributors does not impose additional complications apart from the calculation time.

Subsequently, the boundary condition corresponding to the pressure distribution was removed from the FEM model and a set of acoustic sources and microphones (monitoring points) was added. Such modified FEM model, after a vibro-acoustic coupled analysis, provided the results to be used as input for the MDO procedure.

In particular, a given set of acoustic sources and two different sets of microphones were considered, termed in the followings as SCs: SC1 and SC2. The two SCs correspond to two attempts to replicate

the RC, namely, to replicate the realistic reference solution in terms of acoustic pressure outside the fuselage and, consequentially, in terms of vibro-acoustic response of the structure.

Figure 5 shows the number (four) and positions of the acoustic monopole sources designed to try reproducing the reference sound field and providing the input for the MDO iterations.
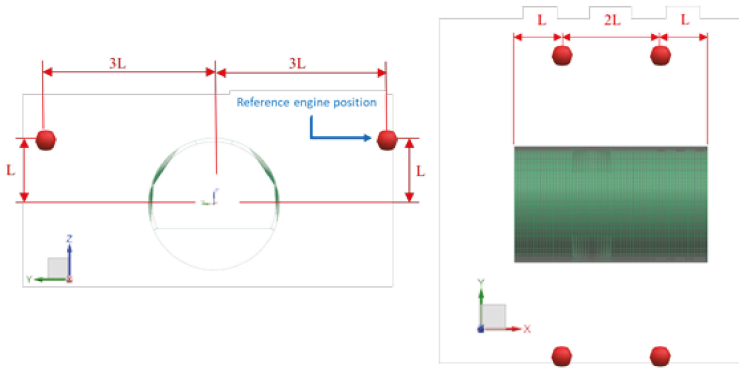
Figure 5. Monopole sources positions (in red) outside the fuselage.

Figure 6 highlights number and position of the microphones required to measure the Acoustic Intensities (AIs) outside the fuselage. Such microphones were required in order to monitor the pressure field on the fuselage surface for each MDO iteration. Two kinds of positioning were considered comprising either 3 or 5 rings having 6 microphones each, for a total of either 18 or 30 microphones.

(**a**)

(**b**)
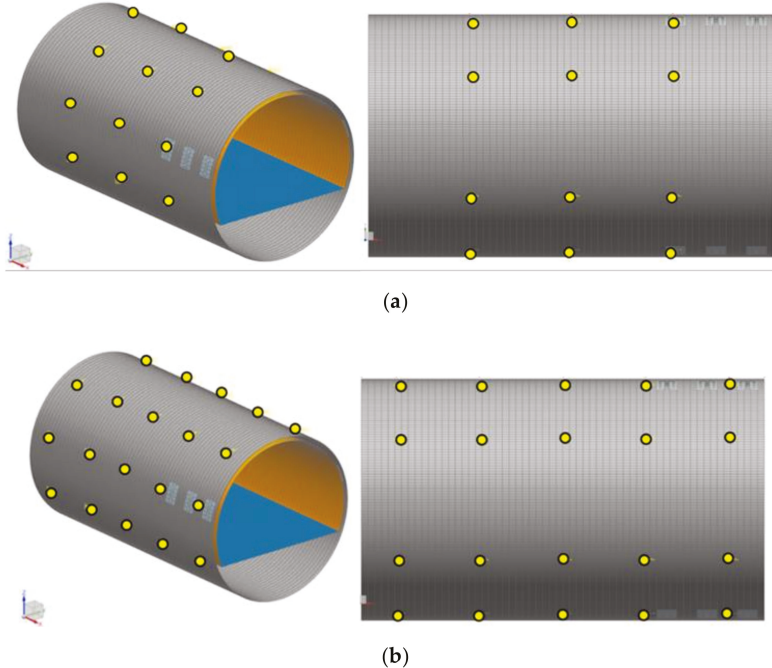
Figure 6. Microphones positions (in yellow) outside the fuselage representing the output positions for the optimization process: configuration with (**a**) 18 and (**b**) 30 microphones.

Such monopoles and microphones were adopted to create two SCs (Figures 6 and 7), i.e.,

- SC1 (Figure 7a), comprising 18 output microphones,
- SC2 (Figure 7b), comprising 30 output microphones.

(a)   **(b)**
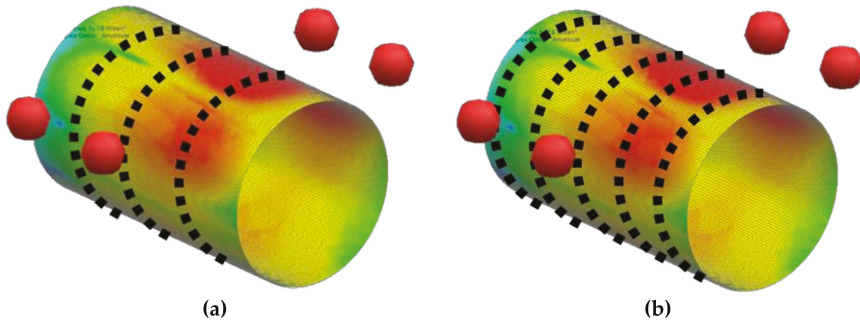
Figure 7. Simulated Cases overview: (**a**) Simplified Case 1 (SC1), (**b**) SC2; red dots representing the monopoles and dotted black lines representing the rings along which microphones are positioned.

Both SCs comprised 4 monopole sources positioned as shown in Figure 5.

3.3. Boundary Conditions

Apart from the previously described boundary conditions, all the remaining settings were corresponding for both RC and SCs. In particular, a fully clamped condition (Figure 8a) was imposed at the two ends of the barrel (no translations neither rotations were allowed for such nodes). The two fuselage ending surfaces were considered as acoustically fully reflecting, thus assuming that no interaction between internal and external fluids was allowed. Moreover, the six faces of the cube volume, representative of the external fluid, were modeled as anechoic walls, thus assuming that no reflection was allowed (Acoustically Matched Layer; Figure 8b) [9]. Finally, a strong coupling condition between fluids and structural nodes was set up to allow for a bidirectional interaction between structure and surrounding fluid [9].

(a)   **(b)**
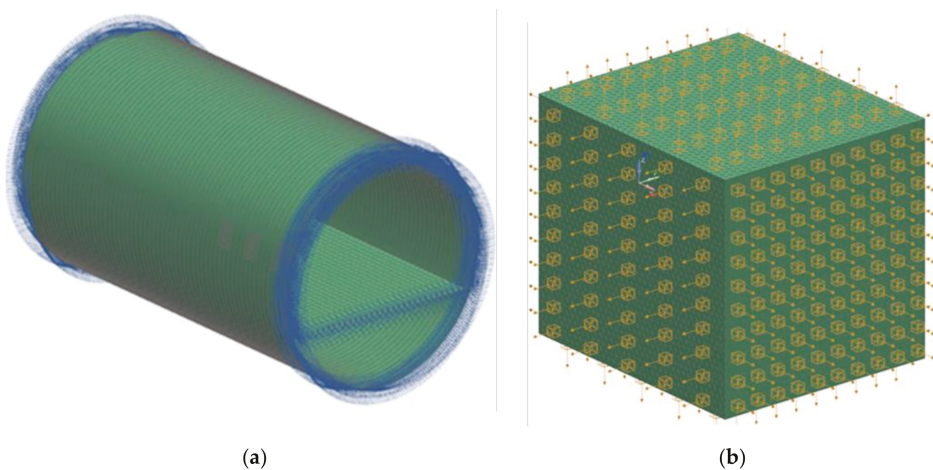
Figure 8. Boundary conditions: (**a**) clamped structural nodes, (**b**) non-reflecting boundary conditions.

Initial sound power amplitudes and phases were assigned for each monopole source and, step-by-step, adjusted by the optimization procedure.

At this stage, the goal of the work was not an accurate reproduction of the real fuselage response to the sound pressure coming from the engines, but only the implementation and validation by comparison between RC and SCs of a general MDO procedure to solve a complex optimization problem such as the one here proposed. It is worth noting that the MDO procedure here proposed required many FEM solutions of the current model to provide a stable solution; therefore, some simplifications were considered as a trade-off between a sufficiently accurate physical replication of the vibro-acoustic fuselage behavior and an acceptable computational burden.

A comparison between the cross sections of the so created FEM models built up for RC and SC is shown in Figure 9.

(**a**)   (**b**)
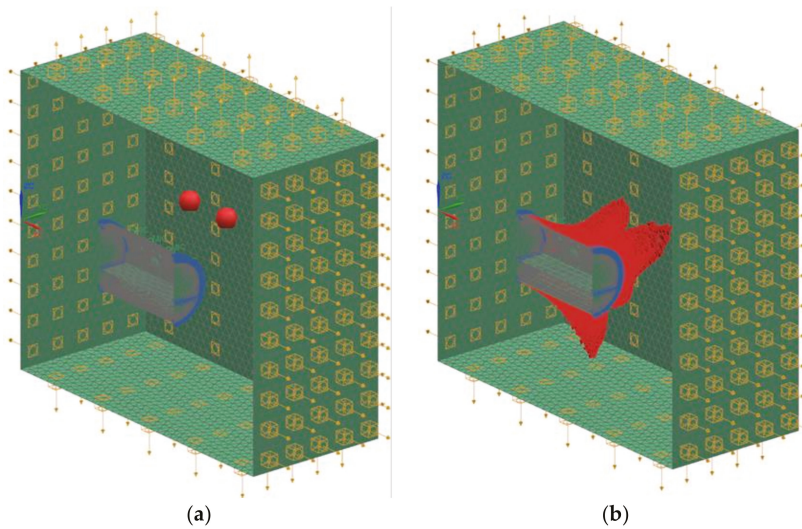
Figure 9. Cross section of the model adopted for (**a**) SC and the (**b**) RC, respectively.

4. Optimization Process

4.1. Process Integration and Design Optimization (PIDO)

The optimization procedure was implemented in the commercial Process Integration and Design Optimization (PIDO) platform Optimus [12,13]. The software provides a wrapper where different simulation tools (Commercial Off-The-Shelf or specifically created) can be implemented, connected and investigated, using a suite of design and optimization methods. To achieve this automatic analysis of the model behavior, the simulation requires an a priori study to determine its parameters (input variables not under user control), design variables (number, type, range), outputs, constraints (limitations to the design space) and objective(s).

Depending on the structure of the problem and its behavior, different analysis methodologies can be implemented. The first step typically involves one or more Design of Experiments (DOE) to gain knowledge on the design variable to outputs relationship.

A set of experiments, decided using only the range of the design variables (as for the factorial-class methods, or Latin Hypercube methodology just to name some of the most commonly used) is performed and the values of the outputs are studied either directly or involving more elaborate data post-processing as correlation studies, clustering, meta-modeling.

The acquired insight on the problem responses can then be re-used to determine the best algorithm to assess the design that better respond to a specific need (single objective optimization) or satisfies multiple criteria at the same time (multi-objective optimization).

The same general approach can be extended to include uncertainties, both in the variables and the analyses, and perform uncertainties propagation and robust optimization.

4.2. Modeled Problem

In the modeled problem, the sound power and phase of each monopole source represented the input data for the MDO process, whereas the Acoustic Intensities (AIs) at microphones provided the output. Thus, a parametrization of the model for the SCs was required to change the input values for the FEM simulations and to get the output to compare with RC data. Such parametrization of the model was implemented in the PIDO platform, using the related interfaces after an appropriate setup and validation of the FEM model.

The interfaces are designed to simplify the access to the identified model parameters and, during the execution of the analyses, automatically map the desired values of the design variables to the model itself and extract the values of the outputs of interest. The information gathered through analyses are processed to determine the relationships between inputs and outputs; this knowledge can then be passed to different post-process tools or used to perform design optimization, reliability study, robust design.

The same validated workflow with parametrized FEM model, analysis, results extraction and post-process has been used both to perform DOE and optimizations. DOEs have been run both to provide a clear overview of the design variables' impact and to generate a re-usable database of simulations. Due to the nature of the design variables (and specifically the periodicity of the phase) some of the DOE approaches would have been ineffective (in particular, the members of the factorial-class, that explore the combinations of the lower and higher values of the design variables, but also other methods like the Plackett–Burman are affected by the same limitations). The final objective was to determine configuration of the sources able to provide the best approximation of the known RC pressure field; this has been organized as an optimization problem where a dedicated performance indicator (Equation (1)), able to describe the difference between the reference and the simulated values, had to be minimized. A single averaged, performance indicator was selected.

The problem to be solved was far from trivial; exploratory DOE and subsequent correlation studies highlighted that, although the amplitude of the sources had a relevant and, within certain conditions, predictable impact on the pressure field, the phase was significantly less manageable. PIDO platforms typically rely on black-box optimizers, algorithms that neither have insight on the problem physics, nor make assumptions about its continuity or smoothness.

The initial studies underlined the non-linear and non-monotone behavior of the outputs with respect to design variables; from the optimization point of view, this creates several local minima that hinder the convergence of the algorithm.

Global optimizers are methodologies that explore the whole design space, therefore they are suitable for this kind of problem; however, this exploration requires a relevant number of experiments [14]. On the other hand, local optimizers explore limited regions of the domain and often rely on the analytical or numerical evaluation of the gradient to determine the local solution. They are usually attracted by minima close to the starting point, whose setup becomes critical, although gradient-based line search can be exploited to extend the investigated portion of the domain.

4.3. Efficient Global Optimization (EGO)

Instead of a standard algorithm, a tailored one was created and exploited for this problem; the optimization strategy was an Efficient Global Optimization (EGO) [15] derived methodology, simplified (without the stochastic process model) and customized to better drive the optimization algorithm to find a solution in such a complex optimization problem.

Due to the computational cost of the simulations, the methodology had to be able to re-use all the previous analyses; additionally, surrogate models had been used to approximate the model and identify candidate points without the need for extensive simulation campaigns.

The implemented MDO optimization procedure is composed of an initial DOE (either performed as part of the optimization or previously run) and a sequence of iterations with a stopping criterion. Among the possible DOEs, the Latin Hypercube Design (LHD) [13] was the first choice in force of its extensive design space exploration and orthogonality of the experiments, however, other methods or combination of methods can be used. Traditional DOEs are not iterative in nature, therefore all the experiments are decided before the first analysis is performed. This can limit the effectiveness in identifying the problem characteristics.

For each configuration of the sources, a single, systematic LHD has been performed, accompanied by prior secondary DOEs, mainly used to validate the integration and analysis procedure, and therefore verify their reliability for a wide range of scenarios.

The decision to aim for a single DOE has been driven by the computational effort of the simulations; in order to provide a quantitative representation of the problem (required by its planned applications, namely the database and the metamodels generation, and the non-linear behavior of the outputs), the DOE required a significant number of experiments. In force of the LHD nature, it would have not been possible to perform smaller, independent and differently initialized DOEs and later combine them in a single database while preserving the experiments decoupling. Random initialization has been used.

The main DOE has been merged with the lesser ones (different by both seed and number of experiments) and compared with the unmerged one in terms of correlation (Spearman and Pearson), showing no significant variations.

The general pattern of almost null linear and monotone correlation between phase and outputs and average (around 0.5) between amplitude and outputs has been observed in all the source configurations.

The dataset generated by the optimization procedure can be used to replace (or integrate) the original DOE, due to its compatibility in terms of inputs and outputs.

4.4. MDO Optimization Procedure

The MDO optimization procedure proceeded by iterating the following steps:

- generation of the interpolated response surfaces, based on the DOE table data;
- identification of the best model using cross-validation;
- run of the global optimization method on the response surface, to find a candidate point that minimizes the metrics (Equation (1));
- check of the proximity of the candidate point to the existing samples and, if needed, apply a random shift;
- space-filling, to balance for the global optimization (based on surrogate models with known data) to fall into local minima without performing additional exploration;
- run the FEM analyses on the two new points;
- update the initial DOE data and iterate until a terminate criterion is satisfied.

Thus, the starting point of the MDO strategy is an existing DOE database, not necessarily tailored for optimization. Then, the global optimization method Differential Evolution (DEVOL) [14], was executed to find a "good" candidate point [12] on the Response Surface Method (RSM).

From the algorithm perspective, there are no differences between a run on real analyses or on surrogated models, and this represents a trade-off between accuracy and simulation time. Models reproduce all the outputs of the simulation, including the constraints, in order to preserve results consistency.

The used metamodel, interpolated Radial Basis Functions (RBFs), use multi-quadratic, linear, cubic and thin-plate kernels; other numerical formulations, like approximated or neural-network-based, have been considered but not included.

Every time models are created or updated, their predictive capabilities were evaluated by means of cross-validation, using the R2press regression parameter (PRESS stands for Predicted Residual Error Sum of Squares). Every model is repetitively generated for datasets with one experiment removed and then evaluated on the missing experiment, to compare predicted and simulated results. The results of all these calculations are added into one regression value that, if close to 1, indicates that the model will perform well for points that were not simulated. Only the best model with the highest R2press was used for optimization. The automated validation and selection of the model with the higher predictive capability is part of the functionalities provided by the PIDO platform; the best kernel varied through the campaign but on average, cubic was the most exploited.

Initial value of the cross-validation (DOE only) was low, 0.3 or less in a range between -1 and $+1$, where $+1$ indicates that the model's predictions always match perfectly the reference (the model is iteratively re-built without a sample and the prediction is compared with the sample) whereas post-optimization values were between 0.65 and 0.7. This value is still not enough to provide results without proper validation; all the candidate configurations are investigated numerically and not just on the metamodel.

RBFs have been preferred over approximated ones (such as the least square) for the higher accuracy without significant overhead in their construction (in the order of a few seconds with 300 experiments, 8 inputs, 30 outputs), whereas like Kriging and Light Weight Neural Network had similar accuracy with slightly superior construction time.

Models assembly time was important as this operation was performed for each iteration.

4.5. Global Optimization Method

DEVOL was selected as the global optimization method to guarantee complete coverage of the design space even if its computational burden can represent a drawback. This was not the case for our problem as the evaluation of hundreds of candidate points on the surrogate models was executed in sub-second time. Other algorithms were tested (like Simulated Annealing) achieving comparable results; the accuracy of the RSM was significantly more relevant than the algorithm itself.

Subsequently, a proximity check was performed to avoid oversampling of the same design region and/or "cornered" RSMs, (measuring the distance between the proposed optimal point and the existing experiments). Differences in design variables ranges were removed through a normalization of the design space. The distance was determined using the design variable only, not the results of the simulation.

Candidate points within an arbitrary threshold were moved by a limited, random offset to preserve the general location but avoid duplicated samples, as would happen when the solver is trapped in a local minimum.

The random offset reduces but does not solve entirely, the potential oversampling problem, thus resulting in new experiments still focused on a specific region of the domain.

To address this limitation, a dedicated space-filling was performed; this improved the overall RSM and reduced the chances of local minima traps [16] by setting up one experiment in the less explored region of the design space.

The resulting continuous MaxMin optimization problem was replaced with a discretized version, based on a dense, support LHD [17]. The identification of the design point that has the maximum, minimum distance from all the existing ones requires the evaluation of the distance of all the points in the support from all the previous experiments. L1 norm was used both to reduce the effort and due to its representativeness in higher dimensions [18].

MaxMin and discrete space-filling offer comparable solutions (provided a dense enough support) for single-point applications, whereas if multiple experiments had to be added, the discrete space-filling

results were sub-optimal. This limitation has been considered acceptable due to the nature of the envisioned optimization method.

As a final step, the FEM simulations for both candidate and space-filling points were performed, and the results included in the DOE dataset used in the following iterations. From the operative point of view, running two experiments in a single batch was more efficient than 2 separated experiments. The adopted termination criterion was the total number of analyses, whereas the implementation of a convergence check was postponed to a later stage.

The simulation workflow illustrated in Figure 10 was constructed in Optimus to run the MDO process.
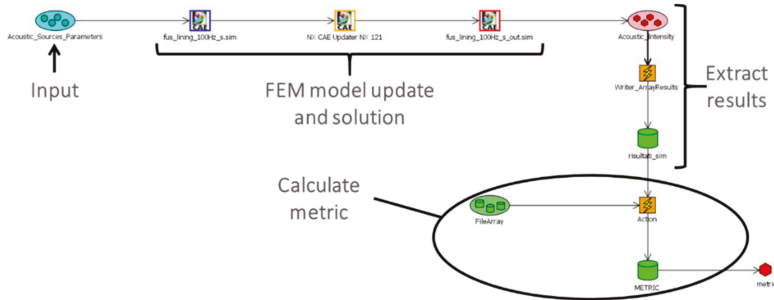

Figure 10. Optimus workflow to run the Multi-Disciplinary Optimization (MDO) process.

This optimization strategy made the structure flexible since the DOE results were independent of the chosen function for the metrics, i.e., the target function; the latter was defined in a python script loaded in the software when calculating the metrics (see Figure 10). The separation between the outputs generated by the simulations and the post processing allowed for different metrics to be tested preserving the experiments database.

The choice of the metric function was a key point of the work in order to get the most appropriate comparison between RC and SC data. Different functions were tested and the current choice (this aspect is still under study) is reported in Equation (1): it represents a normalized percentage difference among the AI values for each microphone:

$$\text{Normalized metric} = \frac{\sum_{i=1}^{n} \left| \frac{AI_i^{RC} - AI_i^{SC}}{AI_i^{RC}} \right|}{n} = \frac{\text{metric}}{n} \tag{1}$$

where n is the number of microphones, AIRC is the acoustic intensity array for the RC, and AISC is the acoustic intensity array calculated for each iteration. The metric is not entirely symmetric due to the normalization and the fact that AIs are positive only values; the normalization was required due to the reference values range that could be significantly different among the microphones.

5. Results

The MDO procedure iterated changing repeatedly the sound powers and phases of the monopole sources in such a way to get AIs at the microphones for the SCs as close as possible to the AIs calculated for the RC. The results for each SC are reported in the followings.

5.1. SC1 Results

SC1 optimization process was stopped after a predefined (500) number of iterations. The finally obtained AIs are shown in Figure 11 together with the RC data. Figure 12 shows the SC1 whole pressure field on the external skin of the fuselage, where the horizontal axis is the fuselage axis whereas the vertical axis is the angular coordinate around the fuselage.

Figure 11. Acoustic Intensities (AIs) measured at the 18 microphones (3 rings of 6 microphones each) compared between RC and SC1 (the ordinate axis does not cross the abscissa at a null value having to mask the magnitude values as prescribed by a non-disclosure agreement).

Figure 12. Overall pressure field [dB] on the external skin for SC1.

5.2. SC2 Results

SC2 optimization process elapsed nearly 320 iterations. The final comparison of the so obtained AIs at the microphone locations is shown in Figure 13 together with the RC ones. The whole pressure field on the external skin of the fuselage is reported in Figure 14.
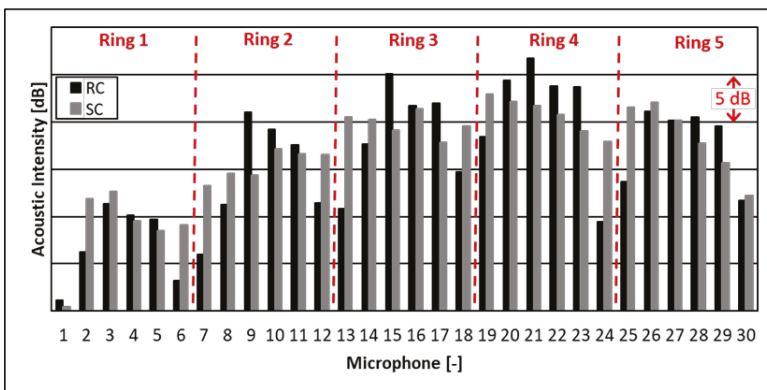
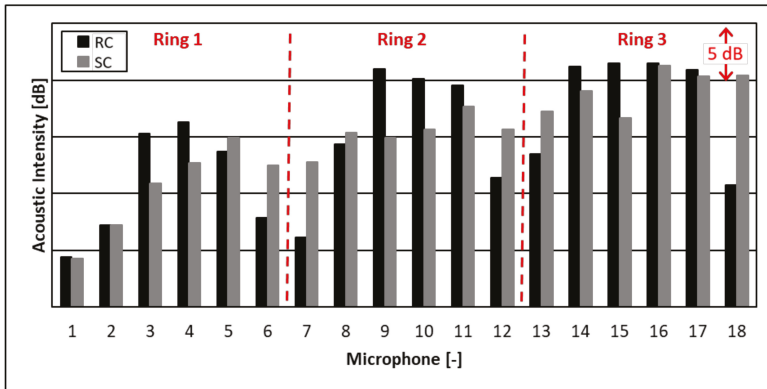**Figure 13.** AIs measured at the 30 microphones (5 rings of 6 microphones each) compared between RC and SC2 (the ordinate axis does not cross the abscissa at a null value having to mask the magnitude values as prescribed by a non-disclosure agreement).
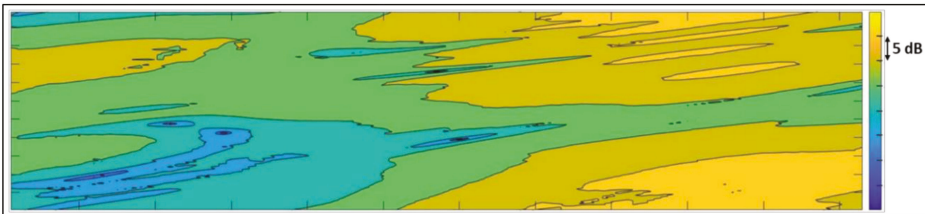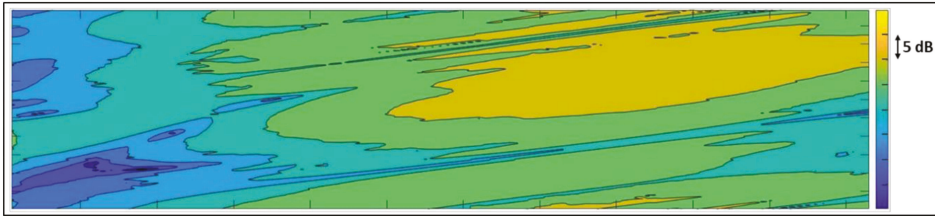
Figure 14. Overall pressure field [dB] on the external skin for SC2.

6. Discussion

Figures 11 and 13 show the comparisons between the SCs AIs at the microphones and the AIs for the RC. The reference pressure field in the volume surrounding the barrel is shown in Figure 15. The best metric values (Equation (1)) and the RSM quality R2press index are reported in Table 1.
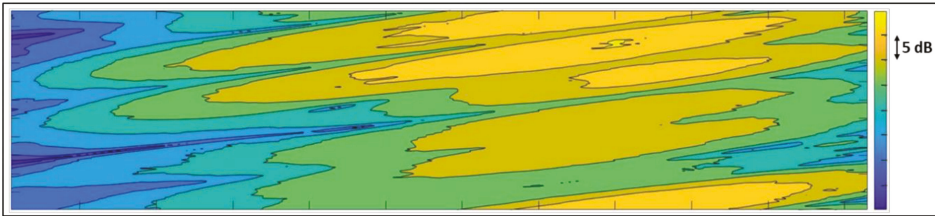
Figure 15. Overall pressure field [dB] on the external skin for RC.

Table 1. Best metric values and R^2_{press} for both SCs.

	Best Metric Value [-]	R^2_{press} [−]
SC1	0.039	0.951
SC2	0.047	0.983

The final metrics values are equal to nearly 4%–5%, stating that the average error between the reference and the simulated data was equal to nearly 4%–5% for each microphone. Such discrepancies were judged as acceptable, especially if considering the complexity of the study case here proposed for the presented optimization algorithm.

The evolutions of the metric values for the two considered SCs vs. iterations are reported in Figure 16. Scattering of data was given by the space filling algorithm, since a "far" candidate point was evaluated for each iteration, thus generally giving a higher metric value. However, the general trend happens to be decreasing for both SCs. This can be confirmed also in terms of R2press index (Table 1).
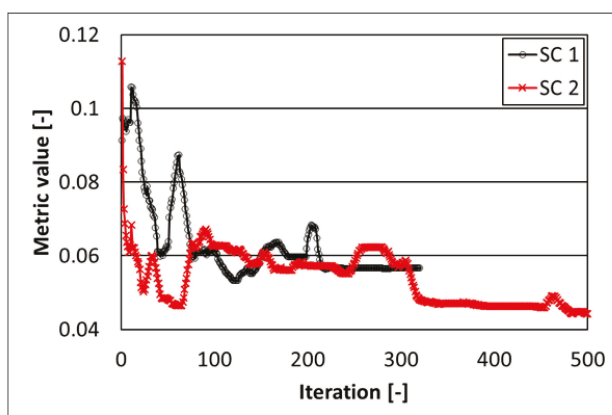
Figure 16. Metric value evolutions during iterations for the two SCs.

As a final outcome, the SC2 was judged as more adequate than SC1 to replicate the reference pressure field. This was attributed to the fact that as an overall the pressure field was better captured by the optimization procedure, see Figures 12, 14 and 15 for a qualitative comparison and Table 1 (correlation in terms of R2press index). Thus, the solution with an increased number of microphones rings (3 for SC1 to 5 for SC2) should be selected to better drive the optimization toward a more accurate sound field replication.

7. Conclusions

A novel optimization framework, based on a MDO procedure applied to the vibro-acoustic FEM model of a fuselage mock-up, has been presented in this work.

The MDO procedure, based on an EGO-like approach, has been adopted to characterize acoustic sources that replicate the sound pressure field generated by the engines on the fuselage. A predetermined sound pressure field was considered as a reference data, whereas two tentative sound fields were calculated by leveraging on the proposed FEM-MDO framework.

The comparisons between the reference and the calculated data in terms of pressure fields, quality indexes and metric values, have been judged as acceptable even if further refinements, considering different setup of monopole sources and microphone locations together with a different metrics, are currently under development.

The proposed FEM-MDO procedure can be considered as a potential tool to set up ground experimental tests on aircraft components to replicate their vibro-acoustic performances as if tested in flight.

References

1. Citarella, R.; Federico, L. Advances in Vibroacoustics and Aeroacustics of Aerospace and Automotive Systems. *Appl. Sci.* **2018**, *8*, 366. [CrossRef]
2. Barbarino, M.; Adamo, F.P.; Bianco, D.; Bartoccini, D. Hybrid BEM/empirical approach for scattering of correlated sources in rocket noise prediction. *J. Sound Vib.* **2017**, *403*, 90–103. [CrossRef]

3.   Barbarino, M.; Bianco, D. A BEM–FMM approach applied to the combined convected Helmholtz integral formulation for the solution of aeroacoustic problems. *Comput. Methods Appl. Mech. Eng.* **2018**, *342*, 585–603. [CrossRef]

4.   Bianco, D.; Adamo, F.P.; Barbarino, M.; Vitiello, P.; Bartoccini, D.; Federico, L.; Citarella, R. Integrated Aero–Vibroacoustics: The Design Verification Process of Vega-C Launcher. *Appl. Sci.* **2018**, *8*, 88. [CrossRef]

5.   Casalino, D.; Barbarino, M.; Genito, M.; Ferrara, V. Hybrid Empirical/Computational Aeroacoustics Methodology for Rocket Noise Modeling. *AIAA J.* **2009**, *47*, 1445–1460. [CrossRef]

6.   Lighthill, M.J. On sound generated aerodynamically I. General theory. *Proc. R. Soc. Lond. Ser. A Math. Phys. Sci.* **1952**, *211*, 564–587.

7.   Lighthill, M.J. On sound generated aerodynamically II. Turbulence as a source of sound. *Proc. R. Soc. Lond. Ser. A Math. Phys. Sci.* **1954**, *222*, 1–32.

8.   Williams, J.E.F.; Hawkings, D.L. Sound generation by turbulence and surfaces in arbitrary motion. *Philos. Trans. R. Soc. Lond. Ser. A Math. Phys. Sci.* **1969**, *264*, 321–342.

9.   Siemens PLM Software Inc. *Users' Manual*; NX Nastran 12.0.; Siemens PLM: Plano, TX, USA, 2019.

10.   Marburg, S. Six boundary elements per wavelength: Is that enough? *J. Comput. Acoust.* **2002**, *10*, 25–51. [CrossRef]

11.   Zaleski, O. Anforderungen an die Diskretisierung bei der Schallabstrahlungsberechnung. Ph.D. Thesis, Technische Universitat Hamburg-Harburg, Arbeitsbereich Meerestechnik II —Mechanik, Hamburg, Germany, 1998.

12.   *Optimus 2019.1–Users' Manual*; Noesis Solutions N.V.: Leuven, Belgium, 2019.

13.   *Optimus 2019.1–Theoretical Background for Optimus*; Noesis Solutions N.V.: Leuven, Belgium, 2019.

14.   Storn, R.; Price, K. Differential Evolution—A Simple and Efficient Heuristic for global Optimization over Continuous Spaces. *J. Glob. Optim.* **1997**, *11*, 341–359. [CrossRef]

15.   Jones, D.R.; Schonlau, M.; Welch, W.J. Efficient Global Optimization of Expensive Black-Box Functions. *J. Glob. Optim.* **1998**, *13*, 455–492. [CrossRef]

16.   McKay, M.D.; Beckman, R.J.; Conover, W.J. Comparison of Three Methods for Selecting Values of Input Variables in the Analysis of Output from a Computer Code. *Technometrics* **1979**, *21*, 239–245.

17.   Van Dam, E.; den Hertog, D.; Husslage, B.; Rennen, G. Department of Econometrics and Operations Research, Tilburg University, The Netherlands. 2009. Available online: http://www.spacefillingdesigns.nl/ (accessed on 5 March 2020).

18.   Aggarwal, C.C.; Hinneburg, A.; Keim, D.A. On the Surprising Behavior of Distance Metrics in High Dimensional Space. In *Computer Vision*; Springer Science and Business Media LLC: Berlin, Germany, 2001; Volume 1973, pp. 420–434.

Research on Leakage Location of Spacecraft in Orbit Based on Frequency Weighting Matrix Beamforming Algorithm by Lamb Waves

Lei Qi [1,2], Zhoumo Zeng [1], Yu Zhang [1,*], Lichen Sun [2], Xiaobo Rui [1], Xin Li [3], Lina Wang [2], Tao Liu [2] and Guixuan Yue [1]

[1] State Key Laboratory of Precision Measurement Technology and Instrument, School of Precision Instruments and Optoelectronics Engineering, Tianjin University, Tianjin 300072, China; qilei@tju.edu.cn (L.Q.); zhmzeng@tju.edu.cn (Z.Z.); ruixiaobo@126.com (X.R.); yueguixuan@tju.edu.cn (G.Y.)

[2] Beijing Institute of Spacecraft Environment Engineering, Beijing 100094, China; sunlichen-007@163.com (L.S.); wangxiweigood@163.com (L.W.); liutao_1224@163.com (T.L.)

[3] China Academy of Launch Vehicle Technology, Beijing 100076, China; lxlxlx-2002@163.com

* Correspondence: zhangyu@tju.edu.cn; Tel.: +86-022-2740-2366

Featured Application: The Frequency Weighting Matrix Beamforming Algorithm proposed in this paper has the potential to locate leakages in large structures such as spacecraft, and the algorithm can adapt the characteristics of leaks.

Abstract: Clashes between space debris and spacecraft in orbit may cause air leakages, which pose a substantial danger to the crew and the spacecraft. Lamb wave dispersion in spacecraft structures and the randomness of leak holes are the difficulties in leak location. To solve these problems, a frequency weighting matrix beamforming algorithm is proposed in this paper. The elastic Lamb waves that are caused by leakages are acquired by an 'L' shaped sensor array consisting of eight acoustic emission sensors. The angle of a leak can be obtained through the superposition of different time delays, and the intersection of two angles can be used to find the location of the leak. Traditional beamforming is improved by matching the wave speeds in different frequency bands and weightings according to the energy distribution. Narrowband filtering is used to delay overlay different signal speeds with different frequency bands via a dispersion curve. The weighting method is used to compensate the frequency band response of different leak holes. The detailed location algorithm process is introduced and verified by experiments. For 1.5 and 2 mm leak holes, location direction accuracies of 1.33° and 1.93° for one sensor array were obtained, respectively.

Keywords: leakage location; Lamb wave; beamforming; spacecraft in orbit

1. Introduction

Orbital objects, such as meteoroids and space debris, are among the serious and inevitable threats to spacecraft [1]. Technically, collisions caused by debris larger than 10 cm can be avoided by using databases that are compiled by debris-tracking systems [2]. Meanwhile, strikes by objects that are smaller than 10 cm lack an efficient detecting approach. A collision may damage the bulkhead of the spacecraft, causing internal pressure to leak, which seriously threatens the flight and the safety of astronauts and leads to severe consequences [3]. Thus, the detection and location of leakages would be of significant use for spacecraft in orbit.

For the problem of leak source location, some related findings have been reported. According to different principles, the currently representative methods include the optical imaging method [4],

the optical fiber method [5], the helium mass spectrometry method [6], and the acoustic detection method [7]. Compared with other methods, the acoustic detection method can achieve the non-destructive detection and real-time location of leakages in a larger range with a high location accuracy and stability. Moreover, acoustic sensors are easy to integrate with spacecraft structures, thus eliminating the need for complex processes such as laying optical fibers or using noble gases. Therefore, the acoustic detection method is a potential leakage location technology for spacecraft in orbit [8].

For leakage location based on acoustic methods, the key difficulty lies in the continuity of the leakage acoustic signal. For a collision with a time point of occurrence, location can be performed by calculating the time difference of arrival. To solve the above problems, Holland et al. [9,10] carried out research on cross-correlation and two-dimensional Fourier transform techniques to determine air leakages on the International Space Station (ISS). In the study, two 16×16 sensor arrays were applied to locate a leak. All possible cross-correlations between the 256 sensor positions in each array were recorded. A large number of sensors and millions of data samples led to a time- and finance-consuming task. Al-Jumaili et al. [11] proposed a T-mapping method. This method obtains time-domain eigenvalues from a prior meshing experiment and uses a clustering algorithm to identify the position of the signal source. This scheme has good adaptability to complex structures, but the initial workload is huge and it has no application potential for huge spacecraft.

In order to reduce the number of sensors and the algorithm complexity of the leak location scheme, the beamforming technique was firstly applied to the method of leakage detections with acoustic emission sensors by McLaskey et al. [12]. The beamforming algorithm has been primarily used in radar, sonar and exploratory seismology [13]. However, the specimen tested in their experiment was a steel-reinforced concrete bridge ramp instead of a thin plate. The work was based on Rayleigh wave theory, which is not applicable to the thin plates used in spacecraft. Tian et al. [14] tested a thin plate that was equipped with near-field beamforming analysis, which was suitable for Lamb wave theory. Burst acoustic emission signals that were created by breaking a mechanical pencil lead on the surface of the specimens were applied in their tests, and the propagation speeds of the signals were obtained by time difference of arrival (TDOA) techniques. This method is not ideal for a leak-generated continuous signal. However, the difficulties of using beamforming techniques for acoustic emission signal processing lie in the confirmation of wave speeds due to their dispersion. Zhang et al. [15] considered the effect of dispersion, but their scheme did not consider the diversity of the frequency bands that are generated by leakage in practical applications. Thus, it can be seen that the difficulties in the leakage location of thin plates such as those used spacecraft are the effects of dispersion on wave speed and the band adaptability of practical applications.

In order to solve the above problems and to improve the accuracy of the beamforming algorithm for leak location, a frequency weighting matrix beamforming (FWMB) algorithm is proposed in this paper. In this method, narrowband filtering is used to match the dispersion curve to achieve the matrix superposition of wave speeds at different frequencies. An energy evaluation on the frequency band of the signal is performed to determine the selected frequency band and its weighting coefficient matrix, and the weighting method is used to compensate for the frequency band response that is caused by different leaks to achieve a frequency band adaptation. The FWMB algorithm was validated by laboratory tests that used an L-shaped acoustic emission array, and its performance was evaluated. The method in this paper has the potential to be used in spacecraft in orbit due to its light weight and easy integration.

The remainder of this paper is organized as follows. In Section 2, the FWMB process is proposed. In Section 3, the experiment platform in the laboratory is introduced. In Section 4, the conducted experiments are described in order to demonstrate the performance of the FWMB algorithm. The conclusions are presented in Section 5.

2. Method

2.1. Delay-and-Sum Beamforming Algorithm

Beamforming is a mature digital signal processing technology that is commonly used in the fields of radar, sonar, and seismic detection. The basic idea of the beamforming algorithm is to calculate the energy of a wave in a certain hypothetical direction by summing the delays of the signal of each array element to give an estimate of the wave arrival direction. The beamforming method uses a sensor array with a fixed spatial position to measure the spatial sound field, and it processes the signals that are measured by each sensor to obtain detailed sound source information. In the leak detection method that is covered in this paper, the direction of a leak can be obtained by a set of sensors. The final location point can be obtained by the intersection of two sets of sensor arrays.

In beamforming algorithms, the choice of sensor array shape is critical. According to the characteristics of spacecraft structures, a planar array can be used for detection. The shape of a planar array is usually circular, square, triangular, cross, and the like. For spacecraft, the load needs to be as small and light as possible. Research by Cui et al. [16] showed that L-type arrays can obtain the best experimental results with the smallest number of sensors. Therefore, in the following research, an L-shaped array with 8 sensors was used as an example. Moreover, the method proposed in this paper is applicable to other array formats. The demonstration of the beamforming algorithm is shown in Figure 1.
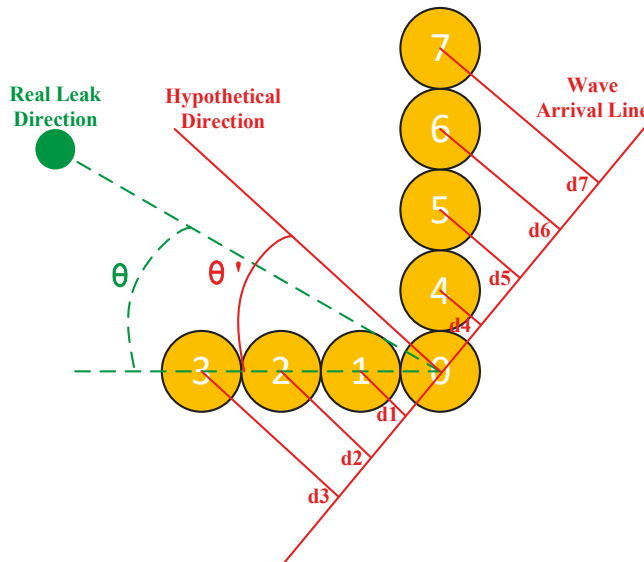
Figure 1. Demonstration of beamforming.

As shown in Figure 1, the sensor array in the figure is labeled n, including #0–7. Among them, the #0 sensor is for reference. When a leak occurs, sound waves propagate through the plate and are acquired by the sensor. $f(t,n)$ is defined as the signal that is acquired by each sensor at the time of t. The relative angle θ between the leak source and the array is defined as the actual direction of the leak source, and θ' represents the hypothetical direction.

When the distance between the sensor array and the leakage source is far greater than the size of the array, the signal waves are considered to propagate along parallel paths. Under this assumption, the signal sampled by the reference sensor #0 is the replica of time-delayed signals that are recorded by other array elements. The time delays between array elements are determined by both by the relative

distance from the signal source to array element #*n* compared to the reference sensor #0 under the direction of arrival and by the wave speeds. Usually, the direction of arrival is unknown; a hypothetical direction of arrival θ' is set. According to the geometric relationship of Figure 1, the time delay of each signal for #0 can be expressed as:

$$\Delta t_n = \frac{d_n}{v},\tag{1}$$

where d_n represents the relative distance as shown in Figure 1 and v represents the wave speed. d_n can be defined as:

$$d_n = \begin{cases} n \times d \times \cos\theta', [n = 1,2,3] \\ (n-3) \times d \times \sin\theta', [n = 4,5,6,7] \end{cases},\tag{2}$$

where d represents the distance between the sensors; this distance is the same as the diameter of the sensor and is 8 mm.

If θ' is consistent with the true angle θ, the signal will be concentrated through the superposition of time delay. Therefore, the signals of each sensor are delayed and superimposed to obtain the following delayed sum signal $g(t,\theta')$:

$$g(t, \theta') = \sum_{n=1}^{7} f(t - \Delta t, n) + f(t, 0),\tag{3}$$

The energy of the signal can be obtained by squaring and integrating the superimposed signal in the time domain. By scanning calculations for different hypothetical angles, an energy function $B(\theta')$ related to the angle can be obtained:

$$B(\theta') = \int g^2(t, \theta')) dt,\tag{4}$$

After obtaining the angle of the peak, it can be used as the result. The location of the leak source can be obtained by the intersection of the two arrays' straight lines.

2.2. Dispersion of Lamb Wave

Considering that the bulkhead structure of an orbiting spacecraft is a thin metal plate, due to its large curvature, it is approximated as a metal flat plate in this paper to simplify the research. In thin metal plates, ultrasonic waves propagate in the form of Lamb waves. Lamb waves have less attenuation than body waves, which is beneficial to the location of leaks. However, the propagation velocity of Lamb wave varies with wave frequency, which is called the dispersion characteristic of Lamb waves. Frequency dispersion complicates the characteristics of ultrasonic waves, and it is difficult to directly determine the speed of waves to complete the beamforming algorithm. As a consequence, studying the dispersion characteristics of Lamb waves is critical. There are two modes of waves—symmetric and anti-symmetric—that independently propagate in plates. By equipping a numerical method, equations known as the Rayleigh–Lamb frequency relations for both symmetric and anti-symmetric waves expressed as Equations (5) and (6) can be solved [17].

$$\text{Symmetric mode}: \frac{\tan(qh)}{q} + \frac{4k^2 p \tan(ph)}{(q^2 - k^2)^2} = 0,\tag{5}$$

$$\text{Anti-symmetric mode}: q\tan(qh) + \frac{(q^2 - k^2)^2 \tan(ph)}{4k^2 p} = 0,\tag{6}$$

where k represents the wave number, ω is the angular frequency, and d is the thickness of the plate.

When the thickness of a plate and the frequency of the signals are given, a set of numerical solutions, denoted by k_a and k_s, are acquired by solving the Rayleigh–Lamb equations. k_a and k_s

represent the wave numbers of anti-symmetric and symmetric waves, respectively. This phenomenon proves that multiple Lamb wave modes exist in the plate, and each mode has its own phase velocities and group velocities. The number of the numerical solutions increases with the frequency of the signals and the thickness of the plates, which means that the number of wave modes increases. Usually, symmetric modes are represented by $S_0, S_1, \ldots, S_n$, and anti-symmetric modes are represented by $A_0, A_1, \ldots, A_n$. In each mode, the corresponding phase velocity also varies with the frequency, and the phenomenon is called the frequency dispersion. Dispersion curves consist of a set of curves can be drawn to depict these characteristics. From the dispersion curves, the theoretical values of phase speeds at any particular frequency–thickness product of any specific mode can be obtained.

2.3. Frequency Weighting Matrix Beamforming Algorithm

The traditional beamforming algorithm and the dispersion phenomenon in the plate are introduced above. From the analysis, it can be understood that the traditional beamforming method has the following two difficulties for the leakage location of thin plates such as spacecraft shells:

(1)   Lamb wave velocity is difficult to determine, and there is an error in the delay matrix.
(2)   For practical applications, it is difficult to determine the characteristics of frequency bands by different leaks.

The FWMB algorithm that is proposed in this paper solves the above problems through the following two angles:

(1)   Narrowband filtering is used to delay different overlaid signal speeds with different frequency bands via the dispersion curve.
(2)   A weighting method is used to compensate the frequency band response of different leak holes in real applications. The weighting matrix is determined by the different energy ratios of different frequency bands to adapt to the frequency band changes.

A flowchart comparison between the traditional beamforming [18] and the FWMB algorithm is shown in Figure 2. In the figure, the main differences between the two algorithms are marked by a red border. The following describes the FWMB algorithm based on the traditional beamforming algorithm with some improvements in detail.

First, the frequency band of the signal needs to be determined. The signal from sensor #0 is processed by the fast Fourier transform and meshed at 10 kHz intervals (for example, 100–110 kHz). Since the number of points in each frequency band is consistent, all the values in each frequency band are summed and normalized as the energy value of the frequency band. The frequency bands that reach more than 50% of the peak value are reserved, and the bands are defined by the internal frequency as *f1, f2, ... , fk* (for example, 100–110 kHz is 105 kHz). The total number of the reserved frequency bands is *k*. The weight of the peak frequency band is 1, and the corresponding weights determine the frequency weighting matrix *mf1, mf2, ... , mfk* of the different frequency bands.

The signals of sensors #0–7 are narrow-band filtered on the above frequency bands to obtain a processed signal matrix. The processed signal is represented as $f_k(t,n)$. For leakage excitation in the thin plate, a large out-of-plane displacement is generated [19]. For the out-of-plane motion, compared to the A_0 mode, the energy of the S_0 mode in the Lamb wave is relatively small [17]. Because the beamforming method mainly focuses on energy, not the arrival time in the TDOA, the wave velocity of the A_0 mode is selected as the wave velocity for each bands. The wave velocity matrixes *sf1, sf2, ... , sfk* at the above frequencies are determined by the dispersion curve. Therefore, the signals of each sensor are delayed and superimposed to obtain the following delayed sum signal $h(t,\theta')$ (corresponds to $g(t,\theta')$ in Section 2.1.):

$$h(t,\theta') = \sum_{n=1}^{7}\sum_{k=1}^{K} mfk \times \left[f_k(t - \frac{d_n}{sfk}, n) + f_k(t,0) \right],$$
(7)
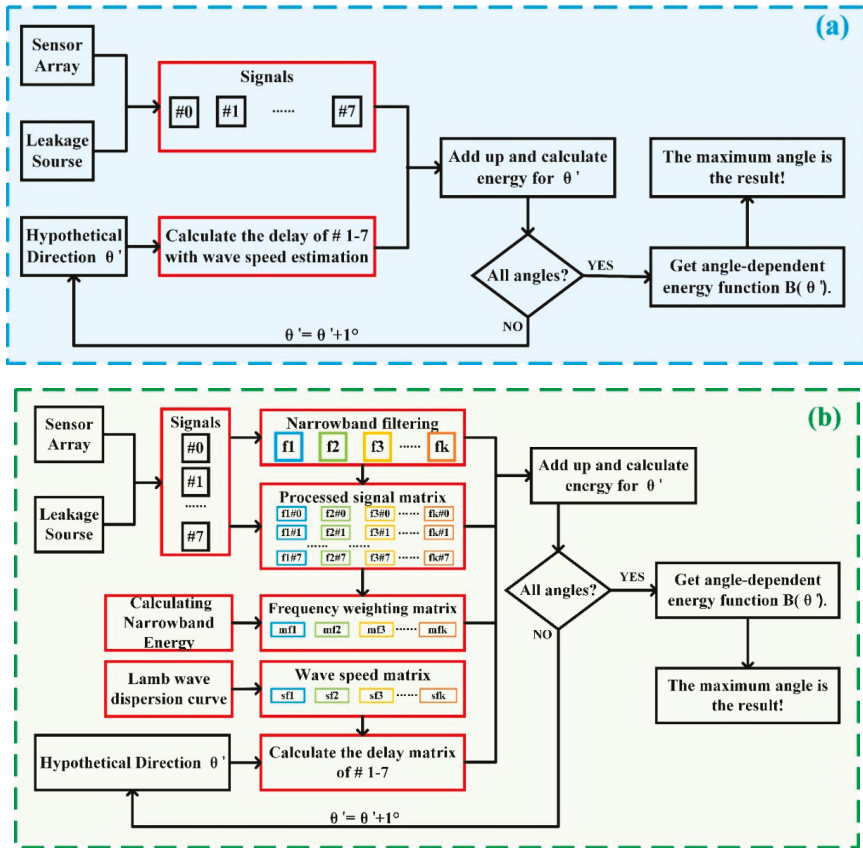
Figure 2. Algorithm flowcharts: (**a**) traditional beamforming algorithm and (**b**) frequency weighting matrix beamforming (FWMB) algorithm.

Through the above changes, the FWMB algorithm can improve the traditional beamforming algorithm's ability to locate thin plate leaks and its adaptability to different leaks.

3. Experimental Validation

3.1. Experimental Setup

The performance of the proposed method was evaluated experimentally. The experimental setup is first introduced in this section. The schematic diagram and photo of the experimental setup are shown in Figures 3 and 4, respectively.

A 5A06 aluminum alloy plate, which is consistent with the material of spacecraft bulkheads, was chosen. The test plate had a diameter of 100 × 100 cm and a thickness of 2 mm. A 1 mm diameter hole was drilled in the center of the board, and this was used to simulate the damage on the spacecraft. Grids with dimensions of 5 × 5 cm were drawn onto the plate to indicate the position of the sensor array.
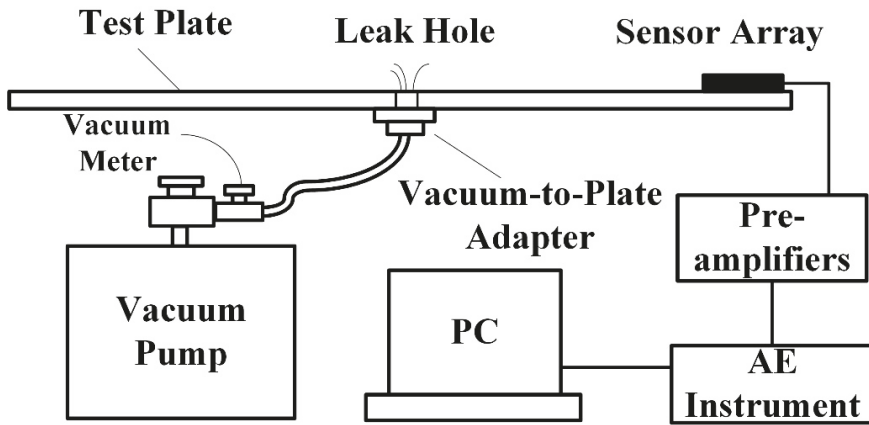
Figure 3. A schematic diagram of the experimental setup.
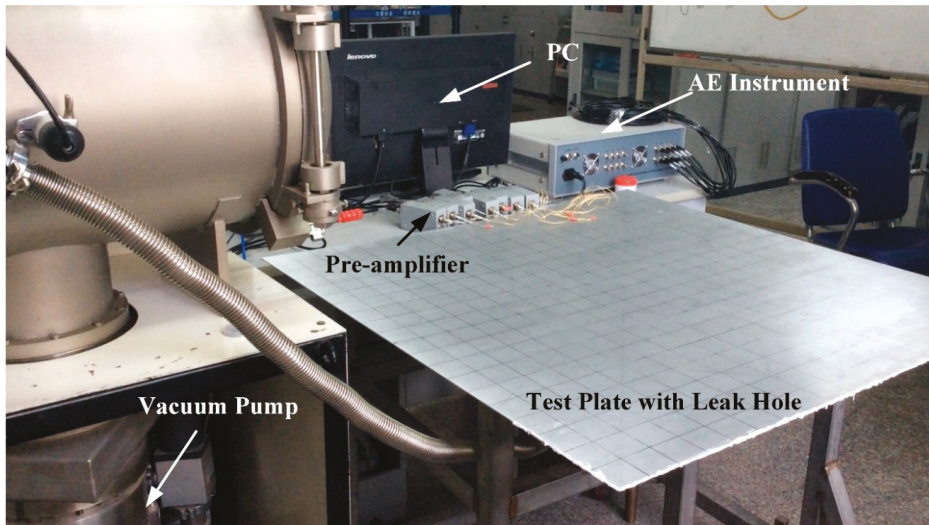
Figure 4. A photo of the experimental setup.

The vacuum pump was used to provide a stable leakage pressure differential to simulate actual leakage conditions. After putting the vacuum-to-plate adapter under the leak hole of the plate, the pumped was turned on until the adapter was attached tightly to the plate. After adjusting the vacuum pump control valve, the subsequent experimental research was able to be started when the measured value of the vacuum degree was less than 10,000 Pa.

The signal acquisition part of the experiment setup was made up by an acoustic emission sensor array, pre-amplifiers, and an acoustic emission instrument. The sensor used in the experiment was a Nano30 sensor (Physical Acoustics Corp., New Jersey, USA) that was 8 mm in diameter and 7.5 mm in height. The Nano30 sensor has a stable frequency response from 100 to 750 KHz. Eight sensors, numbered from 0 to 7, were fixed by special fixtures as 'L,' as shown in Figure 5. The piezoelectric acoustic emission sensors were mounted perpendicular to the plate. The elastic Lamb waves that were caused by the leakage were acquired by the sensor array, and the out-of-plane displacements were mainly measured [20]. The acoustic emission instrument was a DS2-16A instrument (Soft Island Corp.,

Beijing, China), which can realize multi-channel synchronous acquisition with a 3 MHz sampling rate. The sensors were connected to the pre-amplifiers (Soft Island Corp., Beijing, China). The signals were amplified by 40 dB through the preamplifiers and collected by the acoustic emission instrument.
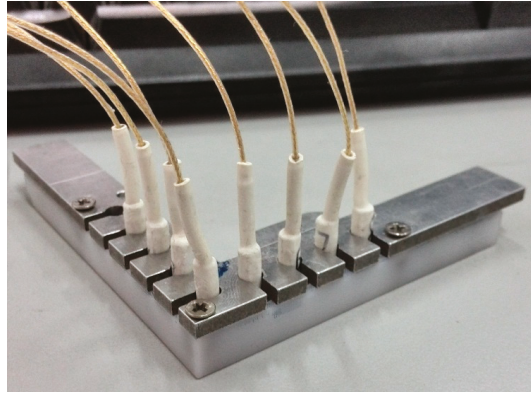
Figure 5. A photo of the sensor array.

3.2. Experimental Process

A hole located at (0, 0) was drilled into the plate, and it is marked as red circular in Figure 6. Once the set-up was equipped with the air exhaust system, the air evacuated from the hole to the vacuum-to-plate adapter could simulate the leakage. Leak-generated ultrasounds spreading through the plate as guided Lamb waves were acquired by the sensors. The sensor array was placed at position A, of which the actual azimuthal direction of the leak was 9°, and the signal sampling was started as depicted in Section 3.1. The collection of simultaneous leak signals of 8 sensors was repeated 5 times; each data series lasted 0.5 s and was split into 4 segments. Thus, a total of up to 20 segments of data at each position were gained at position A. A series of experiments was done with our array at 9 positions. The positions are marked with green marks in Figure 6. The corresponding azimuthal direction of the leak at positions B, C, D, E, F, G, H and I was 13°, 20°, 24°, 31°, 45°, 57°, 73°, and 79°, respectively. The distance from the sensor array to the leak source was maintained at R = 30 cm during the experiment. Thus, 180 segments of data were acquired in total for one leakage hole. In order to test the leakage of different holes to verify the adaptability of the method in this paper, two plates with 1.5 and 2.0 mm holes were used.

Figure 6. The position of sensor array in the experiment.

From the FWMB theory, the location of signal source can be determined by applying two sensor arrays. Thus, in the rest part of the paper, the orientation accuracy of the leak source is discussed instead of the positioning accuracy.

4. Results and Discussions

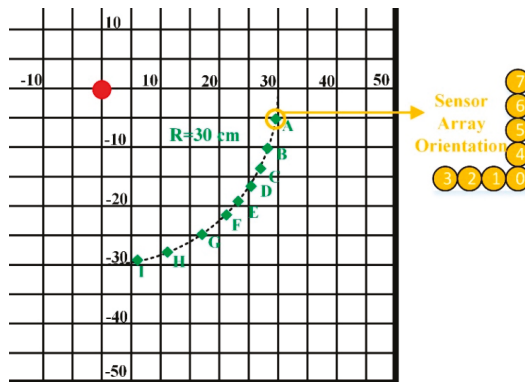In this section, the above experimental data are processed and described. First, by taking the experimental data as an example, the calculation method of the related matrix is demonstrated to introduce the method proposed in this paper. Subsequently, the results of the experiment are counted to evaluate the performance of the FWMB algorithm.

4.1. The Frequency Weighting Factors with Different Holes

One advantage of the FWMB algorithm is that it can be adaptively optimized for different leakage holes. In practical applications, the causes of leaks are abundant, so the shapes and sizes of leaks are various. For different leaks, the spectral characteristics may vary greatly. In order to verify this problem, 1.5 and 2.0 mm standard circular leaks were selected for testing.

Because signals below 100 kHz have strong background noises and signals above 500 kHz are very weak, signals between 100 and 500 kHz were chosen for signal processing. The time domain plot, frequency spectrum, and frequency weighting factors for the signals that were sampled at position A of sensor #0 are illustrated in Figure 7.
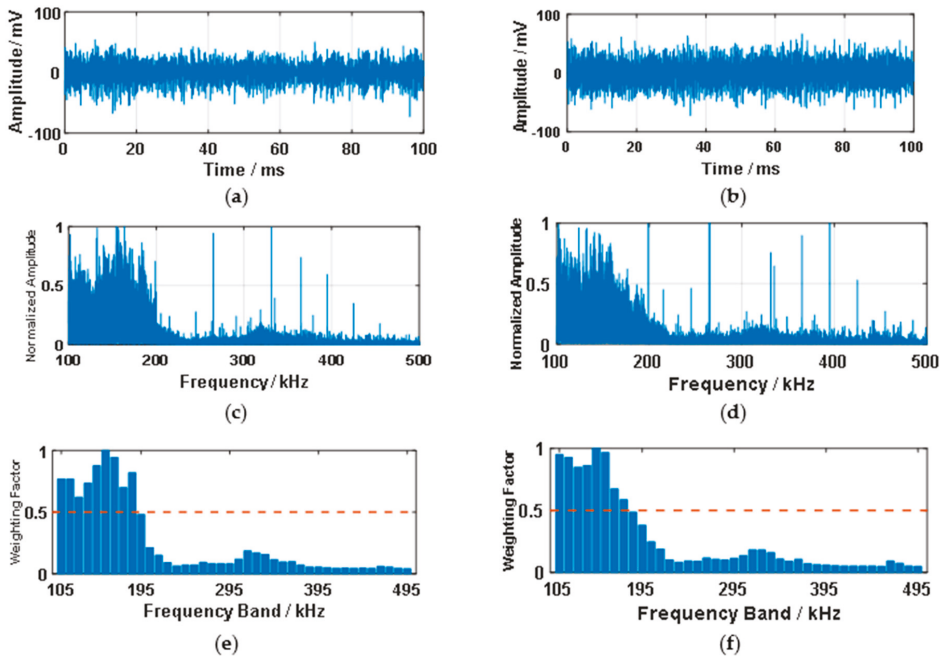
Figure 7. Time domain plot, frequency spectrum, and frequency weighting factors for different holes. (**a**) Time domain plot of a 1.5 mm hole in 100 ms, (**b**) time domain plot of a 2.0 mm hole in 100 ms, (**c**) frequency spectrum of a 1.5 mm hole, (**d**) frequency spectrum of a 2.0 mm hole, (**e**) frequency weighting factor of a 1.5 mm hole, and (**f**) frequency weighting factor of a 2.0 mm hole.

The amplitudes of the acoustic emission signals that were generated by the two leaks in the time domain were close, and from the waveform point of view, they were both difficult to obtain effective

information from and were confusing. After performing FFT on the signal, the spectrum energy of different frequency bands was integrated at 10 kHz intervals and normalized to obtain its weighting coefficient matrix. In the figure, the center frequency of the band is used as the label (for example, 100–110 kHz is represented as 105 kHz). It can be seen from the results that the acoustic emission signal that was generated by the 1.5 mm leak was in a higher frequency band. This is consistent with the physical understanding that smaller gaps result in sharper and higher frequency sounds.

In order to further optimize the algorithm, a band energy threshold was set. The bands with energy smaller than 50% of the peak value were discarded in subsequent processing. It can be seen from the figure that the 1.5 mm leak reserved nine frequency bands of 100–190 kHz, while the 2.0 mm leak reserved eight frequency bands of 100–180 kHz. For the above two leaks, although the frequency bands were similar, the weighting coefficients were significantly different. For holes with more specific shapes, larger differences will occasionally be encountered. The above results illustrate the adaptive ability of the method in this paper to different leaks.

4.2. The Speed Matrix

In the previous section, the frequency weighting matrix was obtained. In the FWMB algorithm, another key parameter is the wave velocity matrix. Its role is to accurately match the wave speed in different frequency bands to solve the wave speed error that is caused by the dispersion effect in the flat plate. From the perspective of beamforming theory, wave speed is a critical parameter. An inaccurate wave speed results in the wrong delay, which leads to the wrong location result.

Due to the dispersion characteristics of Lamb waves, signals with different frequency components have different phase velocities. It was assumed herein that the phase velocities were approximately the same in a narrow band of 10 kHz. The numerical solution of the Rayleigh–Lamb equation of the test plate is shown in Figure 8.
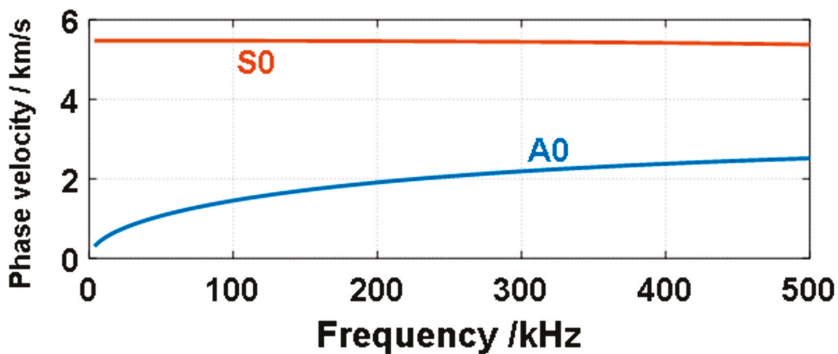
Figure 8. Dispersion curves of the A_0 (symmetric) and S_0 (anti-symmetric) mode waves for test plate.

The data were processed into eight or nine frequency bands by narrow band-pass filtering: 100–110, 110–120, . . . , 180–190 kHz. The corresponding phase velocities of different frequency components in the dispersion curve were recorded as a velocity matrix. For the low frequency thickness product, between 0.3 and 0.6 MHz · mm, there were only two wave modes (the A_0 and S_0 modes). Since the A_0 mode is dominant in the energy of the wave [17], the A_0 mode signal is discussed in the rest of this article. Table 1 lists the corresponding phase speeds c_p and the weighting factors in different frequency bands.

Table 1. Phase speeds of different frequency bands of the A_0 mode signals.

Frequency Band (kHz)	Phase Speed c_p (m/s)	Weighting Factor of 1.5 mm	Weighting Factor of 2.0 mm
100–110	1482	0.7679	0.9516
110–120	1537	0.7693	0.9269
120–130	1593	0.6198	0.8478
130–140	1640	0.7351	0.8617
140–150	1692	0.8770	1.0000
150–160	1735	1.0000	0.9669
160–170	1776	0.9451	0.6732
170–180	1815	0.6996	0.5864
180–190	1856	0.8209	/

Once the phase speeds and the geometry of a sensor array are given, the time delay matrix can be obtained via Equations (1) and (2). With the process in Figure 2, the FWMB algorithm can be produced. When the power gets its maximum, the corresponding assumed angle is the best estimate of the actual direction of arrival.

4.3. Location Results

This section gives a preliminary introduction and discussion of the location results. The 20° leakage at sensor array position C for 1.5 mm is taken as an example. Figure 9 shows the results of the traditional beamforming algorithm and the FWMB algorithm proposed in this paper.
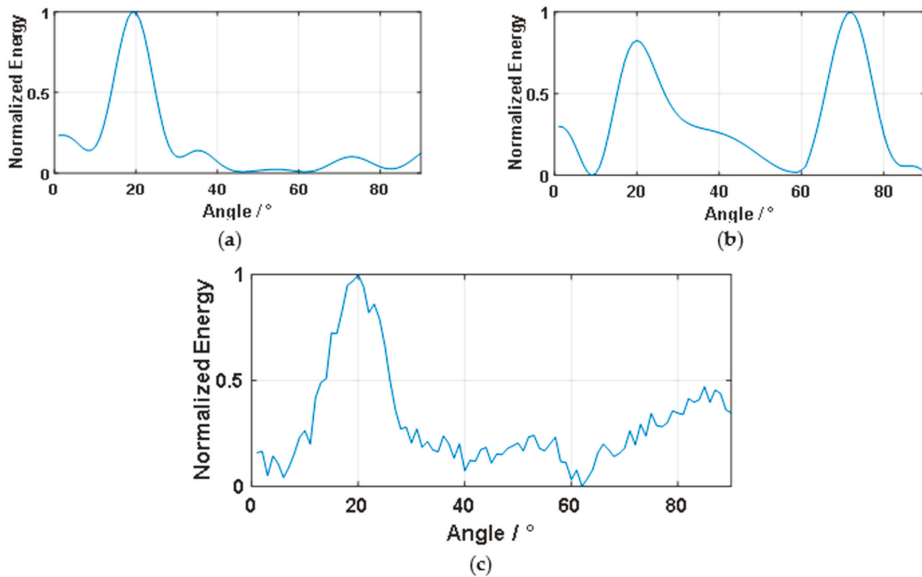
Figure 9. The results for the 20° with different algorithms. (**a**) Traditional beamforming with a 120–130 kHz filter, (**b**) traditional beamforming with a 150-160 kHz filter, and (**c**) result with the FWMB algorithm.

For the traditional beamforming, a separate frequency band is usually used to approximate the wave speed information. In order to have more contrast with the FWMB algorithm, a narrow band similar to that in the FWMB algorithm was selected. Figure 9a shows the results in the case of the 120–130 kHz filtering. It can be seen that a maximum value could be obtained near 20°, and a good

result was obtained. However, the obtained result was 19°, which, although very close to 20°, still had some errors. In Figure 9b, another frequency band is used as an example. In this example, two peaks appeared, although there was also a significant peak at 20°. However, a higher peak appeared at around 70° and misjudgment occurred. The reason for the above phenomenon is probably that the traditional beamforming only used one single narrow frequency band, and the energy carried by this frequency band was limited and not necessarily the largest. Therefore, there is a certain possibility that the superposition energy obtained from multiple angles was approximated, thereby obtaining multiple peaks. At the same time, the reflection was also a main interference factor for location. Though the energy was reduced for reflection, it was still a source of interference for positioning. The FWMB method can remove the effect of false peaks by superimposing more frequency band results. The above results show that the traditional beamforming algorithm is prone to errors because it uses less frequency band information and is less robust.

To overcome the above problems, under the conditions of this paper, 64 sets of data overlay were used in the FWMB algorithm to improve the eight sets of data overlay in the traditional beamforming. Therefore, it can be seen in Figure 9c that the result graph of the FWMB algorithm has more fluctuations compared to traditional beamforming. Though the data are not smooth, more accurate results were obtained due to the weighted superposition of the multiple sets of frequency band data. In view of the above preliminary conclusions, we show the data of several other points as further displays.

The results for the leakages in positions I and B are shown in Figure 10. The graphics use a circular coordinate system for easier display and understanding. The red curve and angle value represent the FWMB result, and the blue curve and angle value represent the traditional beamforming result. The frequency band in the label indicates that it is used in traditional beamforming. For the FWMB algorithm, the frequency band is adaptive and does not require manual selection.
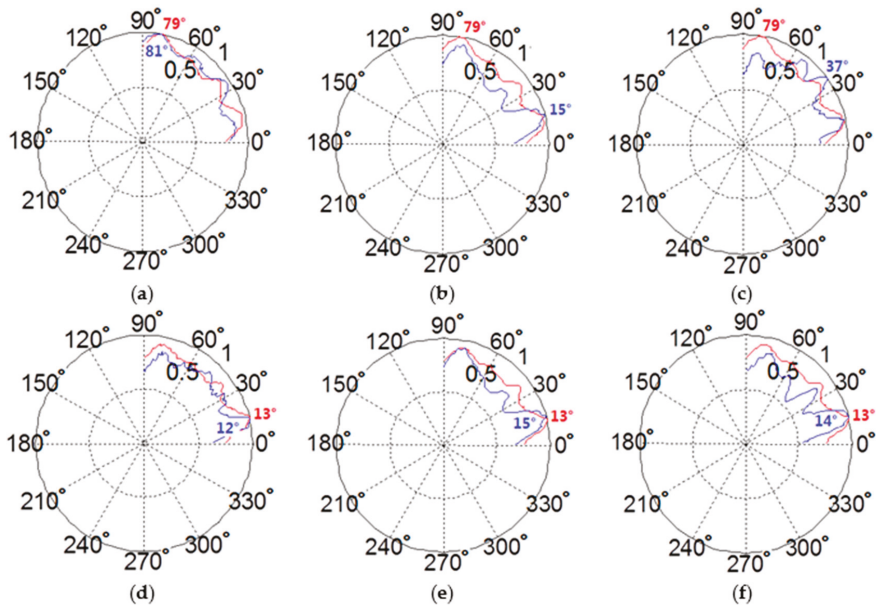
Figure 10. The results for the leakages in position I (real angle = 79°) with a 1.5 mm hole and position B (real angle = 3°) with a 2.0 mm hole by different algorithms in polar coordinates. The polar axis value represents the normalized energy. Red and blue curves represent the normalized energy results with the FWMB algorithm and the traditional beamforming, respectively. (**a**) "I," 1.5 mm, 100–110 kHz; (**b**) "I," 1.5 mm, 110–120 kHz; (**c**) "I," 1.5 mm, 120–130 kHz; (**d**) "B," 2.0 mm, 100–110 kHz; (**e**) "B," 2.0 mm, 110–120 kHz; and (**f**) "B," 2.0 mm, 120–130 kHz.

It can be further seen from the results that the FWMB algorithm optimized the results from two perspectives for traditional beamforming. First, due to the matrix-type multi-data superposition, the discrimination of the results was further enhanced and small errors were resolved, such as within 2° in Figure 10a,d,e,f. In addition, through the selection of the energy band and the calculation of the weighting coefficient, the situations where multiple peaks appeared and misjudgment occurred, such as in Figure 10b,c, were improved.

It can also be seen that the FWMB algorithm results also had obvious fluctuations. For example, there is a multiple peak at about 13° in Figure 10a–c. This shows that the FWMB algorithm may have misjudged the location, especially when the leakage was near the edge, which was mainly related to the reflection of the boundary. However, due to the large number of FWMB overlays, this problem was compensated for by averaging, and correct results were almost obtained.

4.4. Results Statistics and Evaluation

This section summarizes the results and evaluates the performance of the FWMB algorithm. The statistics of the leakage angle location results for two different holes are shown in Figure 11. The upper and lower ends of the error bar in the figure indicate the maximum and minimum values in the measurement data.
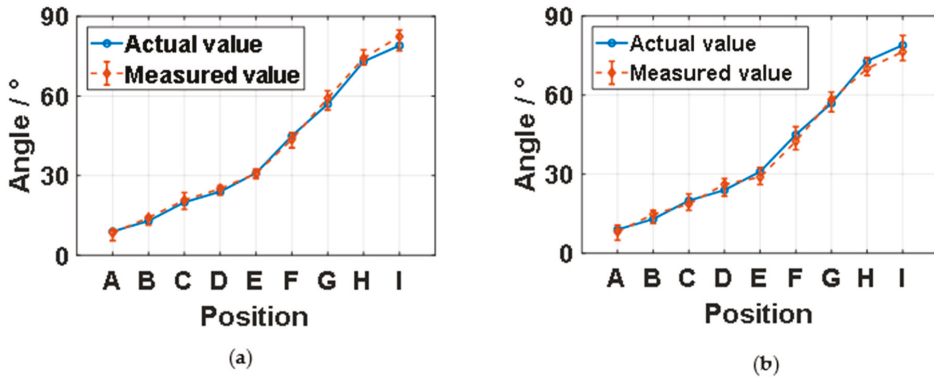
Figure 11. Result statistics for different sensor positions (A–I). (**a**) The results statistics of a 1.5 mm hole, and (**b**) the results statistics of a 2.0 mm hole.

As can be seen from the figure, the FWMB algorithm was able to get a close location result for different angles. Judging from the average error, reading errors of 1.33° and 1.93° were obtained in the holes of 1.5 and 2.0 mm, respectively, and the comprehensive error was 1.63°. The above results prove that the FWMB method proposed in this paper is adaptive to different leaks. The above advantages are obtained by weighting the energy ratios of different frequency bands in the FWMB method. Due to the use of narrow frequency band, the dispersion problem of Lamb waves is solved, and the wave velocity parameter in the algorithm is more accurate.

4.5. Discussion and Prospection

The above experiments confirm the improvement of traditional beamforming by the FWMB algorithm. However, the FWMB algorithm still has some issues that need to be addressed in future research.

- The leak hole that was used in this paper was a circular hole. In subsequent research, irregular holes that are caused by real collisions will be tried to more comprehensively evaluate the effectiveness of the method.

- This paper evaluated the positioning performance at different angles, and further experimental and theoretical analyses of the effective distance of the method and the key influencing factors will be made in subsequent research centers.
- Boundary reflection is also an important factor that causes mispositioning, and no relevant experiments were done in this paper. For large spacecraft structures, the attenuation of waves reduces the effects of reflections. However, the above issues are still worthy of discussion and research. In subsequent experiments, a non-reflective case by adding sound-absorbing cement can be tried.
- In an actual application environment, the structure may have complex structures such as curved surfaces or stiffeners. The effectiveness or compensation method of the FWMB algorithm is also worthy of attention and research.
- The ability to locate leaks at different locations needs to be further evaluated, especially for leaks that are close to the boundary. Though the FWMB algorithm's multi-layer overlay scheme can obtain more accurate results, there will still be multi-peak situations, and the algorithm needs to be improved in the follow-up.

In summary, for continuous leakage, the FWMB algorithm provides significant improvements. In subsequent developments, optimization and further testing are needed based on actual applications.

5. Conclusions

This paper proposes a frequency weighting matrix beamforming algorithm to solve the problem of locating continuous leaking sound sources in plate structures. Compared with the traditional beamforming algorithm, this algorithm uses a narrow frequency band to match the wave speed to solve the influence of the Lamb wave dispersion of the thin plate on the signal positioning. Through the energy-weighted method, the algorithm can adapt to different leaks, which has obvious advantages in application. The above scheme was verified through experiments, and 1.5 and 2 mm leaks were tested. The results showed that the frequency weighting matrix beamforming algorithm that is proposed in this paper can obtain a location accuracy of 1.63°. The above results can be used for the leak detection of on-orbit spacecraft, because the shape of the leak holes that are generated by space debris is inconsistent, so the adaptability of this method can solve the above problems.

References

1. Bradley, A.M.; Wein, L.M. Space debris: Assessing risk and responsibility. *Adv. Space Res.* **2009**, *43*, 1372–1390. [CrossRef]
2. DeLuca, L.T.; Bernelli, F.; Maggi, F.; Tadini, P.; Pardini, C.; Anselmo, L.; Grassi, M.; Pavarin, D.; Francesconi, A.; Branz, F.; et al. Active space debris removal by a hybrid propulsion module. *Acta Astronaut.* **2013**, *91*, 20–33. [CrossRef]
3. Losacco, M.; Schirru, L. Orbit Determination of Resident Space Objects Using the P-Band Mono-Beam Receiver of the Sardinia Radio Telescope. *Appl. Sci.* **2019**, *9*, 4092. [CrossRef]
4. Dykema, J.A.; Anderson, J.G. A Methodology for Obtaining on-orbit SI-traceable Spectral Radiance Measurements in the Thermal Infrared. *Metrologia* **2006**, *43*, 287–293. [CrossRef]
5. Klar, A.A.; Linker, R.; Herrmann, S. Leakage-induced pipeline stressing and its potential detection by distributed fiber optic sensing. *Geotech. Eng.* **2019**, *50*, 85–90.

6. Wang, G.; Li, N.; Li, W.; Li, F.; Wu, W.; Liu, Y. Important Improvements of Helium Mass Spectrometry Test for Sealability. *J. Electr. Electron. Eng.* **2019**, *7*, 8–22. [CrossRef]

7. Li, Y.; Wang, Z.; Rui, X.; Qi, L.; Liu, J.; Yang, Z. Impact Location on a Fan-Ring Shaped High-Stiffened Panel Using Adaptive Energy Compensation Threshold Filtering Method. *Appl. Sci.* **2019**, *9*, 1763. [CrossRef]

8. Bian, X.; Zhang, Y.; Li, Y.; Gong, X.; Jin, S. A new method of using sensor arrays for gas leakage location based on correlation of the time-space domain of continuous ultrasound. *Sensors* **2015**, *15*, 8266–8283. [CrossRef] [PubMed]

9. Holland, S.D.; Roberts, R.; Chimenti, D.E.; Strei, M. Leak detection in spacecraft using structure-borne noise with distributed sensors. *Appl. Phys. Lett.* **2005**, *86*, 174105. [CrossRef]

10. Holland, S.D.; Roberts, R.; Chimenti, D.E.; Song, J.H. An ultrasonic array sensor for spacecraft leak direction finding. *Ultrasonics* **2006**, *45*, 121–126. [CrossRef] [PubMed]

11. Al-Jumaili, S.K.; Pearson, M.R.; Holford, K.M.; Eaton, M.J.; Pullin, R. Acoustic emission source location in complex structures using full automatic delta T mapping technique. *Mech. Syst. Signal Process.* **2016**, *72*, 513–524. [CrossRef]

12. McLaskey, G.C.; Glaser, S.D.; Grosse, C.U. Beamforming array techniques for acoustic emission monitoring of large concrete structures. *J. Sound Vib.* **2010**, *329*, 2384–2394. [CrossRef]

13. Cao, Y.; Zhao, N.; Chen, Y.; Jin, M.; Fan, L.; Ding, Z.; Yu, F.R. Privacy Preservation via Beamforming for NOMA. *IEEE Trans. Wirel. Commun.* **2019**, *18*, 3599–3612. [CrossRef]

14. He, T.; Pan, Q.; Liu, Y.; Liu, X.; Hu, D. Near-field beamforming analysis for acoustic emission source localization. *Ultrason.* **2012**, *52*, 587–592. [CrossRef] [PubMed]

15. Zhang, Y.; Wang, J.; Bian, X.; Huang, X.; Qi, L. A continuous gas leakage localization method based on an improved beamforming algorithm. *Meas.* **2017**, *106*, 143–151. [CrossRef]

16. Cui, X.; Yan, Y.; Hu, Y.; Guo, M. Performance comparison of acoustic emission sensor arrays in different topologies for the localization of gas leakage on a flat-surface structure. *Sensors Actuators A: Phys.* **2019**, *300*, 111659. [CrossRef]

17. Rose, J.L. *Ultrasonic Guided Waves in Solid Media*; Cambridge university press: Cambridge, UK, 2014.

18. Qi, L.; Sun, L.; Meng, D.; Wang, Y.; Sun, W.; Yan, R. *A Method for Leak Detection of Spacecraft in Orbit Based on Beam-Forming[C] World Conference on Acoustic Emission*; Springer: Cham, Switzerland, 2017; pp. 421–427.

19. Tsuda, H.; Ohiwa, K.; Urabe, K. Response of Michelson interferometric fiber-optic sensors to plate waves generated by out-of-plane motion. *J. Mater. Sci. Lett.* **2001**, *20*, 983–985. [CrossRef]

20. Theobald, P.D. Optical calibration for both out-of-plane and in-plane displacement sensitivity of acoustic emission sensors. *Ultrasonics* **2009**, *49*, 623–627. [CrossRef] [PubMed]

Substructuring of a Petrol Engine: Dynamic Characterization and Experimental Validation

Enrico Armentani [1], Venanzio Giannella [2,*], Roberto Citarella [2], Antonio Parente [3] and Mauro Pirelli [3]

[1] Department of Chemical, Materials and Production Engineering, University of Naples Federico II, P.le V. Tecchio, 80, 80125 Napoli, Italy; enrico.armentani@unina.it

[2] Department of Industrial Engineering, University of Salerno, via Giovanni Paolo II 132, 84084 Fisciano (SA), Italy; rcitarella@unisa.it

[3] Fiat Chrysler Automobiles (FCA) Powertrain S.p.A., via ex Aeroporto, 80038 Pomigliano D'Arco (NA), Italy; antonio.parente2@fcagroup.com (A.P.); mauro.pirelli@fcagroup.com (M.P.)

* Correspondence: vgiannella@unisa.it; Tel.: +39-089-96-4111

Abstract: In this work, the vibration behavior of a 4-cylinder, 4-stroke, petrol engine was simulated by leveraging on the Finite Element Method (FEM). A reduced modelling strategy based on the component mode synthesis (CMS) was adopted to reduce the size of the full FEM model of the engine. Frequency response function (FRF) analyses were used to identify the resonant frequencies and corresponding modes of the different FEM models, and the obtained results were compared with experimental data to get the model validation. Subsequently, modal-based frequency forced response analyses were performed to consider the loads acting during the real operating conditions of the engine. Finally, the impact on vibrations at the mounts, produced by an additional bracket connecting the engine block and gearbox, was also investigated. Both the full and reduced FEM model demonstrated and reproduced with high accuracy the vibration response at the engine mounts, providing a satisfactory agreement with the vibrations measured experimentally. The reduced modelling strategy required significantly shorter runtimes, which decreased from 24 h for the full FEM model to nearly 2 h for the reduced model.

Keywords: FEM; component mode synthesis; petrol engine; NVH; FRF

1. Introduction

Due to the ever-increasing complexity of problem solving and the limitations of power computing, several methods have been developed, since the early days of numerical computation, to improve the efficiency of numerical simulations. Many techniques have been investigated to reduce the computational effort required to solve large static and dynamic problems. Modal analysis techniques have been developed to decouple the large set of ordinary differential equations and to minimize the effort required to solve an iteration of the equations of motion [1,2]. Substructuring methods have been developed to approximate complex big structures as a collection of smaller single components, allowing the simulation process to be performed in a sequence of intermediate computationally lighter steps. These advances proved beneficial, especially in the simulation of dynamic systems, which require the solution of equations of motion over large time intervals and with many individual time steps.

Accurately assessing the dynamic behavior of these elements requires the use of large finite element (FE) models [3–7] to represent the geometry in considerable detail. Assembling the individual sub-components to build up a global FE model of the entire structure results in very large models having a degrees of freedom (DoFs) number which easily exceeds the limits of computer capacity, at least for reasonable runtimes. The question arises whether such FE models can be reduced in

size, preserving at the same time the capability to represent the dynamic characteristics of the entire structure with sufficient accuracy. The substructuring method leverages on dividing a large model into subcomponents that are separately analyzed and afterward re-assembled in a global model, through coupling of their mathematical description.

In recent decades, a variety of methods aimed at a model order reduction of dynamic problems have been developed within the area of structural mechanics, with mode-based methods being the most frequently used. Fairly recently, methods originating from control theory have been employed within structural mechanics. In contrast to mode-based methods, which have an explicit physical interpretation, such modern reduction methods are developed from a purely mathematical point of view, see, e.g., [8–11].

Due to several contributors, such as unbalanced reciprocating and rotating parts, cyclic variations in gas pressure generated by the combustion process, misfire, and inertia forces of the reciprocating parts, significant levels of vibration are induced in internal combustion engines (ICEs). The vibration signals are categorized as torsional, longitudinal, and mixed vibrations. Torsional vibrations are mainly caused by the exertion of cyclic combustion forces within the cylinder as well as the inertial forces of rotating parts, such as the crankshaft, camshaft, and connecting rods. The primary sources of longitudinal vibrations are the unbalanced forces acting on reciprocating and rotating components of the engine which propagate in the structure. The interactions of both longitudinal and torsional vibrations are called mixed vibrations. The inertial forces of rotating components, as well as harmonic combustion forces in the cylinders, eccentric rotation of journal bearing support and flywheel, and transient contact dynamics of the cam/follower, are further contributors to the problem of vibrations in ICEs. Noises generated by these vibrations are transmitted through the engine mounts and chassis to backrests, which can affect passenger comfort and the safety of the vehicle. The level of safety and vibration isolation depends on the amplitude, wave shape, and duration of exposure to these noises. In the review paper [12], different types of vibration in ICEs and their fundamental sources can be found.

In the proper use of the engine mounting system (EMS), when a high transmission ratio is selected, the vibration and noise can be remarkably isolated before they are transferred to the chassis and body of the vehicle. EMS plays an inevitable role in isolating the driver and passenger from the noise, vibration and harshness (NVH) produced by power-intensive engines in modern light-weight vehicles. Therefore, the performance and reliability of these systems require further improvements for a better NVH refinement.

To minimize the transmitting vibrations, the stiffness of the engine block can be enhanced by applying structural modifications such as thickening the crankcase walls, front gear cover, back flywheel cover, as well as adding ribs to its driveshaft.

In a numerical work by Junhong and Jun [13], finite element analysis (FEA) and multi-body analysis (MBA) tools were implemented for modeling the dynamics of the acoustical components of a six-cylinder in-line diesel engine, and also to understand the interaction between excitation mechanisms and noise transmission in the system. To minimize the vibration transferred through the internal paths and to enhance the structural stiffness of the engine, a modification to the design was proposed, namely adding ribs to the drive shaft of the engine.

In the present study, a substructuring technique is applied to a car petrol engine, modelled considering explicitly all its sub-components, i.e., gearbox, exhaust system, alternator, etc.

The objective of the analyses carried out in the present investigation was to validate the adopted approach, based on the component mode synthesis (CMS), to assess the vibrational behavior of an in-line 4-cylinder, 4-stroke, petrol engine, with manual transmission and a total displacement of 1200 cc. A reference solution for the engine was provided by a full FEM model and experimental results from dynamic bench tests were also available as a benchmark.

A frequency response function (FRF) analysis was used to identify the resonant frequencies and mode shapes of the different FEM models. The results were compared in terms of the vibrational

response at the mounts, i.e., the gear mount and the engine mount. Experimental results were also available and used for the FEM model validation.

The commercial FEM code MSC Nastran [14] was selected as the FEM solver whereas the commercial code Siemens LMS Virtual Lab [15] was used for the dynamic analyses.

The proposed CMS-based strategy provides the opportunity to circumvent non-disclosure limitations when dealing with original equipment manufacturers (OEMs), since only the subset of few strictly needed data can be exchanged with OEMs without affecting the accuracy of their calculations for those parts of the powertrain designed and manufactured in outsource. Moreover, a further validation concerning the accuracy of such an approach when dealing with complex problems was provided in this work.

2. Full FEM Engine Modelling

The FEM model of the entire engine created by means of the commercial code Altair Hypermesh [16] is shown in Figure 1. Tetrahedral quadratic elements were used to model components such as the engine crankcase, cylinder head, crankshaft, gearbox, etc., whereas quadrilateral quadratic surface elements were used to model thin elements such as the exhaust pipe or the oil pan. Bar elements were used to model the bolts that connect the various components. The average element size was set to 3–6 mm. The final full FEM model comprised nearly 5.7×10^6 elements and 4.7×10^6 nodes.
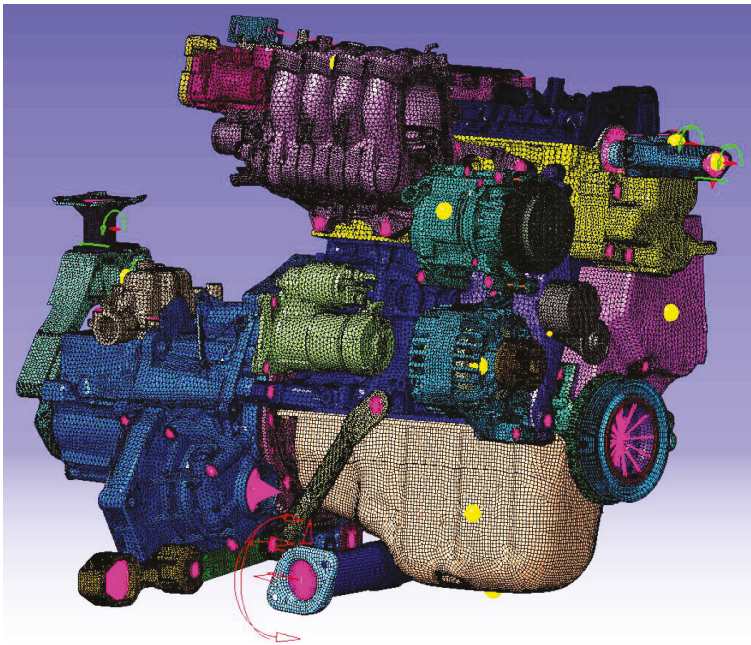
Figure 1. FEM model of the engine with all its sub-components.

In order to validate the full FEM model, two frequency response function (FRF) analyses were performed: one for the vertical bending and one for the lateral bending. An FRF analysis consists of the application of a unitary force in a given node, followed by measurements of the related accelerations in different nodes of the model. Such relevant points selected for the FRF analyses of the engine are shown in Figure 2 for both the vertical and the lateral bending load case. These numerical analyses replicated the experimental tests previously performed and the results are compared in the following section.

(**a**)

(**b**)

Figure 2. Full FEM model with details of the relevant points for the FRF analyses for load cases of (**a**) vertical bending and (**b**) lateral bending.

The FEM model was imported in the MSC Nastran to calculate the modal basis of the engine up to a frequency of 1500 Hz (the Lanczos algorithm was used for such a purpose). A damping coefficient equal to 0.03 was considered for all the structural elements. Subsequently, the modal basis was imported in the Siemens LMS Vir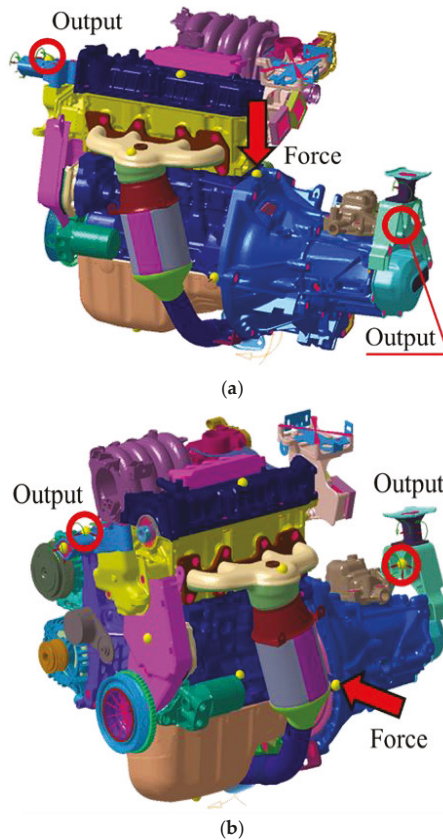tual Lab environment, with input and output points defined for either the vertical (Figure 2a) or lateral (Figure 2b) bending. Finally, FRF and modal-based frequency response analyses were performed to calculate the accelerations at the relevant points.

A free-free condition was simulated in all the presented cases. As a matter of fact, the engine mounts are capable of decoupling the dynamic engine behavior from the supporting structure in the whole frequency range considered.

Moreover, the impact of the crankcase–gearbox bracket shown in Figure 3 on the acceleration levels at the previously mentioned relevant points was assessed. Such evaluation was needed to understand whether the impact on the dynamic behavior of the engine was necessary, since its removal would have a positive impact on cost reduction.
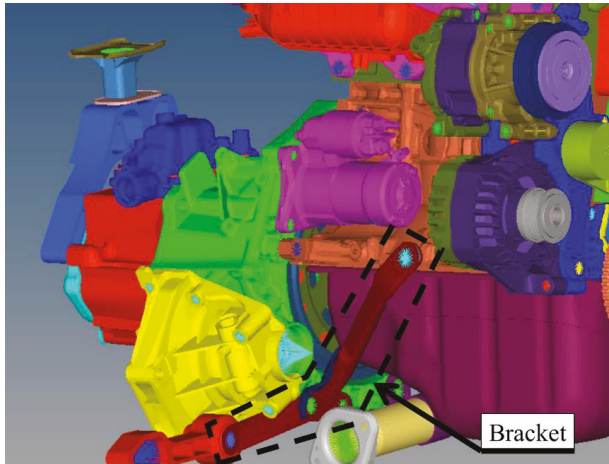
Figure 3. Close up of the crankcase–gearbox bracket under analysis.

3. FRF Results of the Full FEM Model

The accelerations were calculated at the engine and gear mounts for the two analyses of vertical and lateral bending (Figure 2). The ratio between acceleration and input force is shown in Figures 4 and 5. In particular, Figure 4 shows results for the vertical bending at both mounts, with and without the engine bracket shown in Figure 3. It is worth noting that the impact of the engine bracket was much more relevant for the vertical bending load case (Figure 4), whereas it played a minor role for the lateral bending load case (Figure 5). This result was expected due to the geometry of the bracket, which allows it to stiffen the engine–gearbox connection, especially when undergoing vertical loads.
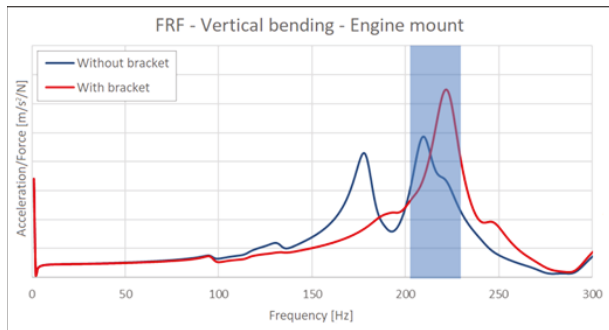
(**a**)

Figure 4. *Cont.*
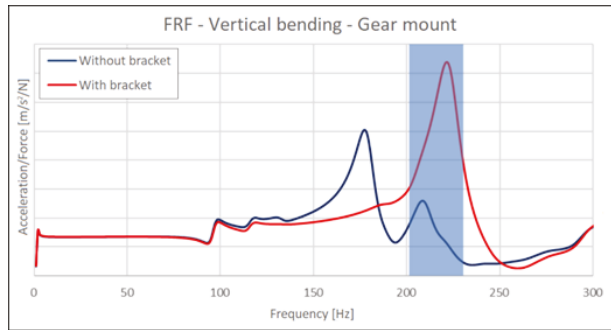
(**b**)

Figure 4. Acceleration/force ratio for the full FEM model for the vertical bending load case with and without the crankcase–gearbox bracket (shown in Figure 3) at: (**a**) engine mount; (**b**) gear mount.
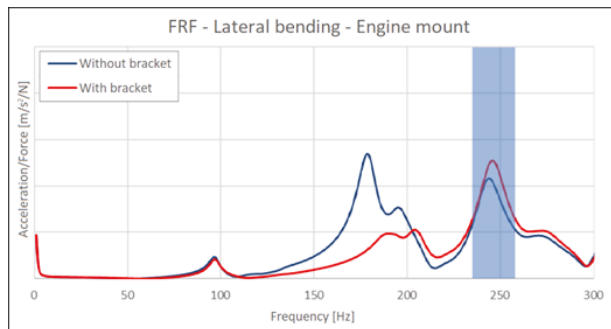
(**a**)
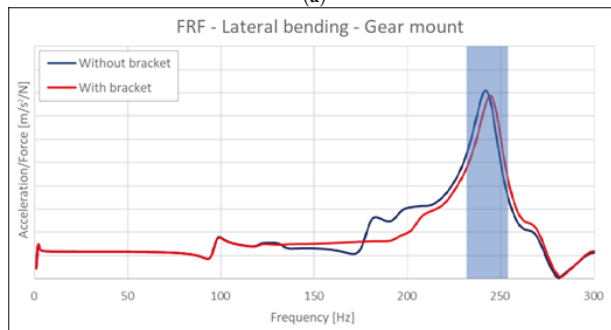
(**b**)

Figure 5. Acceleration/force ratio for the full FEM model for the lateral bending load case with and without the crankcase–gearbox bracket (shown in Figure 3) at: (**a**) engine mount; (**b**) gear mount.

From Figure 4, it is possible to see that the bracket introduction is effective in increasing the first natural frequency, in such a way as to avoid any activation of such mode in the whole engine operating range, up to 6000 rpm. As a matter of fact, the second order engine's highest frequency is equal to 200 Hz, well below the first natural mode whose frequency is now nearly 220 Hz.

From Figure 5, it is possible to see that even if the increase in the first natural frequency is not sufficient to overcome 200 Hz, the corresponding peak is severely smoothed in such a way that it no longer represents a problem, whereas the second more relevant peak is relegated to a frequency much higher than 200 Hz.

A comparison between the numerical and experimental results is also provided in Figure 6. The FRF results show a satisfactory correlation between experimental outcomes in terms of peak frequencies. The discrepancy in terms of magnitudes was judged as physiological for this kind of analyses because of uncertainties on the correct damping value to be used for the simulation, and because, when modal reduction techniques are adopted it is difficult to make the experimental and numerical exciting/accelerometer points coincident. Figure 6a shows a discrepancy between the peak frequencies of nearly 5 Hz for the model with the engine bracket, whereas Figure 6b shows a discrepancy of nearly 10 Hz between the peak frequencies for the model without the engine bracket. In both cases, such approximations are judged acceptable.

(**a**)

(**b**)
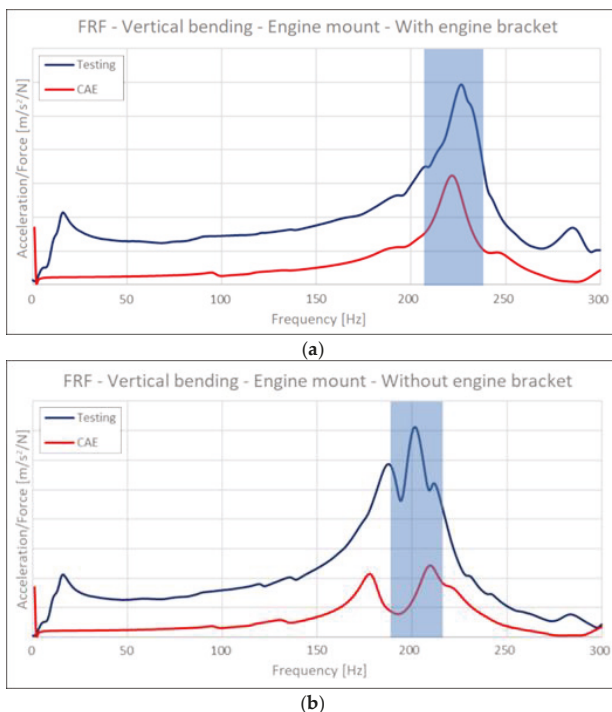
Figure 6. Numerical/experimental comparison on the acceleration/force ratio measured at the engine mount for the vertical bending load case: (**a**) with and (**b**) without the crankcase–gearbox bracket shown in Figure 3.

4. Frequency Response Results of the Full FEM Model

Modal-based frequency response analyses were performed for the full FEM engine model, considering the real loads occurring during the operation of the engine. In particular, the wide open throttle (WOT) condition was simulated, thus the maximum intake of air–fuel mixture, occurring when the throttle is completely opened, was considered as the engine working condition. Moreover, vertical loads representing the pistons and roll loads (from crankshaft rotation) were considered. For the former, only loads corresponding to the second engine order were needed (being the remaining negligible), whereas the fourth and sixth order were also added for the latter. Such loads were applied on a RBE3 element that in turn distributed the load onto the elements of interest. The objective of these analyses was to simulate the impact of the aforementioned bracket on the vibrations measured at the mounts during the engine operation. Experimental measurements of the mount vibrations were also available and were used here for validation.

Figure 7 shows the magnitude of the numerical displacement evaluated at the engine and gear mounts, with and without consideration of the presence of the bracket. It is worth noting that the adoption of the bracket has a positive effect at the engine mount just inside the range 5000–5500 rpm, whereas it seems to be ineffective elsewhere. On the contrary, a sensible positive bracket impact on the gear mount total displacement is evident above 4500 rpm. Apparently, only the bracket turns out to increase the magnitude of gear mount vibrations in the 5500–6000 rpm range because, as shown in the following, the model prediction in such a range, with reference to the gear mount, is inaccurate. Considering the experimental outcomes, as expected, the impact of the bracket introduction is also positive in the range 5500–6000 rpm: it is therefore sufficient to compare the blue testing lines of Figure 8a,b to understand that the total displacement is always lower when considering the bracket addition.

(a)

(b)
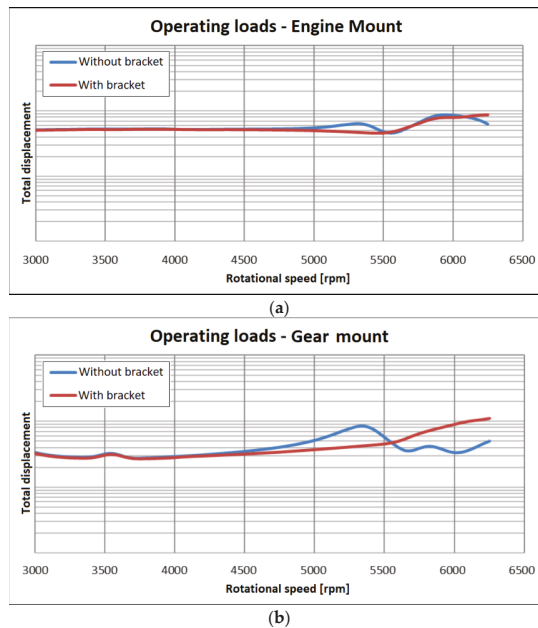
Figure 7. Displacement magnitude calculated at the (**a**) engine and (**b**) gear mounts considering the realistic operating loading condition.

Figures 8 and 9 show the experimental/numerical comparisons in terms of the displacements at the gear and engine mounts respectively. The setup for the experimental modal analyses is shown in Figure 10, which also highlights the supporting structure adopted to hold the engine.

As previously anticipated, an acceptable correlation was obtained between the data but not for the gear mounts without the bracket (Figure 8b). A possible explanation could be related to the approximations inherent in the modelling of interface connections between the engine parts, where nonlinear contact conditions are skipped in order to reduce the computational burden but with the consequence of possible unrealistic interpenetration between interface surfaces. This aspect can become critical at high frequency (or namely at high engine rpm) as shown in Figure 11, where it is possible to observe that the gear mount presented excessive relative motions with reference to the gearbox at 210 Hz (referring to the second order, this corresponds to engine rpm slightly higher than 6000). Some remaining discrepancies can be ascribed to the uncertain damping attributed to the structural elements and to the simplified modelling of the bolts that interconnect the different parts of the engine. In any case, the full FEM modelling was considered as validated.

(**a**)

(**b**)

Figure 8. Experimental/numerical comparison in terms of displacements at the gearbox mount (**a**) with and (**b**) without consideration of the bracket highlighted in Figure 3.

(**a**)

(**b**)

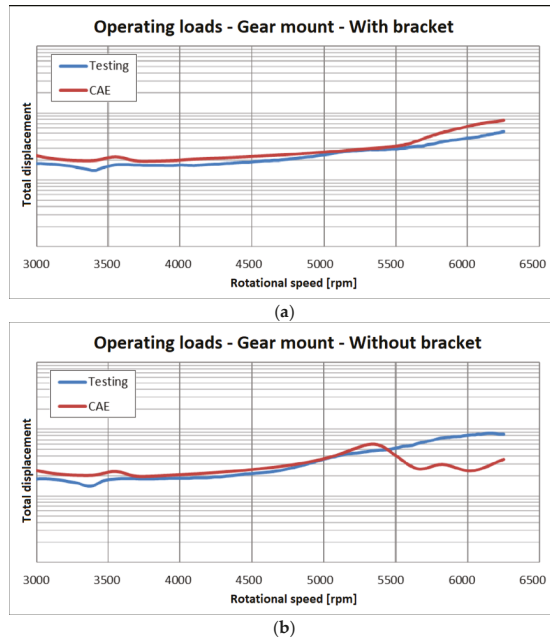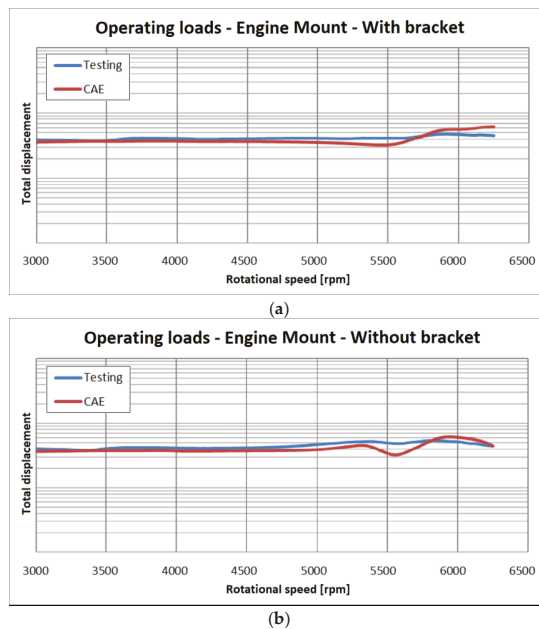**Figure 9.** Experimental/numerical comparison in terms of displacements at the engine mount (**a**) with and (**b**) without consideration of the bracket (highlighted in Figure 3).
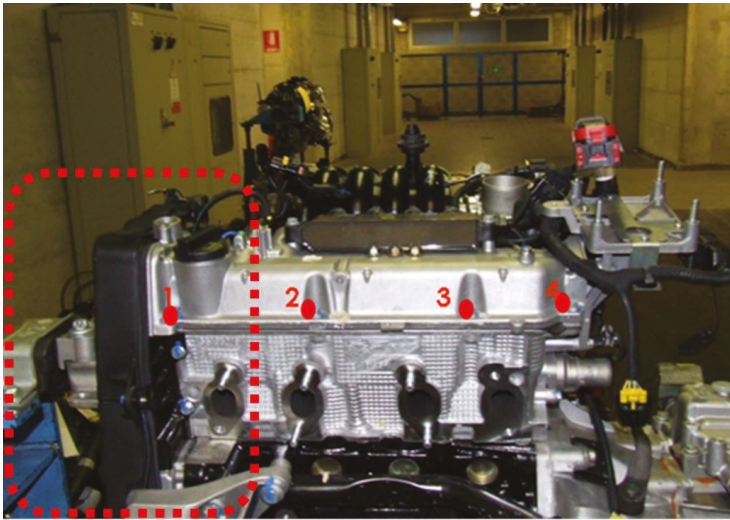
Figure 10. Experimental setup for modal analyses with highlights of the supporting structure.
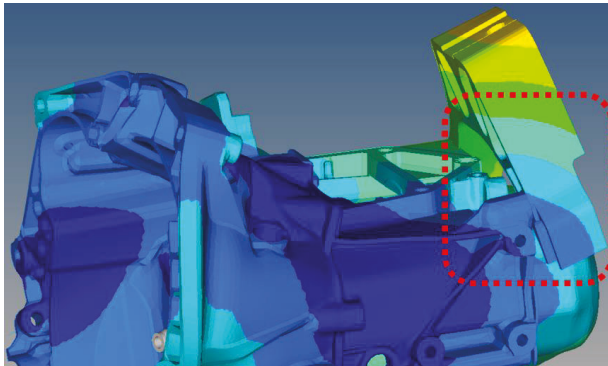
Figure 11. Evidence of the limitations given by the modelling strategy of the contacts, with reference to the relative motion between gear mount and gearbox at 210 Hz.

5. Model Reduction

The reduced FEM model was created starting from the full FEM engine model previously presented and validated. This was achieved by means of the ANSA MetaPost [17] code together with the pre-processor Altair Hypermesh and MSC Nastran.

The reduction of the model was performed for the whole engine apart from the sub-components. Namely, the reduced model comprised a fully reduced engine model with the addition of the engine's non-reduced sub-components (still fully modelled by FEM). This modelling strategy was preferred since it allowed efficient accommodation of the OEMs (Original Equipment Manufacturers) requirements, as they generally require the explicit modelling of their specific sub-components when assembled to an engine. From this standpoint, the model reduction of the engine allowed the significant reduction of the size of the FEM model, and also enabled the possibility of sharing the model without disclosing proprietary information about the engine design.

Sub-components were removed from the full FEM model and PLOTEL elements (PLOT ELements) [14] were used to display the engine shape and size. PLOTEL elements are MSC Nastran

dummy elements used only for display purposes and without significance from the dynamic standpoint. Such elements were adopted to represent the correct shape in the relevant positions, e.g., load application points or bolt positions, and also to visualize the correct engine shape and size.

The total mass and stiffness of the engine was associated with an RBE3 [14] element positioned in the cylinder head, whereas further RBE3 elements were also introduced to link the sub-components to the engine, in correspondence with the connecting bolts (these elements allowed transmission of displacements at the relevant positions where sub-components are directly connected).

The final reduced model is shown in Figure 12.

(**a**)

(**b**)
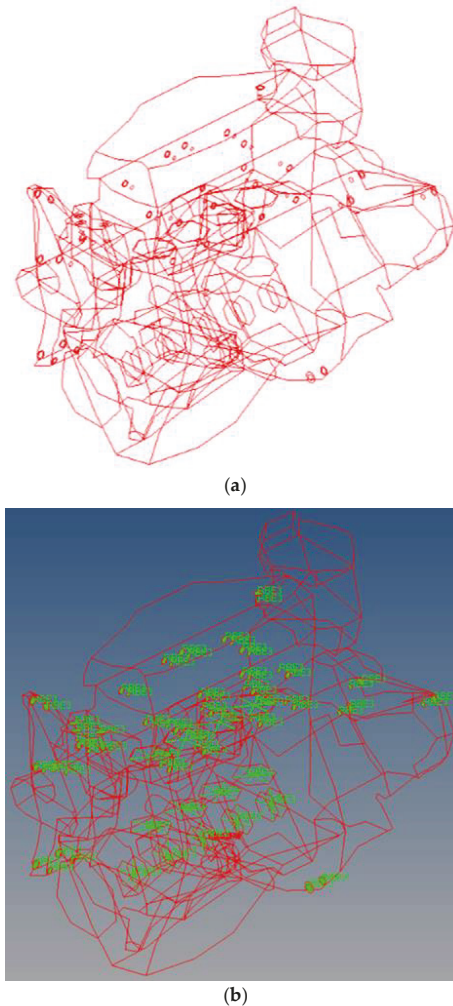
Figure 12. (**a**) Engine model built up with PLOTEL elements; (**b**) highlight of RBE3 elements.

The model built up with PLOTEL elements is shown in Figure 12a. It comprised 1885 elements and 1755 nodes (whereas the full FEM model required nearly 5.7×10^6 elements and 4.7×10^6 nodes). Such a model was then imported in the ANSA MetaPost code, in which the modal model was built up by considering the modes of the full FEM model as input data for the reduced model. Consequently,

further RBE3 elements were used to link the sub-components at the bolt position, see Figure 12b. The final reduced model comprising all the FEM sub-components is shown in Figure 13.
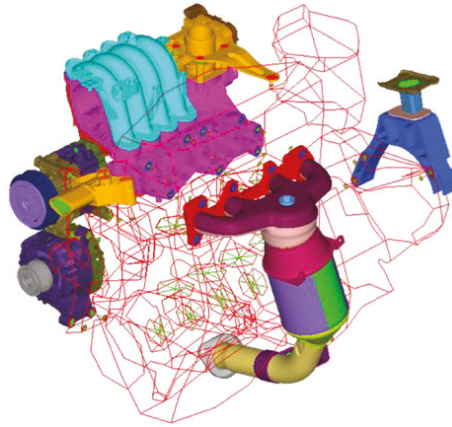
Figure 13. Reduced model of the engine with all sub-components modelled by FEM.

FRF analyses were used to calculate the accelerations at the mounts for the full and reduced FEM model. In this case, unitary forces were applied on the sub-components and the corresponding accelerations were obtained (in the same position of excitation). For instance, Figure 14 shows the points considered in the FRF analyses on the gear mount (Figure 14a), on the alternator (Figure 14b) and on the intake manifold.

(**a**)

(**b**)

(**c**)
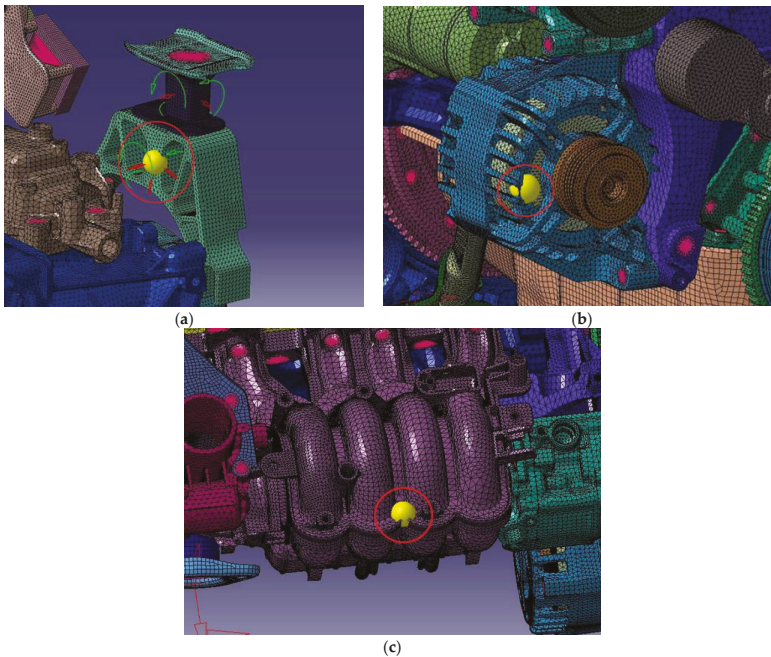
Figure 14. Relevant points (yellow dots) on the (**a**) gear mount; (**b**) alternator and (**c**) intake manifold considered in the FRF analyses.

6. Results of the Reduced FEM Model

Figure 15 shows the ratios of acceleration over force calculated for the two FRF analyses performed for the alternator and for the gear mount: a quite satisfactory matching was obtained.
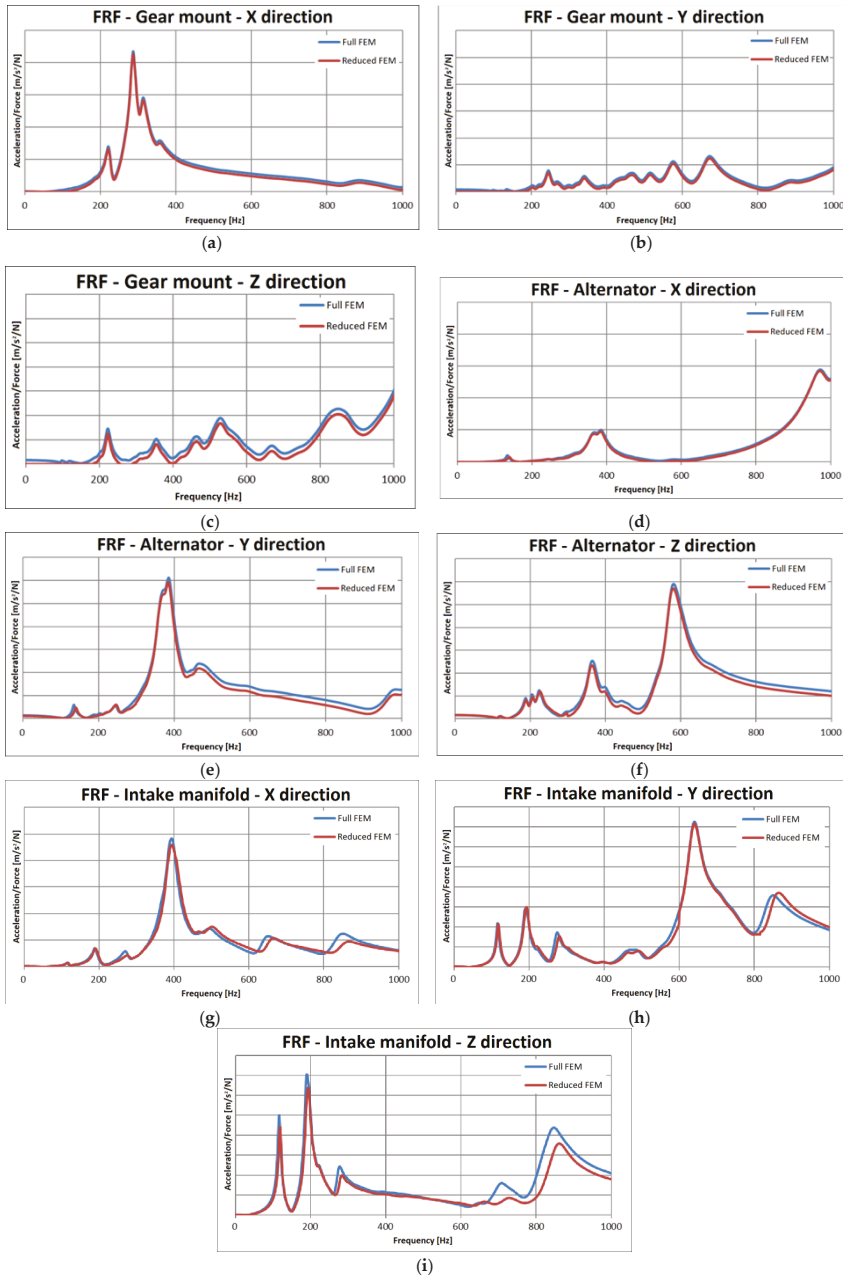
Figure 15. Comparisons of the acceleration/force ratio in the three directions for the full and reduced models at: (**a–c**) gear mount; (**d–f**) alternator; (**g–i**) intake manifold.

Figure 16 shows three examples of the modal shapes for the full FEM model and the reduced model for three components.
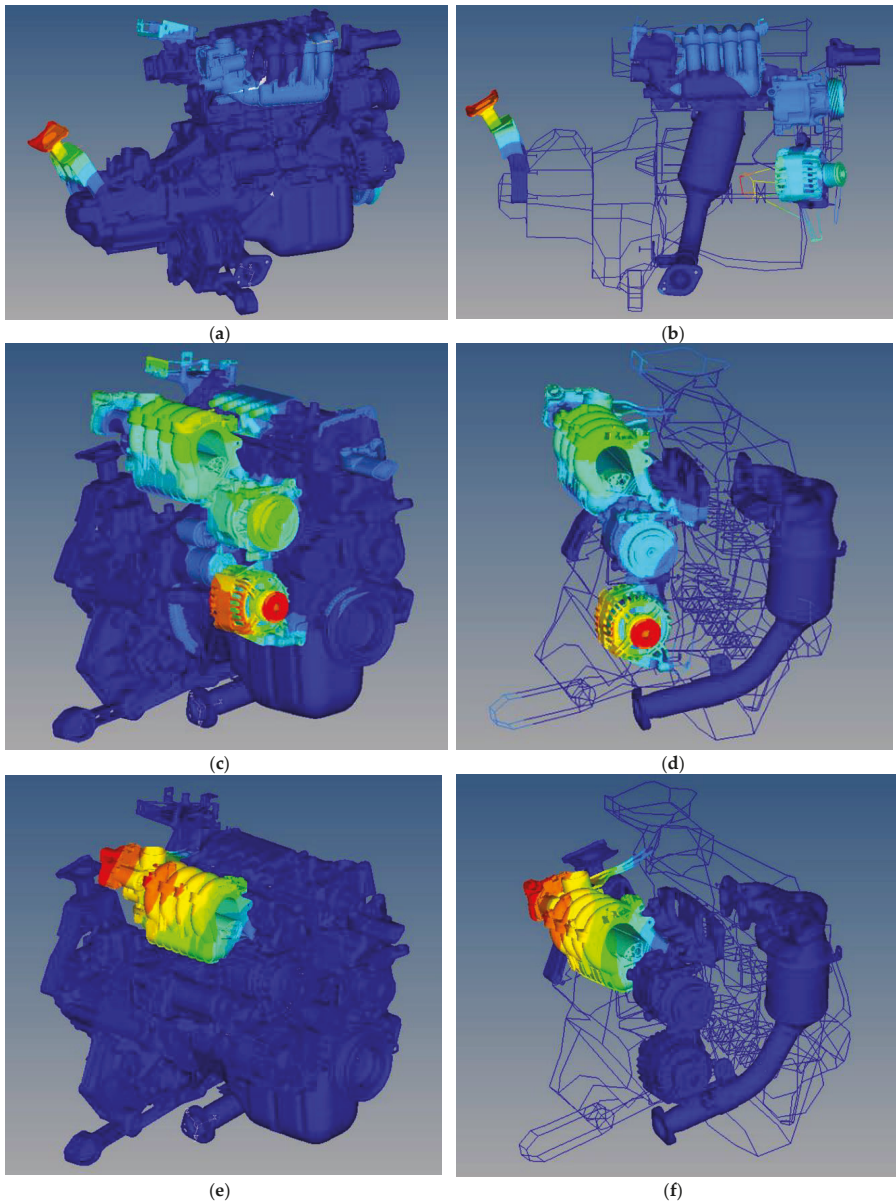
Figure 16. Comparisons of the modal shapes for (**a**,**c**,**e**) the full FEM and (**b**,**d**,**f**) the reduced FEM model for: (**a**,**b**) gear mount, (**c**,**d**) alternator, (**e**,**f**) intake manifold.

Figure 16 shows an example of the modal shapes for the full FEM model and the reduced model: again, a quite satisfactory matching was obtained.

The reduced FEM modelling allowed the calculation of the accelerations at the sub-components with a reduced computational burden. In particular, the runtime for the full FEM model was equal to nearly 24 h, decreasing to nearly 2 h for the reduced FEM model. The reduced model was then able to accurately replicate the engine's vibrational behavior and consequently could be adopted for this kind of analysis. Moreover, since the sub-components are generally designed by external partners who require the analysis of the sub-component assembled to the engine, the adoption of the model reduction can overcome the key concern of not sharing proprietary design solutions.

7. Conclusions

A 4-cylinder petrol engine was simulated from the dynamic standpoint by leveraging on the finite element method (FEM). In particular, a reduced modelling strategy based on the component mode synthesis (CMS) was adopted to reduce the size of the full FEM model of the engine.

The FEM model of the engine, comprising all its sub-components, was preliminarily characterized from the vibration standpoint; subsequently, the CMS was adopted in order to reduce the FEM model DoFs.

FRF analyses were used to reproduce the vibration response of the engine and the corresponding acceleration levels between the models and bench test data were compared, showing a sound agreement. Moreover, frequency response analyses were also performed to replicate the vibrations of the engine during the operation and a satisfactory comparison was obtained against corresponding bench test data.

The adopted reduced modelling strategy turned out to be effective in lowering the computational burden from 24 h to nearly 2 h, keeping at the same time an accurate replication of the engine vibration behavior.

The reduced FEM model was demonstrated to reproduce with high accuracy the vibration response at the engine mounts, providing a satisfactory agreement with the vibrations measured experimentally and with the outcomes of a full FEM model.

Ways to further improve the modelling of the bolts and of the interface contacts between the engine parts are still under investigation.

References

1. Craig, R., Jr. Coupling of Substructures for Dynamic Analyses: An Overview. In Proceedings of the AIAA Dynamic Specialists Conference, Atlanta, GA, USA, 3–6 April 2000. AIAA Paper No. 2000–1573.
2. Zheng, Z.C. Dynamic analysis of nonlinear systems by modal synthesis techniques. *Appl. Math. Mech.* **1983**, *4*, 611–623. [CrossRef]
3. Armentani, E.; Sepe, R.; Parente, A.; Pirelli, M. Vibro-Acoustic Numerical Analysis for the Chain Cover of a Car Engine. *Appl. Sci.* **2017**, *7*, 610. [CrossRef]
4. Armentani, E.; Trapani, R.; Citarella, R.; Parente, A.; Pirelli, M. FEM-BEM Numerical Procedure for Insertion Loss Assessment of an Engine Beauty Cover. *Open Mech. Eng. J.* **2013**, *7*, 27. [CrossRef]
5. Armentani, E.; Caputo, F.; Esposito, L.; Giannella, V.; Citarella, R. Multibody Simulation for the Vibration Analysis of a Turbocharged Diesel Engine. *Appl. Sci.* **2018**, *8*, 1192. [CrossRef]
6. Siano, D.; Citarella, R.; Armentani, E. Simulation of a multi-cylinder engine vibrational behavior. *Int. J. Veh. Noise Vib.* **2018**, *14*, 101–123. [CrossRef]
7. Armentani, E.; Sbarbati, F.; Perrella, M.; Citarella, R. Dynamic analysis of a car engine valve train system. *Int. J. Veh. Noise Vib.* **2016**, *12*, 229–240. [CrossRef]
8. Fehr, J.; Eberhard, P. Simulation process of flexible multibody systems with non-modal model order reduction techniques. *Multibody Syst. Dyn.* **2011**, *25*, 313–334. [CrossRef]

9. Nowakowski, C.; Kurschner, P.; Eberhard, P.; Benner, P. Model reduction of an elastic crankshaft for elastic multibody simulations. *J. Appl. Math. Mech.* **2013**, *93*, 198–216. [CrossRef]

10. Koutsovasilis, P.; Beitelschmidt, M. Comparison of model reduction techniques for large mechanical systems. *Multibody Syst. Dyn.* **2008**, *20*, 111–128. [CrossRef]

11. Witteveen, W. On the modal and non-modal model reduction of metallic structures with variable boundary conditions. *World J. Mech.* **2012**, *2*, 311–324. [CrossRef]

12. Mahdisoozani, H.; Mohsenizadeh, M.; Bahiraei, M.; Kasaeian, A.; Daneshvar, A.; Goodarzi, M.; Reza Safaei, M. Performance Enhancement of Internal Combustion Engines through Vibration Control: State of the Art and Challenges. *Appl. Sci.* **2019**, *9*, 406. [CrossRef]

13. Junhong, Z.; Jun, H. CAE process to simulate and optimise engine noise and vibration. *Mech. Syst. Signal Process.* **2006**, *20*, 1400–1409. [CrossRef]

14. MSC. *Nastran User Reference Manual*; MSC Software Corporation: Santa Ana, CA, USA, 2006.

15. SIEMENS-LMS Virtual Lab. *User Manual*; SIEMENS-LMS Virtual Lab: Plano, TX, USA, 2011.

16. Altair Engineering. *Hypermesh User Manual*; Altair Engineering: Troy, MI, USA, 2011.

17. *META Post-Processor*, version 16.0; BETA CAE Systems SA: Thessaloniki, Greece, 2015.

Article

Postponing the Onset and Alleviating the Load of Transonic Buffet by Using Steady and Periodic Tangential Slot Blowing

Huixue Dang [1,2,*], Junhai Zhao [1], Zhichun Yang [2] and Huibo Dang [3]

[1] School of Civil Engineering, Chang'an University, Xi'an 710061, China; zhaojh@chd.edu.cn
[2] School of Aeronautics, Northwestern Polytechnical University, Xi'an 710072, China; yangzc@nwpu.edu.cn
[3] Shaanxi College of Communication Technology, Xi'an 710018, China; zhoulinshijie@126.com
* Correspondence: perpetual@mail.nwpu.edu.cn

Featured Application: Transonic buffet alleviation for airplanes.

Abstract: Transonic buffet not only influences the structural integrity, handling quality and ride comfort, but also limits the flight envelope of transporters and airliners. To delay buffet onset and alleviate the buffet load, the effects of both steady and periodic tangential slot blowing are investigated. The results show that steady tangential blowing on the airfoil upper surface can postpone the buffet onset margin and evidently increase the lift coefficient at incidence angles near and above the buffet onset case of the clean airfoil. Under buffeting conditions of the clean airfoil, unsteady aerodynamic loads can be greatly suppressed by both steady and periodic blowing. The control effort is depicted as reduced wedge effect and weakened dynamic effect. The buffet mechanism includes (a) the feedback loop between the Kutta wave and the separation bubble under the shock foot, and (b) the interaction between the shear layer shed by the shockwave and Kutta waves. Under blowing conditions, the upstream creeping Kutta waves are prevented, and the intensity of the shear layer shed by the shockwave into separated flows is evidently reduced. Parametric studies show that the control effect is reduced as the blowing slot moves downstream, and steady blowing at 41% x/c is the most favorable control case.

1. Introduction

To save time and energy, high-speed flights are usually done by modern, large commercial aircraft, which always cruise between Mach 0.7 and 0.9 by employing supercritical wings [1–3]. These Mach numbers fall in the typical transonic flow range; consequently, unsteady shockwave/boundary layer interactions could induce intensive, large-scale, unsteady lift, and transonic buffet will be the result [4–10]. This transonic buffet not only decreases riding comfort [10–12], but structural fatigue could also be triggered, and disastrous accidents could even result [2,4,9,13–15]. Thus, transonic buffet is deemed one of the most important factors limiting the flight envelope [2,7,9,14,16,17], since a margin of 30% on the lift coefficient at cruising conditions must be respected by design standards [7].

To delay the buffet onset margin, alleviate buffet loads, and widen the flight envelope, a lot of effort has been devoted to the development, including unveiling buffet mechanisms [4,8,18–22], of functional control techniques [2,7,9,10,14,16,23,24], and so on. Meanwhile, studies have also been conducted to improve measuring techniques employed in wind tunnel tests [25], buffet onset prediction methods [17,26,27], numerical simulation techniques of shock/boundary layer interactions [6,11,25,28–31], and so on.

One of the most interesting and difficult research targets is to uncover the mechanism of transonic buffet and shock/boundary layer interactions. Among these studies, wind-tunnel tests as well as numerical simulations, stability analyses, and so on, have been conducted, and different academic viewpoints have been proposed. Although the buffet mechanism has remained inexplicable over six decades due to its complexity [2], research is in progress. For example, in the last five years, Szubert et al. [3] presented that frequency modulation was formed by large-scale, periodic oscillations together with secondary oscillations, where low-frequency, large-scale, periodic oscillations and higher frequency secondary oscillations are generated by buffet instability and the von Kármán mode near the trailing edge of the airfoil, respectively. Timme and Thormann [4] stated that lower-frequency results are similar to the forced-response calculations reported on two-dimensional airfoils, but the three-dimensional shock buffet at higher frequencies is linked to the presence of a global destabilizing mode. Sartor et al. [8] presented that the flow is most receptive to harmonic forcing on the upper surface of the profile; besides the low-frequency shock unsteadiness, the flow also exhibits medium-frequency unsteadiness linked to Kelvin–Helmholtz-type instability. Iovnovich and Raveh [32] pointed out that the pre-buffet aerodynamic resonance response and the change in aerodynamic characteristics are governed by the shock-induced separation phenomenon, as a separation bubble was found behind the shock in static analyses.

In the meantime, investigations on control techniques for mitigating buffet loads have also been performed. This research can be roughly divided into passive control techniques and active control techniques. Passive control techniques include suction slots on upper wing surfaces, vortex generators with inclined angles, three-dimensional bumps, and so on, while research on active controls includes trailing edge deflectors, flapping rudders, and so on.

In the published literature on passive control studies, Thiede and Stanewsky [33] examined the impact of slots ejecting airflow normal to the upper surface of a supercritical airfoil. They figured out that the typical normal shock is modified to be two shocks that form a "λ", which notably decreases the total pressure loss and delays the boundary layer separation induced by the shockwave. Babinsky et al. [34,35] tested the effect of streamwise slots located downstream from the airfoil on the shock/boundary layer interference. They pointed out that by introducing streamwise vortices, streamwise slot control may help delay or prevent downstream separation. By solving Navier–Stokes equations enclosed by an IDDES turbulence model, Huang et al. [1] investigated the influence of vortex generators with inclined angles on the transonic buffet of an OAT15A airfoil. They found that the time-averaged location of the shockwave was pushed downstream; thus, the root-mean-square of the oscillating force in the buffeting zone decreases, and the total lift is enhanced. Molton et al. [36] and Dandois et al. [7] tested mechanical, continuous, and pulsed fluidic vortex generators located upstream from the shock foot to reduce the extent of the separated area, and fluidic actuators as well as mechanical vortex generators have proven to be very efficient in postponing buffet onset. Ogawa et al. [37] proposed a method of using three-dimensional bumps on upper wing surfaces to alleviate the strength of flow interference between the shockwave and boundary layers, and the results indicated that a 30% decrease of total drag can be achieved for the best control case. Then, Eastwood and Jarrett [38] optimized the three-dimensional bump shape, and they pointed out that the bump can generate stream-wise vortices at high Mach numbers, suggesting improvement in the buffet margin. Tian et al. [10,24] studied the suppression effect of bumps on the transonic buffet. They found that the strength of the shockwave was weakened, and the location of the shockwave was stabilized; thus, buffet and drag-rise characteristics are improved. Liu and Yang [39] suppressed transonic shock oscillation and alleviated the buffet load for supercritical airfoils by using a micro-tab.

Among the active control works on the transonic buffet, Caruana et al. [23,40,41] developed a trailing edge deflector (TED) with a close-circuit control loop to control the transonic buffet. Results showed that when the oscillating frequency of TED was close to buffeting frequency, evident control effectiveness could be obtained. The drawback of this method is that the control law for three-dimensional flow is very complicated. Iovnovich and Raveh [32] investigated the control effect of

a 20% chord-length trailing edge flap under prescribed oscillation on transonic buffet, and they found that large, prescribed flap motions eliminated the lift resonance response and significantly reduced the lift coefficient amplitude. Gao et al. [9] tested the impact of flapping rudders on the transonic buffet, and they stated that resonant rudders may be a feasible open-loop strategy to suppress buffet loads under different buffet states. Tian et al. [14] tested the control effect of an upper trailing-edge flap (UTEF), and they pointed out that the UTEF prevents flow separation downstream of the shockwave, shifts the buffet boundary to higher angles of attack, and increases the lift coefficients. Ferman et al. [42] and Abramova et al. [43–46] used tangential slot blowing for transonic buffet control of a P-184-158R supercritical airfoil, and they pointed out that tangential blowing can shift the shockwave downstream and increase the lift.

From the published literature, it is found that by adopting passive control techniques such as slots normal to the wall, bumps and vortex generators on the upper surface, and so on, satisfactory control effects can be obtained under design conditions, while off-design conditions engender unexpected effects, and aerodynamic characteristics can even deteriorate. With the utilization of active control techniques, such as trailing edge deflectors, flapping rudders, and so on, the control law proves to be very complicated for three-dimensional flow, and the size of the control surface is relatively large; thus, large driving forces are needed, which depletes extra energy. In published papers, the blowing intensity has been investigated, and the tangential slot-blowing location and blowing directions, which may influence the control effort, should also be studied. Thus, a tangential slot-blowing control method is investigated to test both steady and periodic blowing control effects based on numerical simulations.

2. Numerical Methods and Validation

In the transonic buffet simulation, detached eddy simulation (DES) [1,47–49] and large eddy simulation (LES) [12] series turbulence models can predict three-dimensional buffet flow fields. However, it is not practical to compute various upstream conditions by using DES or LES turbulence models to determine buffet onset boundaries because these methods require a grid resolution that is much higher than that for URANS simulations, resulting in excessively longer computational times. Meanwhile, Soda [50] conceived in their 2007 book that numerical simulations of this phenomenon based on URANS current codes are quite successful in predicting the magnitude and frequency of periodic shock motions during buffet. Thus, in two-dimensional studies of transonic buffet mechanisms and transonic buffet flow controls, URANS [8,9,13,16,24,30,32,43,44] turbulence models such as SA, SST, and so on are widely employed, and favorable results have been obtained. To include transition effects, the transition SA turbulence model [51] was employed in the present study.

The discretization schemes usually employed in compressible Navier–Stokes equations enclosed by URANS turbulence models are HLLC [13,32], Roe [14,16], AUSM + P [8], and AUSP + up [9]. Sartor et al. [8] stated that Roe and Jameson schemes were not considered in their work due to the schemes' poor shock treatment when investigating the stability of the flow, and AUSM+ series schemes were their choice. By improving the AUSM+ scheme for shock-stable and accurate hypersonic heating computations, Kitamura and Shima [52] developed an AUSM + up2 scheme for a wide spectrum of Mach numbers, including hypersonic heating, low speed flow, and 3D aerodynamic applications. This scheme is included in the open source code SU2 [53], and it was employed in the present study to solve the compressible Navier–Stokes equations.

The airfoil profiles widely used in transonic buffet studies are NACA0012 [9,13,17,21,32,54] and OAT15A [1,30,55]. By referring to the well-known NACA0012 2-D airfoil shock-buffet test case by McDevitt and Okuno [54], the NACA0012 airfoil was used in the present study. The steady-state numerical methods were validated by the wind tunnel test results from reference [54]. The free stream Mach number was 0.751, the Reynolds number was 9.5×10^6, and the incidence angle of the NACA0012 airfoil was 1.99°. The chord length of the NACA0012 airfoil was set to be 1.0 m in present study. The computational domain size and the structured grid is shown in Figure 1. The mesh node numbers on both the upper and lower surfaces of the airfoil were set to be 281, respectively. The far-field boundary

was placed at least 50 times that of the chord length. The first grid layer thickness normalized by the chord length was set to be 1×10^{-6}, corresponding to $y^+ \approx 1$. The calculated surface pressure agreed well with test results, as plotted in Figure 2.
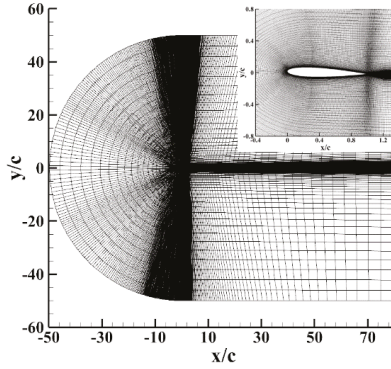
Figure 1. Grid around an airfoil.
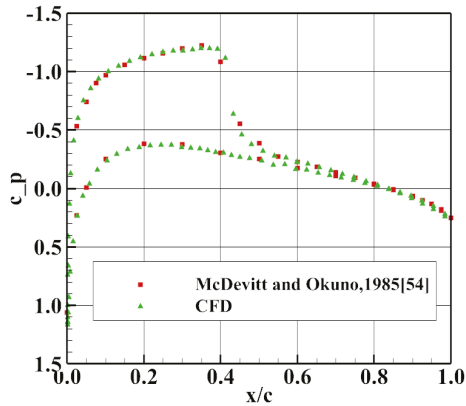
Figure 2. Comparison of numerical and test results.

To check out the unsteady flow simulation's capability of presenting numerical methods, an unsteady transonic flow around an NACA0012 airfoil was simulated at $\alpha = 6°$, $M_\infty = 0.751$, $Re = 1 \times 10^7$. The time history of lift coefficient is compared with that conducted by Raveh [56], as shown in Figure 3. The results indicate that the computed result matched well that from the published literature. Thus, the validated numerical methods and the grid parameters were adopted in the following research.
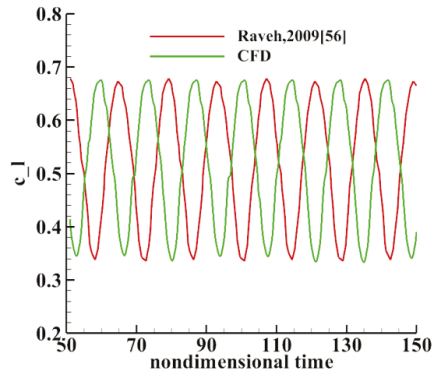
Figure 3. Comparison and validation of unsteady numerical results.

3. Delay of Buffet Onset

Under the same free-stream conditions of the validation case plotted in Figure 2, steady numerical simulations were conducted for the NACA0012 airfoil at different incidence angles. The calculated lift coefficients at different incidence angles are plotted, as shown in Figure 4. By referring to the work conducted by Iovnovich and Raveh [57] and Liu and Yang [26,27], the maximum curvature method proposed by Liu and Yang [26,27] is briefly introduced as follows.
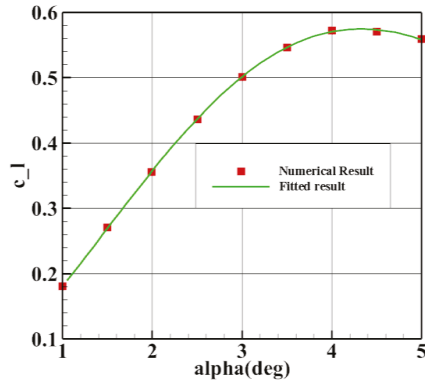
Figure 4. Lift coefficients vs. incidence angle.

By comparing the fitting precisions of polynomial aerodynamic curves, including lift and moment coefficient curves, it was found that a quartic polynomial can give the best fitting precision. It is written as follows:

$$y = ax^4 + bx^3 + cx^2 + dx + e \tag{1}$$

where a, b, c, d, and e are fitting constants obtained by least-squares fitting, x denotes the incidence angle, and y denotes either the lift or moment coefficient. In the present study, the lift coefficient was used.

The calculated curvature of y is as follows:

$$K(x) = \frac{\left|12ax^2 + 6bx + 2c\right|}{\left(1 + (4ax^3 + 3bx^2 + 3cx + d)^2\right)^{3/2}} \tag{2}$$

57

when the minimum curvature radius is achieved, the first-order derivative of K(x) equals zero:

$$K'^{(x)} = 0 \tag{3}$$

By solving Equation (3), the buffet onset incidence angle is obtained. The accuracy of this method is valid for NACA0012 airfoil buffet onset predictions, compared to wind tunnel tests, as validated in reference [26,27].

By using the above method, the curve plotted in Figure 4 was fitted by a quartic polynomial, and the maximum curvature was then obtained to be 0.8, corresponding to a transonic buffet onset margin of 3.9°.

By inspecting the surface pressure distribution curve plotted in Figure 2, it can be found that the shockwave on the upper wing's surface resides in the range of 41%~51% chord length; thus, 41% chord length, 46% chord length, and 51% chord length are denoted as "41% x/c", "46% x/c", and "51% x/c", respectively. The tangential blowing position on the upper surface is first selected to be the "46% x/c" case. The geometric shape of the tangential blowing nozzle and the structured grid is plotted in Figure 5. This tangential blowing nozzle is a Venturi nozzle with its contraction ratio equaling 5.0. Its mass flow flux is governed and can be adjusted by setting the total pressure value at the inlet boundary of the Venturi nozzle.
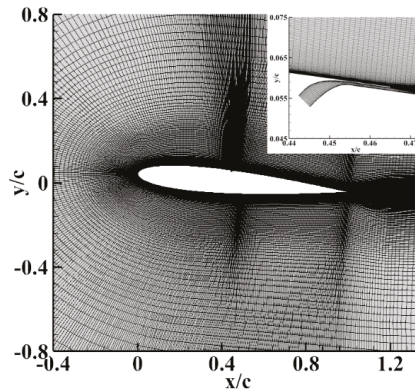
Figure 5. Grid of a tangential blowing slot.

With the blowing total pressure equaling the freestream total pressure, the lift coefficients at different incidence angles were compared with those of a clean airfoil, as plotted in Figure 6. Based on the maximum curvature method, the transonic buffet onset margin with "46% x/c" blowing was found to be 4.5°, and its corresponding curvature was 0.04. It can be seen from Figure 6 that, at Mach 0.751 when the incidence angle is below 2.5°, the airfoil lift with tangential blowing was a little lower. When the incidence angle is greater than 3.0°, and especially when the lift slope of the airfoil without blowing is lower for incidence angles beyond 4.5°, the airfoil lift with tangential blowing was higher. Thus, tangential blowing can not only postpone the transonic buffet onset margin, but the airfoil lift can also be increased.
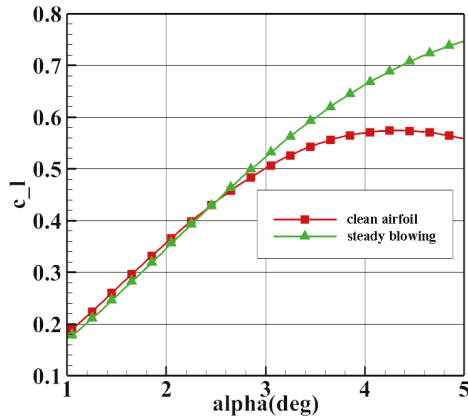
Figure 6. Comparison of lift coefficients with and without blowing.

To investigate the control effort, pressure coefficient distributions, pressure contours, and streamlines will be presented. At incidence angles of 4° and 5°, the surface pressure coefficients of the airfoil with and without tangential slot blowing were plotted together, as shown in Figure 7. It is seen that the shock location is shifted downstream by tangential slot blowing. Besides, with the increase of incidence angle, the distance of the shockwave being pushed downstream will increase. The Mach number contours around airfoils with and without tangential slot blowing are plotted in Figure 8. It is found that the shockwave was sharpened and moved downstream by tangential slot blowing. Also, by comparing the streamline contours plotted in Figure 9 it is seen that there were two flow separation zones in the boundary layer 51% x/c for the clean airfoil (airfoil without blowing) case, which were induced by shockwave/boundary layer interactions and an adverse pressure gradient from the trailing edge, respectively. When tangential slot blowing was utilized, the size of the separation zone induced by the shockwave was reduced, and the other separation zone induced by the adverse pressure gradient disappeared, indicating stabilization of this control technology.
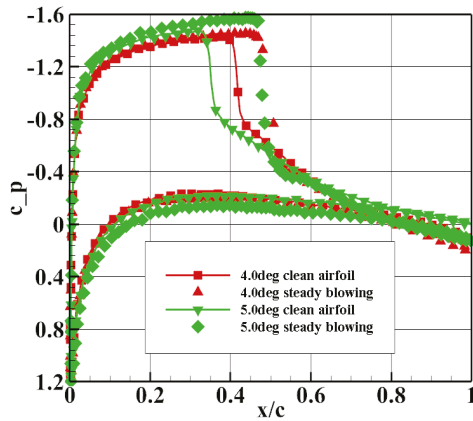
Figure 7. Surface pressure distribution with/without blowing.
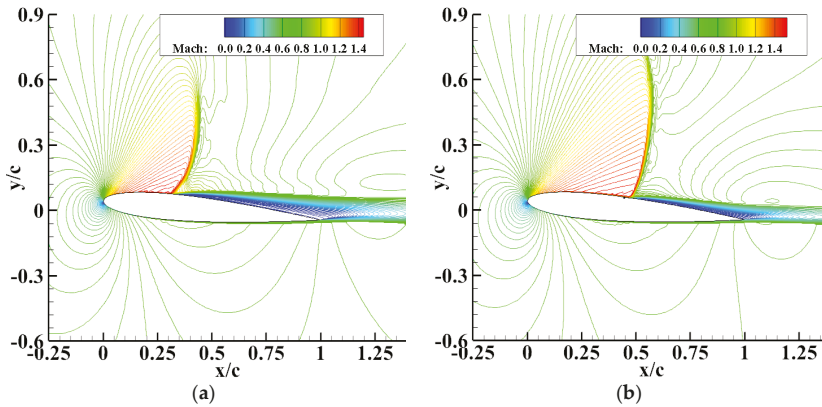
Figure 8. Comparison of unsteady numerical results (**a**) without tangential blowing and (**b**) with tangential slot blowing.
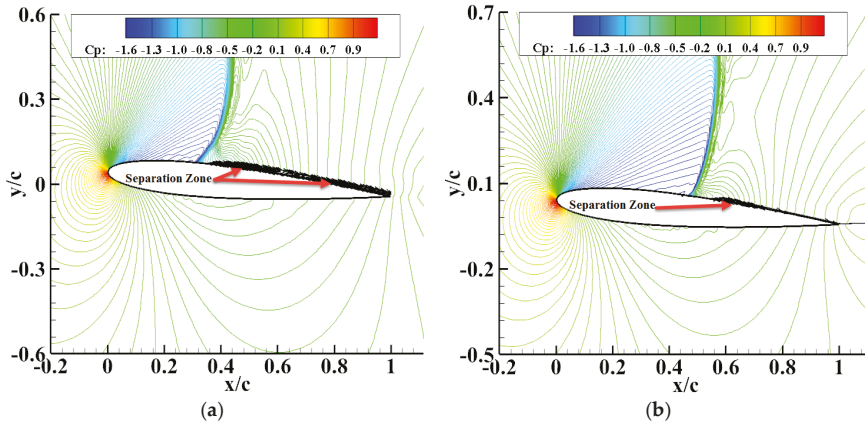
Figure 9. Streamlines at a 5.0° incidence angle (**a**) without tangential blowing and (**b**) with tangential slot blowing.

4. Alleviation of Buffet Load by Tangential Slot Blowing

4.1. Steady Blowing

From the above context, the postponing of buffet onset margin is observed. In present section, the effect of tangential blowing on buffet load will be studies.

4.1.1. Buffet Load Alleviation

As with the buffeting margin, the load characteristics of the transonic buffet are also of great concern in the aviation industry. From the above context, it is seen that when the incidence angle exceeds 3.9°, transonic buffet will occur. At different buffeting states, namely at incidence angles of 5.0°, 5.5°, and 6.0°, the time histories of unsteady lift coefficients of the clean airfoil are plotted in Figure 10, and their corresponding PSD (power spectrum density) results are plotted together in Figure 11. From these two groups of figures, it is seen that with the increase of incidence angle, both the amplitude and peak frequency of the unsteady buffet load increased. Moreover, it should be noted that the peak frequency resides in the frequency range of 88–99 Hz. In the wind-tunnel test of the NACA0012 airfoil given by McDevitt and Okuno [54], by referring to the flow parameters and the reduced frequency

equation, the dimensional frequency was about 89 Hz. Thus, the calculated dominant frequency agreed with that of the wind tunnel test.
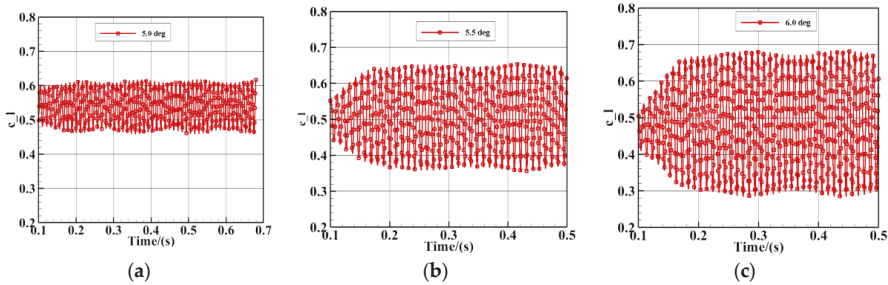
Figure 10. Unsteady lift coefficients at different incidence angles: (**a**) 5.0°, (**b**) 5.5°, and (**c**) 6.0°.
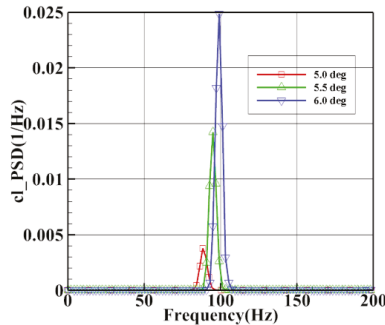
Figure 11. Power spectrum density (PSD) results at different incidence angles.

Accounting for the problem of transonic buffet load alleviation, 27 cases were simulated (i.e., flow fields under three different blowing locations (namely, the "41% x/c" case, "46% x/c" case, and "51% x/c" case) at three different incidence angles with three different blowing total pressures). In the present paper, "Blow_1.0_Ptot", "Blow_1.1_Ptot", and "Blow_1.2_Ptot" denote that the total pressure ratio of blowing to that of freestream flow is 1.0, 1.1, and 1.2, respectively.

The time histories of unsteady airfoil lift coefficients of "41% x/c" under different blowing pressure ratios at incidence angles 5.0°, 5.5°, and 6.0° are plotted in Figure 12. It is indicated that, for these incidence angles, the average airfoil lift increased and buffet loads decreased by using steady blowing with these three blow pressure ratios.
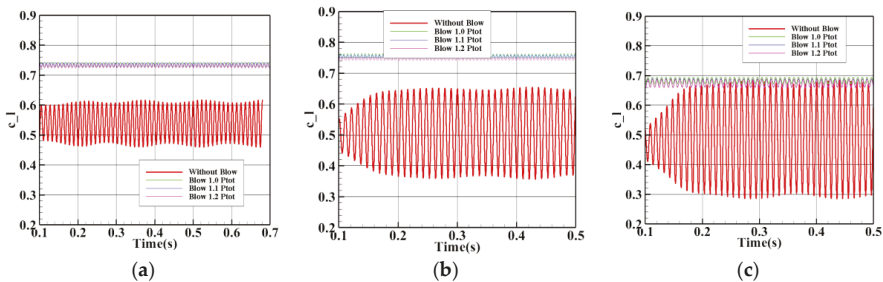
Figure 12. Unsteady lift coefficient histories under different total blowing pressures at different incidence angles: (**a**) 5.0°, (**b**) 5.5°, and (**c**) 6.0°.

The PSD results of unsteady airfoil lift coefficients are plotted in Figure 13. It is shown that transonic buffet was suppressed by tangential slot blowing under the "Blow_1.0_Ptot" condition. With the increase of total pressure ratio from 1.0 to 1.1 and 1.2, the PSDs of unsteady airfoil lift coefficients were nearly the same, and buffet load alleviation was not apparently improved; thus, these two groups of PSD curves were not plotted.
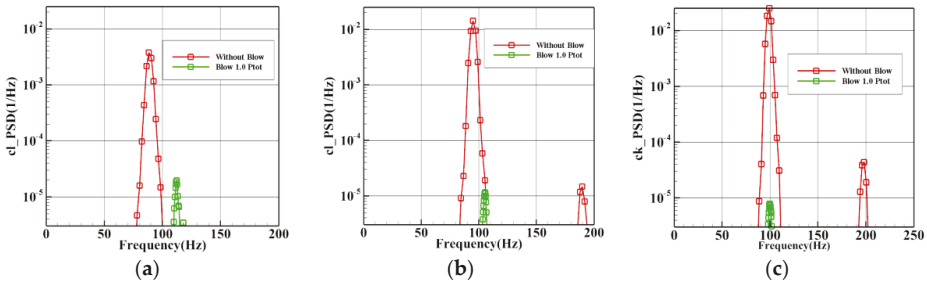
Figure 13. PSDs of unsteady lift coefficient histories under different blowing total pressures at different incidence angles: (**a**) 5.0°, (**b**) 5.5°, and (**c**) 6.0°.

With the blowing slot placed at 41% x/c chord location, the PSDs of airfoil lift coefficients at incidence angles 5.0°, 5.5°, and 6.0°, corresponding to different blowing total pressure ratios, are plotted in Figure 14. It is seen that all these blowing cases with different blowing total pressure ratios can evidently depress buffet loads. For the "5.0 deg" case, an increase of blowing ratio could slightly improve the control effect, while for "5.5 deg" and "6.0 deg" cases, their control effectiveness slightly deteriorated by increasing the total pressure ratio.
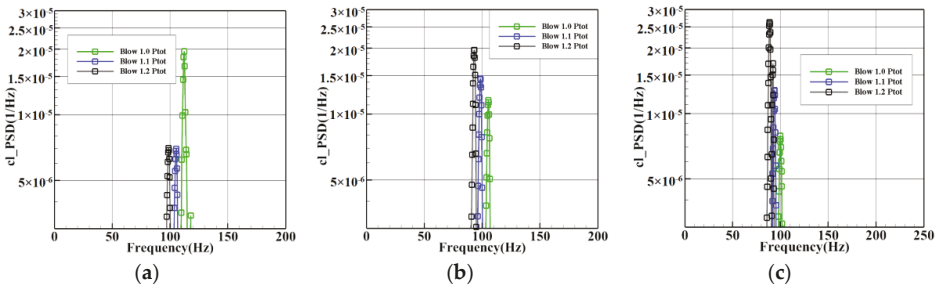
Figure 14. PSDs of unsteady lift coefficient histories under different blowing total pressures at different incidence angles: (**a**) 5.0°, (**b**) 5.5°, and (**c**) 6.0°.

The PSD results plotted in Figure 14 also suggest that, for all these blowing cases, the buffeting frequencies were nearly 100 Hz, which indicates that the transonic buffet was alleviated, but the buffeting frequency was not evidently modified.

By comparing the PSD results of 27 cases, it is found that the influence of blowing conditions on the buffeting frequency is marginal, whereas the PSD peak increases at incidence angle $\alpha = 5.5$ and 6.0 and experiences a small decrease at $\alpha = 5.0$ as the blowing location moves from 41% x/c to 51% x/c, which is evident in Table 1. The results also show that the effectiveness of the blowing attains the peak at 41% x/c, which suggests the blowing location is the key factor in buffeting control via steady blowing.

Table 1. PSD peak values under the "Blow_1.0_Ptot" condition.

	5.0°	5.5°	6.0°
41% x/c	1.96×10^{-5}	1.16×10^{-5}	7.86×10^{-6}
46% x/c	1.88×10^{-5}	1.36×10^{-3}	8.70×10^{-3}
51% x/c	1.58×10^{-5}	5.49×10^{-3}	1.63×10^{-2}

4.1.2. Flow Characteristics of the "41% x/c" Case

From the above context, it can be interpreted that flow characteristics are altered under the "41% x/c" case. The airfoil surface pressure coefficient distributions corresponding to maximum, median, and minimum lift states under "Blow_1.0_Ptot" tangential blowing are plotted in Figure 15. It is seen that shockwave location nearly did not oscillate, but surface pressure in the separation zone downstream of the shockwave varied with time.
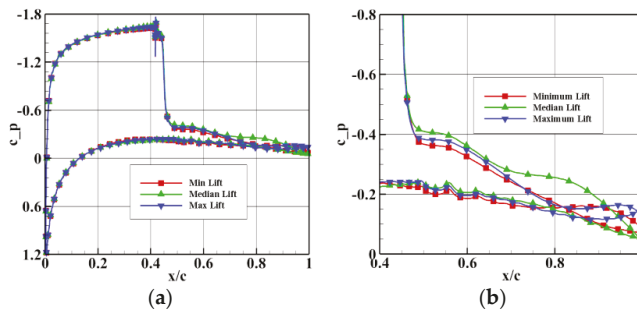
Figure 15. Surface pressure distributions corresponding to maximum/median/minimum lifts with tangential blowing. (**a**) Surface pressure distribution; (**b**) zoomed version.

Given that the most severe buffeting occurs at an incidence angle 6.0°, it was selected to highlight the control effort. Three streamline contours corresponding to maximum lift, mean lift, and minimum lift for clean airfoil and "Blow_1.0_Ptot" blowing cases are plotted in Figure 16. It is seen that, for the clean airfoil without tangential blowing, the aspects depicting the unsteady shock/separation bubble interaction intensity can be summarized as follows [57]: (a) wedge effects—pressure rise due to the shock resulted in flow separation emanating from the shock foot, where this separated region behaved similar to a geometric wedge to strengthen the shock, as shown in Figure 16a; (b) dynamic effects—as the shock moved upstream, the velocity of the shock increased the relative Mach number of the upstream flow, as shown in Figure 16b; (c) airfoil curvature effects—the expansion of flow through the subsonic zone was dependent on the local surface curvature. The thick boundary layer decreased the camber, resulting in a reduction of the airfoil's circulation, as shown in Figure 16c. Under tangential slot-blowing conditions plotted in Figure 16d–f, by ejecting streamwise momentum into the boundary layer from tangential slot blowing, the adverse velocity of the separation bubble was evidently reduced, and the separation bubble could not move to the upstream location of the slot because of the strong ejection momentum. Hence, the shock/separation bubble interaction is evidently suppressed, resulting in (a) a reduced wedge effect as outlined as a smaller separation zone under the shock foot; (b) a weakened dynamic effect portrayed by the regularized bubble position.

Figure 16. Streamlines corresponding to maximum/median/minimum lifts with and without tangential blowing. (**a**) Maximum lift without blowing; (**b**) median lift without blowing; (**c**) minimum lift without blowing; (**d**) maximum lift with blowing; (**e**) median lift with blowing; and (**f**) minimum lift with blowing.

To investigate the flow control mechanism, the Q-criterion results corresponding to those cases in Figure 16 were plotted in Figure 17, respectively. In the subsonic boundary layer, a feedback loop between the Kutta wave at the trailing edge and the location of the shock [58] was seen; the generated shear layer in the separation bubble under the shock foot warped pressure waves that propagated downstream, which interacted with the feedback of the Kutta waves travelling toward the shock from the trailing edge, completing the feedback loop. At the most upstream location, the shockwave shed its shear layer downstream and interacted with the shear layer under the shock foot as well as Kutta waves. These multiple interactions exchanged momentum and energy, sustaining oscillation of the periodic boundary layer, and unsteady buffet loads were generated, as shown in Figure 17a–f, the shear layer was generated by tangential slot blowing, and it continuously carried streamwise momentum. This shear layer prevented the upstream creeping of Kutta waves. Due to the curvature effect, the ejected shear layer uplifted the airfoil surface, and Kutta waves help this uplifting process to form a counter rotating eddy blob. Meanwhile, the shockwave did not shed its shear layer into separated flows, thus the interaction intensity was reduced. The momentum ejected from the blowing slot determines how far the reversed flow in boundary layer is influenced. With the increase of blowing total pressure, the feedback creeping was prevented more profoundly; thus, the buffet frequency slightly decreased.
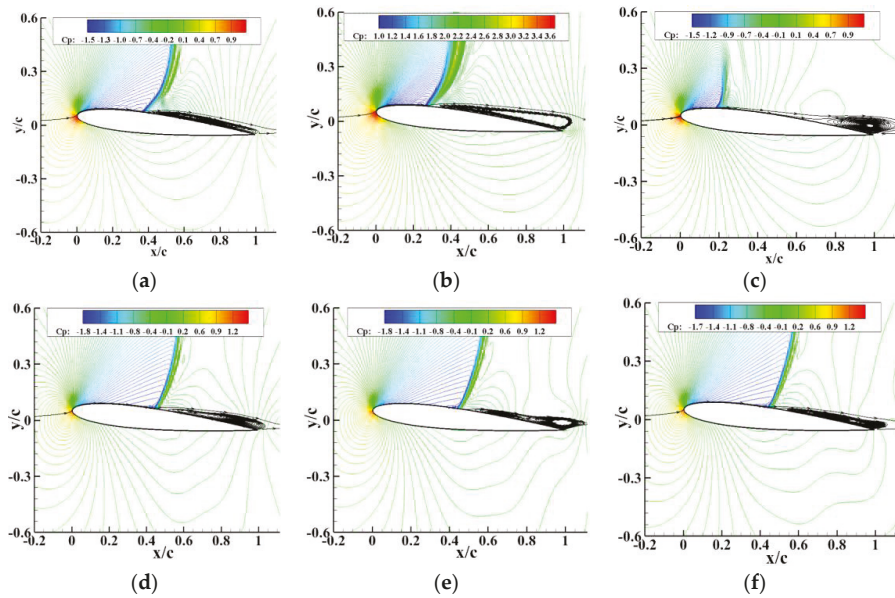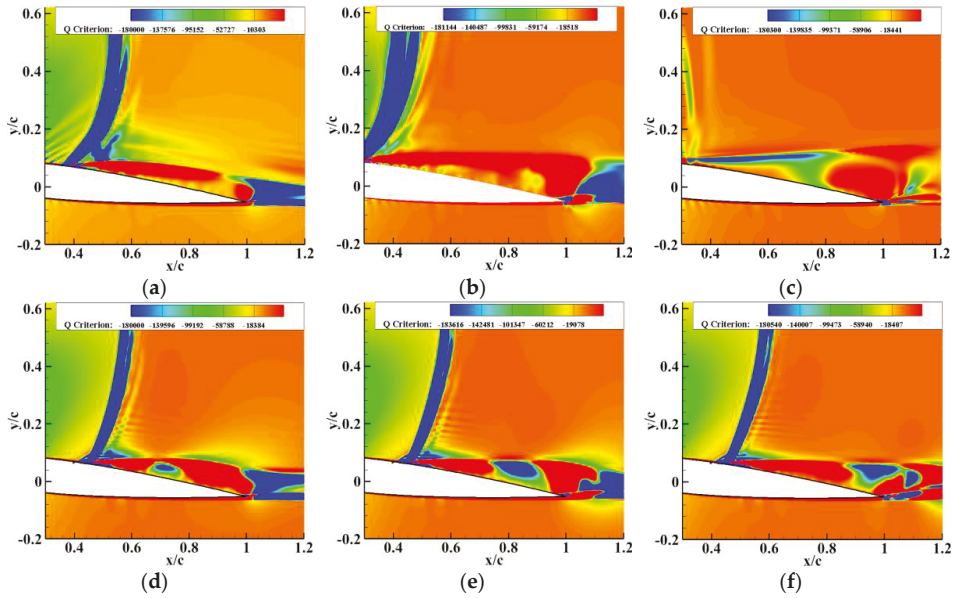
Figure 17. Q-criterion results corresponding to maximum/median/minimum lifts with and without tangential blowing. (**a**) Maximum lift without blowing; (**b**) median lift without blowing; (**c**) minimum lift without blowing; (**d**) maximum lift with blowing; (**e**) median lift with blowing; and (**f**) minimum lift with blowing.

4.2. Periodic Blowing

The effect of periodic tangential blowing was also investigated by transient numerical simulations. Given that the total pressure variation does not obviously influence the control effect of steady blowing cases, the variation ratio of total pressure was set to be 0.1, and the periodic total pressure is depicted as

$$P_{tot\_periodic} = (1 + \frac{\gamma - 1}{2}M_\infty^2)^{\frac{\gamma}{\gamma-1}} + 0.1 \times \sin{(2\pi \times f \times t)} \times (1 + \frac{\gamma - 1}{2}M_\infty^2)^{\frac{\gamma}{\gamma-1}} \qquad (4)$$

By referring to the PSD results above, the frequency of periodic blowing was set to be 90 Hz, and γ was 1.4 for calorically perfect gas.

From the above context, it is known that the most effective effect was achieved when the tangential blowing slot was placed at the location denoted as "41% x/c". Thus, the periodic blowing slot was first placed here. The unsteady lift coefficient results under periodic blowing conditions at different incidence angles were compared with those of steady blowing cases, as shown in Figure 18. By examining the results, it is found that the unsteady lift coefficients exhibited an oscillating frequency nearly the same as that of the clean airfoil at incidence angles 5.0°, 5.5°, and 6.0°. However, the mean lift coefficient values under periodic blowing conditions were a little lower compared to their corresponding steady blowing cases, as presented in Table 2.

Table 2. Mean lift coefficients with and without blowing.

	5.0°	5.5°	6.0°
Steady blowing	0.73	0.75	0.71
Periodic blowing	0.71	0.70	0.65
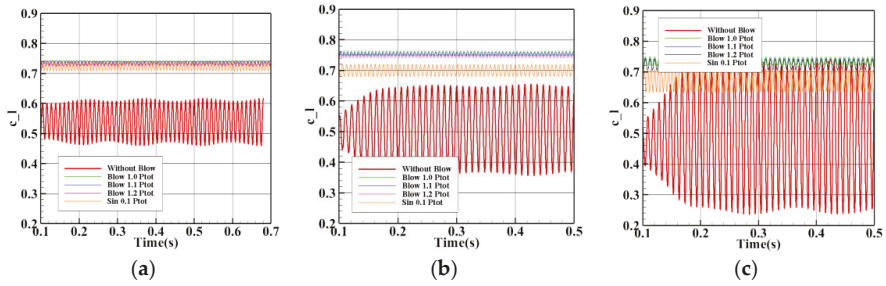
Figure 18. Unsteady lift coefficient histories under the "41% x/c" case at: (**a**) 5.0°, (**b**) 5.5°, and (**c**) 6.0°.

To investigate the frequency characteristics of unsteady lift coefficients, the PSD results of different periodic blowing cases were plotted, as shown in Figure 19. It can be seen from these figures that, for the "41% x/c" case, the peak PSD value of the lift coefficient with periodic tangential blowing was about 5 times larger than that with steady tangential blowing. Moreover, with the increase of incidence angle, frequencies corresponding to the peak PSD values also increased. Compared to the PSD results for steady blowing cases plotted in Figure 14, there was no obvious difference in frequency characteristics. Under all three blowing locations, periodic tangential slot blowing gave higher peak PSD values compared to steady tangential slot blowing at those two blowing locations.
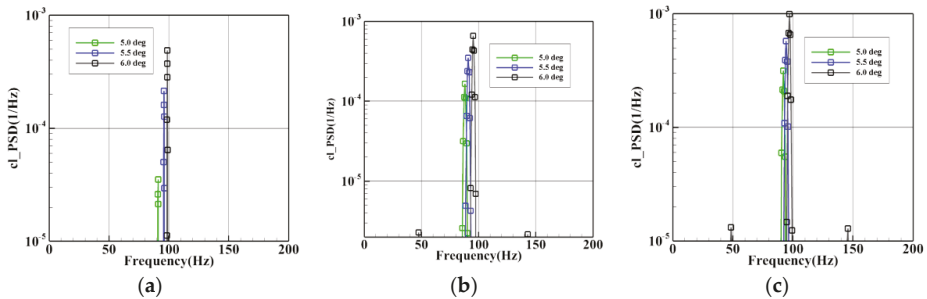
Figure 19. PSDs of unsteady lift coefficient histories under different blowing cases: (**a**) 41% x/c, (**b**) 46% x/c, and (**c**) 51% x/c.

Surface pressure coefficient distributions are plotted in Figures 20–22. Within each figure, surface pressure distribution lines corresponding to maximum, median, and minimum lifts in one oscillating period are plotted together. From these figures, it is observed that these oscillation amplitudes were smaller compared to those without tangential blowing (plotted in Figure 7), while compared to the results of steady tangential blowing cases (plotted in Figure 15), the shock oscillation amplitudes were a little larger, while the surface pressure variation downstream of the shockwave was evidently smaller.
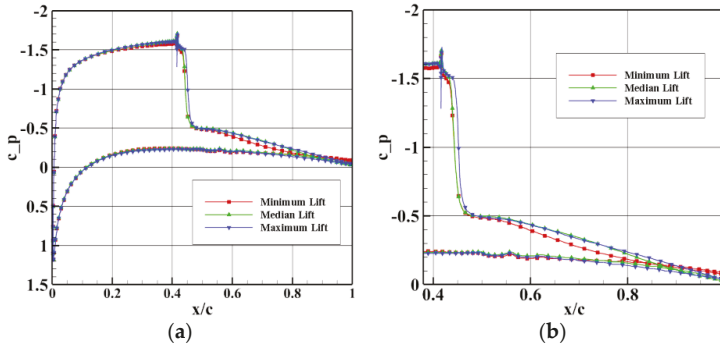
Figure 20. Pressure distributions over the airfoil for the "41% x/c" case at an incidence angle of 6.0°. (**a**) Surface pressure distribution; (**b**) zoomed version.
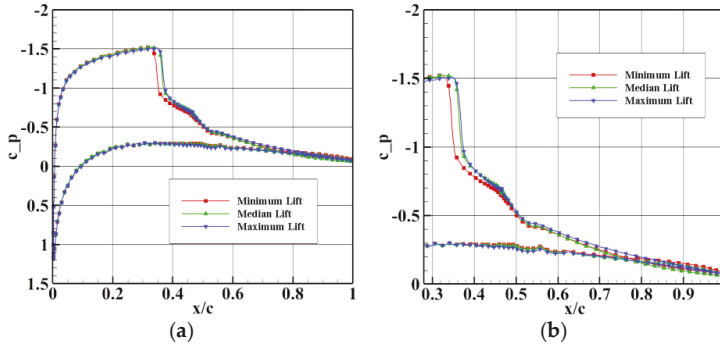
Figure 21. Pressure distributions over the airfoil for the "46% x/c" case at an incidence angle of 6.0°. (**a**) Surface pressure distribution; (**b**) zoomed version.
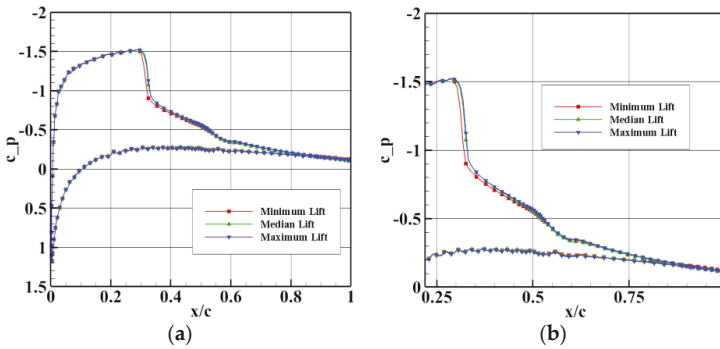
Figure 22. Pressure distributions over the airfoil for the "51% x/c" case at an incidence angle of 6.0°. (**a**) Surface pressure distribution; (**b**) zoomed version.

Q-criterion results corresponding to minimum lift, median lift, and maximum lift, are plotted in Figures 23–25, respectively. It can be seen from these figures that the blowing slots were all downstream of the shock foot. For the "41% x/c" case, the control mechanism was similar to that stated above for steady blowing cases. The difference is that the ejected momentum from periodic blowing was smaller; thus, Kutta waves can creep more upstream comparing to steady blowing cases, inducing a relatively larger buffet load. As the blowing slot moved downstream, the distance between shock and blowing

slot increased. Although the ejected momentum could also reduce the reverse boundary layer velocity to suppress Kutta waves on the upper surface of airfoil, its control effect on the separation bubble was obviously weakened; thus, the buffet load increased as the blowing slot moved downstream.
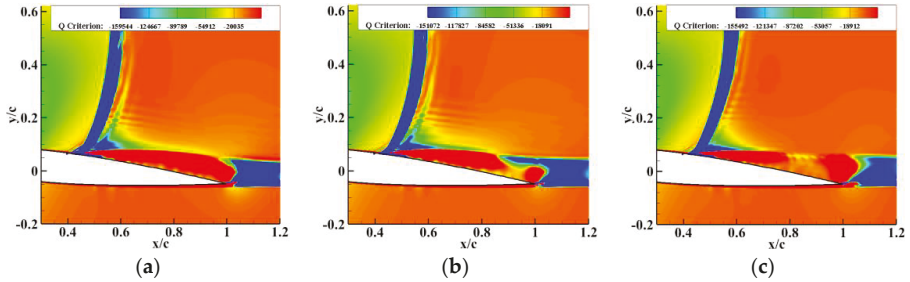
Figure 23. Q-criterion results for the "41% x/c" case. (**a**) Maximum lift; (**b**) median lift; and (**c**) minimum lift.
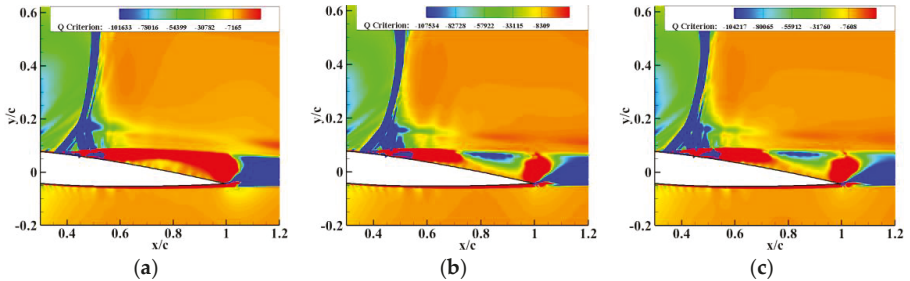
Figure 24. Q-criterion results for the "46% x/c" case. (**a**) Maximum lift; (**b**) median lift; and (**c**) minimum lift.
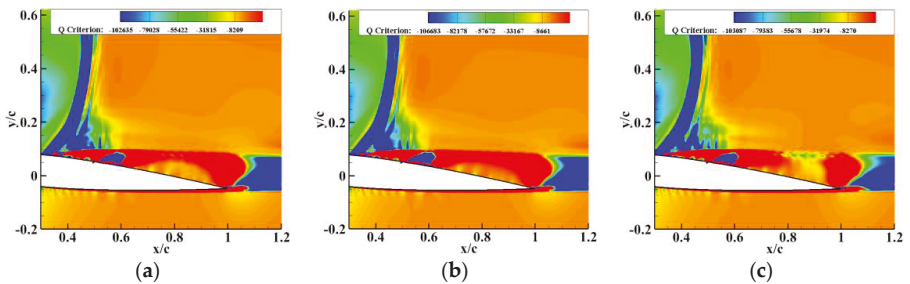
Figure 25. Q-criterion results for the "51% x/c" case. (**a**) Maximum lift; (**b**) median lift; and (**c**) minimum lift.

With the increase of incidence angle, the separation bubble increased, inducing increases in interference intensity, feedback control, and a decrease in the interference zone size. This induces the increase of buffet frequency with incidence angle.

5. Conclusions

By using a Venturi nozzle over the upper surface of an airfoil, the control effects of tangential slot blowing on postponement of the transonic buffet onset margin and alleviation of buffet load were investigated numerically. It was found that steady tangential blowing could delay buffet onset, and an

evident increase of the lift coefficient was discerned at incidence angles near and exceeding the buffet onset margin of the clean airfoil. In the investigation of buffet load alleviation, both steady and periodic tangential blowing with slots placed at three different chord-wise locations were tested under buffeting states of a clean airfoil. The results indicated that unsteady buffet loads could be greatly suppressed by both steady and periodic blowing. An increase in total blowing pressure does not apparently improve the reduction effect of dynamic loads for steady blowing cases; the control effect is reduced as the blowing slot moves downstream. The control effort is as follows: the shock/separation bubble interaction is evidently suppressed, resulting in (a) a reduced wedge effect as outlined as a smaller separation zone under the shock foot; (b) a weakened dynamic effect portrayed by the regularized bubble position. The buffet mechanism includes (a) the feedback loop between the Kutta wave and the separation bubble under the shock foot, and (b) the interaction between the shear layer shed by the shockwave and Kutta waves. Under blowing conditions, the upstream creeping Kutta waves are prevented, and the intensity of the shear layer shed by the shockwave into separated flows is evidently reduced. Parametric studies show that, with the increase of total blowing pressure for steady blowing cases, or with the increase of incidence angle for periodic blowing cases, the feedback distance decreases; thus, the buffet frequency increases. The mean lifts of steady cases are slightly higher compared to their corresponding periodic blowing cases. Steady blowing at a 41x/c chord location is suggested among the presented test cases.

Author Contributions: investigation, H.D. (Huixue Dang); methodology, J.Z. and Z.Y.; writing and editing, H.D. (Huibo Dang).

Conflicts of Interest: The funders had no role in the design of the study; in the collection, analyses, or interpretation of data; in the writing of the manuscript; or in the decision to publish the results.

References

1. Huang, J.; Xiao, Z.; Liu, J.; Fu, S. Simulation of shock wave buffet and its suppression on an OAT15A supercritical airfoil by IDDES. *China Phys. Mech.* **2012**, *55*, 260–271. [CrossRef]
2. Giannelis, N.F.; Vio, G.A.; Levinski, O. A review of recent developments in the understanding of transonic shock buffet. *Prog. Aerosp. Sci.* **2017**, *92*, 39–84. [CrossRef]
3. Szubert, D.; Grossi, F.; Jimenez Garcia, A.; Yannick, H.; Julian, C.R.H.; Marianna, B. Shock-vortex shear-layer interaction in the transonic flow around a supercritical airfoil at high Reynolds number in buffet conditions. *J. Fluid Struct.* **2015**, *55*, 276–302. [CrossRef]
4. Timme, S.; Thormann, R. Towards Three-Dimensional Global Stability Analysis of Transonic Shock Buffet. In Proceedings of the AIAA Atmospheric Flight Mechanics Conference, American Institute of Aeronautics and Astronautics, Washington, DC, USA, 13–17 June 2016. [CrossRef]
5. Zhang, Z.; Qu, K. Numerical Investigation of Transonic Airfoil Buffet Suppression. In Proceedings of the 53rd AIAA Aerospace Sciences Meeting, American Institute of Aeronautics and Astronautics, Kissimmee, FL, USA, 5–9 January 2015. [CrossRef]
6. Ohmichi, Y.; Ishida, T.; Hashimoto, A. Numerical Investigation of Transonic Buffet on a Three-Dimensional Wing using Incremental Mode Decomposition. In Proceedings of the 55th AIAA Aerospace Sciences Meeting, American Institute of Aeronautics and Astronautics, Grapevine, TX, USA, 9–13 January 2017. [CrossRef]
7. Dandois, J.; Lepage, A.; Dor, J.B.; Molton, P.; Ternoy, F.; Geeraert, A.; Brunet, V.; Coustols, É. Open and closed-loop control of transonic buffet on 3D turbulent wings using fluidic devices. *C. R. Mécanique* **2014**, *342*, 425–436. [CrossRef]
8. Sartor, F.; Mettot, C.; Sipp, D. Stability, Receptivity, and Sensitivity Analyses of Buffeting Transonic Flow over a Profile. *AIAA J.* **2014**, *53*, 1980–1993. [CrossRef]
9. Gao, C.; Zhang, W.; Ye, Z. Numerical study on closed-loop control of transonic buffet suppression by trailing edge flap. *Comput. Fluids* **2016**, *132*, 32–45. [CrossRef]
10. Tian, Y.; Liu, P.; Li, Z. Multi-objective optimization of shock control bump on a supercritical wing. *Sci. China (Technol. Sci.)* **2014**, *1*, 192–202. [CrossRef]

11. Ishida, T.; Ishiko, K.; Hashimoto, A.; Aoyama, T.; Takekawa, K. Transonic Buffet Simulation over Supercritical Airfoil by Unsteady-FaSTAR Code. In Proceedings of the 54th AIAA Aerospace Sciences Meeting, American Institute of Aeronautics and Astronautics, San Diego, CA, USA, 4–8 January 2016. [CrossRef]

12. Fukushima, Y.; Kawai, S. Wall-modeled Large-Eddy Simulation of Transonic Buffet over a Supercritical Airfoil at high Reynolds Number. In Proceedings of the 55th AIAA Aerospace Sciences Meeting, American Institute of Aeronautics and Astronautics, Grapevine, TX, USA, 9–13 January 2017. [CrossRef]

13. Raveh, D.E.; Dowell, E.H. Aeroelastic Responses of Elastically Suspended Airfoil Systems in Transonic Buffeting Flows. *AIAA J.* **2014**, *52*, 926–934. [CrossRef]

14. Tian, Y.; Li, Z.; Liu, P.Q. Upper Trailing-Edge Flap for Transonic Buffet Control. *J. Aircr.* **2017**, *1*, 8. [CrossRef]

15. Quan, J.; Zhang, W.; Gao, C.; Ye, Z. Characteristic analysis of lock-in for an elastically suspended airfoil in transonic buffet flow. *Chin. J. Aeronaut.* **2016**, *29*, 129–143. [CrossRef]

16. Tian, Y.; Feng, P.; Liu, P.; Hu, T.; Qu, Q. Spoiler Upward Deflection on Transonic Buffet Control of Supercritical Airfoil and Wing. *J. Aircr.* **2016**, *54*, 1229–1233. [CrossRef]

17. Crouch, J.D.; Garbaruk, A.; Magidov, D. Predicting the onset of flow unsteadiness based on global instability. *J. Comput. Phys.* **2007**, *224*, 924–940. [CrossRef]

18. Dietz, G.; Schewe, G.; Mai, H. Amplification and amplitude limitation of heave/pitch limit-cycle oscillations close to the transonic dip. *J. Fluid Struct.* **2006**, *22*, 505–527. [CrossRef]

19. Lee, B.H.K. Self-sustained shock oscillations on airfoils at transonic speeds. *Prog. Aerosp. Sci.* **2001**, *37*, 147–196. [CrossRef]

20. Hermes, V.; Klioutchnikov, I.; Olivier, H. Numerical investigation of unsteady wave phenomena for transonic airfoil flow. *Aerosp. Sci. Technol.* **2013**, *25*, 224–233. [CrossRef]

21. Bouhadji, A.; Braza, M. Organised modes and shock–vortex interaction in unsteady viscous transonic flows around an aerofoil: Part I: Mach number effect. *Comput. Fluids* **2003**, *32*, 1233–1260. [CrossRef]

22. Bouhadji, A.; Braza, M. Organised modes and shock–vortex interaction in unsteady viscous transonic flows around an aerofoil: Part II: Reynolds number effect. *Comput. Fluids* **2003**, *32*, 1261–1281. [CrossRef]

23. Caruana, D.; Mignosi, A.; Corrège, M.; Le Pourhiet, A.; Rodde, A.M. Buffet and buffeting control in transonic flow. *Aerosp. Sci. Technol.* **2005**, *9*, 605–616. [CrossRef]

24. Tian, Y.; Gao, S.; Liu, P.; Wang, J. Transonic buffet control research with two types of shock control bump based on RAE2822 airfoil. *Chin. J. Aeronaut.* **2017**, *30*, 1681–1696. [CrossRef]

25. Murman, S.M.; Diosady, L.T.; Blonigan, P.J. Comparison of Transonic Buffet Simulations with Unsteady PSP Measurements for a Hammerhead Payload Fairing. In Proceedings of the 55th AIAA Aerospace Sciences Meeting, American Institute of Aeronautics and Astronautics, Grapevine, TX, USA, 9–13 January 2017. [CrossRef]

26. Liu, J.; Yang, Z. A Maximum Curvature Method for Predicting Transonic Buffet Onset Based on Steady Aerodynamic Parameters. *Procedia Eng.* **2013**, *61*, 363–369. [CrossRef]

27. Yang, Z.; Liu, J. A Precise Approach to Predict Transonic Wing Buffet Boundary. *Mech. Sci. Technol. Aerosp. Eng.* **2013**, *12*, 1717–1721. (In Chinese)

28. Kou, J.; Zhang, W. An improved criterion to select dominant modes from dynamic mode decomposition. *Eur. J. Mech. B Fluids* **2017**, *62*, 109–129. [CrossRef]

29. Barakos, G.; Drikakis, D. Numerical simulation of transonic buffet flows using various turbulence closures. *Int. J. Heat Fluid Flow* **2000**, *21*, 620–626. [CrossRef]

30. Thiery, M.; Coustols, E. Numerical prediction of shock induced oscillations over a 2D airfoil: Influence of turbulence modelling and test section walls. *Int. J. Heat Fluid Flow* **2006**, *27*, 661–670. [CrossRef]

31. Bonnifet, V.; Gerolymos, G.A.; Vallet, I. Transonic Buffet Prediction using Partially Averaged Navier-Stokes. In Proceedings of the 23rd AIAA Computational FLUID DYNAMICS Conference, American Institute of Aeronautics and Astronautics, Denver, CO, USA, 5–9 June 2017. [CrossRef]

32. Iovnovich, M.; Raveh, D.E. Transonic unsteady aerodynamics in the vicinity of shock-buffet instability. *J. Fluid Struct.* **2012**, *29*, 131–142. [CrossRef]

33. Thiede, P.K.P.; Stanewsky, E. *Active and Passive Shock/Boundary Layer Interaction Control on Supercritical Airfoils*; AGARD CP-365, DEUTSCHE FORSCHUNGS-UND VERSUCHSANSTALT FUER LUFT-UND RAUMFAHRT EV GOETTINGEN (GERMANY FR); Reston: Brussels, Belgium, 1984.

34. Smith, A.; Babinsky, H.; Fulker, J.L.; Ashill, P.R. Shock Wave/ Boundary-Layer Interaction Control Using Streamwise Slots in Transonic Flows. *J. Aircr.* **2004**, *41*, 540–546. [CrossRef]

35. Holden, H.A.; Babinsky, H. Separated Shock-Boundary-Layer Interaction Control Using Streamwise Slots. *J. Aircr.* **2005**, *42*, 166–171. [CrossRef]

36. Molton, P.; Dandois, J.; Lepage, A.; Brunet, V.; Bur, R. Control of Buffet Phenomenon on a Transonic Swept Wing. *AIAA J.* **2013**, *51*, 761–772. [CrossRef]

37. Ogawa, H.; Babinsky, H.; Pätzold, M.; Lutz, T. Shock-Wave/Boundary-Layer Interaction Control Using Three-Dimensional Bumps for Transonic Wings. *AIAA J.* **2008**, *46*, 1442–1452. [CrossRef]

38. Eastwood, J.P.; Jarrett, J.P. Toward Designing with Three-Dimensional Bumps for Lift/Drag Improvement and Buffet Alleviation. *AIAA J.* **2012**, *50*, 2882–2898. [CrossRef]

39. Liu, J.; Yang, Z. Numerical study on transonic shock oscillation suppression and buffet load alleviation for a supercritical airfoil using a microtab. *Eng. Appl. Comput. Fluid Mech.* **2016**, *10*, 529–544. [CrossRef]

40. Caruana, D.; Mignosi, A.; Correge, M.; Le Pourhiet, A. Buffeting Active Control in Transonic Flow. In Proceedings of the 21st AIAA Applied Aerodynamics Conference, American Institute of Aeronautics and Astronautics, Orlando, FL, USA, 23–26 June 2003. [CrossRef]

41. Caruana, D.; Mignosi, A.; Robitaillié, C.; Corrège, M. Separated Flow and Buffeting Control. *Flow Turbul. Combust.* **2003**, *71*, 221–245. [CrossRef]

42. Ferman, M.A.; Huttsell, L.J.; Turner, E.W. Experiments with Tangential Blowing to Reduce Buffet Response on an F-15 Model. *J. Aircr.* **2004**, *41*, 903–910. [CrossRef]

43. Abramova, K.A.; Khairullin, B.M.A.; Petrov, K.G.; Potapchik, A.V.; Soudakov, V.G. Buffet Delay on Transonic Airfoil by Tangential Jet Blowing. In Proceedings of the 7th European Conference for Aeronautics and Space Sciences (Eucass), Milan, Italy, 3–6 June 2017.

44. Abramova, K.A.; Ryzhov, A.A.; Sudakov, V.G.; Khairullin, K.G. Numerical modeling of transonic buffeting and its control by means of tangential jet blowing. *Fluid Dyn.* **2017**, *52*, 329–335. [CrossRef]

45. Abramova, K.A.; Petrov, A.V.; Potapchick, A.V.; Soudakov, V.G. Investigations of Transonic Buffet Control on Civil Aircraft Wing with the Use of Tangential Jet Blowing. *AIP Conf. Proc.* **2016**, *1770*, 020017. [CrossRef]

46. Abramova, K.A.; Soudakov, V.G. Numerical optimization of flow control by tangential jet blowing on transonic airfoil. In Proceedings of the 31st Congress of the International Council of the Aeronautical Sciences, Belo Horizonte, Brazil, 9–14 September 2018. [CrossRef]

47. Grossi, F.; Braza, M.; Hoarau, Y. Prediction of Transonic Buffet by Delayed Detached-Eddy Simulation. *AIAA J.* **2014**, *52*, 2300–2312. [CrossRef]

48. Deck, S. Numerical Simulation of Transonic Buffet over a Supercritical Airfoil. *AIAA J.* **2005**, *43*, 1556–1566. [CrossRef]

49. Chen, L.W.; Chang-Yue, X.U.; Xi-Yun, L.U. Numerical investigation of the compressible flow past an aerofoil. *J. Fluid Mech.* **2010**, *643*, 97–126. [CrossRef]

50. Soda, A. Numerical Investigation of Unsteady Transonic Shock/Boundary-layer Interaction for Aeronautical Applications. Ph.D. Thesis, Fakultät für Mathematik, Informatik und Naturwissenschaften, Aachen, Germany, 2007.

51. Medida, S.; Baeder, J. Numerical Prediction of Static and Dynamic Stall Phenomena Using the γ-$\overline{Re\theta t}$ Transition Model. American Helicopter Society 67th Annual Forum. Available online: https://www.researchgate.net/publication/288661255_Numerical_prediction_of_static_and_dynamic_stall_phenomena_using_the_g-Retht_transition_model (accessed on May 2011).

52. Kitamura, K.; Shima, E. Towards shock-stable and accurate hypersonic heating computations: A new pressure flux for AUSM-family schemes. *J. Comput. Phys.* **2013**, *245*, 62–83. [CrossRef]

53. Economon, T.D.; Francisco, P.; Sean, R.C.; Trent, W.L.; Juan, J.A. SU2: An Open-Source Suite for Multiphysics Simulation and Design. *AIAA J.* **2015**, *54*, 828–846. [CrossRef]

54. McDevitt, J.B.; Okuno, A.F. Static and Dynamic Pressure Measurements on a NACA0012 Airfoil in the Ames High Reynolds Number Facility. NASA TP-2485; June 1985. Available online: https://www.mendeley.com/catalogue/static-dynamic-naca-0012-airfoil-ames-high-reynolds-number-facility-naca-0012-reynolds-number-facili/ (accessed on June 1985).

55. Ribeiro, A.F.; Konig, B.; Singh, D.; Fares, E.; Zhang, R.; Chen, H. Buffet Simulations with a Lattice-Boltzmann based Transonic Solver. In Proceedings of the 55th AIAA Aerospace Sciences Meeting, American Institute of Aeronautics and Astronautics, Grapevine, TX, USA, 9–13 January 2017. [CrossRef]

56. Raveht, D.E. Numerical Study of an Oscillating Airfoil in Transonic Buffeting Flows. *AIAA J.* **2009**, *47*, 505–515. [CrossRef]

57. Iovnovich, M.; Raveh, D.E. Reynolds-Averaged Navier-Stokes Study of the Shock-Buffet Instability Mechanism. *AIAA J.* **2012**, *50*, 880–890. [CrossRef]

58. Lee, B.H.K. Oscillatory shock motion caused by transonic shock boundary-layer interaction. *AIAA J.* **1990**, *28*, 942–944. [CrossRef]

Article

Analysis of Aerodynamic Noise Characteristics of High-Speed Train Pantograph with Different Installation Bases

Yongfang Yao [1,2], Zhenxu Sun [1,*], Guowei Yang [1,2], Wen Liu [3] and Prasert Prapamonthon [1,4]

[1] Key Laboratory for Mechanics in Fluid Solid Coupling Systems, Institute of Mechanics, Chinese Academy of Sciences, Beijing 100190, China; yaoyongfang@imech.ac.cn (Y.Y.); gwyang@imech.ac.cn (G.Y.); prasert.pr@kmitl.ac.th (P.P.)
[2] School of Engineering Sciences, University of Chinese Academy of Sciences, Beijing 100190, China
[3] Industrial Software (Beijing) Co., Ltd., Beijing 100101, China; wenliu@siemens.com
[4] International Academy of Aviation Industry, King Mongkut's Institute of Technology Ladkrabang, Bangkok 10520, Thailand
*   Correspondence: sunzhenxu@imech.ac.cn; Tel.: +86-10-82543815

Abstract: The high-speed-train pantograph is a complex structure that consists of different rod-shaped and rectangular surfaces. Flow phenomena around the pantograph are complicated and can cause a large proportion of aerodynamic noise, which is one of the main aerodynamic noise sources of a high-speed train. Therefore, better understanding of aerodynamic noise characteristics is needed. In this study, the large eddy simulation (LES) coupled with the acoustic finite element method (FEM) is applied to analyze aerodynamic noise characteristics of a high-speed train with a pantograph installed on different configurations of the roof base, i.e. flush and sunken surfaces. Numerical results are presented in terms of acoustic pressure spectra and distributions of aerodynamic noise in near-field and far-field regions under up- and down-pantograph as well as flushed and sunken pantograph base conditions. The results show that the pantograph with the sunken base configuration provides better aerodynamic noise performances when compared to that with the flush base configuration. The noise induced by the down-pantograph is higher than that by the up-pantograph under the same condition under the pantograph shape and opening direction selected in this paper. The results also indicate that, in general, the directivity of the noise induced by the down-pantograph with sunken base configuration is slighter than that with the flush configuration. However, for the up-pantograph, the directivity is close to each other in Y-Z or X-Z plane whether it is under flush or sunken roof base condition. However, the sunken installation is still conducive to the noise environment on both sides of the track.

Keywords: high-speed train; pantograph; aerodynamic noise; large eddy simulation; acoustic finite element method

1. Introduction

Over the last twenty years, high-speed trains have played a major role in community and urban development. It is well known that, as the speed of a high-speed train increases, aerodynamic problems that can be neglected at low speeds become more serious. For such cases, the problem of aerodynamic noise cannot be avoided and must be addressed. Therefore, better understanding of the aerodynamic noise characteristics is needed. To alleviate the aerodynamic noise problems, the shape of complex parts is optimized and appropriate sound barriers are commonly used. Presently, a large number of high-speed trains can reach an operating speed of about 300–350 km/h. With these speeds, the trains cause serious aerodynamic noise pollution to passengers and surroundings. Zhang [1] indicated

that aerodynamic noise becomes a main pollution source when train speed exceeds 250–300 km/h. His results indicated that, with the increase of train speed, the noise increases rapidly and the aerodynamic noise almost increases with the sixth power of the train speed. To date, the aerodynamic noise characteristics of high-speed trains have been investigated numerically and experimentally. Based on numerical approaches, aero-acoustic analysis is applied to simplified and real-oriented high-speed train geometries to evaluate aerodynamic noise. The numerical approaches could be divided into direct and hybrid methods. The direct methods commonly use the direct numerical simulation (DNS), large eddy simulation (LES), or detached eddy simulation (DES) to simulate the flow field and aerodynamic noise simultaneously. In this kind of methods, the grid scale and energy capture requirements differ between the analysis of the flow field and the analysis of the acoustic propagation. It is found that the magnitude of sound pressure is smaller when compared to that of the dynamic pressure in the flow field. The direct methods are required to adopt high-order, low-dissipation, low-dispersion discretization schemes to produce appropriately accurate solutions [2]. Moreover, since the shape of high-speed trains is rather complex, the use of the direct methods can suffer from high computational costs. Consequently, the hybrid methods seem at present more attractive for practical engineering problems. In the hybrid methods, sound sources in the near field and sound propagation in the far field are solved separately. The pressure fluctuations are solved using a high-order technique of LES, DES or are modeled from turbulence statistics obtained from Reynolds Average Navier-Stokes (RANS) simulations. Then, the pressure fluctuations are analyzed by means of acoustic methods to solve the acoustic propagation. Presently, the trend of the research on the aerodynamic noise of high-speed trains is mostly based on the hybrid methods.

On simplified train geometries, it is found that effects of flow separation and vortices from the head, the tail, and the car connections are the main sources of aerodynamic noise. Sun et al. [3] studied the near-field and far-field aerodynamic noise characteristics and comprehensively assessed the noise level of the key parts in a simplified CRH3 high-speed train model using the Non-Linear Acoustic method (NLAS) and the Ffowcs Williams–Hawkings (FW-H) acoustic analogy approach. Their results indicated that the head and the tail are the main noise sources. In addition, the results indicated that the rough areas with cavities or hump faces on the train structure contribute significantly to the aerodynamic noise. Moreover, it was found that the car connection area is also a noise source. Liu et al. [4] used unsteady incompressible flow analysis to obtain the fluctuation pressure on the train surface, and the FW-H method was adopted to predict the noise propagation to the far field. They studied the spectral characteristics of the head surface of a simplified high-speed train, and the aerodynamic noise sources and the aerodynamic noise distribution in the far-field region. Their results revealed that aerodynamic noise could be greatly reduced as long as the shapes of train head and body are optimized. Aerodynamic noise of more realistic high-speed geometries has been investigated by including more complicated components, such as pantographs and bogies. It was observed by Zhu and Jing [5], and Sun et al. [6] that the aerodynamic noise sources come from the pantographs, the bogies, the car head, and the rear of the car. Previously, King et al. [7] showed that the correlation between the logarithm of the aerodynamic noise and the running speed of the pantograph is approximately linear. Takaishi et al. [8,9] used LES and the compact Green's function to simulate the distribution of the dipole noise source on the bogie and the surface of the pantograph. Their results showed that periodic vortices induced by unstable shear layer separation at the leading edge of the bogie section in the flow provide the major part of sound generation [8]. Furthermore, Takaishi et al. [9] indicated that the dipole sound sources around the pantograph make a strong aerodynamic noise source due to the fact that the dipole sound sources are formed strongly in the shear layer close to the model surface. Yoshiki et al. [10] used the Lattice Boltzmann Method (LBM) to calculate the aerodynamic noise of the pantograph, and numerical results gave good agreement with the experimental results obtained by wind tunnel test. Liu [11] used LES to simulate the unsteady incompressible flow on the pantograph, and the far-field aerodynamic noise of pantograph was calculated by Lighthill's acoustic analogy. The characteristics of sound pressure level, frequency spectrum and the relationship between

sound pressure level and speed was investigated. It was found that the sound pressure level increases significantly with the increase of vehicle speed and is approximately linear with the logarithm of vehicle speed. Tan and Xie [12] used LES, the scale adaptive simulation(SAS), the improved delayed detached eddy simulation with shear-stress transport k-ω (IDDES SST k-ω), the delayed detached eddy simulation with shear-stress transport k-ω (DDES SST k-ω), and the delayed detached eddy simulation with realizable k-ε(DDES Realizable k-ε) models to investigate the flow-field structures, the aeroacoustic sources, and the aeroacoustics of pantographs. By means of a hybrid method of NLAS and FW–H acoustic analogy, Yu et al. [13] studied the aerodynamic noise of the pantograph system, specifically to predict the influence of the pantograph covers on noise in the speed range. Besides the methods used to conduct acoustic propagation as mentioned above, there are still other methods for universal acoustic propagation calculations such as the acoustic boundary element method (BEM) and the acoustic finite element method (FEM). CFD transient simulation is used to obtain the fluctuating pressure in the time domain on the boundary of the pantograph, and is transformed into the frequency domain to form the boundary conditions of the acoustic finite element to further solve the far-field noise. By means of the combined CFD/FW-H the acoustic analogy with BEM, aerodynamic noise from a pantograph was predicted by Sun et al. [14] and by Zhang et al. [15]. According to Zhang et al. [15], they used LES with high-order finite difference schemes to analyze the near-field unsteady flow around the pantograph, while the far-field aerodynamic noise was predicted using the CFD/FW-H acoustic analogy. The results of the surface pressure fluctuations were used in BEM to predict aerodynamic noise sources of the pantograph and the far-field sound radiation. The results showed that the aerodynamic noise originates mainly from the top regions of the pantograph rather than from the bottom regions. Also, the results indicated that the noise generated from the pantograph oriented opposite to the direction to the motion is lower than that oriented in the same direction to the motion, by as much as 3.4 dB(A). Sun et al. [14] used DES to analyze the flow field. They also used BEM to predict the aerodynamic noise from a pantograph, giving the spatial and spectral characteristics of the noise around the pantograph. Several previous experiments also showed evidence that the pantograph is an important component that generates high intensity of noise. For example, Kitagawa and Nagakura [16,17] showed that the main road-side noise is the aerodynamic noise produced by the pantograph and bogie. Noger et al. [18] tested a 1/7th scaled train model with and without pantograph in a wind tunnel and showed that the space near the rear vertical face of the cavity is the most complex and turbulent region. This is the origin of the most important noise generation. Their research suggested that the modification of the cavity geometry with passive devices or active control can be an effective method for reducing the radiated noise. Lawson and Barakos [19] indicated that the length/height ratio of the cavity has a greater impact on its internal flow field, which then also affects pantograph noise. However, the spatial distribution and directivity of far-field noise in the experiment was not discussed deeply in their work. Hence, the influence on noise from the cavity needs to be further explored.

Overall, few studies on the effects of the installation base configuration of the pantograph on the aerodynamic noise characteristics have been done so far. In fact, the flow field of a high-speed train can be seriously disturbed by non-flush surfaces of the train body and then complex flow separation and vortex shedding are caused. This disturbance leads to fluctuating surface pressure that becomes a significant aerodynamic noise source, which radiates to far field regions. The mechanism of aero-acoustic propagation and aerodynamic noise physical characteristics caused by complex structures such as the pantograph and the bogies remain challenging and need to be further discussed. The objective of the present work is to numerically investigate the effects of the pantograph with different installation bases of a high-speed train on the aerodynamic and on the acoustic characteristics using LES with the acoustic FEM. The spectral characteristics and directivity of the aerodynamic noise are discussed. This work can provide high-speed train designers and investigators with useful knowledge of the aerodynamic noise characteristics under different configurations of the installation base of the pantograph.

2. Computational Models

The pantograph used in the present study consists of insulators, chassis, upper arm, lower arm rod and double slide, as depicted in Figure 1. The upper arm and lower arm rod can move vertically, and are controlled by the base frame mechanism. On the roof of the train body, the pantograph is installed, either flush or sunken. Namely, the flush surface configuration of the roof is used as the baseline for a comparison with the sunken surface configuration. Scenarios of the up and down pantograph with the different configurations of the pantograph installation on the surface roof are shown in Figure 2.
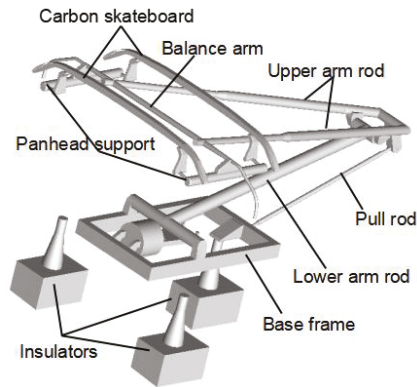
Figure 1. Model of pantograph.
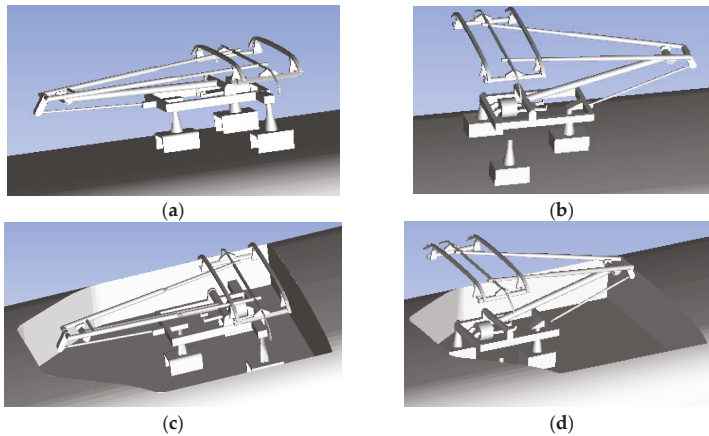
Figure 2. Scenarios of pantograph with different configurations of installation base: (**a**) model of down-pantograph with flush installation; (**b**) model of up-pantograph with flush installation; (**c**) model of down-pantograph with sunken installation; and (**d**) model of up-pantograph with sunken installation.

3. Computational Methods

The commercial CFD program STAR-CCM+, which is based on the finite-volume method, is used to simulate the flow field around the pantograph and the installation base. The LES method is used to conduct the dynamic flow characteristics, including the fluctuating pressure on the pantograph and the base. Then, the fluctuating pressure in the time domain is transformed into the frequency domain by the Fast Fourier Transform (FFT) method and the acoustic FEM with commercial program LMS Virtual lab is used to evaluate the acoustic noise of radiation from the pantograph.

3.1. Large Eddy Simulation

According to LES, the large-scale eddies in a fully turbulent flow are computed directly and the influence of the small eddies on the large-scale eddies is modeled. The continuity equation and the Favre averaged compressible Navier–Stokes equations, as expressed mathematically in Equations (1) and (2), respectively, are solved implicitly.

$$\frac{\partial \rho}{\partial t} + \frac{\partial}{\partial x_i}(\rho \bar{u}_i) = 0 \tag{1}$$

$$\frac{\partial}{\partial t}(\rho \bar{u}_i) + \frac{\partial}{\partial x_i}(\rho \bar{u}_i \bar{u}_j) = \frac{\partial}{\partial x_j}(\sigma_{i,j}) - \frac{\partial \bar{p}}{\partial x_i} - \frac{\partial \tau_{i,j}}{\partial x_j} \tag{2}$$

where $\sigma_{i,j}$ and $\tau_{i,j}$ are defined as Equations (3) and (4), respectively.

$$\sigma_{i,j} = [\mu(\frac{\partial \bar{u}_i}{\partial x_j} + \frac{\partial \bar{u}_j}{\partial x_i})] - \frac{2}{3}\mu \frac{\partial \bar{u}_i}{\partial x_j}\delta_{i,j} \tag{3}$$

$$\tau_{i,j} = \rho \overline{u_i u_j} - \rho \bar{\bar{u}}_i \bar{u}_j \tag{4}$$

where $\bar{u}_i$ is the resolved filtered velocity vector, $\sigma_{i,j}$ is the stress tensor caused by molecular viscosity, and $\tau_{i,j}$ is the sub-grid scale (SGS) stress tensor, representing the diffusive effect of the sub-grid scale eddies on the resolved ones. The Smagorinsky model [20] is used to model the SGS stresses because of its simplicity.

3.2. Acoustic Finite Element Method

The acoustic FEM is used to compute the sound pressure level (SPL). This method can take the reflection effect of the car body structure surface on the noise [21] into consideration. The acoustic FEM procedure starts from calculating the noise propagation from the Hemholtz equation as defined in Equation (5):

$$\overline{\nabla}^2 \cdot p(x,y,z) + k^2 p(x,y,z) = \mathrm{f}(x,y,z) \tag{5}$$

where $p(x,y,z)$ is the acoustic pressure, $k = 2\pi f/c$ is the wave-number, and f is the frequency. The corresponding wavelength is computed from Equation (6):

$$\lambda = 2\pi/k = 2\pi c/\omega = c/f \tag{6}$$

where c is the free-stream speed of sound. Then, the FFT method is adopted for spectral analysis. The square of the amplitude of pressure wave is expressed in terms of the summation of sine and cosine functions, as shown in Equation (7):

$$A^2(\omega_k) = 2\left[\frac{1}{N}\sum_{n=1}^{N-1}(p_n - \bar{p})\cos[\frac{2\pi nk}{N}]\right]^2 + 2\left[\frac{1}{N}\sum_{n=1}^{N-1}(p_n - \bar{p})\sin[\frac{2\pi nk}{N}]\right]^2 \tag{7}$$

where P_n is a data set and represents the fluctuating pressure of the *Nth* step; $n = 0, \ldots, N-1$. Meanwhile, $\omega_k = k/N\delta t$, where δt is the time step. Finally, the SPL is computed by Equation (8).

$$SPL(\omega_k) = 10\log(A^2/P_{ref}^2) \tag{8}$$

where P_{ref} is constant and equal to 2×10^{-5} Pa.

3.3. Computational Domain and Boundary Conditions

The computation domain is depicted in Figure 3. The flow field is tested to confirm that it is large enough to eliminate boundary effects. The computational domain size is $96.5H \times 45H \times 20H$, where H is the height of the train and $H = 3.55$ m. The origin of the Cartesian reference system locates at the distance x = 29 m from the train geometry. The inflow velocity is 350 km/h. The Reynolds number, *Re,* is 2.25×10^7 based on inflow velocity and the train's height H. A three-car train model with the pantograph is used to study the effects of the pantograph with different configurations of the installation base on the aerodynamic noise characteristics. The effects of other complicated components, such as bogies and windshields, are neglected to save computational cost.
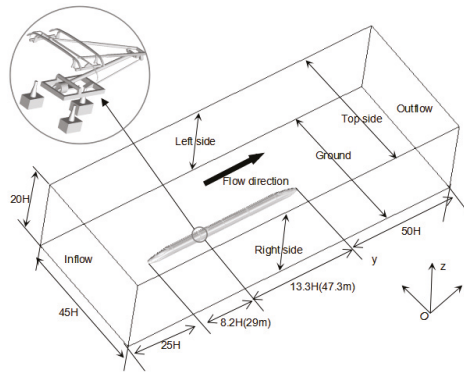
Figure 3. Computational domain for flow field and aerodynamic noise.

The physical time step of the calculation is 10^{-4} s and 20 sub-steps are used within each time step. The total physical calculation time is 0.4 s. The Courant–Friedrichs–Lewy number (CFL $= u \Delta t/\Delta x$) is less than 1 so that the calculation is converged within each time step. Boundary conditions are set as follows: (1) The surface of the train is a fixed wall with non-slip and penetration conditions. (2) Both lateral sides and the top of the computational domain are given as the far field condition with the characteristic line method, and the air flows in the positive x-direction. (3) The ground is set to be a moving wall, and its velocity is the same as the incoming velocity of the air. Figure 4 shows the observer locations used to evaluate the acoustic pressure spectrum and directivity in the near and far field of the pantograph, namely, two positions at y = 5 and 25 m for the spectrum characteristics, and planes y = 0, 10 and 20 m for the distributions of aerodynamic noise, respectively. Furthermore, five positions in the x-direction i.e. x = 0, 5, 10, 15 and 20 m are monitored to investigate the overall sound pressure level (OASPL) caused by the pantograph with the different base configurations. It should be noted that these five positions are 3.5 m above the ground.

Figure 4. Locations of aerodynamic noise observers.

3.4. Mesh Strategy

The STAR-CCM+ mesher is used to generate the computational grids. On the grid arrangement of flow field computation domain, the first layer thic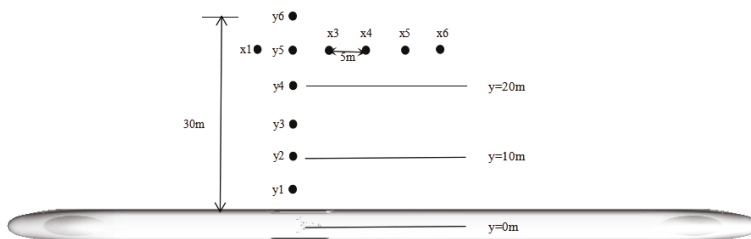kness is 0.05 mm, the geometric grid growth rate is 1.1, and the number of the grid layers close to the train surface is 10 to resolve flow in the boundary layer. The grid size on the pantograph surface and train body surface is 10 mm and 60 mm, respectively, and mesh refinement rear the train body and pantograph is employed to make the computational grid fine enough to capture flow field physics. An isotropic mesh is used in the whole flow field except near wall boundaries. Three sets of grids, i.e., coarse, medium and fine grids, are used to test the grid sensitivity of the simulations. The total number of grid cells in the three grid configurations are 15, 30 and 60 million cells, respectively. Four mesh refinement zones including small, middle, big and wake region are set up, as shown in Figure 5. The mesh size of each refinement zone is listed in Table 1.
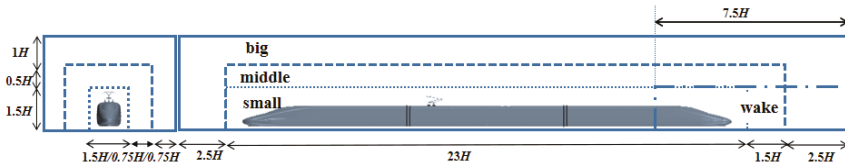
Figure 5. The distribution of refinement zone.

Table 1. The mesh size of the refinement zone.

Grids	Coarse	Medium	Fine
Grid size settings (mm) (small, middle, big, wake)	18, 18, 36, 9	8, 12, 24, 6	6, 9, 18, 6
Total numbers	15 million	30 million	60 million

Figure 6 shows the distribution of time-averaged slipstream velocity along a sampling line at a distance of 2 m from the center of the train, 1.3 m above the ground predicted by the coarse, medium and fine meshes. The non-dimensional results of slipstream velocity U_{non} is defined as:

$$U_{non} = \sqrt{(V_x - V_\infty)^2 + V_y^2 + V_z^2}/V_\infty \tag{9}$$

where V_x, V_y and V_z are the velocity components along the x-direction, y-direction and z-direction, respectively, as shown in Figure 3.
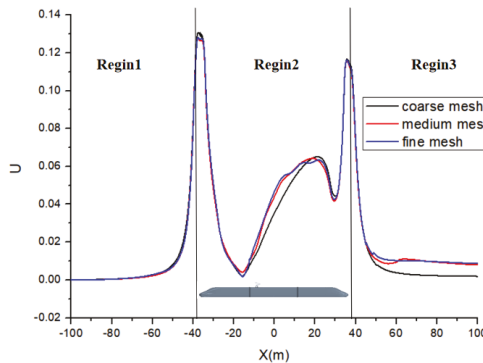
Figure 6. The distribution non-dimensional time-averaged slipstream velocity.

Figure 6 shows that the time-averaged non-dimensional slipstream velocity shows larger difference between the coarse and the fine meshes near the train in Region 2 and in the wake propagation Region 3, indicating that the coarse mesh is inadequate analytical accuracy, while the medium mesh exhibits good consistence with the fine mesh. Thus, the medium grid configuration is adopted to calculate characteristics of flow field, as it gives a satisfactory balance between accuracy and computational costs. Figure 7 shows the medium grids around the train surfaces. Because pantograph noise is the main research content, the area near the pantograph is refined. The total number of the computational cells used is about 32 million.

(a) (b)
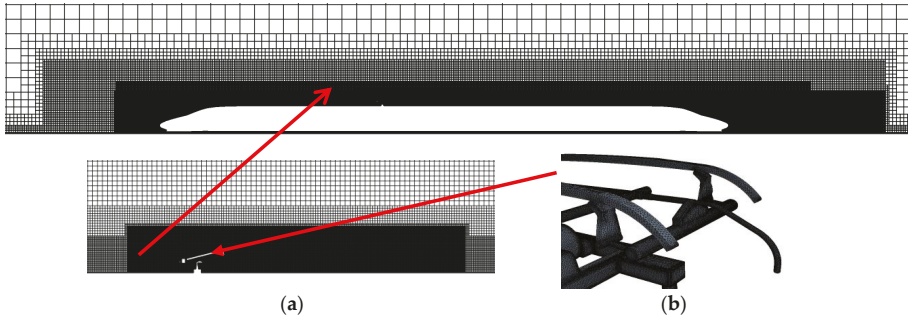
**Figure 7.** Medium sized computational mesh: (**a**) grid around pantograph; and (**b**) enlarged view of pantograph grid.

3.5. Validation of Computational Methods

Many structures of the pantograph could be treated as cylinders. The acoustic finite element method is first validated by a cylindrical flow calculation, as shown in Figure 8. The cylinder has a diameter of 10 mm, the length of the cylinder is πD, and the radius of the flow field is 15D. The trimmer meshing method is employed, and the first layer thickness is 0.0035 mm with a growth ratio of 1.1 in the wall-normal direction. The value of normalized wall-normal distance y+ is defined as:

$$y^+ = \frac{u_* y}{\nu} \tag{10}$$

where y is the distance from the wall, u_* is the friction velocity ($u_* = \left(\frac{\tau_w}{\rho}\right)^{1/2}$), τ_w is wall shear stress, ρ is the air density and ν is the air kinetic viscosity. The values of y+ are below 1 in downstream of the front facing stagnation line on the cylinder surface, which is adequate for the LES model. The cylindrical surface grid size is 0.25 mm. The total number of cells is about 6 million. Figure 8 shows the boundary conditions, namely, the pressure far-field boundary with a uniform inlet velocity of 72 m/s and a gauge pressure of 0 Pa, and the parallel plane (on the two ends of a cylinder) is set as periodic.

Figure 8. Circular cylinder model domain and discretization.

The LES method is used to calculate the flow field. The pressure–velocity coupling method is addressed by the Semi-Implicit Method for Pressure Linked Equations (SIMPLE) algorithm. The discrete algebraic equation is solved by the Gauss–Seidel iteration technique. Figure 9 shows the generation, development, and detachment of the leeward vortices downstream of the cylinder. 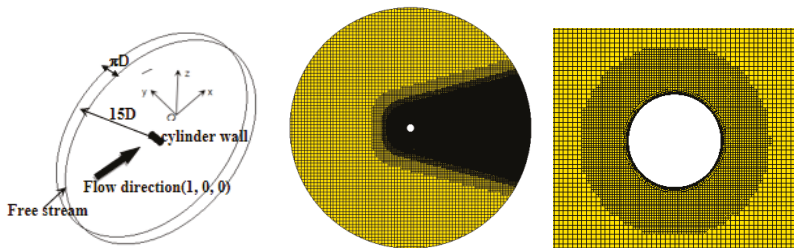The vortices alternate axially in the downstream direction of the flow, forming a von Karman vortex street. It can be seen that the leeward side vortices are mainly generated when the airflow flowing from the cylindrical wall surface leaves the leeward side wall surface. The generation, development and shedding of the vortices lead to noise generation. The acoustic FEM is used to solve the far-field noise at an inflow Mach number is 0.21. In this study, Kato equation [22] is used to correct the SPL obtained from numerical simulations because the spanwise length of the LES computational domain is limited by the available computational resources. As a result, the simulation spanwise length, L_{sim}, of the geometry is shorter than the experimental spanwise length, L_{exp}, reported in Jacob et al. [23]. To compare the predicted SPL with experimental data, the value obtained from numerical simulations must be corrected. The SPL is monitored 185D above directly the cylinder. Figure 10 shows the validations of the aerodynamic results and SPL results of 185D. It can be seen that the pressure coefficient (Cp) and the corresponding Strouhal number (St) of the vortex shedding predicted by the present study agrees with the experimental results and other numerical simulation solutions obtained in [23–26]. Therefore, it is reasonable to use the FEM for the far-field noise characteristic prediction in the following analysis.
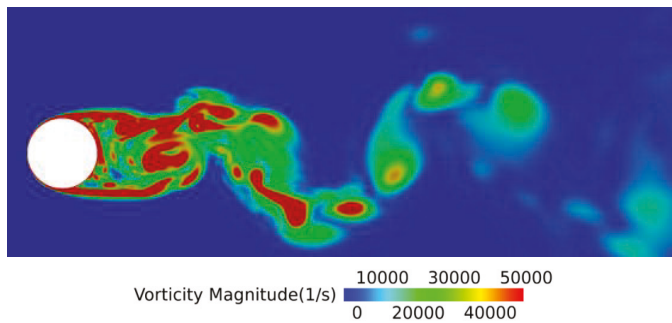
Figure 9. Vortex shedding on plane at 50% span(s^{-1}).
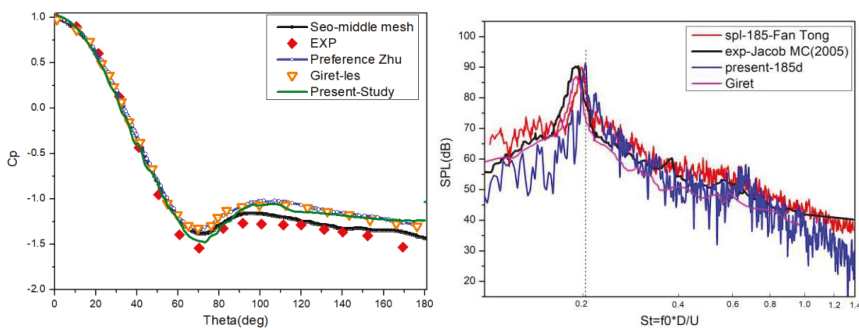
Figure 10. Validations of the Cp and SPL results at 185D (where f_0. = 1508Hz).

This paper seeks to show that the numerical method is able to model the evolution of the structures in the gap between the solid bodies. A comparison between downstream flow characteristics of the cylinder obtained by measurements and simulation using the same mesh level changes in the cylinder wake as used for the pantograph simulation is performed. As shown in Figure 11, the cylinder has a diameter of 0.05715 m, the separation distance, L, between the cylinders is 3.7D. The length is 3D.

The trimmer meshing method is employed, the first layer thickness is 0.001 mm with a growth ratio of 1.2 in the wall-normal direction. The cylindrical surface grid size is 1 mm. The total number of cells is about 8.5 million. The pressure outlet is set as a gauge pressure of 0 Pa, the inlet condition is set as a uniform velocity of 44 m/s, and the other parallel planes are given as symmetry.
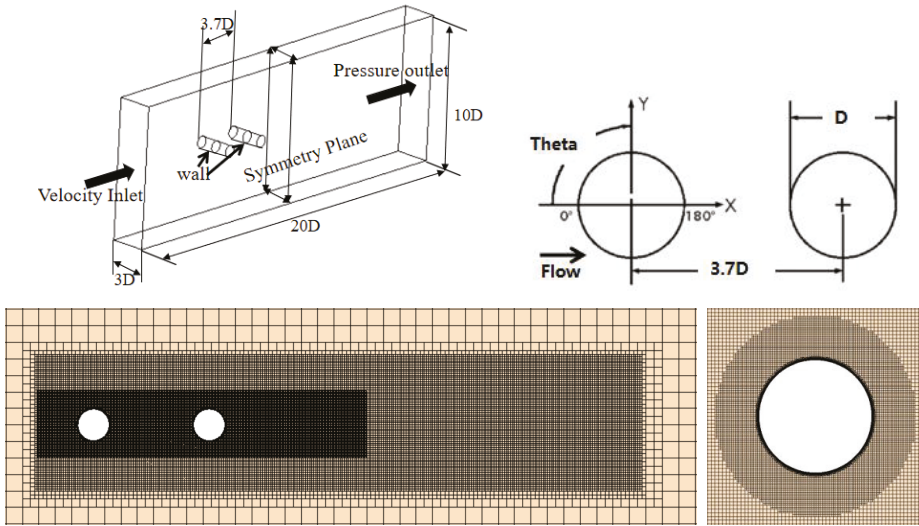
Figure 11. Geometry and computational domain for flow field of two cylinders in tandem.

Figure 12a shows the generation, development and detachment of the leeward vortices downstream of the two cylinders. The predicted root-mean-square (rms) of the pressure coefficient (Cp) on the cylinder downstream cylinder surfaces is compared with the previous work [27], in Figure 12b. The angle "Theta" is measured from the upstream stagnation point and is positive in the clockwise direction. The predicted results show that this method is suitable to obtain the flow characteristics in the gap and downstream between the solid bodies.

(**a**) (**b**)
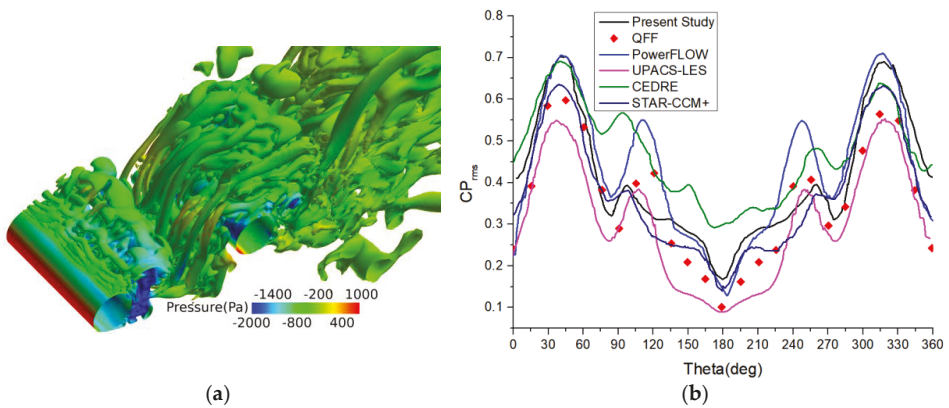
Figure 12. (**a**) Instantaneous iso-surface normalized Q-criterion (Q = 100); and (**b**) the root-mean-square (rms) of the perturbations in Cp.

4. Results and Discussion

4.1. Flow Characteristics of Pantograph Area

In this section, the flow characteristics around the pantograph and the installation bases are discussed. As shown in Figures 13 and 14, the vorticity and the instantaneous iso-surface vorticity as shown by the normalized Q-criterion, and the velocity streamlines around the pantograph are presented, respectively. In Figure 13, the flow separates over the pantograph surface. A series of vortices detaches from the leeward side of each rod and they interact with each other downstream. The hairpin vortices of different size are observed. In addition to the common characteristics of the flow field mentioned above, Figure 13a,b also shows that the flow field characteristics of the pantograph are different due to the opening directions of the pantograph. For the down-pantograph with flush installation base, the incoming flow first impacts on the corner of the upper and lower arm rods, and then strikes the rear of the carbon skateboard and the base in the downstream area. The turbulent upstream flow field hits downstream complex structure like the carbon skateboard and base again, which makes the flow field in the wake region more complex. Because the contact area between the pantograph and the incoming flow is concentrated, the eddy size under the larger contact area is also larger. For the up-pantograph, the distance between different structures on the pantograph is larger, and the inflow flows directly to the downstream area after impact with the carbon skateboard. Compared with the down-pantograph, the rear eddy scale is smaller. For Figure 13c, when the pantograph is placed in the cavity, the flow field above the cavity shielding part is almost the same as when it is installed on the flush surface. However, for the case that the pantograph is installed in the sunken base, the flow field characteristics have something in common with the general flow field in a cavity, as previously studied in [28–30]. However, the presence of the pantograph affects the pressure fluctuation on the cavity surface, and then it further affects the noise induced by the pantograph. For a pantograph that is installed in the sunken cavity, the base and insulator are basically located in the cavity, avoiding direct collision with the incoming flow. Generally, the flow past a cavity exhibits a strong relationship with the cavity length (L) to height (D) ratio as studied by Lawson and Barakos [19]. For the present study, the ratio of L/D of the cavity with pantograph is about 4.7. Therefore, according to the criterion of Lawson and Barakos [19], it is considered as the open cavity. In addition, the pressure field in the cavity is coupled with the shear layer shed from the cavity upstream edge, and the pressure fluctuation intensity in the cavity depends on the characteristics of the shear layer and on the evolution of momentum and vorticity during the impact of the shed shear layer with the cavity rear bulkhead as studied by Ouyang et al. [31]. Because the presence of the pantograph, the typical open cavity flow field structure is destroyed. As shown in Figure 14, one can observe that the air-flow acts on the pantograph first, and then vortices shed by the pantograph impinge on the surface downstream. A part of the air flow returns to the front of the cavity and continues to act on the pantograph. This differs from an empty cavity flow in which the shear layer shed at the cavity upstream edge impacts the cavity downstream edge, unobstructed. The pressure wave (feedback pressure wave) propagating upstream after acting on the surface of the cavity collides with the pressure wave reflected from the front wall when it arrives upstream at the last time. The air circulation inside and outside the cavity exchanges, resulting in pressure fluctuation in the cavity. The pressure fluctuation on the base and insulator surface even as well as the overall pressure fluctuation on the surface of the pantograph is affected by the flow in the cavity.
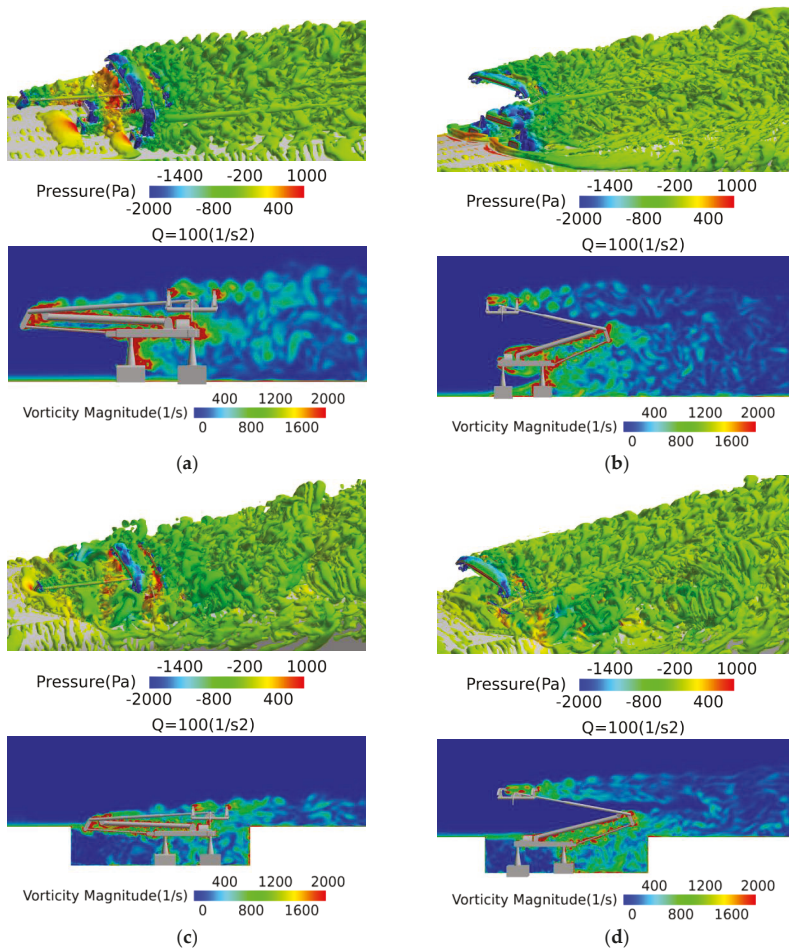
Figure 13. Instantaneous iso-surface normalized Q-criterion (Q = 100/s^2) and vorticity magnitude(1/s) on: (**a**) down-pantograph with flush base; (**b**) up-pantograph with flush base; (**c**) down-pantograph with sunken base; and (**d**) up-pantograph with sunken base.
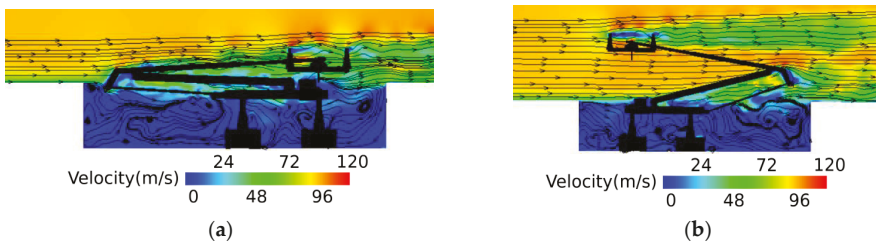
Figure 14. Streamlines superimposed on color iso-levels of the time-averaged velocity vector magnitude: (**a**) down-pantograph with sunken base; and (**b**) up-pantograph with sunken base.

4.2. Aerodynamic Noise Characteristics

4.2.1. Aerodynamic Noise Source

In this section, sources of aerodynamic noise are discussed as it is expected that the flow field of the different base configurations of the pantograph may have significant effects on noise spectrum characteristics and on the noise directivity, which could lead to a change in the perceived noise along the train track. Therefore, the aerodynamic pressure amplitude distributions on the pantograph at 200 Hz and 1000 Hz are compared. As shown in Figure 15, it can be observed that along the direction of the flow velocity, the aerodynamic pressure amplitude in the front regions of the pantograph is lower than that in the rear regions of the pantograph. This may be explained by the fact that the front parts always collide with the incoming flow sharply, forming a windward stagnation area. As a result, the fluctuating pressure is relatively small. Flow with higher levels of vorticity, as shown in Figure 13, passes over the rear parts of the pantograph. As a result, the amplitude of aerodynamic pressure fluctuation in the rear region is larger. Meanwhile, the amplitude of the aerodynamic pressure decreases when the frequency increases from 200 Hz to 1000 Hz. Where the flush configuration is used under the down-pantograph condition, the maximum aerodynamic pressure fluctuation at 1000 Hz is smaller than that at 200 Hz by as much as 18 dB. The phenomenon that the maximum aerodynamic pressure fluctuation decreases with the increasing frequency also can be observed by Zhang et al. [15]. At the low frequency, the SPL distribution of the aerodynamic pressure on the surface of the pantograph is non-uniform. The largest amplitude aerodynamic pressure mainly features on the supporting slide, the rotating shaft, the lower arm, and the leeward surface of the installation base. At 1000 Hz, the aerodynamic pressure amplitude distribution is more uniform than that at 200 Hz. It seems that, although the aerodynamic pressure amplitude distribution over the pantograph surfaces are different at these two frequencies, the largest amplitudes are always located on the downstream base frame, the connection between the upper and lower arms and the downstream position of the double skateboard bow. These aerodynamic pressure fluctuations act as dipole noise sources.

(**a**)

(**b**)

(**c**)

(**d**)

200 Hz

Figure 15. *Cont.*

(a)

(b)

(c)

(d)
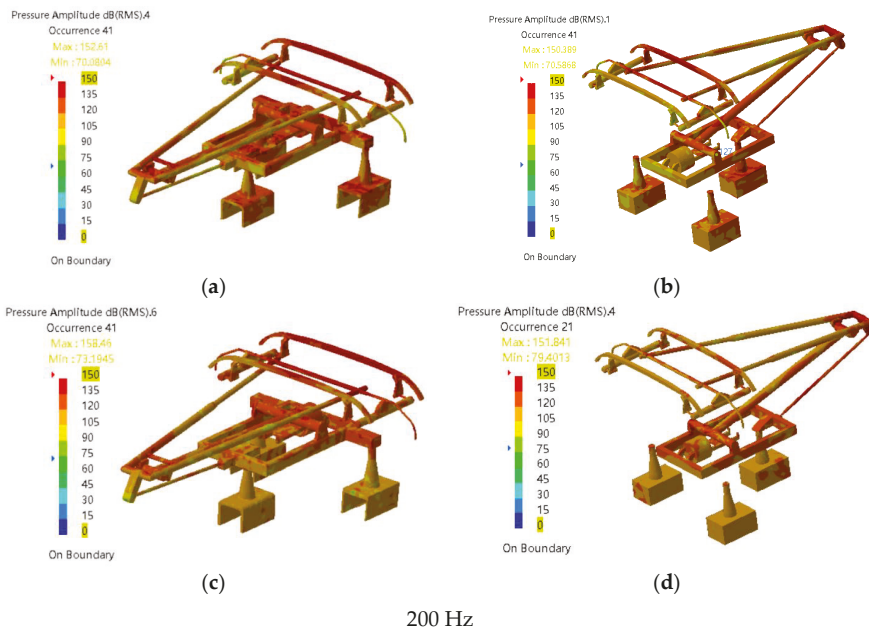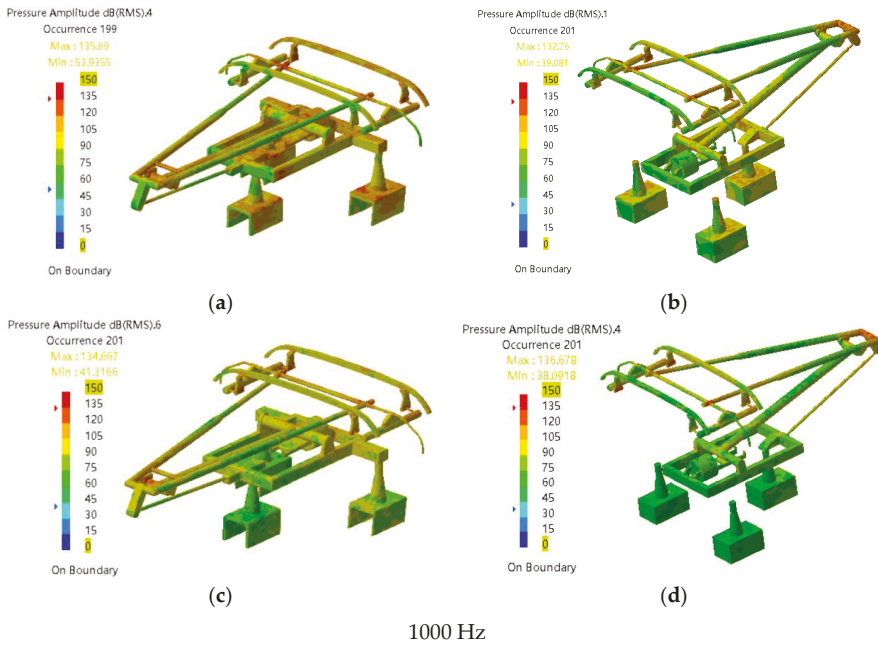
1000 Hz

Figure 15. Normalized aerodynamic pressure fluctuation amplitude at 200 and 1000 Hz on: (**a**) down-pantograph with flush base; (**b**) up-pantograph with flush base; (**c**) down-pantograph with sunken base; and (**d**) up-pantograph with sunken base.

4.2.2. Aerodynamic Noise Radiation and Attenuation Characteristics

To study aerodynamic noise radiation and attenuation characteristics induced by the up- and down-pantograph with the different base configurations, the contours of spatial distribution in near-field and far-field noise at three planes in the y-direction i.e. y = 0 (near-field), 10 and 20 m (in far-field) are compared, as depicted in Figure 16. In this analysis, the acoustic finite element method is directly used to deal with the whole field noise, including near-field y = 0 plane noise, without considering the effect of quadrupole noise and corresponding convection effect. The main reason is that Mach number of the incoming flow is only 0.278 in this calculation. As it is known that the ratio of quadrupole noise to dipole noise is proportional to the square of Mach number [32], the influence of the quadrupole noise at this speed is relatively small, and it is reasonable to ignore it in the present study. As the pantograph is the noise source, the sound pressure decreases with the y distance. The contours also indicate that the regions with higher sound levels for both frequencies are in the vicinity of the pantograph. These distributions are more uniform at the high frequency. It is shown that, as frequency increases, the sound pressure amplitude decreases.
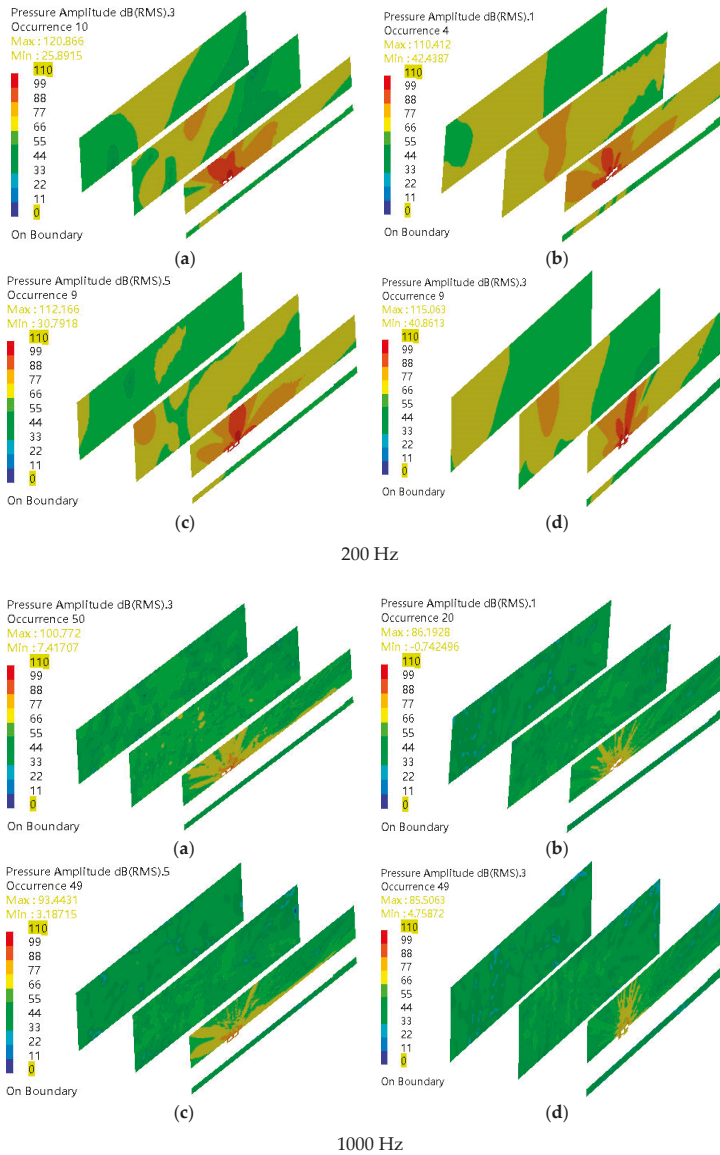
Figure 16. Spatial distribution of near-field (Y = 0 m) and far-field (Y = 10 m, Y = 20 m) noise at 200 Hz and 1000 Hz on: (**a**) down-pantograph with flush base; (**b**) up-pantograph with flush base; (**c**) down-pantograph with sunken base; and (**d**) up-pantograph with sunken base.

To obtain the noise characteristics in the far field, two positions in the y-direction, i.e. at y = 5 m and y = 25 m from the center line of the train, as shown previously in Figure 4, are evaluated, as plotted in Figure 17. Some phenomena are observed. Firstly, the noise amplitude at y = 25 m is lower than that at y = 5 m at all frequencies. Next, it is shown that the noise caused by the down-pantograph is higher than that by the up-pantograph. Finally, the noise from the pantograph with the flush base configuration is of higher amplitude than that with the sunken base configuration irrespective of

whether the pantograph is under the up or down condition. These phenomena could be explained by the fact that, for the sunken configuration, the vortices generated in the rear of the insulator and the base move inside the cavity and the movement to the surroundings is blocked by the cavity surface. This may explain the predicted weakening of the far-field noise. Additionally, one can see that, for frequencies below 200 Hz, the noise caused by the sunken type configuration is almost the same as that from the flush. However, at higher frequencies, the noise caused by the sunken configuration of the pantograph is lower than that by the flush configuration in general. This is because the large vortices produced by the sunken insulator are blocked by the cavity, therefore their streamwise growth and spread are constrained. As a result, large eddies are not easily broken into small ones.
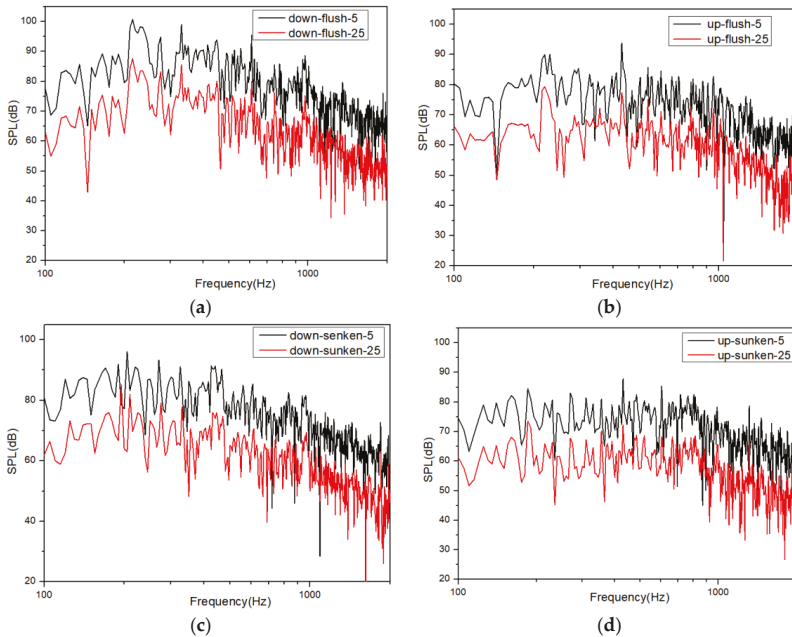
Figure 17. Noise predictions at the far field monitoring points. (**a**) Noise of down-pantograph with flush base; (**b**) Noise of up-pantograph with flush base; (**c**) Noise of down-pantograph with sunken base; and (**d**) Noise of up-pantograph with sunken base.

To further study the trend of the overall sound pressure levels (OASPL) at different distances along x (parallel to the train) and y (normal to the train) directions, Figure 18a,b shows the OASPL in the far field along the x and y directions, respectively. Figure 18a indicates that the OASPL is inversely proportional to the distance of sound source for all cases. To predict the OASPL in the region from the pantograph to the far field, it is found that the logarithm function, $OASPL = OASPL_0 - b \times \ln(x + c)$, is fitted appropriately using the values of the OASPL under the relation between the OASPL and the distance in the range of $0 \leq y \leq 30$ m. The four correlations obtained by the fitted curves are mathematically expressed as follows: (1) $OASPL = 107.3 - 8.9 \times \ln(x - 0.50)$ for the down-pantograph with the flush base; (2) $OASPL = 105.5 - 8.8 \times \ln(x - 0.03)$ for the up-pantograph with the flush base; (3) $OASPL = 102.9 - 9.1 \times \ln(x - 0.12)$ for the down-pantograph with the sunken base; and (4) $OASPL = 97.1 - 7.9 \times \ln(x - 0.46)$ for the up-pantograph with the sunken base. Another observation is that the differences between the OASPL obtained by the up- and down-pantograph with the flush configuration base at each position are about 1–2 dB, whereas the differences between the OASPL obtained by the up- and down-pantograph with the sunken base at each position are about 4–5 dB. Besides, under the same configuration base, the OASPL obtained by the down-pantograph is higher

than that by the up-pantograph. To evaluate the OASPL caused by the pantograph in the far-field region, it is acceptable if the distance from the sound source is more than 25 m, the sound source is assumed as a point source [13]. Therefore, the sound pressure propagation can be considered as the spherical surface from the point source center and the attenuation value ΔL of the OASPL from the point source in the far-field regions is computed by the equation: ΔL = 20log(r/r0). This can be used to the predict the geometric attenuation of noise. Figure 18b shows the OASPL along the x direction at y = 25 m. The down-pantograph always produces higher noise than the up-pantograph for both configuration bases. Besides, Figure 18a,b indicates that the OASPL in the far field along the x and y directions are always found that for all x and y positions the down-pantograph with the flush base provides the highest OASPL. The lowest OASPL is obtained by the up-pantograph with the sunken base. In addition, the OASPL caused by the up-pantograph with the flush base is higher than that by the down-pantograph with the sunken base.
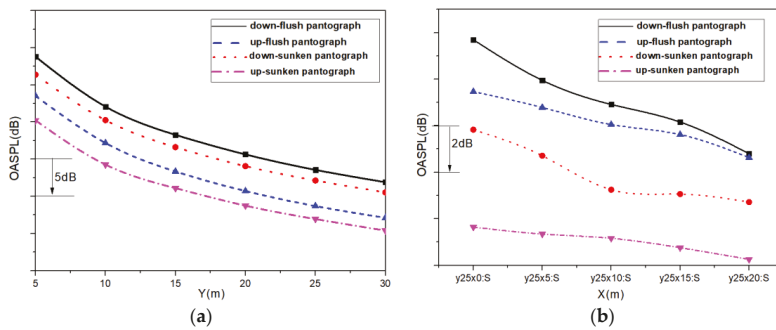

Figure 18. Comparison of OASPL at different distances of pantographs with different configuration bases: (**a**) with pantograph as reference position, OASPL at different vertical distances from center line of track in horizontal plane; and (**b**) OASPL of up- and down-pantograph with different configuration bases at different monitoring points along moving direction of train.

4.2.3. Aerodynamic Noise Directivity

In this section, the aerodynamic noise directivity around the pantograph with the different configurations is presented. According to the ISO3095-2013 standard [33], the far-field noise receivers should be located 7.5 or 25 m away from the center line of the track and 1.2 or 3.5 m above the ground. The present study investigates the far-field noise characteristics around the pantograph with a distance of 7.5 m in the radial direction and 3.5 m above the ground. The OASPL in the X-Y, Y-Z and X-Z planes is discussed, as shown in Figure 19, and the OASPL is considered at every five degrees. It is found that in all the planes the noise directivity induced by the sunken pantograph is slightly smaller than the flush pantograph in general. Only at some angles, the noise induced by the sunken pantograph is equal to or larger than that by the flush pantograph. Besides, some interesting phenomena are observed in each plane. First, in the X-Y plane, when the pantograph is used with the flush surface, a relatively high OASPL is found in the rear arc of the pantograph ($-5° \leq \theta \leq 5°$), and along the sideline over the ranges $85° \leq \theta \leq 125°$ and $235° \leq \theta \leq 275°$. When the pantograph is installed in the sunken surface, the rear arc still has the higher OASPL. However, the high OASPL values are also predicted at other angles. In the down-pantograph, a large part of the structure is located inside the cavity. The corresponding amplitude of the four corners of the cavity is slightly higher than that of other positions. This may be because of the effects of the sunken configuration. Specifically, during the process of noise propagation, the sound wave can reflect within the cavity of the sunken surface, four corners can easily become the convergence area of reflected sound waves. One can see that the directivity of noise is not completely symmetrical the X-Y plane. Similar instances of incomplete symmetry are also reported in the literature [13]. The main reason is that the far-field noise monitors are usually placed at

every 5–10 degrees around the pantograph in different planes. This may omit part of the amplitude between the monitors, resulting a certain impact on the results. In addition, in the calculation of the sound field, the frequency resolution has a slight impact on the results. However, further detailed analysis of the up- and down-pantograph in the cavity has shown that there is almost no difference when the frequency resolution is increased from 10 Hz to 5 Hz, namely, the overall noise difference is less than 1 dB. In the Y-Z plane, the noise distributions obtained by the two installation bases are nearly symmetric and the higher sound level area is found in in the range of $60° \leq \theta \leq 120°$. It also shows that, in this range of theta with the pantograph under the down configuration, the OASPL obtained by the flush installation base is higher than that by the sunken base configuration. However, under the up-pantograph condition, the OASPL values obtained by the two configuration bases are close to each other. In the X-Z plane, the down-pantograph with the flush base produces higher noise than the sunken base in all directions. For the up-pantograph, the noise amplitudes of the flush and sunken bases are very close to each other in general. Nonetheless, it is seen that at some angles, the noise induced by the sunken base is higher than the flush base. In both Y-Z and X-Z plane, for the up-pantograph with the flush base or sunken base, it can be seen that the noise amplitudes are very close to each other in general, especially in the Z direction directly above the body. This may be due to the effect of sound wave reflection from the cavity floor and that the up-pantograph itself is a large source of noise in this direction.

(a) Directivity of X-Y plane

(b) Directivity of Y-Z plane

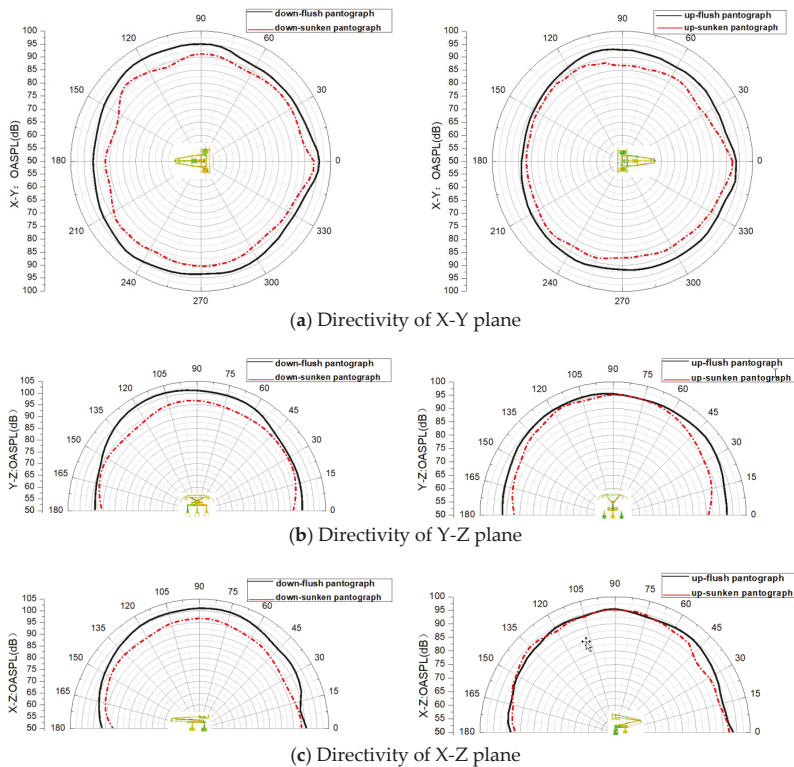(c) Directivity of X-Z plane

Figure 19. Noise directivity induced by pantograph in different planes (the left side figures show the down condition and the right side figures show the up condition): (**a**) directivity of X-Y plane; (**b**) directivity of Y-Z plane; and (**c**) directivity of X-Z plane.

5. Conclusions

This work presents the numerical study of the aerodynamic noise characteristics induced by a pantograph over a simplified train geometry with the different configurations of the installation base using the large eddy simulation (LES) with finite element method (FEM). The numerical results are carried out in terms of the flow field around the pantograph and its installation base, the spatial distribution and spectrum characteristics, and the noise directivity in near and far fields under the up and down conditions at the train speed of 350 km/h. Through the discussion, the following interesting phenomena are drawn:

(1) The complex shape of the pantograph is the main reason for its induced aerodynamic noise. A series of vortices detaches from the leeward side of each rod and they interact with each other and with downstream solid structures. The aerodynamic pressure fluctuation is generated on the rods induces aerodynamic noise. The main aerodynamic noise sources are located on the downstream base frame and on the double skateboard bow, at the connection between the upper and lower arms. The aerodynamic noise sources over the pantograph surfaces are different at 200 Hz and at 1 kHz.

(2) For the spatial distributions, along the direction of the flow velocity, the aerodynamic pressure fluctuation amplitude in the front regions of the pantograph is lower than that in the rear regions of the pantograph. These distributions are more uniform at 1 kHz than at 200 Hz. In addition, the amplitude of the noise is lower at the higher frequency.

(3) In the far-field regions along the x and y directions, for all x and y positions under the pantograph shape and opening direction selected in this paper, the down-pantograph with the flush configuration provides the highest OASPL. The up-pantograph with the sunken configuration produces the lowest OASPL. In addition, the OASPL caused by the up-pantograph with the flush base is higher than that by the down-pantograph with the sunken base. Thus, the pantograph with sunken configuration is a better choice in a practical engineering application.

(4) On the directivity, the noise induced by the pantograph with the sunken surface is of lower amplitude than that with the flush surface, especially in the down-pantograph. For up-pantograph, the amplitude of the noise from the sunken surface configuration is close to that from the flush surface configuration in Y-Z plane and in the X-Z plane. In the X-Z plane, the results even show noise amplitude from the sunken surface configuration is predicted to be higher than that from the flush configurations at some angles in some angles. However, this still does not affect the fact that the sunken installation is conducive to a quieter noise environment on both sides of the road.

It should be noted that effects of noise transmission to the exterior and interior of high-speed train need to be further studied, especially in the case of the pantograph with the sunken configuration. The present study considers only the aerodynamic noise generated by the wall fluctuating pressure of the pantograph in the exterior noise transmission to the environment. In fact, there are strong vortices in the regions near the pantograph and spatial distribution of near-field, such as Y = 0 m, may obtain a more accurate result. These are the quadrupole noise sources that contribute to aerodynamic noise. Since the operating speed is not too high (Ma = 0.278), the proportion of noise generated by the quadrupole source, which scales by u^8 [34], is smaller than that from dipole sources, which scales as u^6 [35], where u is the train velocity. Thus, the induced noise by the quadrupole source is not included in this study.

Author Contributions: Conceptualization, Z.S. and G.Y.; Data curation, Y.Y.; Formal analysis, Y.Y.; Funding acquisition, Z.S. and G.Y.; Investigation, Y.Y. and Z.S.; Methodology, Y.Y. and W.L.; Project administration, Z.S. and G.Y.; Resources, Z.S. and G.Y.; Software, Y.Y. and W.L.; Supervision, Y.Y. and Z.S.; Validation, Y.Y. and Z.S.; Visualization, Y.Y.; Writing—original draft, Y.Y.; and Writing—review and editing, Y.Y., P.P., and Z.S.

Conflicts of Interest: The authors declare no conflict of interest.

References

1. Zhang, S.G. Noise mechanism, sound source identification and control of high-speed train in the speed of 350 km·h-1. *Chin. Railw. Sci.* **2009**, *30*, 86–90. (In Chinese) [CrossRef]
2. Lele, S.K. Compact finite difference schemes with spectral-like resolution. *J. Comput. Phys.* **1992**, *103*, 16–42. [CrossRef]
3. Sun, Z.X.; Song, J.J.; An, Y.R. Numerical simulation of aerodynamic noise generated by crh3 high speed train. *J. Peking Univ.* **2012**, *48*, 701–711. (In Chinese)
4. Liu, J.L.; Zhang, J.Y.; Zhang, W.H. Numerical analysis of aerodynamic noise of high-speed train head. *J. Railw.* **2011**, *9*, 19–26. (In Chinese)
5. Zhu, J.Y.; Jing, J.H. Research and control of aerodynamic noise in high speed trains. *Foreign Railw. Cars* **2011**, *48*, 1–8. (In Chinese)
6. Sun, Y.J.; Xia, J.; Mei, Y.G. Introduction of aerodynamic noise generated by high-speed train and the reduction of the noise. *Railw. Locomot. Car* **2009**, *29*, 25–28. (In Chinese)
7. King, W.F. A precise of development in the aeroacoustics of tast trains. *J. Sound Vib.* **1996**, *193*, 349–358. [CrossRef]
8. Takaishi, T.; Ikeda, M. Method of evaluating dipole sound source in a finite computational domain. *Railw. Tech. Res. Inst.* **2004**, *116*, 1427–1435. [CrossRef]
9. Takaishi, T.; Sagawa, A.; Nagakura, K.; Maeda, T. Numerical analysis of dipole sound source around high-speed trains. *Railw. Tech. Res. Inst.* **2002**, *111*, 2601–2608.
10. Yoshiki, K.; Yusuke, W.; Fumio, M. Numerical simulation of aerodynamic noise from high-speed pantographs using lattice Boltzmann method. In Proceedings of the International Symposium on Speed-Up, Safety and Service Technology for Railway and Maglev Systems, Seoul, Korea, 17–19 September 2012; pp. 1–9.
11. Liu, J.L.; Yu, M.G.; Tian, A.Q. Study on the aerodynamic noise characteristics of the pantograph of the high-speed train. *J. Mech. Eng.* **2018**, *54*. [CrossRef]
12. Tan, X.M.; Xie, P.P. Vortex structures and aeroacoustic performance of the flow field of the pantograph. *Sound Vib.* **2018**, *432*, 17–32.
13. Yu, H.H.; Li, J.C.; Zhang, H.Q. On aerodynamic noises radiated by the pantograph system of high-speed trains. *Acta Mech. Sin.* **2013**, *29*, 399–410. [CrossRef]
14. Sun, X.Q.; Xiao, H. Numerical modeling and investigation on aerodynamic noise characteristics of pantographs in high-speed trains. *Complexity* **2018**, *2018*, 1–12. [CrossRef]
15. Zhang, Y.D.; Zhang, J.Y.; Li, T.; Zhang, L. Investigation of the aeroacoustic behavior and aerodynamic noise of a high-speed train pantograph. *Technol. Sci.* **2017**, *60*, 561–575. [CrossRef]
16. Kitagawa, T.; Nagakura, K. Aerodynamic noise generated by shinkansen cars. *J. Sound Vib.* **2000**, *231*, 913–924. [CrossRef]
17. Nagakura, K. Localization of aerodynamic noise sources of shinkansen train. *J. Sound Vib.* **2006**, *293*, 547–556. [CrossRef]
18. Noger, C.; Patrat, J.C.; Peube, J. Aeroacoustical study of the TGV pantograph research. *J. Sound Vib.* **2000**, *231*, 563–575. [CrossRef]
19. Lawson, S.J.; Barakos, G.N. Review of numerical simulations for high-speed, turbulent cavity flows. *Prog. Aerosp. Sci.* **2011**, *47*, 186–216. [CrossRef]
20. Smagorinsky, J. General circulation experiments with the primitive equations. *Basic Exp.* **1963**, *93*, 99–165. [CrossRef]
21. Fioravanti, A.; Lenzi, G.; Ferrara, G.; Vichi, G.; Ricci, S.; Bagnoli, L. Assessment and experimental validation of a 3D acoustic model of a motorcycle muffler SAE. *Int. J. Eng.* **2015**, *8*, 266–276.
22. Kato, C.; Lida, A.; Fujita, H.; Ikegawa, M. Numerical prediction of aerodynamic noise from low Mach number turbulent wake. In Proceedings of the AIAA 93-0145, 31st Aerospace Sciences Meeting & Exhibit, Reno, NV, USA, 11–14 January 1993.
23. Jacob, M.C.; Boudet, J.; Casalino, D.; Michard, M. A rod-airfoil experiment as benchmark for broadband noise. *Theor. Comput. Fluid Dyn.* **2005**, *19*, 171–196. [CrossRef]

24. Giret, J.C.; Sengissen, A.; Moreau, S.; Sanjosé, M.; Jouhaud, J.C. Prediction of the sound generated by a rod-airfoil configuration using a compressible unstructured LES solver and a FW-H analogy. In Proceedings of the 18th AIAA/CEAS aeroacoustics conference, Colorado Springs, CO, USA, 4–6 June 2012; pp. 2012–2058.

25. Fan, T.; Qiao, W.Y.; Chen, W.J.; Wang, L.F.; Wang, X.N. Broadband noise prediction using large eddy simulation and a frequency domain method. *Appl. Acoust.* **2017**, *117*, 94–105.

26. Zhu, W.Q.; Luo, K.Y.; Xiao, Z.X. Numerical simulations of the flow dynamics past an oscillating rod-airfoil configuration. In *Symposium on Hybrid RANS-LES Methods*; Springer: Cham, Switzerland, 2016; pp. 433–443.

27. Lockard, D.P. Summary of the tandem cylinder solutions from the benchmark problems for airframe noise computations–Workshop. In Proceedings of the 49th AIAA Aerospace Sciences Meeting including the New Horizons Forum and Aerospace Exposition, Orlando, FL, USA, 4–7 January 2011.

28. Plentovich, E.B.; Stallings, J.R.L.; Tracy, M.B. *Experimental Cavity Pressure Measurements at Subsonic and Transonic Speeds. Static-Pressure Results*; Nasa Technical Paper; NASA Langley Research Center: Hampton, VA, USA, 1994; pp. 687–714.

29. Ukeiley, L.; Murray, N. Velocity and surface pressure measurements in an open cavity. *Exp. Fluids* **2005**, *38*, 656–671. [CrossRef]

30. Sinha, N.; Arunajatesan, S.; Shipman, J. High fidelity simulation and measurements of aircraft weapons bay dynamics. In Proceedings of the 7th AIAA/CEAS Aeroacoustics Conference and Exhibit, Berlin, Germany, 27–29 May 2013; pp. 6331–6335.

31. Ouyang, S.X.; Liu, X.Q.; Zhang, B.B. Cavity Flow Simulation and Noise Analysis Using DES Method. *J. Nanjing Univ. Aeronaut. Astronaut.* **2012**, *44*, 6.

32. Xiao, Y.G.; Kang, Z.C. Numerical prediction of aerodynamic noise radiated from high speed train head surface. *J. Cent. South Univ.* **2008**, *39*, 6.

33. European Committee for Standardization. *ISO 3095: 2013 Railway Application Acoustics Measurement of Noise Emitted by Railbound Vehicles*; British Standards Institution: London, UK, 2013.

34. Lighthill, M.J. On sound generated aerodynamically I. General Theory. *Proc. R. Soc. Lond. A* **1952**, *211*, 564–587.

35. Curle, N. The influence of solid boundaries upon aerodynamic sound. *Proc. R. Soc. Lond. Ser. A Math. Phys. Eng. Sci.* **1955**, *231*, 505–514.

Vibroacoustic Optimization Study for the Volute Casing of a Centrifugal Fan

Jianhua Zhang [1,*], Wuli Chu [2,3], Jinghui Zhang [1] and Yi Lv [1]

[1]   School of Aircraft, Xi'an Aeronautical University, Xi'an 710072, China; zhangjinghui2004@163.com (J.Z.); lvyi112@aliyun.com (Y.L.)
[2]   School of Power & Energy, Northwestern Polytechnical University, Xi'an 710072, China; wlchu@nwpu.edu.cn
[3]   Collaborative Innovation Center of Advanced Aero-Engine, Beijing 100191, China
*   Correspondence: lieying.2004@163.com

Featured Application: Authors are encouraged to provide a concise description of the specific application or a potential application of the work. This section is not mandatory.

Abstract: A numerical optimization is presented to reduce the vibrational noise of a centrifugal fan volute. Minimal vibrational radiated sound power was considered as the aim of the optimization. Three separate parts of volute panel thickness (ST: the side panel thickness; BT: the back panel thickness; FT: the front panel thickness) were taken as the design variables. Then, a vibrational noise optimization control method for the volute casing was proposed that considered the influence of vibroacoustic coupling. The optimization method was mainly divided into three main parts. The first was based on the simulation of unsteady flow to the fan to obtain the vibrational noise source. The second used the design of experiments (DoE) method and a weighted-average surrogate model (radial basis function, or RBF) with three design variables related to the geometries of the three-part volute panel thickness, which was used to provide the basic mathematical model for the optimization of the next part. The third part, implementing the low vibrational noise optimization for the fan volute, applied single-objective (taking volute radiated acoustical power as the objective function) and multi-objective (taking the volute radiated acoustical power and volute total mass as the objective function) methods. In addition, the fan aerodynamic performance, volute casing surface fluctuations, and vibration response were validated by experiments, showing good agreement. The optimization results showed that the vibrational noise optimization method proposed in this study can effectively reduce the vibration noise of the fan, obtaining a maximum value of noise reduction of 7.3 dB. The optimization in this study provides an important technical reference for the design of low vibroacoustic volute centrifugal compressors and fans whose fluids should be strictly kept in the system without any leakage.

Keywords: centrifugal fan; unsteady flow; vibroacoustics; fluid-structure-acoustic coupling; optimization

1. Introduction

The centrifugal fan is considered a common turbomachinery that is widely used in the ventilation systems of the ship cabin and other sites, bringing comfortable working and living environments for people. However, the noise and vibrations generated with the fan running troubled researchers; thus, the study of the mechanisms of noise and vibration generation and propagation became more and more important. Most of the current studies on fan noise have dealt with aeroacoustic problems. However, the noise is induced not only by internal turbulent flow, but also by flow-induced structure

vibration. In some particular application environments, the fluid should be strictly kept within the fan's systems (e.g., petrochemical compressors and large fans with fan system inlets and outlets are entirely connected to the extended pipe) without any leakage, and the aerodynamic noise-induced unsteady flow of a fan cannot directly spread to the outside. At this moment, the fan casing and the inlet and outlet pipe vibration noise caused by the vibrations of the volute surface are predominant. Therefore, an intensive study of the generation mechanism of the vibrational noise and the noise reduction method is necessary.

In fact, the fan noise induced by unsteady flow belongs to fluid–structure coupling noise, and the impeller and volute can be classified as an elastomer; in particular, the volute vibration cannot be neglected in large fans [1]. In addition, the aeroacoustic and vibroacoustic calculations usually require high computational resources; in order to reduce the computational cost and have an accurate response, hybrid methods are applied. With respect to the vibroacoustics of casings, such as the vibrational noise of car body and compressor casings, the hybrid finite-element method/boundary-element method (FEM/BEM) approach and the hybrid finite-element method/statistical energy analysis (FEM/SEA) approach are often used. It could be also appropriate to cite Citarella and Federico [2], who have made a comprehensive literature review of both the structural and acoustic modeling methods that are used nowadays to predict the vibroacoustics' performance. They pointed out that lower frequencies, where the tonal resonances are significant, are calculated applying finite element methods (FEM), whereas for higher frequencies, a statistic energy approach can be chosen. Besides, the FEM/BEM method is usually used to perform the free-field sound radiation analysis of open domains. Armentani [3,4] carried out a vibroacoustic analysis for the chain cover of a four-stroke four-cylinder diesel engine through an FEM–BEM coupled approach, while Bianco [5] described an innovative integrated design verification process, based on the bridging between a new semiempirical jet noise model and a hybrid finite-element method/statistical energy analysis (FEM/SEA) approach for calculating the acceleration produced at the payload and equipment level within the structure, vibrating under the external acoustic forcing field. However, there are few studies on the vibration noise induced by the vibration of the casing in a centrifugal fan. This type of noise is prominent in large-scale fan systems and fans with closed pipelines.

At present, research on the vibration noise induced by casing vibration resulting from impeller outlet unsteady flow is usually conducted using simulation methods. A prediction method based on a method of combining boundary element method (BEM) calculations with experimental measurement was proposed by Koopmann [6]. In this method, the aerodynamic noise is isolated, the volute vibrations induced by the unsteady flow are calculated separately, and the pressure fluctuations required for noise and vibration calculations are obtained experimentally. On this basis, some scholars such as Hwang [7], Cai [8,9], and Lu [10] have used the same method to calculate the vibrational sound radiation of a compressor and the T9-19 No.4 industrial centrifugal fan. Cai Jiancheng [11] calculated the vibrational sound radiation of a volute casing of the same centrifugal fan using a fluid–structure–acoustic coupling method. Indeed, this BEM method discretizes the Lighthill equations by applying a free-field Green function integral. At present, the Green function integral method can only solve problems with simple geometric boundaries, and those complex boundaries must be simplified in the free field. Without doubt, this simplification does not consider reflection and scattering effects in the noise propagation. Based on the above advantages, the finite element method (FEM) for solving noise radiation has been recognized by scholars. Durand [12] predicted the structural acoustics of automotive vehicles through using the FEM model. However, there is a computational disadvantage when the finite element method solves the structural acoustic problem of a closed domain. To overcome this disadvantage, automatically matched boundary layers (AMLs) were introduced to simulate the unbound boundary of the exterior computational domain. The outermost layer exposed to the AML surface that satisfied the Sommerfeld radiation condition was defined as a non-reflecting boundary. Based on the FEM method, Zhang [13] performed the aerodynamic noise of the centrifugal fan using the FEM method, and achieved higher prediction accuracy while using less computing resources. To reveal and reduce

the noise primarily generated by the freezer fan unit, Onur [14] investigated the vibration and acoustic interactions between the structure and the cavity inside the freezer cabinet, and the FEM method was also used. Zhou [15] performed a vibroacoustic analysis of a centrifugal compressor with connecting piping systems, in which the sound was induced by the unsteady flow in the centrifugal compressor and pipes, and the same FEM method was used. These studies have been of benefit in promoting the development of the research of vibrational sound radiation on structural casing, allowing for a deeper understanding of vibrational noise during the fan operation, and have provided a useful reference for the noise reduction of such machinery.

The purpose of vibrational noise research is to explore the generation mechanism of vibrational noise, and then propose targeted methods of vibration and noise reduction. Concerning vibration and noise control, there are certain means: controlling the vibrational source, such as vibration absorption and vibration isolation [16]; dynamic vibration absorption; damping vibration control [17]; and structural vibration control [18–27]. At present, a structural vibration control method that meets specific requirements by modifying the dynamic characteristics of the controlled object without adding any subsystem is a research hotspot. Moreover, current structural vibration control is focused on structural optimization. However, a centrifugal fan casing belongs to a thin-casing structure, and the vibrational sound power of the thin casing is a quadratic function of the structural vibration velocity [18,19]. As optimization reduces the structural vibration speed of a fan casing, it can be concluded that the sound power radiation must be reduced within a specific range. The optimal design of a thin-casing structure usually uses the panel thickness as the design variable and the square sum of the vibration velocities of the nodes on the wall as the optimization target function [20,21]. Adopting the mentioned method, Zhou et al. [22] and Lu et al. [23] implemented the optimization study on structure vibration control and noise reduction for the T9-19 No.4A centrifugal fan.

By reducing fan casing vibration, an effect of casing noise reduction is achieved using the aforementioned optimization method, which sets the vibration (node vibrational speed) as the target function. However, this method does not consider the propagation of sound waves and sound boundary influences on the calculation results; thus, deviation is nearly inevitable. The integration of structural–acoustic optimization correctly eliminates these drawbacks. This method has been used in the automotive field, and shows that the sound radiation generated by the excitation of body surface vibrations on the engine is substantially reduced [24–27] after optimization. Based on the aforementioned advantages of optimization, the authors proposed a vibration–acoustic integrated optimization design method that is suitable for turbomachinery volute. In investigating the vibrational noise of the studied marine centrifugal fans, the following three aspects were the focus:

(1) In this study, we proposed a numerical method for one-way fluid–solid–acoustic coupling. The rationality of this one-way coupling is verified by a volute wall vibration test.

(2) To analyze the influence factors of vibrational noise and reduce the vibrational sound radiation induced by unsteady flow in the fan, a detailed theoretical derivation of vibration noise is put forward.

(3) To control the vibrational noise of a certain type of marine centrifugal fan volute, an optimization method considering the influence of vibroacoustic coupling is proposed. Under the premise of whether volute total mass constraints, accordingly taking the panel thickness of the volute casing (FT: the front panel thickness, ST: the side panel thickness, BT: the back panel thickness) as the design variable, this study conducted low vibrational noise single target (taking the volute vibrational radiated sound power as the target function) and multi-target optimization (taking the volute vibrational radiated sound power and total mass as the target function).

2. Centrifugal Fan Description

The studied machine was a ventilating centrifugal fan with four main components (conical bell mouth, shrouded impeller, volute casing with conventional tongue, and conical flow rates throttle) driven by an AC inverter motor with adjustable angular speed between ~0–3600 r/min; the design rotational speed was specified as 2920 r/min, as shown in Figure 1. The main dimensions and

characteristics of the investigated fan for this study are presented in Table 1. The ambient air was intake from the inlet pipe. The tests for characterizing the aerodynamic and acoustic behaviors of the fan system were made in a resilient installation to fulfill ship system noise and vibration requirements (according to standards GJB4058-2000 China [28] and GB-T1236-2000 China [29]). Figure 2a shows the details of the test system installation and data collection procedure. The following maximum measurement errors were obtained for the different magnitudes: total pressure ±2% (±10 Pa), flow rate: ±2% (±0.05 m^3/s), and shaft power ±2% (±50 W).

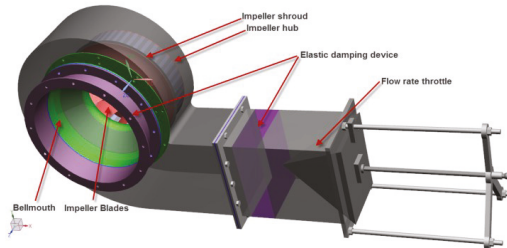**Figure 1.** Component representation for the test fan.

(**a**)

(**b**)   (**c**)
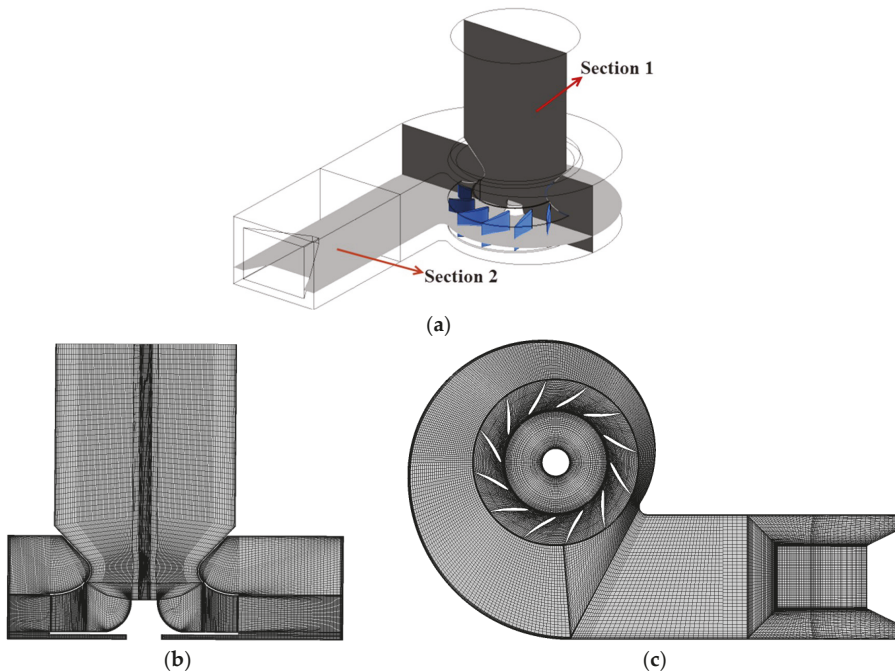
Figure 2. Mesh details of fan. (**a**) Section workspaces; (**b**) Mesh details of Section 1; (**c**) Mesh details of Section 2.

Table 1. Fan dimensions.

Parameters Description	Parameter Values
Impeller blade outlet diameter D_2 (mm)	520
Impeller blade inlet diameter D_1 (mm)	328
Impeller outlet width b_2 (mm)	102
Impeller inlet width b_1 (mm)	138
Blade number Z_n	12
Volute width B (mm)	286
Impeller-tongue distance (mm)	38
Impeller-tongue distance (% of D_2)	13.2%

3. Vibroacoustic Aerodynamics

3.1. Numerical Methods

CFD (Computational fluid dynamics) technology has been proven to be a very useful tool in the analysis of the internal flow of turbomachinery both in design and performance prediction. It has been widely applied to simulate the fully three-dimensional (3D) unsteady flow in centrifugal turbomachinery. In this part, the unsteady aerodynamic forces that excite vibrational noise are calculated by CFD. The whole unsteady flow for the entire impeller-volute configuration was conducted using the computational fluid dynamics (CFD) code ANSYS CFX. The numerical simulation is based on a finite-volume numerical method that employs an incompressible flow model to solve the Unsteady Reynolds Averaged Navier–Stokes equations (URANS). The characteristic Mach number of the simulated fan described by the blade tip circumferential velocity was $u_2/c = 0.18$ (<0.3); therefore, the flow was guaranteed to be incompressible. The continuity equation and momentum equations were solved independently of the energy equation because of the isothermal flow. The standard k-ε turbulence model, which Ballesteros-Tajadura [30] and Cai [31] applied to capture wall pressure fluctuations, was used in the present simulation of the unsteady flow field. A coupled solver, which uses a fully implicit discretization scheme to solve all of the equations (corresponding to the velocity and pressure), was used. However, a second-order high-resolution discretization scheme was used for the convection terms, and a second-order backward Euler scheme was used for the transient terms.

For the three-dimensional calculations, a couple of high-quality hexahedral structural grids were employed to define the flow domains. Details of the grid features and meridian grid cross-section, including the radical gap and cavity around the volute, are shown in Figure 2. More details about the grids of this fan have been reported in the previous work (Jianhua Zhang et al.) [13]. The numerical deviations result from the grid number needed to be removed, and a grid-independent validation of the fan total pressure coefficient and efficiency was performed. Figure 3 shows the influence of the grid size on the fan total pressure coefficient and efficiency. From Figure 3, we can see that the grid was independent when the total number of grid points exceeded 2.8 million. In addition, by increasing the grid size to 5.7 million, the total pressure coefficient with respect to the flow rate was nearly unchanged, compared with the smaller total pressure coefficient over a small flow rate range that was close to the best efficiency point (BEP).
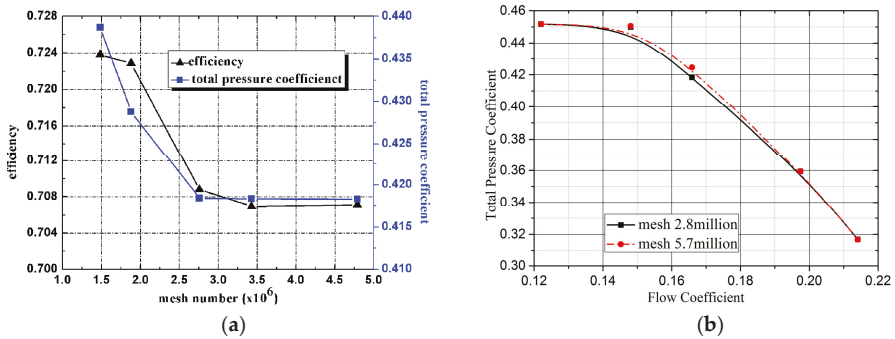
Figure 3. Gridsize independent: (**a**) fan total pressure and efficiency with grid size; (**b**) total pressure coefficient with flow rate.

The modeled boundary conditions were considered to have greater physical meaning for turbomachinery flow simulations. In this case, the CFD simulation process began with a steady flow calculation using the frozen-rotor approach, and nonslip conditions were specified at the solid walls. In addition, for the near-wall flow region, a scalable wall function treatment based on the logarithmic law [32] was applied to cause the mean value of y^+ ($y+$ is the dimensionless distance from the wall; it is used to check the location of the first node away from a wall) to vary between 30–300 (the recommended values by ANSYS CFD code to ensure a high calculation accuracy), as shown in Figure 4. Therefore, by applying this method, the number of the grid points was greatly reduced without reducing the calculation accuracy. For the unsteady flow, a transient rotor/stator grid interface based on the sliding grid technique was applied, which allowed unsteady interactions between the impeller and volute casing. A time step of $5.7089e^{-5}$ s was used for the calculation of the unsteady interactions, which was sufficient for the dynamic analysis. The time step was related to the rotational speed of the impeller, and the time step was specified such that the impeller rotated once in 360 steps (a blade passage defined 30 steps). The number of iterations was adjusted to reduce the residual below an acceptable value at each time step. At each time step, a reduction of 10^{-5} (five orders of magnitude) in the residuals for the given variables in the cells was required. The unsteady simulation was initialized using a steady solution, and over 15 revolutions (approximately 5400 time steps) were required to converge on a periodic unsteady solution.
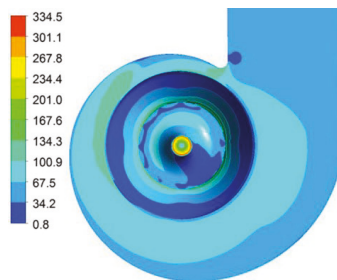

Figure 4. y^+ of the simulated fan.

3.2. CFD Validation

3.2.1. Experiments Description

In this part, the Dynamic Pressure Testing System (DPTS) was employed to obtain the information of the casing pressure fluctuations. This system contained XCQ-080-5G Kulite highfrequency dynamic

pressure sensors (Kulite, Leonia, NJ, America), standard power supplies, 8300 AU amplifiers (Econ, Hangzhou, China), and AVANT MI-7016 signal acquisition (Econ, Hangzhou, China). The test system installation is shown in Figure 5. There are 44 measurement locations on the casing surface, which were at five locations (p01–p05) in the vicinity of the volute tongue, and another six monitoring locations (p06–p11) were evenly distributed along the circumferential direction of the volute. Table 2 summarizes the angular coordinates of the measurement positions over the volute surface. The locations of monitoring points are shown in Figure 6. The origin of the angle is the volute tongue. At each angular position, four axial measurements were made at the following Z/B coordinates: 0.17, 0.27, 0.34, and 0.75 (B is the volute axial width, and Z is the axial measurement position from the volute rear casing). $Z/B = 0.07$ corresponds to the impeller hub, and $Z/B = 0.36$ corresponds to the impeller shroud. More details about the DPTS installation and test have been reported in the previous work (Jianhua Zhang et al.) [13].

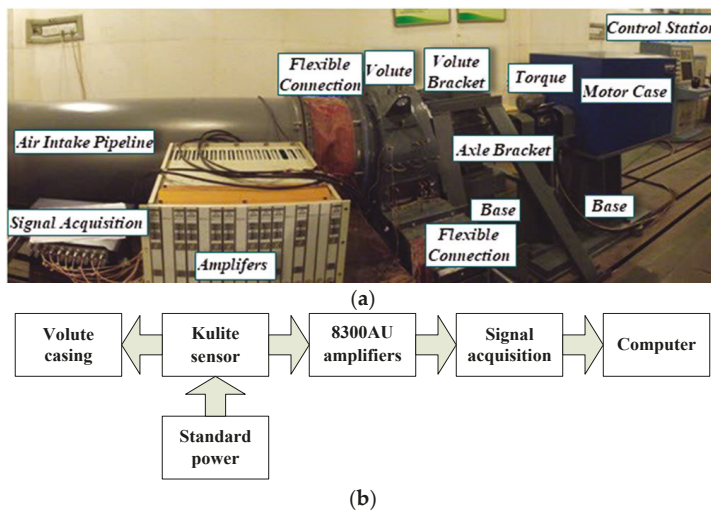**Figure 5.** Installation of test system. (**a**) Test equipment; (**b**) The flow chart of test system installation.

Table 2. Angular coordinate of the measurement points over the volute.

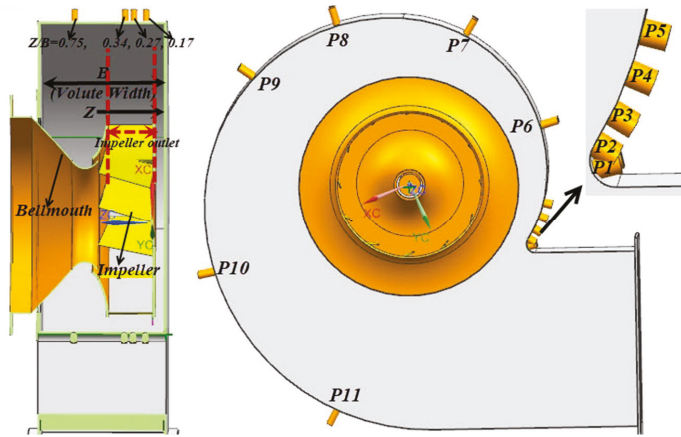| Tongue Points	Angular Position (°)	Volute Points	Angular Position (°)
P1	0	P6	52
P2	3	P7	97
P3	8	P8	142
P4	14	P9	187
P5	20	P10	232
-	-	P11	280

Figure 6. Sketches of the fan with the measurement points.

3.2.2. Aeodynamic Characteristics Validation

Using the defined test bench, the overall performance of this fan as predicted by the CFD calculations was compared for different flow rates. The non-dimensional flow rate and the total pressure rise were transformed by:

$$\varphi = \frac{4Q}{D_2^2 u_2 \pi} \tag{1}$$

$$\psi = \frac{P_T}{\rho u_2^2} \tag{2}$$

The best efficiency point (BEP) at a rotational speed 2920 rpm corresponded to a flow rate $Q = 3.3614$ kg/s ($\varphi = 0.1659$) and a total pressure rise $P_T = 3182$ Pa ($\psi = 0.41954$). Figure 7 indicates that the measured total pressure coefficient and efficiency agreed well with the three-dimensional steady-state calculations. The expected trend of decreasing total pressure coefficients with increasing flow rates can be observed in the experimental and numerical curves. In addition, the performance curves between the numerical simulation and experimental test results were perfectly consistent regards of larger grids (nearly double the size of the small grids).

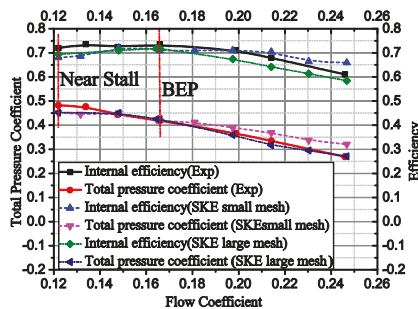**Figure 7.** Comparison results between numerical and experimental curves.

3.2.3. Unsteady Pressure Fluctuation Validation

The pressure fluctuations on the volute casing induced by the unsteady flow at the impeller outlet are the significant vibration noise sources; thus, the validation of the unsteady aerodynamics is very important. In this study, to confirm the simulation accuracy, a comparison analysis between the

dynamic pressure measurement results of volute casing and the numerical calculation was conducted. Due to the similar spectrum signals of the different measurement points on the volute surface, only a few typical points were selected for analysis and confirmation. Figure 8 shows the power spectrum of the volute pressure fluctuations at the BEP at the typical selected measurement points: point 01, point 06, and point 09. The left figure shows the experimental measurement results, and the right figure shows the numerical results. It can be found that the numerical and experimental amplitude of the blade-passing frequency (BPF), which presented the predominant frequency component, were in good agreement at the three most important axial positions ($Z/B = 0.17$, 0.27, and 0.34). More details about the results discussion have been reported in the previous work (Jianhua Zhang et al.) [13].
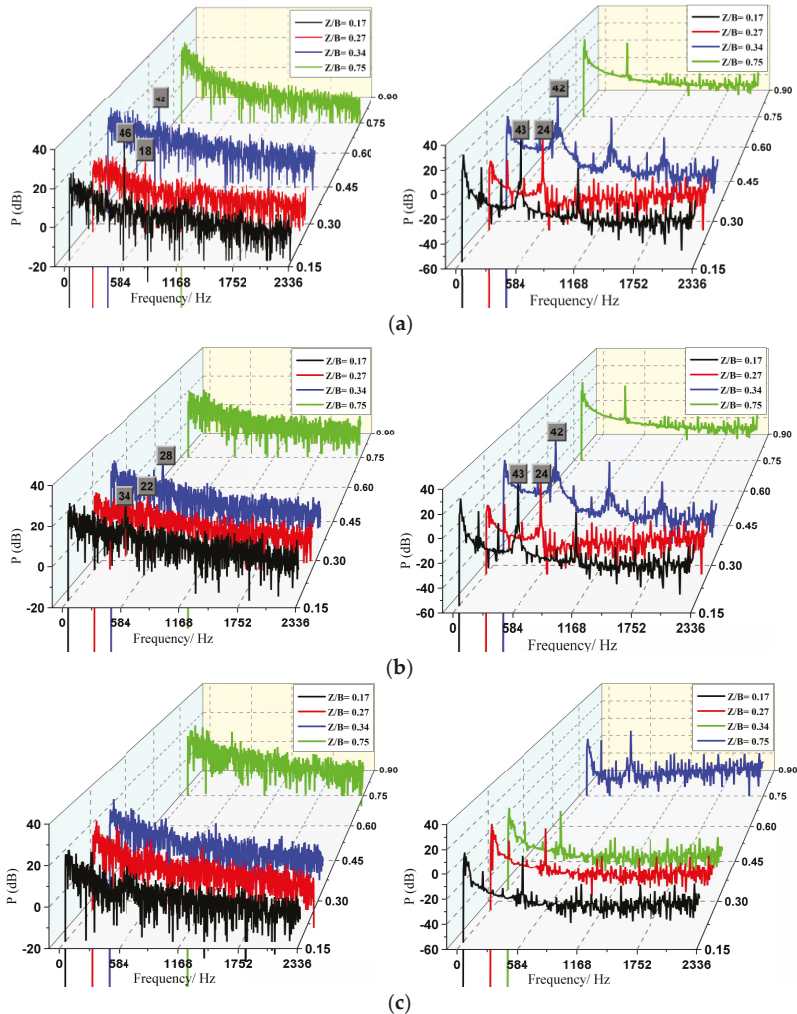

Figure 8. Power spectrum of volute pressure fluctuation at three measurement points with the flow rate best efficiency point (BEP); (**a**) Point 01 (exactly at the tongue); (**b**) Point 06 (52◦ from the tongue); (**c**) Point 09 (187◦ degree from the tongue).

4. Volute Vibroacoustic Model, FEM Validation, and Simulation

For the simulated fan, the displacement of the volute vibration was very small, and the flow was incompressible. Furthermore, the characteristic Mach number was smaller than 0.3. Therefore, the volute's vibration influence on the internal flow was neglected. Therefore, one-way fluid–solid coupling was applied in the simulation. Jiang et al. [33] applied a one-way coupling technique that validated the rationality of an unsteady flow-induced vibration of a centrifugal pump. The validation of one-way coupling is also presented in this study. For details, please refer to Section 4.2.

4.1. Vibroacoustic Mathematical Model

For a continuous system of an actual structure, which was dispersed by FEM, the dynamic balance equation is as follows:

$$\mathbf{M}\ddot{x}(t) + \mathbf{C}\dot{x}(t) + \mathbf{k}x(t) = \mathbf{F}(t) \tag{3}$$

As the structure is subjected to external harmonic force, the external force can be expressed as follows:

$$\mathbf{F}(t) = \mathbf{F} \cdot e^{jwt} \tag{4}$$

The modal vectors are linearly independent of each other. Therefore, the response of the dynamic under any excitation can be regarded as the coupling of the systematic modes and the modal participation factors (MPFs) of each order. At this point, the displacement response can be expressed as follows:

$$x(t) = \sum_{i=1}^{n} \boldsymbol{\varphi}_i y_i(t) = \boldsymbol{\Phi}\mathbf{Y} \tag{5}$$

In the formula, φ_i represents the ith mode shape of the structure, and $y_i(t)$ represents the ith mode coordinate, which is called the ith MPFs; $\boldsymbol{\Phi} = [\boldsymbol{\varphi}_1 \boldsymbol{\varphi}_2 \cdots \boldsymbol{\varphi}_n]$; $\mathbf{Y} = [y_1 y_2 \cdots y_n]$. Substituting Equation (5) into Equation (3) and multiplying $\boldsymbol{\Phi}^T$ on the two laterals yields the following:

$$\boldsymbol{\Phi}^T\mathbf{M}\boldsymbol{\Phi}\ddot{\mathbf{Y}} + \boldsymbol{\Phi}^T\mathbf{C}\boldsymbol{\Phi}\dot{\mathbf{Y}} + \boldsymbol{\Phi}^T\mathbf{K}\boldsymbol{\Phi}\mathbf{Y} = \boldsymbol{\Phi}^T\mathbf{F}e^{jwt} \tag{6}$$

Using the orthogonality of the modal vectors for the mass, damping, and stiffness matrixes, we obtain independent coefficients of the single degrees of freedom of n items. Therefore, the original system can be regarded as linear superposition independent coefficients of single degrees of freedom of n items.

If,

$$\boldsymbol{\Phi}^T\mathbf{M}\boldsymbol{\Phi} = m_i, \quad \boldsymbol{\Phi}^T\mathbf{C}\boldsymbol{\Phi} = C_i, \quad \boldsymbol{\Phi}^T\mathbf{K}\boldsymbol{\Phi} = K_i, \quad \boldsymbol{\Phi}^T\mathbf{F} = F_i \tag{7}$$

Then, substituting Equation (7) into Equation (6), the transformation is as follows:

$$m_i\ddot{y}_i(t) + C_i\dot{y}_i(t) + K_i y_i(t) = F_i e^{j\omega t} \tag{8}$$

If,

$$\omega_n = \sqrt{\frac{k_i}{m_i}}, \quad \zeta_i = \frac{c_i}{2\sqrt{k_i m_i}} \tag{9}$$

Then, substituting Equation (9) into Equation (8) results in the following:

$$\ddot{y}_i(t) + 2\zeta_i\omega_n\dot{y}_i(t) + \omega_n^2 y_i(t) = F_i e^{j\omega t} \tag{10}$$

Using the theory of ordinary differential equations, we obtain the stable solution of Equation (4) as follows:

$$y_i(t) = \frac{F_i}{\omega_n^2 - \omega^2 + 2j\zeta_i\omega\omega_n}e^{j\omega t} \tag{11}$$

Introducing the frequency ratio $\lambda = \omega_n/\omega$ and the dimensionless vibration mode amplification factor β_i results in the following:

$$\beta_i = \frac{1}{\sqrt{(\lambda^2 - 1)^2 + (2\zeta_i\lambda)^2}} \tag{12}$$

Ordering:

$$\psi_i = \arctan\frac{2\zeta_i\lambda}{\lambda^2 - 1} \tag{13}$$

Substituting equations (12) and (13) into Equation (11) results in the following:

$$y_i(t) = \frac{F_i}{\omega^2}\beta_i e^{j(\omega t - \psi)} \tag{14}$$

At this point, the vibrational displacement is as follows:

$$x(t) = \sum_{i=1}^{n}\boldsymbol{\varphi}_i y_i(t) = \sum_{i=1}^{n}\boldsymbol{\varphi}_i\frac{F_i}{\omega^2}\beta_i e^{j(\omega t - \psi)} \tag{15}$$

The vibrational velocity is as follows:

$$\dot{x}(t) = \sum_{i=1}^{n}\boldsymbol{\varphi}_i y_i(t) = \sum_{i=1}^{n}\boldsymbol{\varphi}_i\frac{F_i}{\omega}\beta_i e^{j(\omega t - \psi + \frac{\pi}{2})} \tag{16}$$

The active output power is as follows:

$$W_{o,active} = \int_S Re(I_n)ds = \frac{1}{2}\int_S Re(pv_n^*)ds \tag{17}$$

The relationship between the plane wave sound pressure p and the surface velocity v_n^* is as follows:

$$p = \rho_0 c_0 v_n^* \tag{18}$$

Substituting Equation (18) into Equation (17) results in the following:

$$W_{o,active} = \int_S Re(I_n)ds = \frac{1}{2}\rho_0 c_0 \int_S Re(v_n^{*2})ds \tag{19}$$

Substituting Equation (16) into Equation (19) results in the following:

$$W_{o,active} = \int_S Re(I_n)ds = \frac{1}{2}\rho_0 c_0 \int_S Re(\sum_{i=1}^{n}\boldsymbol{\varphi}_i\frac{F_i}{\omega}\beta_i e^{j(\omega t - \psi + \frac{\pi}{2})})^2 ds \tag{20}$$

According to Equation (20), it can be concluded that the structural acoustic radiation power is mainly determined by the modal shape φ_i, the applied exciting force F_i, and the frequency amplification factor β_i. Therefore, the following methods can be used to control vibrational noise:

(1) With the structural model and material determined, the vibrational sound radiation can be weakened by attenuating the amplitude of the applied exciting force;

(2) With the determination of the exciting force, the geometric parameters of the structural model are modified to reduce the modal shape;

(3) To reduce the amplitude amplification factor, the natural frequency and the external excitation force frequency should be avoided.

Regarding the studied fan volute structure, the structural mode can be changed by controlling the thickness distribution of the structure if the geometry, the stiffness, and the constraint position are all fixed.

4.2. Volute Vibration Simulation and Validation

The finite element analysis method is one of the important methods to obtain the vibrations of the structure surface. In this study, N × Nastran, the commercial software made by the Siemens Company, was used to calculate the modal and vibration response of the volute. The finite element model (FEM) of the volute was selected by using a high-quality surface quadrilateral mesh, as shown in Figure 9. The thickness of the volute panel is relatively small (up to six mm), and the shell63 element is selected for the FEM, as the shell63 element has both bending and membrane capabilities, and can suffer from both plane and normal loads. The volute FEM with a total of 46,182 shell63 element grids was divided into three main sections according to the different thickness properties. The front panel thickness (FT) and the back panel thickness (BF) were set to six mm, and the volute side panel thickness was set to five mm (ST). In addition, the model material was steel, the density $\rho = 7800 \text{ kg/m}^3$, the elastic modulus = 2.06e11 pa, and Poisson's ratio $v = 0.3$. The volute casing was fixed to a supporting stand by 10 fastening bolts at the casing front. The volute panel rear (near the motor) was connected by four fixed bolts, and the three translational degrees of freedom of the nodes at the bolts were restricted to zero. The panel thickness distribution and the degree of freedom constraints on the volutes are shown in Figure 9.
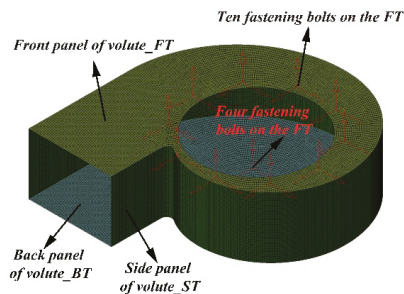

Figure 9. The finite element model (FEM) of the volute.

To validate the one-way fluid–solid coupling, vibration analysis was performed, and the results were compared with those of experimental vibrational analysis. The LMS Test Lab test system was used to complete the vibrational test of the fan casing. To eliminate the vibrational disturbances on the volute originating from the imported pipe and outlet throttle flow, elastic connections were used in two positions: at the connection between the transition section of an inlet and the volute, and between the volute outlet and the throttle valve. The flexible installation should meet the requirements of GJB4058-2000 (The Noise and Vibration Measurement Method of Ship Equipment) [28]. There is some major equipment required for this test, such as an LMS SC310W signal analyzer, a B&K 4513 accelerometer, and a B&K 4514 accelerometer. The background noise is ignored because of the lower value compared to the actual value of the fan. One hand of the accelerometer is fixed on the volute by bonding, and the other hand is directly connected to the data processing and analysis notebook by the data line. The arrangement of the vibration sensor is shown in Figure 10. There are 16 vibration measurement locations on the casing surface. The first five measuring points are arranged near the border between the back panel of the volute and the side panel of the volute. The first measuring point is located near the tongue, and the second through fifth measuring points, #2–5, are respectively arranged at the positions of 0°, 90°, 180°, and 270°. The sixth to ninth measuring points, which are located at the edge of the plate between the back panel of the volute and the motor along with the

connecting plate in the circumferential direction, are arranged at an interval of 90 degrees. At the front panel of the volute, with a 90-degree interval in the direction of a counterclockwise rotation layout, are measuring points 10 to 12. The vibration measuring point of the volute side panel is in the middle of the axial width of the volute arranging measuring points 13 to 15. Measuring point 13 is defined as the starting point; measuring points 14 and 15 are also arranged in the side volute at an interval of 140 degrees; and the measuring point 16 is at the outlet of the volute side panel. The vibration test and the dynamic pressure test of the volute are carried out at the same time, and the data are, respectively, collected in different control computers. Then, the data are sequentially extracted to complete the post-processing.
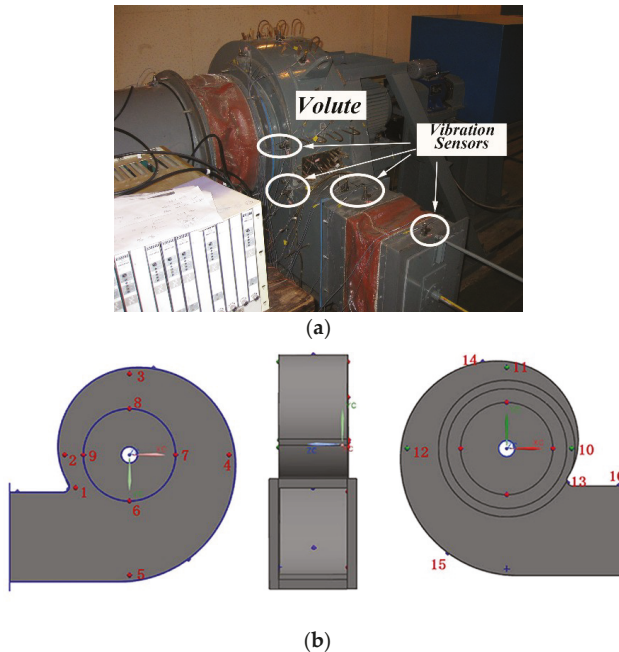

(**a**)

(**b**)

Figure 10. The arrangement of the vibration sensor. (**a**) The distribution of measuring points of experiments; (**b**) The distribution of measuring points of simulation.

The definition of the total vibrational amplitude is shown as follows:

$$VAL = \sqrt{\sum_{i=1}^{n} a_{fei}^2} \qquad (21)$$

where, a_{fei} represents the vibration acceleration at any frequency in the spectrum.

Figure 11 shows a comparison of the numerical and experimental results of the total vibration levels of various vibrational positions in the range of 20 to 3000 Hz. The calculated vibrational measurement positions are arranged according to the vibrational test. Most importantly, it should be stated that the volute casing vibration measurements, the vibration response calculation, and the vibrational noise production are all carried out on the fan design flow rate, the best efficiency point (BEP). As seen in the Figure 11, the calculations are in good agreement with the experiments; the detailed results and analysis refer to the reference [34]. Moreover, a comparison between the experimental and the numerical results shows that it is reasonable and effective to adopt the one-way fluid–structure–acoustic coupling method. Figure 12 presents the vibration acceleration spectrum of

the selected three measuring positions (corresponding to the volute rear panel [BT], the volute front panel [FT], and the volute side panel [ST]). It can be seen from Figure 12 that the spectrum waveforms at each measuring position are similar, and the maximum amplitude of vibration acceleration presents at the fundamental frequency, indicating that the fundamental frequency, the blade-passing frequency (BPF), is the major component for volute vibrations induced by unsteady flow.
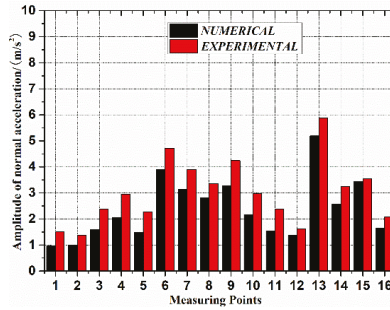

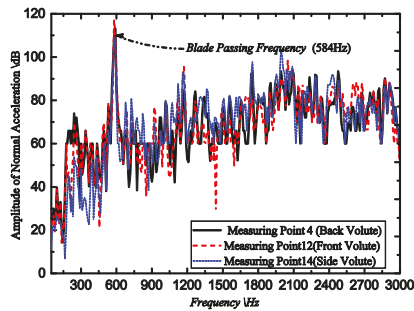**Figure 11.** The compassion of numerical and experimental amplitude of normal acceleration.

Figure 12. The spectrum of acceleration on the three different measuring points.

4.3. Volute Vibroacoustics Estimation Method

The vibroacoustic simulation was performed using the LMS Virtual Acoustics commercial code, and the volute acoustical FEM model is shown in Figure 13. It was similar to the acoustical finite element mesh that was used for aerodynamic noise calculations [13]. Taking into account the characteristic of radiated vibrational noise, the volute's inlet and outlet were completely enclosed. More importantly, according to the requirements on element size driven by maximum frequency, the computational acoustic mesh had to satisfy each wavelength corresponding to six elements. An acoustical mesh with a maximum element size of 15 mm was applied in the sound computation, and guaranteed a spatial resolution at the maximum frequency of 3236 Hz of six points per wavelength. Atmospheric boundary layers (AMLs) were introduced to simulate the unbound boundary of the exterior fluid domain. The outermost layer exposed to the AML surface that satisfied the Sommerfeld radiation condition was defined as a non-reflecting boundary. Then, a field point mesh based on standard ISO3744 [35] that enclosed the entire calculation domain was established using an approximate free-field engineering method.
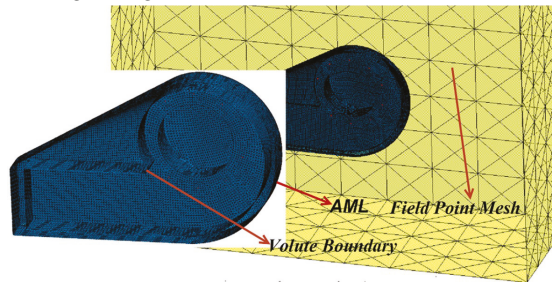
Figure 13. The volute acoustical FEM model.

Figure 14 shows the numerical evaluation method of the volute vibroacoustic coupling. It can be seen that the one-way fluid–structure–acoustic coupling method is divided into three main steps. The first involves the acquisition of the vibrational source of the volute based on the unsteady flow calculation on the centrifugal fan, and then transformation of the extracted time-domain fluctuation data into frequency-domain data through FFT, providing basic data for the next vibration response and vibroacoustic calculation. The second steps involves the interpolation of the frequency-domain node pressure of the fluid into the corresponding structural FEM nodes according to Equation (5) (where P_i (i = 1, 2, 3, 4) is the source node pressure load, P_A is the target node pressure load, and d_i (i = 1, 2, 3, 4) is the distance from the source node to the target node; Figure 15 is a sketch of the geometric interpolation algorithm), assignment of the interpolated node pressure of the structure to the boundary loads of vibroacoustics, and then application of the structural FEM to obtain the modal participation factor of the volute. The third step involves loading the modal participation factor and vibroacoustic boundary loads that were obtained during the second step in order to calculate the volute vibrational sound radiation using the modal superposition vibroacoustic method.

$$P_A = \frac{P_1\frac{1}{d_1} + P_2\frac{1}{d_2} + P_3\frac{1}{d_3} + P_4\frac{1}{d_4}}{\frac{1}{d_1} + \frac{1}{d_2} + \frac{1}{d_3} + \frac{1}{d_4}} \tag{22}$$
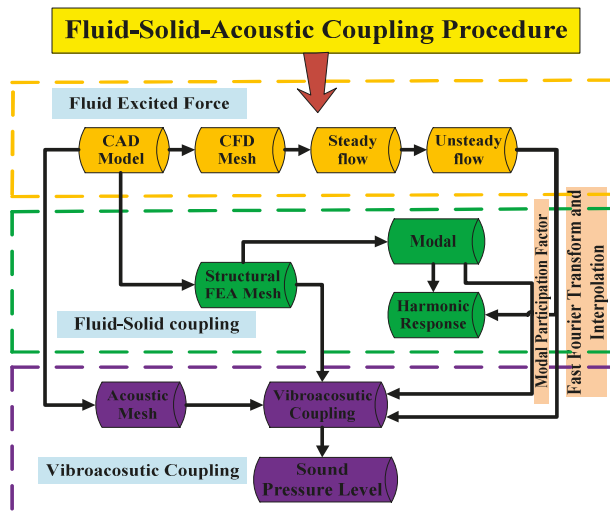

Figure 14. The flow chart of the numerical evaluation method of volute vibroacoustic coupling.
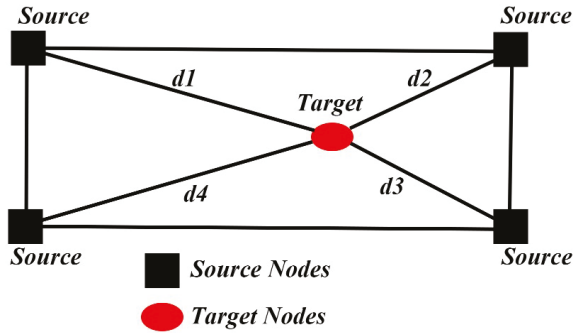
Figure 15. The diagram of the geometric interpolation algorithm.

Figure 16 presents the spectrum chart of the vibrational sound radiation of volute casing, and the vibrational noise at the fundamental frequency (BPF) is obvious. Besides, the distribution of the vibrational sound radiation and the normalized velocity of the volute casing surface at the fundamental frequency is presented in Figures 17 and 18. It can be observed that the distribution shape of the surface sound pressure and surface normal velocity on the volute have identical characteristics, and the outlet of the volute side panel near the volute tongue region and the volute back panel at 180° from the tongue presented very strong vibrational acoustic radiation values. In addition, the previous study [36] showed that the normal vibration velocity of the volute was the decisive factor that determined the volute surface acoustic radiation. Moreover, the theoretical derivation of Section 4.1 (according to Equation (19)) shows that the acoustical power that characterized the vibrational acoustic energy is also a quadratic function of the vibrational velocity (according to Equation (19), Zhou [22]) indirectly reducing the volute surface acoustical radiation through a decrease in the surface normal velocity of the volute casing.
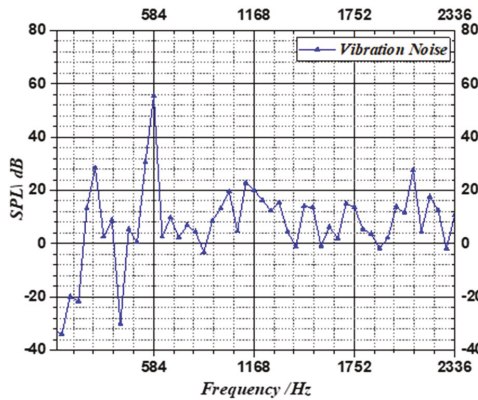

Figure 16. The spectrum chart of vibrational sound radiation of the volute casing (numerical).
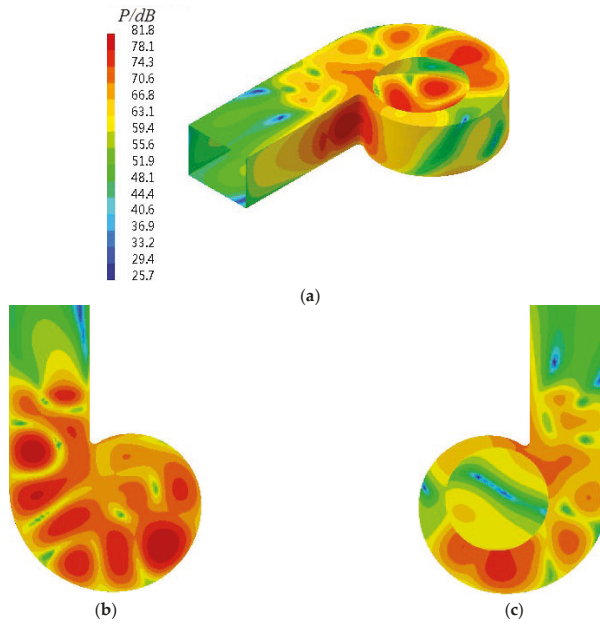
Figure 17. The distribution of the vibrational sound radiation of the volute casing surface at the fundamental blade-passing frequency (BPF). (**a**) Side; (**b**) Back; (**c**) Front.
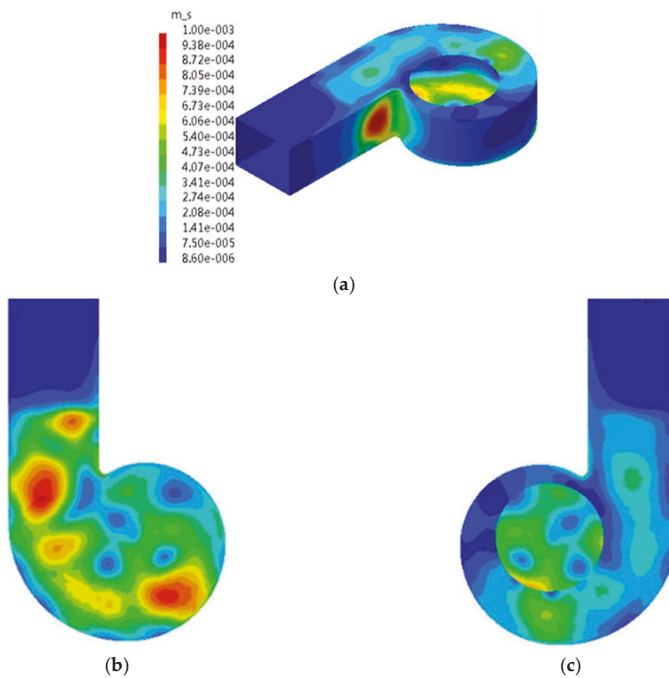

Figure 18. The distribution of the vibrational velocity of the volute casing surface at the fundamental frequency (BPF). (**a**) Side; (**b**) Back; (**c**) Front.

5. Vibroacoustic Optimization Strategy

5.1. Optimization Objective Selection and Volute Panel Thickness Parametrization

Determining the appropriate optimization objective function is the key problem of optimizing calculations. Section 4.1 of this paper provides two means to control vibroacoustics. Control method (1) can be used to modify the geometrical shape of the volute tongue or wavy edge of the blade to weaken the pressure fluctuations on the volute casing. Control method (2) can be used to modify the model geometry, thickness distribution, and constrained position, and reduce the modal shapes. However, the shapes and natural frequency are determined by the structural thickness distribution, structural stiffness, and the constrained position. The modal shapes can be changed by controlling the thickness distribution, when the geometry, stiffness, and constrained position of the structure are fixed.

Concerning the studied centrifugal fan volute with several welding panels, this study developed an optimization method of vibroacoustics by changing different panel thicknesses (FT, BT, and ST) to attenuate the volute vibrational acoustic radiation. Regarding vibroacoustic optimization, we must first determine the optimization target function. From the literature review, it is generally considered that the uniform sound pressure at the received position or the radiated sound power at the structural surface should be set as the optimization function. The selection of the target function depends on the research problems, and the target function is divided into two categories according to different attributes. One is a noise optimization problem (internal noise control problem) applied in a closed domain. In this case, one or a few sound pressure levels of a specific measuring point are taken as the target function [24–27]. Concerning the noise control problem in the open domain, the external acoustic power on the structural surface was chosen as the optimal target function. This method has been proven by many scholars [24,25,37].

For the type of target function, the sound pressure at the arranged receiving position can be clearly determined, but it may result in judgments distortion, such that a low sound pressure value at an arranged position may be obtained, and a high sound pressure value at other points can be presented. Thus, it is very important to choose such target functions. Fortunately, Marburg [38] proposed an improved target function (F), which is defined as follows:

$$F = \widetilde{F}^{\frac{1}{n}} = \left(\frac{1}{\omega_{max} - \omega_{min}} \int_{\omega_{min}}^{\omega_{max}} \phi\{p_l(\omega)\}d\omega \right)^{\frac{1}{n}} \tag{23}$$

In Equation (23), $\phi\{p_l(\omega)\}$ represents the given weighting function, which is replaced by the following equation:

$$\phi\{p_l(\omega)\} = \begin{cases} (p_l - p_{ref})^n, & p_l > p_{ref} \\ 0, & p_l < p_{ref} \end{cases} \tag{24}$$

Where $n = 1$, which is the average value of sound pressure in the frequency spectrum; and $n = 2$, which is the root mean square (RMS) value of the sound pressure.

For the second type of problem, Koopmann and Fahnline [6] proposed an optimization method that takes the external radiated sound power as the target function, and is suitable for the optimal noise control method in this study. They provided the root mean square (RMS) expression of sound pressure in an enclosed space as follows:

$$W = \int_S Re(I_n)ds = \frac{1}{2} \int_S Re(pv_n^*)ds \tag{25}$$

Where S refers to the structural surface, and the structural surface is discretized based on FEM. At this time, the structural radiated sound power can be regarded as the sum of the individual radiated

sound power on the FEM mesh [39]. Thus, after organization, Equation (25) can be changed to the following:

$$W = \sum_{j=1}^{N_e} W_j = \frac{1}{2} Re(\sum_{j=1}^{N_e} \frac{1}{2} \int_{S_j} p_j v_{nj}^* dS)$$ (26)

In the formula:

N_e—the number of finite elements on the structural casing;

S_j—the area of *j*th finite element, m^2;

P_j—the sound pressure of *j*th finite element, p$_a$;

v_{nj}^*—the normal velocity of *j*th finite element, m/s.

The vibrational noise of the volute structure of the marine centrifugal fans that is studied in this paper belongs to the typical external opening noise radiation problem. Therefore, the second type of optimization target function should be adopted.

The previous analysis in Section 4 shows that the structure modal shape can be changed by controlling the structural thickness distribution. Therefore, the volute thicknesses of the three panels (FT, BT, and ST in mm) were specified as the design variables. Thus, the design objectives can be achieved by adjusting the combination of different volute panel thicknesses in the optimization design. The thickness of each volute panel is parameterized using FEM. Figure 19 shows the volute parameterization structural FEM. Since the panel thickness of each volute is generally less than 10 mm, we assigned the panel thickness of each volute to be from four mm to 10 mm.
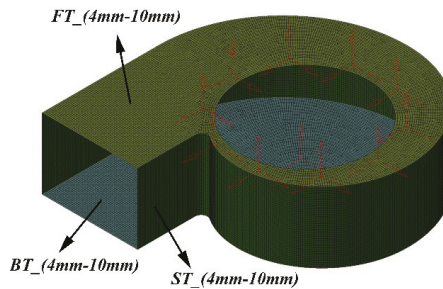

Figure 19. The volute parameterization structure.

5.2. RBF Approximation Surrogate Models and Validation

The high computational cost of each vibration and acoustic simulation to predict the vibroacoustics performance of each volute panel thickness design makes a direct optimization approach to find an optimum low-vibration noise volute unfeasible. Indeed, an optimized cycling takes 24–26 h. In addition, the optimization process terminates due to the failure of a single simulation program. Therefore, the long time of the optimal iterative procedure is the major bottleneck in the optimization of acoustics performance for all complex structures. Instead, the use of a surrogate model, which was constructed from and used in lieu of the actual simulation model, represents a valuable alternative to increase the speed of the optimization. For this reason, a metamodeling approach was chosen for vibroacoustic optimizations. Therefore, the combination of a design of experiment (DoE) and an approximation model (AM) was used to determine the relationship between the structural design variables and the target function, and provide the basic data and models for the subsequent optimization. According to the studied centrifugal fan volute, taking each volute thickness (FT, BT, and ST) as design variables, each design variable was given five levels. Table 3 provides the levels of distribution of the design variables. Due to the smaller number of design variables, the full-factor

method was adopted to collect sample points of the design space constructed by the three variables collected; thus, a total of 125 sample points was collected.

Table 3. The levels of distribution of each volute panel thickness. FT: the front panel thickness, ST: the side panel thickness, BT: the back panel thickness.

Variables	Range/mm	Levels of Distribution/mm				
FT	5.00~10.0	5.00	6.25	7.50	8.75	10.0
ST	5.00~10.0	5.00	6.25	7.50	8.75	10.0
BT	5.00~10.0	5.00	6.25	7.50	8.75	10.0

For each sample point, the aforementioned vibroacoustic coupling assessment method was used to calculate the radiated sound power and the total volute mass of the volute structure surface of each combination. The approximate model approach is generally divided into two broad categories: first, least squares fitting, also known as response surface methodology (RSM); and the second, interpolation. RSM uses polynomial functions to fit the design space. In addition, the RSM fitted the complex response relationships through regression models due to the simple algebraic expression. In addition, because of the advantages of being systematic and practical, the RSM had been used in a broad range [40–43], but the approaching effect is not as good as that of neural network and other methods for highly complex functional relationships (a complex relation of nonlinear function). The radial basis function (RBF) belongs to the interpolation algorithms, and is the second approximate model method. Since the neural network model has a strong ability to approximate complex nonlinear functions, the learning speed is fast, has excellent generalization ability, and is highly fault-tolerant. It is used by many scholars and engineers in aircraft wingtips [44], highway traffics [45], turbomachinery [46], engineering optimization [47], compressors [48], gas cyclone separator [49], MMES controllers [50], and many other applications. The relationships between the vibrational sound radiation of the volute casing surface and the volute panel thickness are typically nonlinear. Thus, this study used the RBF model to approximate and fit the design space.

Figure 20 shows the fitting procedure of the vibroacoustic optimization of volute casing. It can be seen from Figure 20 that this procedure is mainly divided into two parts. The first is the creation of a design space for the collected sample points using the assessment method of vibroacoustic coupling. The FEM model of fan volute was established by UG; then, ANSA constructed FEM mesh, and the Nastran code solved the volute modal participation factor. At last, the vibrational sound radiation of volute was used by LMS Virtual Acoustics. In addition, all the calculation codes were integrated into the multi-disciplinary optimization platform, Isight. The second built an RBF approximation model (RBF surrogate model) instead of a simulation loop, as mentioned for the first part. Thus, the RBF method with Isight code was used to establish an approximate alternative model.

In fact, the approximate model can be considered an approximate approach for the physical model, in which the precision of the approximate model is affected by the number of sampling points. At present, statistical theory with analysis of variance is usually used to verify the effectiveness of an approximate model. However, the approximate model is usually tested by the complex correlation coefficient R^2 ($0 < R^2 < 1$) in engineering, and Shi [51] provided its mathematical expression. The closer the value of R^2 is to one, the more precise the approximation model. Figure 21 shows the error schematic diagram of each response surface model. In Figure 21, the Kirchhoff SPW (dB) represents the radiated sound power of the volute surface, and the mass (kg) represents the total mass of the volute. It can be seen that all the response surface models are infinitely close to the value one; thus, the approximate model that was established using the mentioned method can completely replace the real simulation loop. The parametric analysis related to the radiated sound power of the volute surface is performed, which will be discussed in the following sections.
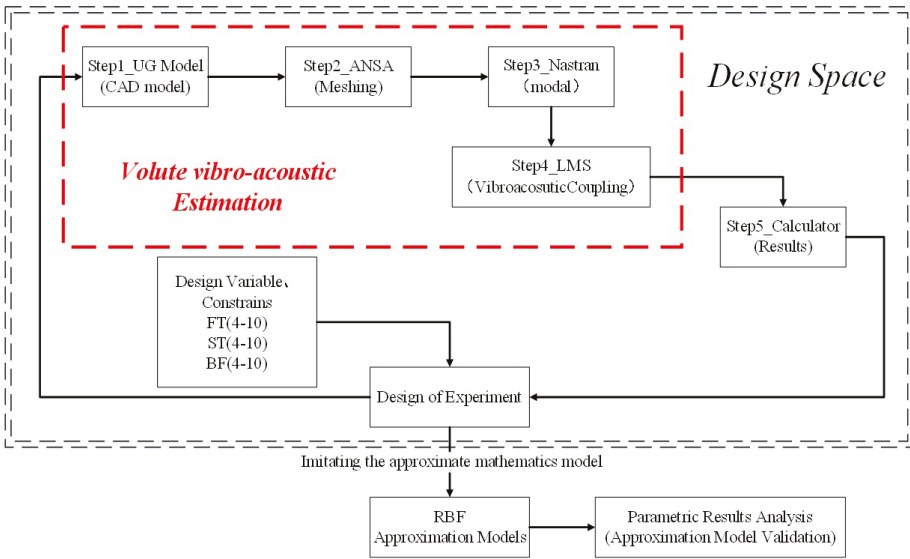
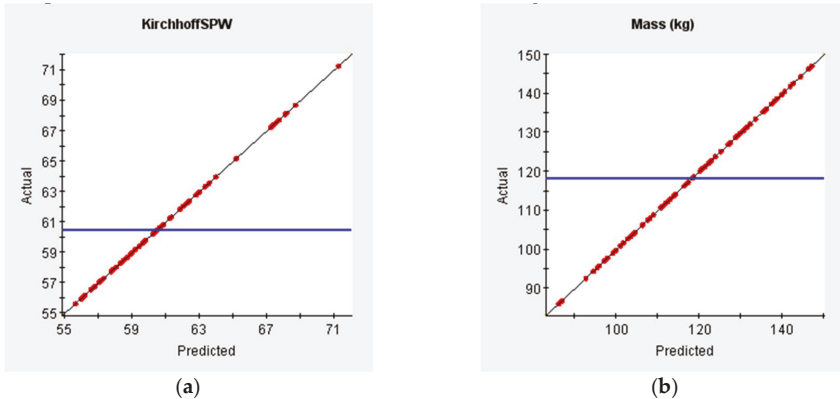**Figure 20.** Design space and radial basis function (RBF) approximation model processing for optimization.

(**a**)	(**b**)

Figure 21. The error schematic diagram of each response surface model. (**a**) The precision of sound power on the volute surface; (**b**) The precision of total mass.

5.3. Single-Objective Optimization Procedure

The single-objective optimization was conducted to improve the radiated sound power of the fan volute by using a weighted-average surrogate model with three design variables related to the geometries of the three-part volute panel thickness. The collection of sample points that was described in the previous text, and based on the RBF approximation model, provides the basic database and the analysis model of the target function for the optimization of the vibroacoustic coupling of the volute structure. In this part, the single-objective optimization took three panel thicknesses (FT, BT, and ST in mm) as design variables, and took the vibrational sound radiated power of the volute surface (Kirchhoff SPW (dB)) as the target function. In addition to these, the single-objective optimization was divided into two parts: the first part maintained the volute total mass as invariable, and for the second

part, there was no mass constraint on the volute. Since the thickness of the volute panel is generally less than 10 mm, the author assigned the volute panel thickness as from four mm to 10 mm. Therefore, the mathematical model optimized in this section is as follows:

The objective function, W_s (minimum):

$$W_s = \sum_{j=1}^{N_e} W_j = \frac{1}{2} Re(\sum_{j=1}^{N_e} \frac{1}{2} \int_{S_j} p_j v_{nj}^* dS), \text{ (vibrational sound radiated power of volute surface , W)} \quad (27)$$

Variables:

$$[FT, ST, BT] \quad (28)$$

Constrained conditions:

$$
\begin{aligned}
4 &\leq FT \leq 10 \\
4 &\leq ST \leq 10 \\
4 &\leq BT \leq 10
\end{aligned}
\quad (29)
$$

Constrained variable:

$$M_T = S_{FT} \cdot FT + S_{ST} \cdot ST + S_{BT} \cdot BT, \text{ (total mass, kg)} \quad (30)$$

Defining the sound power level as follows:

$$10 \times \lg^{(W_s/W_{ref})} \quad (31)$$

In Equation (31), W_{ref} represents the reference value of sound power, $W_{ref} = 1 \times 10^{-12}$ W

Figure 22 shows the flow chart of the single-objective optimization. The single objective optimization uses the simulated annealing algorithm (ASA) to implement a global search. The optimal result of the approximate model in the previous text is assigned as the initial value, and the global optimization iterates 10,000 steps and takes 12 minutes. Then, the value is locally optimized using mixed integer sequential quadratic programming (MISQP), which iterates more than 12 steps in several seconds. The results of the single-objective optimization of the vibroacoustics of a volute surface will be discussed in the following sections.
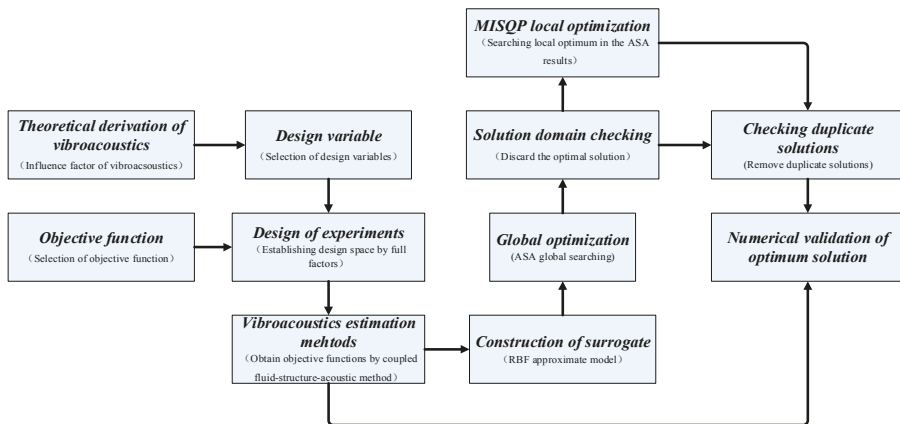

Figure 22. The flow chart of the single-objective optimization.

5.4. Multi-Objective Optimization Procedure

In fact, the parameters of the vibrational sound power and total mass on the volute surface are somewhat contradictory. Thus, a multi-objective optimization method is needed to obtain the optimal volute thickness combination. The definition of the multi-objective optimization mathematical model is presented as follows:

The objective function, W_s, M_T (minimize):

$$W_s = \sum_{j=1}^{N_e} W_j = \frac{1}{2}Re\left(\sum_{j=1}^{N_e}\frac{1}{2}\int_{S_j} p_j v_{nj}^* dS\right), \text{ vibrational sound radiated power of volute surface, W :} \quad (32)$$

$$M_T = S_{FT} \cdot FT + S_{ST} \cdot ST + S_{BT} \cdot BT, \text{ (total mass, kg)} \quad (33)$$

Variables:

$$[FT, ST, BT] \quad (34)$$

Constrained conditions:

$$\begin{aligned} 4 \leq FT \leq 10 \\ 4 \leq ST \leq 10 \\ 4 \leq BT \leq 10 \end{aligned} \quad (35)$$

Figure 23 presents a flow chart of multi-objective optimization. The multi-objective genetic algorithm termed NSGA_2 was adopted to solve the multi-objective optimization with the optimal value obtained by taking the single-objective optimization of specific mass constraints as the initial values. The global search iterates 4800 steps, and the Pareto frontier solutions are marked. A solution satisfying the requirement is selected as the initial value of MISQP for mixed integer quadratic programming; then, the final solution satisfying the engineering requirement is obtained by iterating 15 steps again. Finally, the vibroacoustic estimation method mentioned in Section 4.3 is used to verify the precision of the optimal solution. The multi-objective optimization results will be discussed in the following sections.
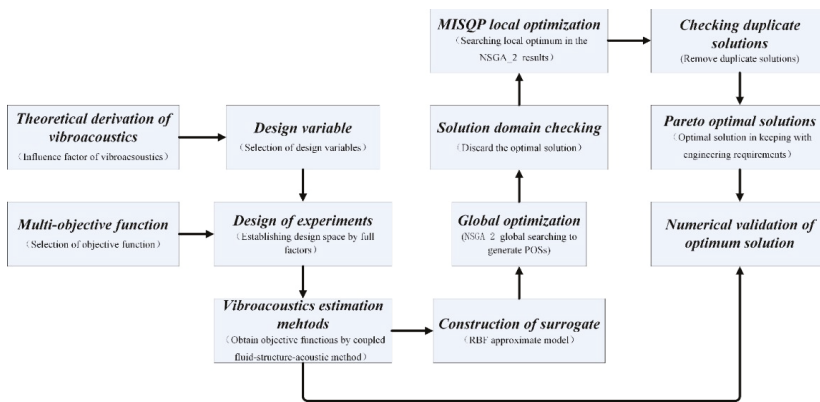

Figure 23. The flow chart of multi-objective optimization.

6. Results and Discussion

6.1. Results of Sensitivity and Parametric Analysis

In order to investigate the influence of each design variable on the optimization objectives, it is necessary to perform the sensitivity analysis for the design variables. Sensitivity analysis is performed by studying the correlations between the design variables and the objectives. Figure 24 shows the

correlation distribution of design variables and optimization objectives (Kirchhoff SPW, volute mass on the volute structure surface); the correlation theory and definition referred to the reference [52]. The positive value indicates that the optimization objective is proportional to the design variable, and otherwise is an inverse relationship. The closer the absolute value of the coefficient is to one, the higher the degree of correlation. It can be seen from Figure 24 that ST had the largest influence on all the objectives, followed by FT, then BT. Concerning radiated sound power, ST and FT present an inverse proportionality to the radiated sound power, which means that the larger the volute panel thickness (ST and FT), the smaller the radiated sound power.
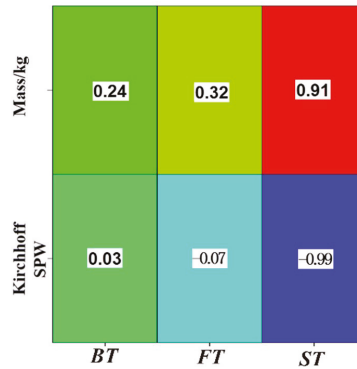

Figure 24. The correlation distribution of design variables and responses (Kirchhoff SPW and volute mass on the volute structure surface).

However, the relationship diagram between each volute panel (ST, BT, FT) and objective functions (the Kirchhoff SPW or the total mass of the volute) in Figure 25 shows that BT and FT present nonlinearity characteristics for the acoustic power of the volute surface. With an increase of BT value, the vibrational radiated sound power of the volute surface increases first, and then decreases, and FT value presents the opposite change. However, the volute radiated sound power decreases with ST value if the ST does not exceed nine mm. This means that each panel thickness (BT, ST, FT) has an optimal value that satisfies the radiated sound power minimum. However, Figure 25 only shows the influence of each single thickness variable on the radiated sound power (the other two variables remain unchanged; the relationship between the other two variables and the noise radiation is determined). To determine the relationship between each variable combination (BT–ST; FT–ST; FT–BT) and the acoustic radiation power, Figure 26 gives the influence of each two-panel thickness variation on the radiated sound power. It can be observed that the FT–ST and BT–ST combinations present similar distribution characteristics. Therefore, the Kirchhoff SPW basically remained a constant smaller value when the ST was greater than 7.0 mm, and the BT was less than 8.5 mm or the FT was less than 7.0 mm. In addition, as the FT is larger and the BT is smaller or the FT and BT are both smaller (less than 5.5), the Kirchhoff SPW is observed to have a smaller value as shown in Figure 26c. Besides, linear relationships could be seen in Figure 25b, which means that the thicker the thickness of each volute panel, the greater the total mass of the casing.
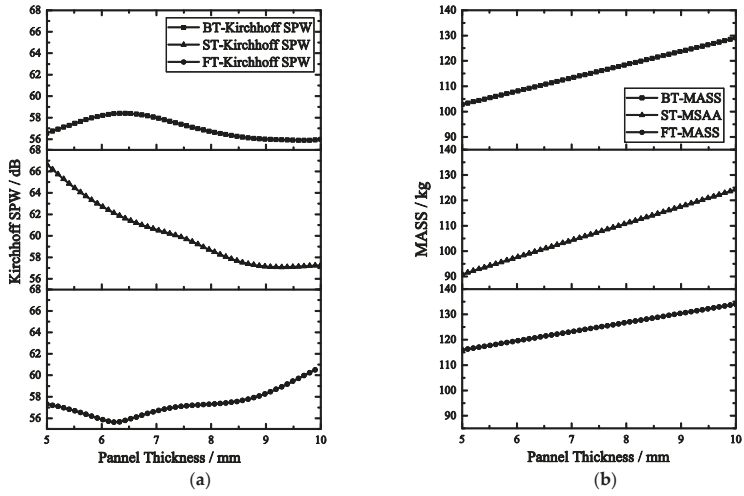
Figure 25. The relationship profile between each panel thickness and objective function (the Kirchhoff SPW or the total mass of the volute). (**a**) The relationship of volute panel thickness and Kirchhoff SPW. (**b**) The relationship of volute panel thickness and total mass.
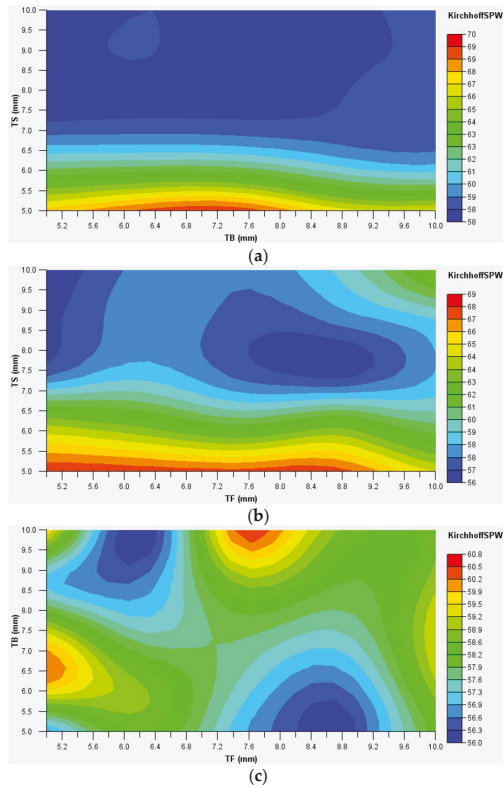

Figure 26. The relationship between each panel thickness (BT–ST; FT–ST; FT–BT) and radiated sound power of volute surface. (**a**) BT-ST; (**b**) FT-ST; (**c**) FT-BT.

In conclusion, the variation in ST is the most sensitive to the sound radiation power of the volute structure surface, while FT is the second-most sensitive, and BT is the least. Therefore, it is possible to obtain the smallest value of radiated sound power of the volute surface by optimizing the panel thickness combination (increasing the ST value and decreasing the FT and BT values).

6.2. Results of Optimization.

After optimization, the vibrational radiated sound power of the volute surface is greatly reduced. Table 4 shows the massless constrained optimization results (the "optimized" represents the calculation results of the approximate model, and the "numerical validated" represents the vibroacoustic analysis with the optimum values). It can be seen that the radiated sound power on the volute structure surface decreases by 9.4 dB when ST increases to a maximum, while BT and ST locate at minimum values; unfortunately, at the same time, the volute total mass increases by 18.13%. Table 5 shows the optimization results with the volute total mass invariable. Even though the volute total mass remains the same, the radiated sound power on the surface of the volute will also be weakened by an average of 6.3 dB. In addition, the radiated sound power spectrum of the volute structural surface shown in Figure 27 also shows that the single-objective optimization significantly improves the radiated sound power on the volute surface at the fundamental frequency (BPF).

Table 4. Massless constrained optimization results.

Table Title	FT (mm)	ST (mm)	BT (mm)	W_s/(dB)	M_T (kg)
Original	6.000	5.000	6.000	63.78	86.592
Optimized	4.000	10.00	4.000	54.38	102.29
Numerically validated	4.000	10.00	4.000	56.25	102.29

Table 5. The optimization results with the volute total mass invariable.

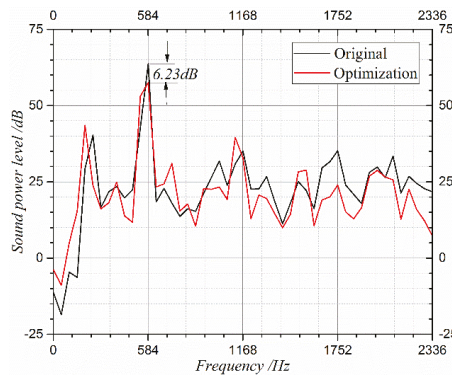| Table Title	FT (mm)	ST (mm)	BT (mm)	W_s / (dB)	M_T (kg)
Original	6.000	5.000	6.000	63.78	86.592
Optimized	4.335	7.470	4.000	57.52	86.592
Numerically validated	4.335	7.470	4.000	58.68	86.592

Figure 27. The radiated sound power spectrum of the volute structural surface.

In order to better understand the improvement effect of optimum panel thickness combinations on vibroacoustic performance before and after optimization, the comparison of distribution of vibrational sound radiation before and after the total mass invariable optimization at the fundamental frequency are given in Figures 28 and 29. From the comparison, it can be concluded that the sound pressure of the vibrational radiation close to the tongue on the side volute is greatly reduced by optimization, and

the other sound pressure of the vibrational radiation on the other area is also weakened to varying degrees. In addition to these results, the optimization also changed the directivity distribution of acoustical radiation, and very strong directivity was produced on the back panel side of the volute.
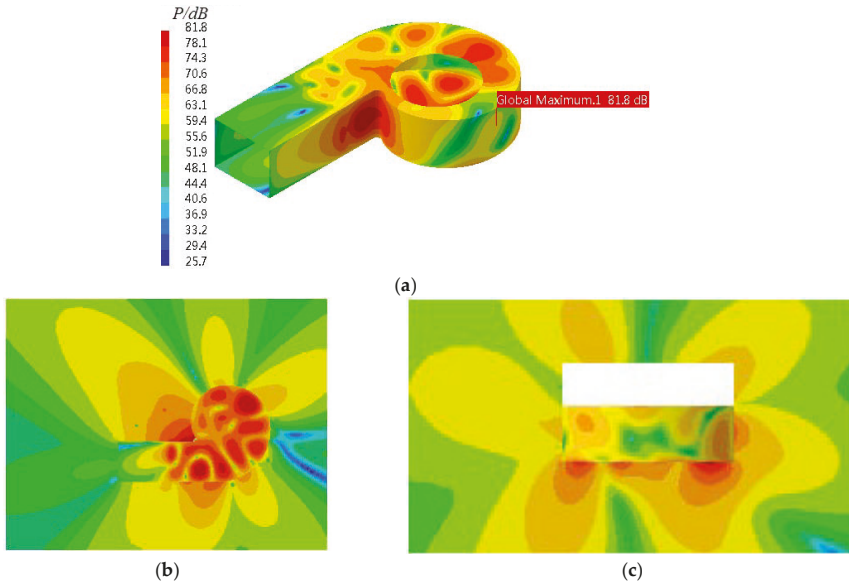

Figure 28. The distribution of vibrational sound radiation of original volute at the fundamental frequency. (**a**) The whole volute body; (**b**) XY section; (**c**) ZY section.
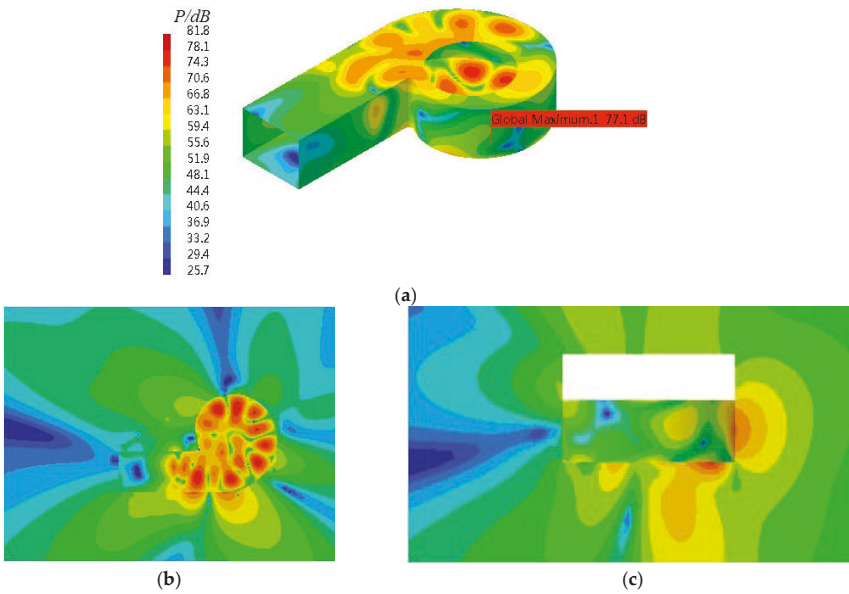

Figure 29. Distribution of vibrational sound radiation after the total mass invariable optimization at the fundamental frequency. (**a**) The whole volute body; (**b**) XY section; (**c**) ZY section.

The multi-objective optimization results, which took the volute surface vibrational radiated sound power and the total mass of the volute as the objective function of the optimization model, conformed to the actual needs. Multi-objective optimization solutions are not unique, and are usually presented in the form of solutions (Pareto front solutions). According to the distribution of Pareto front solutions in Figure 30, it can be seen that the radiated sound power on the volute surface and the total mass of the volute show an approximately linear inverse proportional relationship, and a smaller vibrational sound power can be obtained, when the volute mass (mass increase control: ± three kg) changes within a small range. Moreover, if the volute mass increased by two kg, the total acoustic power of the volute surface and the radiated sound power at BPF decreased by 7.3 dB and 6.9 dB, respectively, as shown in Table 6 and Figure 31. In addition to these, Figure 32 shows a comparison of the radiated sound power of the volute structure surface after multi-objective optimization. It can be seen that after optimization, the multi-objective optimization presents the same noise reduction effect on the volute structure surface as the single-objective optimization. In addition to these, the radiation sound pressure close to the tongue on the volute front panel is greatly reduced, the sound pressure is lower (under 10 dB) than at the other parts of the volute, and the sound pressure of the other volute parts is also greatly weakened. In summary, the radiated sound power of the volute structure surface obtained using the multi-objective optimization method is further reduced by nearly one dB compared to that of the single-objective optimization with mass constraints. It can be concluded that the optimization effect of the multi-objective method is obviously better than the single-objective optimization for this studied fan. Even considering the two conflicting objective functions, the multi-objective optimization can achieve a more balanced effect.
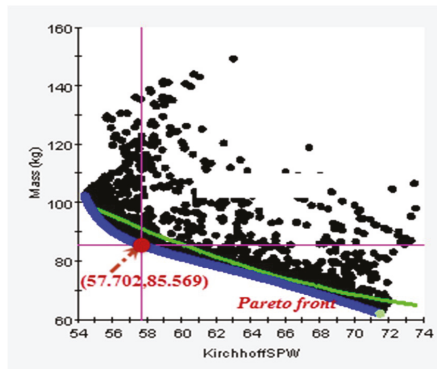

Figure 30. The distribution of Pareto front solutions.

Table 6. The multi-objective optimization results.

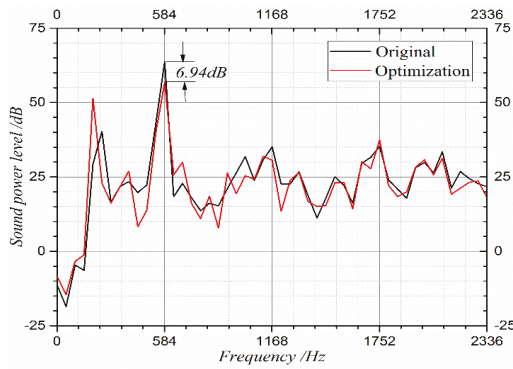| Title	FT (mm)	ST (mm)	BT (mm)	W_s/(dB)	M_T (kg)
Original	6.000	5.000	6.000	63.78	86.592
Optimized	4.001	7.935	4.010	56.53	88.549
Numerically validated	4.001	7.935	4.010	57.16	88.549

Figure 31. The frequency spectrum of total acoustic power of the volute surface.
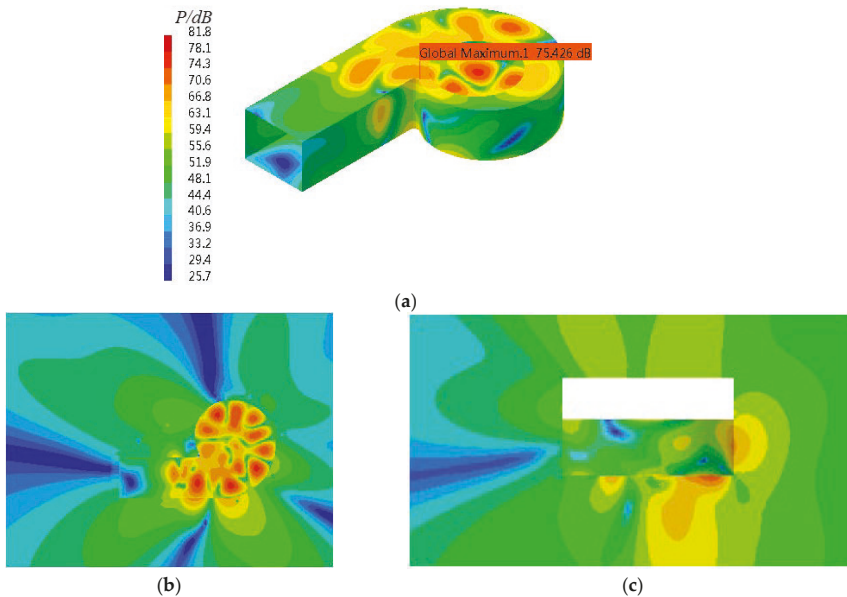

Figure 32. The radiated sound power distribution of the volute structure surface after multi-objective optimization. (**a**) The whole volute body; (**b**) XY section; (**c**) ZY section.

Generally, the noise-reduction mechanism of single and multi-objective optimization is attributed to the major factor: the normal vibration velocity of the three-part volute surface, which was changed to be smaller by controlling the thickness combination with the unsteady aerodynamics determined and volute geometry fixed. The previous study [36] showed that the normal vibration velocity of the volute surface was the decisive factor that determined the radiated sound power. To comment on this major noise-reduction mechanism, the comparison of the normal vibration velocity of the volute surface before and after optimization were presented in Figures 18 and 33. It indicates that the normal vibration velocity of the volute surface was greatly diminished (especially the tongue region) after optimization, which inevitably leads to a significant reduction for the radiated sound power of the volute surface, as shown in Figure 32. In addition, the parametric analysis indicates that ST had the largest influence on sound radiated power of volute surface, followed by FT, and then BT. The sound radiated power of the volute surface could be sharply reduced if ST was much larger (larger than seven mm for this fan), while BT and FT were designed as lower values (the BT was less than 8.5 mm, and the

FT was less than 7.0 mm for this fan). Less noise radiation could be achieved if the ST increased over a certain limit (the setting extremum), but this can lead to unpredictable mass gain and increased costs.
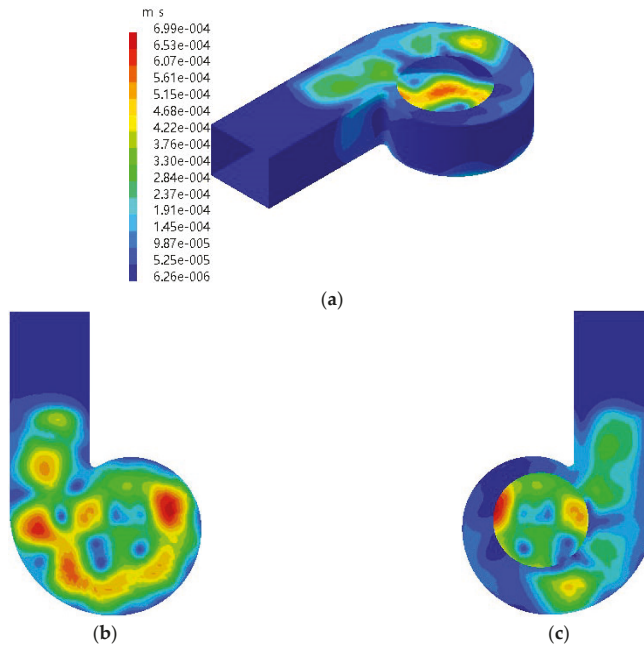

Figure 33. The distribution of the vibrational velocity of the volute casing surface at the fundamental frequency (BPF) after multi-optimization. (**a**) Side; (**b**) Back; (**c**) Front.

7. Conclusions

To reduce this type of vibrational sound radiation, a vibrational noise control method of multi-disciplinary optimization that considered the influence of vibroacoustic coupling was proposed. The strategies employed in the vibroacoustic optimizations based on DoE and RBF optimization techniques were proved to be highly successful, and various optimal solutions were analyzed. Some preliminary conclusions are obtained in this paper as follows:

(1) The optimization results indicate that the three-part volute structure has an optimal thickness combination maintaining the volute mass constant, and the optimal design of the volute radiated sound power can be greatly reduced without any increase in material cost. Besides, the sensitivity analysis showed that ST is the most sensitive to the volute radiated sound power, followed by BT, and then FT, which is the smallest.

(2) The optimization process achieves the purpose of reducing the radiated sound power of the centrifugal fan volute. The radiated sound power on the volute casing surface decreased by 6.3 dB with mass constraint. Without a strict constraint of the volute mass, the optimization can be further applied to get a better thickness combination of the volute, thereby achieving better optimized vibrational noise results. The multi-objective optimization was more advantageous. It was found that the volute acoustical radiated power on the volute surface decreased by 7.3 dB when the total mass of the volute slightly increased (± 3 kg). The optimization in this study provides an important technical reference for the design of low vibroacoustic volute centrifugal compressors and fans whose fluids should be strictly kept within the system without any leakage.

(3) In addition, the optimized thickness combination effectively reduces the normal vibration velocity of the volute surface, especially the volute tongue region, and thus significantly reduces the volute vibration radiation, which is also the noise reduction mechanism of this optimization method.

Author Contributions: J.Z. (Jianhua Zhang) and W.C. conceived the whole numerical simulations; J.Z. (Jinghui Zhang) contributed the optimization tools; Y.L. carried out the experimental validation and J.Z. (Jianhua Zhang) wrote the paper.

Conflicts of Interest: The authors declare no conflict of interest.

Abbreviations

B = volute width (mm)
D_2 = impeller outlet diameter (m)
Q = flow rate (m^3/s)
Z = the axial distance from the monitoring point
BEP = the best design point
BPF = the fundamental frequency, the blade passing

c = speed of sound (m/s)

u_2 = circumferential velocity of impeller outlet (m/s)
P_T = total pressure rise (Pa)
φ = flow coefficient

ψ = total pressure coefficient

[K] = FEM stiffness matrices
[C] = FEM damping matrices
[M] = FEM mass matrices
$F(t)$ = external force
MPFs = modal participation factors
Φ = mode shape of the structure
Y = mode coordinate of the structure
ω_n = natural frequency
ζ = damping ratio
λ = frequency ratio
Re = real part
v_n^* = the node velocity of volute surface
$W_{o,active}$ = active output power
$x(t)$ = vibrational displacement

$\dot{x}(t)$ = vibrational velocity
β_i = amplification factor
ρ = density, ρ = 1.20 kg/m^3
ω = angular velocity (rad/s)to the volute rear casing (mm)
FEM = finite element method
AML = automatically matched layer frequency (Hz)
a_{fei} = active vibration acceleration value of each frequency in the spectrum
$a_{ref} = 1 \times 10^{-6}$ (m/s^2)
P_i = the source node pressure load (i = 1, 2, 3, 4)
P_A = the target node pressure load
d_i = the distance from the source node to the target node (i = 1, 2, 3, 4)
N_e = the number of finite elements on the structural casing
S_j = the area of jth finite element; m^2
P_j = the sound pressure of jth finite element, p$_a$
v_{nj}^* = the normal velocity of jth finite element, m/s.
W_s = vibrational sound power
M_T = total mass of volute
S_{FT}, S_{ST}, S_{BT} = area of FT, ST, and BT respectively
I = structural surface acoustic intensity
DoE = design of experimental
RBF = radial basis functions
SPLs = sound pressure levels (dB)
ST = the side panel thickness of three-part volute
BT = the back panel thickness of three-part volute
FT = the front panel thickness of three-part volute

References

1. Koopmann, G.H.; Cunefare, K.A.; Neise, W. Fan casing noise radiation. *J. Vib. Acoust.* **1991**, *113*, 37–42. [CrossRef]

2. Citarella, R.; Federico, L. Advances in Vibroacoustics and Aeroacoustics of Aerospace and Automotive Systems. *Appl. Sci.* **2018**, *8*, 366. [CrossRef]

3. Armentani, E.; Trapani, R.; Citarella, R.; Parente, A.; Pirelli, M. FEM-BEM Numerical Procedure for Insertion Loss Assessment of an Engine Beauty Cover. *Open Mech. Eng. J.* **2013**, *7*, 27–34. [CrossRef]

4. Armentani, E.; Sepe, R.; Parente, A.; Pirelli, M. Vibro-Acoustic Numerical Analysis for the Chain Cover of a Car Engine. *Appl. Sci.* **2017**, *7*, 610. [CrossRef]

5. Bianco, D.; Adamo, F.P.; Barbarino, M.; Vitiello, P.; Bartoccini, D.; Federico, L.; Citarella, R. Integrated Aero–Vibroacoustics: The Design Verification Process of Vega-C Launcher. *Appl. Sci.* **2018**, *8*, 88. [CrossRef]

6. Koopmann, G.H.; Fahnline, J.B. *Designing Quiet Structures: A Sound Power Minimization Approach*; Academic Press: Cambridge, MA, USA, 1997.

7. Hwang, W.; Oh, I.; Kim, B.; Park, S.; Ryu, K. A study on noise radiation from compressor shell. In Proceedings of the International Compressor Engineering Conference, West Lafayette, IN, USA, 17–20 July 2006.
8. Cai, J.; Qi, D.; Lu, F. Numerical studys on fan casing vibration and noise radiation. In Proceedings of the ASME Turbo Expo, Orlando, FL, USA, 8–12 June 2009.
9. Cai, J.C.; Qi, D.T. A quantitative study of the blade passing frequency noise fan. *J. Vib. Eng.* **2012**, *14*, 1200–1211.
10. Lu, F.A.; Qi, D.T.; Cai, J.C.; Wen, X.F. Study of the Tonal Casing Noise of a Centrifugal Fan at the Blade Passing Frequency. Part II. Vibroacoustics. *J. Low Freq. Noise Vib. Act. Control* **2011**, *29*, 253–266.
11. Cai, J.; Qi, D.; Tang, Y. Quantitative prediction of sound radiation by casing vibration of centrifugal fan. *J. Xi'an Jiao Tong Univ.* **2009**, *43*, 71–74.
12. Durand, J.F.; Soize, C.; Gagliardini, L. Structural-acoustic modeling of automotive vehicles in presence of uncertainties and experimental identification and validation. *J. Acoust. Soc. Am.* **2008**, *124*, 1513. [CrossRef] [PubMed]
13. Zhang, J.; Chu, W.; Zhang, H.; Wu, Y.; Dong, X. Numerical and experimental investigations of the unsteady aerodynamics and aero-acoustics characteristics of a backward curved blade centrifugal fan. *Appl. Acoust.* **2016**, *110*, 256–267. [CrossRef]
14. Celikkan, O.; Haluk, E. Vibroacoustic Analysis of a Refrigerator Freezer Cabinet Coupled with an Air Duct. *Adv. Acoust. Vib.* **2017**, *2017*, 1–18. [CrossRef]
15. Zhou, H.; Mao, Y.; Diao, Q.; Lu, F.; Zhang, Q. Numerical analysis of the vibration and noise induced by the unsteady flow in a centrifugal compressor. *J. Power Energy* **2016**, *230*, 554–569. [CrossRef]
16. Kim, Y.S.; Kim, E.Y.; Lee, S.K. Strategy for vibration reduction of a centrifugal turbo blower in a fuel cell electric vehicle based on vibrational power flow analysis. *J. Automob. Eng.* **2010**, *224*, 985–995. [CrossRef]
17. Han, B.K.; Zhang, W.H.; Cao, S.M.; Song, L.T. Vibration and Noise Radiation Control of the Volute of Centrifugal Fan. *Noise Vib. Control* **2013**, *2*, 201–203.
18. Elliott, S.J.; Johnson, M.E. Radiation modes and the active control of sound power. *J. Acoust. Soc. Am.* **1993**, *94*, 2194–2204. [CrossRef]
19. Johnson, M.E.; Elliott, S.J. Active control of sound radiation using volume velocity cancellation. *J. Acoust. Soc. Am.* **1995**, *98*, 2174–2186. [CrossRef]
20. Li, S.; Zhao, D. Research on modal analysis of structural acoustic radiaton using structural vibration modes and acoustic radiation modes. *ACTA Acust.* **2004**, *29*, 200–208.
21. Yang, D.; Li, Q.; Dai, L. The optimal design of hydrazine bottle system to reduce vibration in satellite. *J. Astronaut.* **2005**, *26*, 804–807.
22. Zhou, Z.; Lu, F.; Qi, D.; Yuan, M. Numerical Optimization on Vibration and Noise Reduction of Centrifugal Fan Volute. *J. Xi'an Jiao Tong Univ.* **2011**, *45*, 59–64.
23. Lu, F.A.; Qi, D.T.; Wang, X.J.; Zhou, Z.; Zhou, H.H. A numerical optimization on the vibroacoustics of a centrifugal fan volute. *J. Sound Vib.* **2012**, *331*, 2365–2385. [CrossRef]
24. Nielsen, J.C.O. Acoustic optimization of railway sleepers. *J. Sound Vib.* **2000**, *231*, 753–764. [CrossRef]
25. Chen, L.Y.; Wang, D.Y. Structural-acoustic optimization of stiffened panels based on a genetic algorithm. *J. Mar. Sci. Appl.* **2007**, *6*, 55–61. [CrossRef]
26. Zhang, J.; Zhong, Z.W.; Ming, X.S.; Ying, Z.W. Acoustic design optimization for coupled acoustic-structural systems. *J. Vib. Eng.* **2005**, *18*, 519–523.
27. Yuksel, E.; Kamci, G.; Basdogan, I. Vibro-Acoustic Design Optimization Study to Improve the Sound Pressure Level Inside the Passenger Cabin. *J. Vib. Acoust.* **2012**, *134*, 61017. [CrossRef]
28. Ma, J.Z.; Zhu, X.M.; Jiang, Y.; Lv, Z.Q.; Gong, X.X.; Qin, H.F. *GJB 4058-2000, Noise and Vibration Measurement Methods for Equipments of Naval Ships*; China Commission of Science Technology and Industry for National Defense: Beijing, China, 2000.
29. *GB/T 1236-2000, Industrial Fan Performance Testing Using Standardized Airway*; Standards Press of China: Beijing, China, 2001.
30. Ballesteros-Tajadura, R.; Velarde-Suárez, S.; Hurtado-Cruz, J.P. Noise Prediction of a Centrifugal Fan: Numerical Results and Experimental Validation. *J. Fluids Eng.* **2008**, *130*, 253–257. [CrossRef]
31. Cai, J.; Qi, D.; Lu, F. Study of the tonal noise of a centrifugal fan at the blade passing frequency. Part I. Vibroacoustics. *J. Low Freq. Noise Vib. Act. Control* **2010**, *29*, 253–266.

32. Launder, E.B.; Spalding, B.D. The numerical computation of turbulent flows. *Comput. Methods Appl. Mech. Eng.* **1990**, *3*, 269–289. [CrossRef]

33. Jiang, Y.Y.; Yoshimura, S.; Imai, R.; Katsura, H.; Yoshida, T.; Kato, C. Quantitative evaluation of flow-induced structural vibration and noise in turbomachinery by full-scale weakly coupled simulation. *J. Fluids Struct.* **2007**, *23*, 531–544. [CrossRef]

34. Zhang, J.H.; Chu, W.L.; Dong, X.J.; Zhang, H.G. Numerical Investigation of Internal Fluid-induced Volute Vibration in a Marine Centrifugal Fan. *Mech. Sci. Technol. Aerosp. Eng.* **2016**, *35*, 523–530.

35. *ISO 3744-1994, Acoustics-Determination of sound power levels of noise sources using sound pressure–Engineering method in an essentially free field over a reflecting plane*; International Organization for Standardization: Switzerland, 1994.

36. Zhang, J.; Chu, W.; Lv, Y. Parametric study of unsteady-flow-induced volute casing vibro-acoustics in a centrifugal fan. In Proceedings of the International Conference on Vibro-engineering, Shanghai, China, 19–21 October 2018.

37. Zhang, Y.; Jiang, W.; Wu, H.; Zhou, X.; Xu, J. A topology optimization design of compressor housing to reduce acoustic noise base on fast BEM. In Proceedings of the 20-th International Congress on Sound & Vibration, Bangkok, Thailand, 7–11 July 2013.

38. Marburg, S.; Hardtke, H.J. Efficient optimization of a noise transfer function by modification of a shell structure geometry—Part II: Application to a vehicle dashboard. *Struct. Multidiscip. Optim.* **2002**, *24*, 60–71. [CrossRef]

39. Raymond, H.M.; Douglas, C.M.; Christine, M.A.C. *Response Surface Methodology: Process and Product Optimization Using Designed Experiments*, 2nd ed.; Wiley Series in Probability and Statistics; Wiley: Hoboken, NJ, USA, 2003.

40. Myers, R.H.; Montgomery, D.C.; Vining, G.G.; Borror, C.M.; Kowalski, S.M. Response Surface Methodology: A Retrospective and Literature Survey. *J. Qual. Technol.* **2004**, *36*, 53–78. [CrossRef]

41. Liu, X.L.; Yuan, M.J.; Miao, Y.; Qi, D.T. Numerical optimization of Volute outlet Structure for Forward-Curved Centrifugal Fan. *J. Xi'an Jiao Tong Univ.* **2009**, *43*, 61–65.

42. Hu, Y.; Hong, H.; Yang, D. Optimization design of vibration response of range hood's shell. *J. Vib. Shock* **2011**, *30*, 179–182.

43. Zangeneh, M.; Mendonça, F.; Hahn, Y.; Cofer, J. 3D Multi-Disciplinary Inverse Design Based Optimization of a Centrifugal Compressor Impeller. In Proceedings of the ASME Turbo Expo 2014: Turbine Technical Conference and Exposition, Düsseldorf, Germany, 16–20 June 2014.

44. Bai, J.; Wang, D.; He, X.; Li, Q.; Guo, Z. Application of an Improved RBF Neural Network on Aircraft Winglet Optimization Design. *Acta Aeronaut. ET Astronaut. Sin.* **2014**, *35*, 1865–1873.

45. Hou, S.; Tan, W.; Zheng, Y.; Han, X.; Li, Q. Optimization design of corrugated beam guardrail based on RBF-MQ surrogate model and collision safety consideration. *Adv. Eng. Softw.* **2014**, *78*, 28–40. [CrossRef]

46. Walther, B.; Nadarajah, S. Optimum Shape Design for Multirow Turbomachinery Configurations Using a Discrete Adjoint Approach and an Efficient Radial Basis Function Deformation Scheme for Complex Multiblock Grids. *J. Turbomach.* **2015**, *137*, 1–20. [CrossRef]

47. Kitayama, S.; Arakawa, M.; Yamazaki, K. Sequential Approximate Optimization using Radial Basis Function network for engineering optimization. *Optim. Eng.* **2011**, *12*, 535–557. [CrossRef]

48. Peng, J.; Xie, S. Compressor characteristic simulation based on RBF neural network. *J. Propuls. Technol.* **2006**, *27*, 30–32.

49. Elsayed, K.; Lacor, C. Modeling and Pareto optimization of gas cyclone separator performance using RBF type artificial neural networks and genetic algorithms. *Powder Technol.* **2012**, *217*, 84–99. [CrossRef]

50. Yu, J. Optimal Design for MMSE Controller Based on RBF Neural Network. *J. Syst. Simul.* **2013**, *25*, 2723–2728.

51. Shi, F. Numerical Study of Pressure Fluctuations Caused by Impeller-Diffuser Interaction in a Diffuser Pump Stage. *Trans. J. Fluids Eng.* **2001**, *123*, 466–474. [CrossRef]

52. SIMULIA support offices. *Isight 5.8 User Guide*; Dassault Systèmes Simulia Corp.: Johnston, RI, USA, 2003.

Analytic Model and the Influence of Actuator Number on the Performance of Plasma Synthetic Jet Actuator Array

Shengfang Huang [1], Zhibo Zhang [1,*], Huimin Song [1,*], Yun Wu [2], Zhengzhong Sun [3] and Yinghong Li [1]

[1] Science and Technology on Plasma Dynamics Laboratory, Air Force Engineering University, Xi'an 710038, China; shengfang_huang@126.com (S.H.); 213120509@seu.edu.cn (Y.L.)

[2] Institute of Aero-engine, School of Mechanical Engineering, Xi'an Jiaotong University, Xi'an 710049, China; wuyun1223@126.com

[3] Department of Mechanical Engineering and Aeronautics, City University London, London, UK; man5658@sina.com

* Correspondence: jiajiangzzb@163.com (Z.Z.); min_cargi@sina.com (H.S.); Tel.: +86-29-84787803 (Z.Z.); +86-29-84787912 (H.S.)

Abstract: Coupled with the multichannel discharge model and plasma synthetic jet actuator (PSJA) aerodynamic model, an analytical model to predict the performance of the PSJA array is put forward. The multichannel discharge model takes these factors into consideration, the delay time in the breakdown process, the electrical transformation of the discharge channel from a capacitor to a resistor induced by the air breakdown, and the varying plasma resistance in the discharge process. The PSJA aerodynamic model is developed based on the conservation equations of mass, momentum, energy, and the lumped capacitance method. The multichannel discharge model can simulate the multichannel discharge process and give the discharge energy in the plasma channel. With a constant heating efficiency, the time-independent heating energy deposition power in a discharge channel is obtained. Importing the heating energy, the PSJA aerodynamic model presents the evolution process of the jet. Simulation results show that the jet strength induced by a single actuator decreases with the number of actuators in the PSJA array. When the actuator number increases from 1 to 20, the weakening extent of mass ejected, peak jet velocity, and jet duration time is 62%, 54%, and 33%, respectively. The discharge efficiency increases with the actuator number, while the thermodynamic efficiency decreases with the actuator number. As a result, the total energy efficiency doesn't always increase with an increase in the number of actuators. When the discharge efficiency of a conventional one channel discharge has been a relatively large value, the total energy efficiency actually decreases with the growth of actuator number.

Keywords: Plasma flow control; multichannel discharge; plasma synthetic actuator; actuator array; analytic model

---

1. Introduction

Plasma actuators have attracted a lot of research attention in recent years because of the associated advantages, such as the absence of moving components, fast response, and wide bandwidth. So far promising control outcomes have been revealed in suppressing flow separation [1,2], alleviating turbomachinery stall [3,4], and shock wave/boundary layer interaction [5,6]. A plasma synthetic jet actuator (PSJA) is one of the typical plasma actuators. The PSJA makes use of the heat released from the spark discharge process between electrodes within a small cavity where the electrodes are

housed. As the velocity of the resulting jet is high (larger than 100 m/s), the PSJA is suitable for high-speed applications. It should be noted that the dielectric barrier discharge (DBD) plasma actuator with annular electrodes can also generate a vertical jet [7,8], and has the name of plasma synthetic jet actuator too [9]. However, the jet velocity from DBD-PSJA is much less. The present work has focused on the PSJA with the principle of spark discharge.

As the diameter of the PSJA orifice is in the order of millimeters, to enlarge the affected area, an array containing distributed actuators is necessary for practical applications [10]. In 2009, Caruana et al. [11] attempted to reduce the jet exhaust noise using six PSJAs. Unfortunately, little effect was achieved, and it was concluded that this was as a result of an insufficient number of actuators. In 2012, an array of three PSJAs was used to control the unsteadiness of a shock wave/turbulent boundary layer by Narayanaswamy et al. [6]. In 2013, an attempt of using 20 PSJAs is made to reduce the trailing edge separation on a NACA-0015 profile [12,13]. Therefore, it can be found that there is a strong desire to implement more PSJAs in various flow controls to deliver a strong actuation.

The arc discharge channel was revealed to feature negative resistant characteristics [14,15], namely, an increase in the current leads to a decrease in the voltage. As a result, the multichannel discharge circuit is difficult to power when using a single power supply. In 2005, M. Samimy et al. [16] tested the discharge in eight channels connected in parallel by using a 30 kΩ current-limiting resistor. This large current-limiting resistor results in a large energy waste. As introduced above, 20 PSJAs were driven simultaneously, but 20 high power supply systems are used by Caruana [12], which is apparently not suitable for on-board applications. Recently, a multichannel discharge technique based on a voltage relay concept is proposed by the authors' group [17–19]. It allows multi-channel discharge without increasing the input voltage and without adding an additional current-limiting resistor. The new voltage relay circuit is a breakthrough. Despite its initial success in experimental testing, the manner in which the channel number affects the jet flow is still not clear, which is of great importance in optimizing the PSJA array's aerodynamic performance.

One efficient way to study the effect of actuator number is to use an analytical model. In 2003, Grossman et al. [20] developed a first-order PSJA model. However, it can only predict the basic performance parameter, such as the jet velocity. In 2010, Haack et al. [21] made a further development where the jet generation process is included, but without modeling the recovery process. In 2015, Zong et al. [22] developed a model that can predict a PSJA's entire working cycle. However, the models introduced above only simulate the operation of a single PSJA. No model is available to predict the performance of a PSJA array, namely a number of PSJAs.

The plasma synthetic jet actuator array (PSJA array) developed by the authors can enlarge the area affected by the actuator greatly, which is more suitable for practical application. A new analytic model is developed in the present work. It consists of two parts: The multichannel discharge model and the PSJA aerodynamic model. The new model enables simulation of the whole working cycle of the PSJA array, and allows the comparison with that of a single PSJA. As the number of PSJAs potentially affects the performance, the effect of the number of PSJAs is also studied using the new model.

2. Analytic Model Development

Same as the conventional PSJA, the working process of the PSJA array consists of three stages: Energy deposition, jet generation, and recovery. However, owing to the disparity in the discharge circuit, the energy deposition process is different. After the energy deposition process, the jet generation and recovery process are similar, which can be described by conservation of mass, momentum, and energy equations. Hence, the analytical model of the PSJA array is divided into two models: A multichannel discharge model and PSJA aerodynamic model. The multichannel discharge model is used to describe the discharge process and calculate the energy deposited in each discharge channel. The PSJA model is used to describe the jet generation and recovery process. The deposited energy of PSJA is obtained from the multichannel discharge model. The multichannel discharge model has been described in reference [23].

2.1. The PSJA Aerodynamic Model

As shown in Figure 1, the PSJA consists of four main parts: Throat, chamber, shell, and electrodes. To simplify the PSJA aerodynamic model, the fluid region including the throat and chamber is treated as two control volumes. The pressure, temperature, and density are averaged over the control volume. Then, the conservation of mass, momentum, and energy equations are manipulated to describe the changes in density, jet velocity, pressure, and temperature in the control volume.
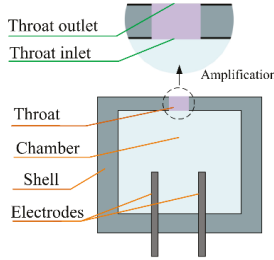
Figure 1. The structure of plasma synthetic jet actuator (PSJA).

To simplify these conservation equations, some assumptions are adopted in this model.

(1) The body forces are negligible. The body forces are contributed to by the gravity and electromagnetic force. Compressed with the pressure force, the body forces are so small that they are negligible in almost all simulations of PSJA in the literature [22,24,25].

(2) The gas velocity in the chamber is negligible, only the velocity of gas in the throat is taken into consideration. The velocity, temperature, density, and pressure across the throat outlet and throat inlet are uniform and represented by scalar values. As heating in the actuator chamber is assumed to be uniform, the error associated with this assumption is small.

(3) The gas is seen as inviscid. As the ratio of throat length to throat diameter is not large, the role of gas viscosity plays a less important role. If the throat was long and narrow, viscous forces would need to be considered.

2.2. The Conservation Equations

For inviscid flow, the integral form of the conservation equations is given as following:

$$\frac{\partial}{\partial t}\iiint_v \rho \, dv + \iint_s \rho \vec{u} \, d\vec{S} = 0 \tag{1}$$

$$\frac{\partial}{\partial t}\iiint_v \rho \vec{u} \, dv + \iint_s \left(\rho \vec{u} \, d\vec{S}\right)\vec{u} = -\iint_s P \, d\vec{S} + \iiint_v \rho \vec{f} \, dv \tag{2}$$

$$\frac{\partial}{\partial t}\iiint_v \rho\left(e+\frac{u^2}{2}\right)dv + \iint_s \rho\left(e+\frac{u^2}{2}\right)\vec{u} \, d\vec{S} = -\iint_s P\vec{u} \, d\vec{S} + \dot{Q} \tag{3}$$

For the chamber control volume, the gas velocity is negligible. These conservation equations are represented as the following:

$$\frac{d\rho_c}{dt} = -\frac{\rho_i u_i A_i}{V_c} \tag{4}$$

$$\frac{dT_c}{dt} = \frac{1}{\rho_c}\left(\frac{\dot{Q} - C_v T_i \rho_i u A_t - 0.5\rho_i u^3 A_t}{C_v V_c} - T_c\frac{d\rho_c}{dt}\right) \tag{5}$$

For the throat control volume, these conservation equations are represented as the following:

$$\frac{d\rho_t}{dt} = \frac{\rho_i u_i A_i - \rho_o u_o A_o}{V_t} \tag{6}$$

$$\frac{du}{dt} = \rho_t \left(\frac{P_i A_i - P_o A_o + \rho_i u^2{}_i A_i - \rho_o u^2{}_o A_o}{V_t} - u\frac{d\rho_t}{dt} \right) \tag{7}$$

$$\frac{dT_t}{dt} = \frac{1}{\rho_t} \left(\frac{(P_i - P_o)u A_t + ((C_v(T_i\rho_i - T_o\rho_o) + 0.5(\rho_i - \rho_o)u^2)u A_t) - V_t\left(2\rho_t u\frac{du}{dt} + u^2\frac{d\rho_t}{dt}\right)}{C_v V_t} - T_t\frac{d\rho_t}{dt} \right) \tag{8}$$

In the Equations (4)–(8), the subscripts c and t represent the averaged parameters over the chamber control volume and the throat control volume, respectively; the subscripts i and o represent the averaged parameters over the throat inlet control face and the throat outlet control face, respectively. The u indicates the averaged gas velocity over the throat control volume.

To solve these equations, these parameters including the pressure, density, and temperature over the throat inlet and outlet control face must be calculated. As shown in Figure 2, in a different working stage, the gas flow direction is the opposite. As a result, the way to calculate the parameters over the throat inlet and outlet control face is different.
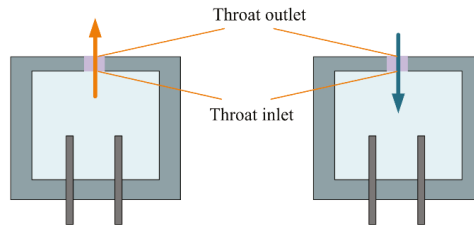

Figure 2. The schematic diagram of the two working stages of PSJA.

In jet stage, the gas flow from the chamber to the outside environment. At this time, the parameters over the throat inlet control face are determined by the gas state parameters in the chamber, and the parameters over the throat outlet control face are determined by the gas state parameters in the throat. Additionally, when the gas flows through the throat, the diameter of the pipeline decreases quickly, which induced the local pressure loss. In this model, the local pressure loss is considered using an engineering method, as shown in Equation (9).

$$P_{loss} = 0.5\rho u^2 * 0.5\left(1 - \frac{A_2}{A_1}\right) + \Delta p_{pl} \tag{9}$$

Taking these factors into consideration, the corresponding functions are presented as the following:

$$\begin{cases} \rho_i = \rho_c \varepsilon(\lambda) \\ P_i = P_c \pi(\lambda) - 0.5\rho_i u^2 0.5\left(1 - \frac{A_i}{A_c}\right) - \Delta p_{pl} \\ T_i = \frac{P_i}{R\rho_i} \\ \rho_o = \rho_t \\ P_o = P_\infty \\ T_o = \frac{P_o}{R\rho_o} \end{cases} \tag{10}$$

However, limiting by the throat geometry, the maximum gas velocity is the local sound speed. That means that the flow condition has two modes: To be chocked and to be unchocked. The criterion for judgment is as follows:

$$\begin{cases} P_i + 0.5\rho_i u^2 \geq 1.89 P_\infty \\ \gamma \geq 1 \end{cases} \tag{11}$$

If flow parameters meet this criterion, the flow is considered to be choked. The pressure at the throat outlet face is calculated as follows:

$$P_o = \frac{1}{1.89}\left(P_i + 0.5\rho_i u^2\right) \tag{12}$$

In recovery stage, the gas flows from the outside environment to the chamber. At this time, the parameters over the throat inlet control face are determined by the gas state parameters in the throat; the parameters over the throat outlet control face are determined by the gas state parameters in the external environment. The corresponding functions are presented as follows:

$$\begin{cases} \rho_i = \rho_t \\ P_i = P_c \\ T_i = \frac{P_i}{R\rho_i} \\ \rho_o = \rho_\infty \varepsilon(\lambda) \\ P_i = P_\infty \pi(\lambda) - 0.25\rho_o u^2 \\ T_i = \frac{P_o}{R\rho_o} \end{cases} \tag{13}$$

In the above functions, λ indicates the velocity coefficient, which is calculated by the following functions:

$$\begin{cases} a_{cr} = \sqrt{\frac{2\gamma}{\gamma+1}RT_t^*} \\ T_t^* = T_t + \frac{u^2}{2C_p} \\ \lambda = \frac{|u|}{a_{cr}} \end{cases} \tag{14}$$

$\varepsilon(\lambda)$ and $\pi(\lambda)$ are calculated as follows:

$$\begin{aligned} \varepsilon(\lambda) &= \left(1 - \frac{\gamma-1}{\gamma+1}\lambda^2\right)^{\frac{1}{\gamma-1}} \\ \pi(\lambda) &= \left(1 - \frac{\gamma-1}{\gamma+1}\lambda^2\right)^{\frac{\gamma}{\gamma-1}} \end{aligned} \tag{15}$$

2.3. The Thermal Modeling

In Equation (5), Q represents the discharge heating power and the thermal energy loss. The discharge heating power can be represented by Ohm heating easily. The thermal energy loss through the wall and the electrode is modeled based on the lumped capacitance method.

The heat transfer process in the PSJA is shown in Figure 3. Firstly, by forced convection, the heat transfers from the chamber gas to the shell inner wall. Secondly, by heat conduction through the electrodes and shell wall, the heat transfers from the shell inner wall to the shell outer wall. Thirdly, by natural convection, the heat transfers from the shell outer wall to the external air.

Similar to the electric circuit, the heat transfer process can be described as a thermal circuit, as shown in Figure 4. T_c, $T_{w,in}$, $T_{w,out}$, and T_∞ indicate the temperature of chamber gas, shell inner wall, shell outer wall, and external air, respectively. R_{in}, R_e, R_w, and R_{out} represent the thermal resistance of force convection, electrode conduction, shell conduction, and natural convection. C_w represents the thermal capacitance of the shell.
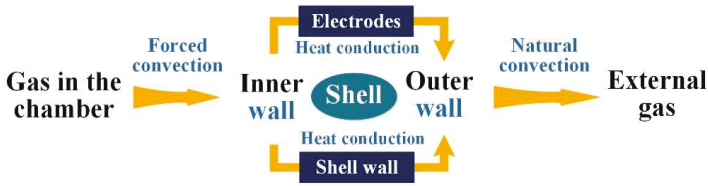
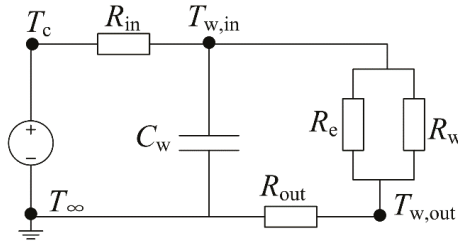**Figure 3.** The schematic diagram of the heat transfer process.

Figure 4. Electrical representation of the thermal heat transfer process.

Based on the theory of engineering thermal transmission, the thermal resistance of force convection, electrode conduction, and natural convection is given as follows.

$$
\begin{cases}
R_{in} = \dfrac{1}{h_{in} A_{c,in}} \\[2mm]
R_{out} = \dfrac{1}{h_{out} A_{c,out}} \\[2mm]
R_e = \dfrac{0.5 l_e}{\kappa_e A_e}
\end{cases}
\tag{16}
$$

The structure of the shell wall is complex, and is regarded as a combination of three simple structures, as shown in Figure 5. The upper structure of the shell is seen as a single wall. The middle structure of the shell is seen as a single hollow cylinder wall. The subjacent structure of the shell is also seen as a single wall. The thermal resistance of the three structures is given as follows.

$$
\begin{cases}
R_{up} = \dfrac{h_3}{\kappa_{up} \dfrac{\pi}{4}(d_1^2 - d_3^2)} \\[4mm]
R_{out} = R_{mid} = \dfrac{\ln \dfrac{d_2}{d_1}}{2\pi \kappa_{mid} h_1} \\[4mm]
R_{sub} = \dfrac{h_2}{\kappa_{sub} \dfrac{\pi}{4} d_1^2}
\end{cases}
\tag{17}
$$

The total thermal resistance of the shell wall is calculated as Equation (18).

$$
R_w = \frac{1}{1/R_{up} + 1/R_{mid} + 1/R_{sub}}
\tag{18}
$$

With all of the circuit components defined, the differential function obtained from the circuit shown in Figure 4 is used to solve for the wall temperature.

$$
\frac{dT_{w,in}}{dt} = \frac{1}{C_w}\left(\frac{T_c - T_{w,in}}{R_{in}} - \frac{T_{w,in} - T_\infty}{R_{out} + R_e R_w/(R_e + R_w)} \right)
\tag{19}
$$

Hence, combined with the discharge heating source, the parameter Q in Equation (10) is given.

$$\dot{Q} = Q_{\text{arc}} - \frac{T_c - T_{w,\text{in}}}{R_{\text{in}}} = 0.5I(t)^2 R(t) - \frac{T_c - T_{w,\text{in}}}{R_{\text{in}}} \tag{20}$$

It must be pointed out that the energy calculated directly using Ohm heating theory is not the heating energy. The sheath energy loss and radiation energy loss must be taken into consideration. Based on the analysis of Guillaume Dufour [19], a heating efficiency of 50% is adopted.
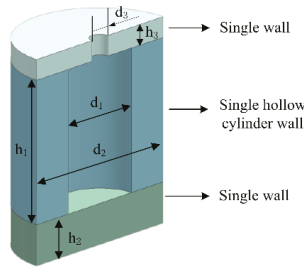
Figure 5. The disassembly structure of the shell wall.

2.4. Model Validation

To validate the model's reliability and accuracy, simulation results with ANSYS CFX software are compared with the results calculated from the PSJA aerodynamic model. The computation mesh created by ANSYS ICEM is fully structured, and the boundary type is labeled in Figure 6. The actuator geometry parameters are shown in Figure 7.
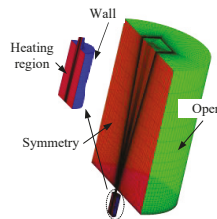
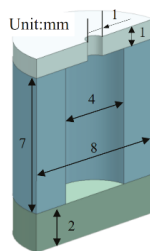

Figure 6. Computation grid.

Figure 7. The geometry parameters of actuator.

The solver is coupled and fully implicit with 2nd order accuracy in both time and space. A variable time step is used, which begins with 5 ns and is increased gradually to 1 µs in the

simulation. Considering the high turbulent vortex produced by PSJA, the SST turbulent model is chosen. The heating power is coupled into the Navier-Stokes equations as a heat source and expressed by a CFX expression. As the purpose of this step is only to validate the PSJA model, the discharge heating source is simplified as a constant value, as shown in Equation (21). Q_h is the total heating energy; 0.005 J is adopted. T is the heating time; 100 ns is chosen. V is the volume of the chamber; approximately $88e^{-9}$ m^{-3}. Additionally, it is assumed the actuator is uniformly heated in this simulation.

$$\dot{Q} = \begin{cases} \dfrac{Q_h}{TV} \text{ Wm}^{-3} \ t \leq T \\ 0 \text{ Wm}^{-3} \ t \geq T \end{cases} \tag{21}$$

The jet velocity at the throat outlet calculated by the ANSYS CFX and PSJA aerodynamic model is shown in Figure 8a. The results obtained from the CFX with different grid number agree well. Therefore, the grid convergence has been reached in CFX. Moreover, the small difference in the results using different turbulent models suggests that the results are not sensitive to the turbulent model. The value obtained by ANSYS CFX is 141 m/s, and the value obtained by the PSJA model is 143 m/s. The difference is only 2 m/s. The disparity of jet termination time is also little, less than 3%. The value obtained by ANSYS CFX is 269 μs, and the value obtained by the PSJA model is 275 μs. The history of gauge pressure in the chamber obtained by the two methods is also similar, as shown in Figure 8b. Overall, the PSJA model can simulate the actuator characteristic with great accuracy.
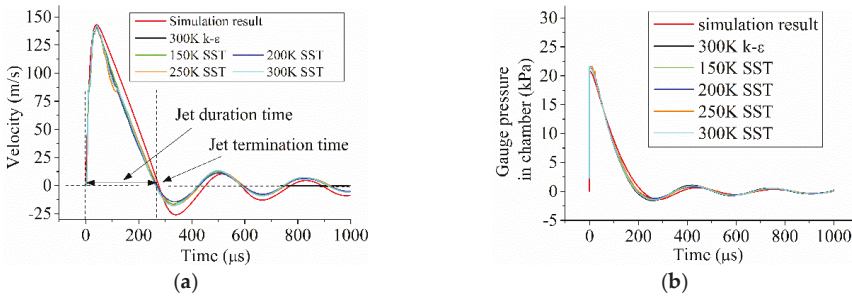

Figure 8. The comparison between the CFD results and model results. (**a**) is the jet velocity at the throat outlet and (**b**) is the gauge pressure in the chamber.

3. Results and Discussion

3.1. The Discharge Energy and Discharge Efficiency

Based on the multichannel discharge technique, the discharge channel number can be increased greatly. When the energy stored in the discharge capacitor is fixed, the energy deposited in each channel varies with the discharge channel number. As energy is a critical factor determining the performance of the PSJA, the energy characteristic is first investigated.

The discharge capacitor is set as 10 nF, and the initial voltage is set as 6 kV. The discharge voltage of each electrode couple is set as 4 kV. The inductance is 1.65 μH. The sum of wire resistance and the equivalent serial resistance of the capacitor are chosen as 1.89 Ω. The discharge voltage and current waveforms with channel numbers of 1, 5, 10, and 20 are simulated. Based on the current and resistance of each discharge channel, the discharge power and discharge energy can be obtained.

The discharge voltage and current waveforms with different actuator numbers are plotted in Figure 9. As described in [16], the breakdown of each electrode couple happens in sequence, the time to form a complete discharge channel increases with the growth of the actuator number. What's more, with the increase in the actuator number, the total length of the discharge channel is enlarged, leading

to the growth of plasma resistance. As a result, the discharge current decreases. The deposited energy in each actuator ought to decrease.
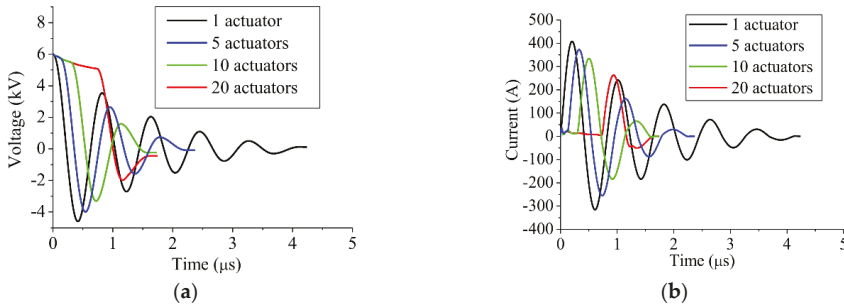

Figure 9. The discharge waveforms with different actuator numbers. (**a**) shows the the voltage waveforms and (**b**) shows the current waveforms.

The energy deposition power and the discharge energy in the first PSJA are obtained from the simulation results, as shown in Figure 10. The energy deposition power ($P_{\text{deposition}}$), and discharge energy ($Q_{\text{discharge}}$) are defined in Equation (22). With the increase in the actuator number, the energy deposition power decreases. However, as shown in Figure 10b, the deposited energy doesn't decrease linearly. Since the gap distance between electrodes in all actuators is the same, and the actuator works in series, the resistance of the plasma channel in each actuator can be considered as the same. The discharge energy in each actuator can be expressed as Equation (23), where Q is the energy stored in the capacitor, R_{arc} indicates the resistance of plasma channel, n is the actuator number, and R_0 is the external resistance in the discharge circuit. Therefore, if the actuator number increases, the deposited energy in one actuator doesn't decrease linearly. When the actuator number increases from 1 to 20, the deposited energy in the first actuator decreases 76.7% instead of 95%. In this way, the total energy deposited in all actuators increases, as shown in Figure 11. This means more energy stored in the capacitor is released in the discharge channel, leading to the improvement of discharge efficiency η_{d}, which is defined in Equation (24).

$$Q_{\text{dishcarge}} = \int P_{\text{deposition}}(t)dt = \int I^2(t)/g(t)dt \tag{22}$$

$$Q_{\text{discharge}} = Q\frac{R_{\text{arc}}}{nR_{\text{arc}} + R_0} = \frac{Q}{n + R_0/R_{\text{arc}}} \tag{23}$$

$$\eta_{\text{d}} = \frac{\sum\limits_{k=1}^{k=n} Q_{\text{discharge},k}}{Q} = \frac{\sum\limits_{k=1}^{k=n} \int I^2(t)/g_k(t)dt}{Q} \tag{24}$$

Figure 12 shows the deposited energy in each actuator with different actuator numbers. This figure shows that in this multichannel discharge mode, the deposited energy in a different actuator is almost the same. The coefficient of variation with 5, 10, and 20 actuators is 3.8%, 3.32%, and 4.77%, respectively. Based on the previous research [18], the breakdown of the electrode couple in each actuator happens in sequence. Coupled with the results shown in Figure 12, it concludes that although the time when the breakdown of the electrode couple in each actuator happens is different, the deposited energy is the same. The breakdown order has little influence on the deposited energy.
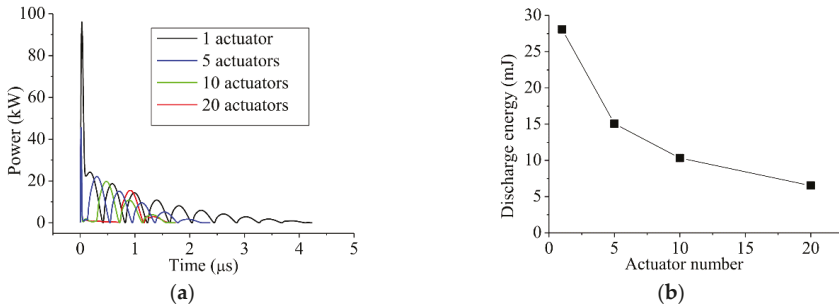
Figure 10. The discharge characteristics with different actuator numbers. (**a**) is the energy deposition power and (**b**) is the discharge energy in one actuator.
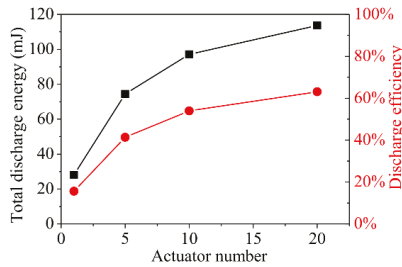

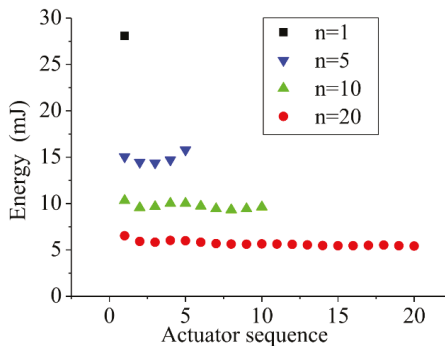**Figure 11.** The total discharge energy and discharge efficiency versus actuator number.

Figure 12. The deposited energy in each actuator versus actuator number.

3.2. The Characteristics of a Composition of PSJA Array

As shown in Figure 12, with the increase in the actuator number, the energy deposited in a single actuator decreases. As a result, the performance of the actuator ought to slow down. The history of jet velocity and gas density at the throat outlet is shown in Figure 13a,b, respectively. Obviously, the jet velocity and duration decreases with the increase in the actuator number. However, the gas density at the throat outlet increases with the increase of actuator number. As the gas kinetic energy is proportional to the gas density, the growth of gas density benefits the gas kinetic energy.
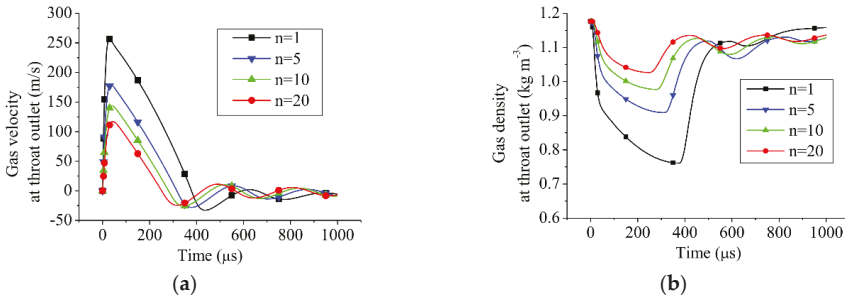
Figure 13. The history of gas velocity and gas density at the throat outlet versus actuator number. (**a**) is the gas velocity and (**b**) is the gas density.

The jet peak velocity, duration time, and mass ejected with different numbers of PSJA are calculated and results are as shown in Figure 14a. The peak velocity is defined as the maximum velocity at the throat outlet. The definition of the jet duration time can be found in Figure 8a. The mass ejected means the total mass of gas left in the PSJA chamber throughout the ejection process. These parameters decrease with the increase in the actuator number, but the rate at which they decline slows. These parameters are normalized by dividing the value with that of only one actuator, as shown in Figure 14b. This figure shows that the mass ejected is greatly influenced by the actuator. The influence of actuator number on jet duration time is weakest compared with the other two parameters. When the actuator increases to 20, the jet duration time decreases by 33%, while the peak velocity and mass ejected decrease by 54% and 62%, respectively.
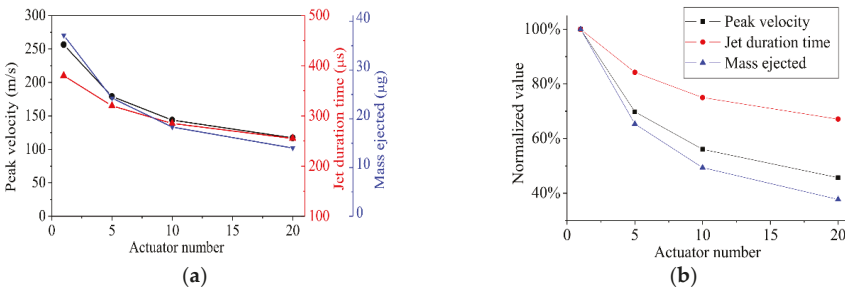

Figure 14. The gas parameters versus actuator number. (**a**) is the real value and (**b**) is the normalized value.

The jet kinetic energy can be calculated as shown in Equation (25), where $\rho_o(t)$ and $u(t)$ are the jet density and velocity at the throat outlet face; A_t indicates the throat outlet area; T_{jet} represents the jet duration time. The variation of jet kinetic energy of a single actuator with actuator numbers is shown in Figure 15. As it is proportional to the third power of the velocity, the kinetic energy decreases quickly with the increase in the actuator number. When the actuator number increases to 20, the jet kinetic energy decreases by 92%.

$$E_{\text{kinetic}} = \int_0^{T_{\text{jet}}} 0.5\rho_o(t)u^3(t)A_t dt \tag{25}$$
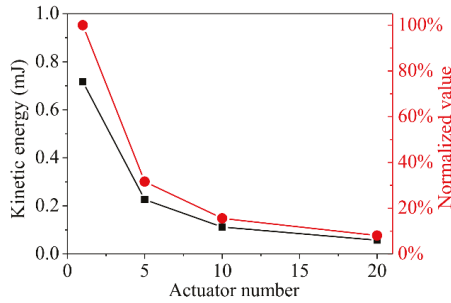
Figure 15. The gas kinetic energy versus actuator number.

3.3. The Energy Characteristics of PSJA Array

The total kinetic energy of all actuators is calculated using Equation (26), which varies with the actuator number, as shown in Figure 16. In Equation (26), k is the concrete actuator; and n is the number of PSJA actuators in the PSJA array. Firstly, the total kinetic energy increases with the number of actuators. Then it begins to decrease, suggesting that the maximum total kinetic energy is not necessarily produced by the array containing more PSJAs and an optimal number of PSJAs exists. The characteristic of total kinetic energy is different from that of the total discharge energy, as shown in Figure 11, which will be investigated below.

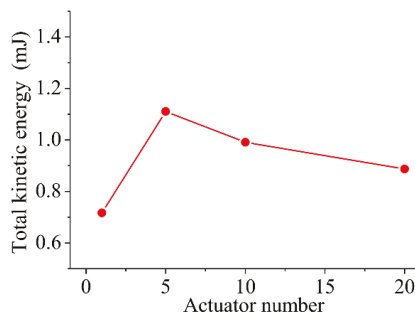$$E_{\text{total}} = \sum_{k=1}^{n} E_{\text{kinetic},k} \tag{26}$$

Figure 16. The total gas kinetic energy versus actuator number.

In the whole working process of the actuator, the energy stored in the capacitor transforms to the kinetic energy indirectly, as shown in Figure 17. The thermodynamic recycle efficiency η_t is defined in Equation (27) follows. The variation of η_t with different actuator number is shown in Figure 18. As the actuator number increases, the energy deposited in an actuator decreases. Based on the research results of Zong et al. [26], the thermodynamic efficiency decreases with the decrease of heating energy. With the increase of actuator number, the heating energy decreases. Therefore, the thermodynamic efficiency decreases when there are more PSJAs. As a result, the total gas kinetic energy doesn't always increase with an increase of actuator number.

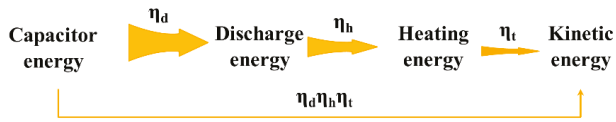$$\eta_t = \frac{E_{\text{total}}}{Q_h} \varnothing \tag{27}$$

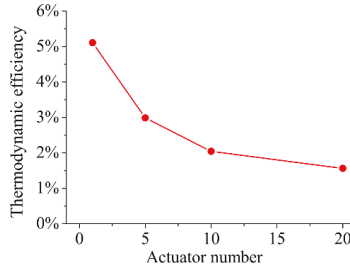**Figure 17.** The total gas kinetic energy versus actuator number.

Figure 18. The thermodynamic efficiency versus actuator number.

3.4. The Influence of Extra Resistance

It is observed that the total extra resistance, including the wire resistance and the equivalent serial resistance of the discharge capacitor, affects the performance of the PSJA array greatly. In this part, these factors are studied. The extra resistance is set as 0.1 Ω and 10 Ω in case 1 and case 2 respectively.

The total discharge energy and discharge efficiency versus actuator number with different extra resistance are shown in Figure 19. In case 1, the extra resistance is only 0.1 Ω, and the discharge efficiency of one actuator is 72%. In contrast, the discharge efficiency of one actuator in case 2 (larger extra resistance) is as low as 5%. With the increase in the actuator number, the discharge efficiency in the two cases increases. However, the increased levels are different. When the actuator number increases to 20, the discharge efficiency in case 1 increases to 94%, which is 30% larger than the initial discharge efficiency (72%). But in case 2, the discharge efficiency increases to 38%, which is almost six times larger than the initial discharge efficiency (5%).
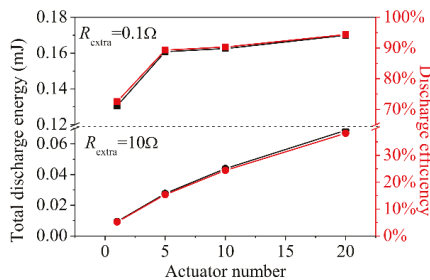

Figure 19. The total discharge energy and efficiency versus actuator number with different extra resistance.

The variation of total gas kinetic energy with actuator number under different extra resistance is shown in Figure 20. The revealed trends are completely different when different extra resistance is used. In case 1, the total gas kinetic energy decreases with the increase in the actuator number. However, in case 2, the opposite trend happens. Instead of decreasing, the total kinetic energy increases

when more actuators are used. In case 2, the total gas kinetic energy with 20 actuators is nearly four times of that with one actuator.
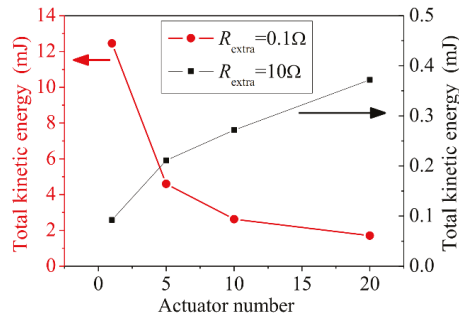

Figure 20. The total gas kinetic energy versus actuator number with different extra resistance.

The reason for the distinctive variations revealed in Figure 20 is given as follows. The discharge efficiency increases with actuator number, but the thermodynamic efficiency decreases, while the variation speed is different. The discharge efficiency and thermodynamics efficiency with different actuator numbers are normalized by that with only one actuator, as shown in Figure 21. The larger the extra resistance is, the larger the increase in the discharge efficiency is, and the smaller the decrease in the thermodynamic efficiency is. As a result, with a large extra resistance, the total efficiency grows with the increase in the actuator number. However, with a small extra resistance, the total efficiency decreases with the increase in the actuator number.
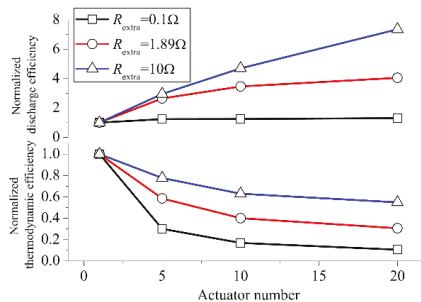

Figure 21. The normalized discharge efficiency and normalized thermodynamic efficiency versus actuator number with different extra resistance.

In conclusion, when the extra resistance is large, the energy efficiency of the PSJA array is higher than that of conventional PSJA. Actually, in the practical application, the extra resistance is relatively large. In the experiment on control of the shock boundary layer interaction using PSJA by Greene et al. [27], a resistance (max 1.5 kΩ) is adopted in the discharge circuit. In the experiment of Narayanaswamy et al. [26,28,29], a ballast resistance is also adopted in the discharge circuit. In the experiment of Jichul Shin [30,31], a ballast resistance (max several kilo Ohm) is adopted in the discharge circuit as well. Therefore, there is reason to believe the PSJA array driven by the multichannel discharge technology can play an important role in the practical flow control application.

4. Conclusions

In this paper, based on the electronic theory, the conservation equations of mass, momentum, energy, and the lumped capacitance method, the multichannel discharge model, and plasma synthesis jet actuator model are put forward. Coupled with the two models, an analytical model to simulate the characteristics of the PSJA array is developed. Based on this model, the influence of actuator number in the PSJA array is investigated. The main conclusions are as follows.

With the increase in the actuator number, the discharge energy in a single actuator decreases. As a result, the jet strength induced by a single actuator decreases. When the actuator number increases from 1 to 20, the weakening extent of mass ejected, peak jet velocity, and jet duration time is 62%, 54%, and 33%, respectively. Therefore, the influence of the actuator number on the jet duration time is the weakest.

As the actuator increases, the discharge efficiency and thermodynamic efficiency show different tendencies. The discharge efficiency increases, while the thermodynamic efficiency decreases. As a result, the total energy efficiency doesn't always increase with the increase in the actuator number. However, in practical application, the extra resistance in the discharge circuit is large (to the order of kilo Ohms), and the discharge efficiency of one channel discharge is low. Therefore, it can be concluded that the PSJA array is more suitable to the practical application.

Author Contributions: Formal analysis, H.S.; Investigation, S.Z.; Supervision, Z.Z. and S.H.; Validation, W.Y. and L.Y.

Conflicts of Interest: The authors declare no conflicts of interest.

References

1. Corke, T.C.; Post, M.L.; Orlov, D.M. Single dielectric barrier discharge plasma enhanced aerodynamics: physics, modeling and applications. *Exp. Fluids* **2008**, *46*, 1–26. [CrossRef]
2. Little, J.; Samimy, M. High-lift airfoil separation with dielectric barrier discharge plasma actuation. *AIAA J.* **2010**, *48*, 2884–2898. [CrossRef]
3. Saddoughi, S.; Bennett, G.; Boespflug, M.; Puterbaugh, S.L.; Wadia, A.R. Experimental investigation of tip clearance flow in a transonic compressor with and without plasma actuators. *J. Turbomach.* **2014**, *137*, 041008. [CrossRef]
4. Jothiprasad, G.; Murray, R.C.; Essenhigh, K.; Bennett, G.A.; Saddoughi, S.; Wadia, A.; Breeze-Stringfellow, A. Control of tip-clearance flow in a low speed axial compressor rotor with plasma actuation. *J. Turbomach.* **2012**, *134*, 021019. [CrossRef]
5. Webb, N.; Clifford, C.; Samimy, M. Control of oblique shock wave/boundary layer interactions using plasma actuators. *Exp. Fluids* **2013**, *54*, 1545. [CrossRef]
6. Narayanaswamy, V.; Raja, L.L.; Clemens, N.T. Control of unsteadiness of a shock wave/turbulent boundary layer interaction by using a pulsed-plasma-jet actuator. *Phys. Fluids* **2012**, *24*, 076101. [CrossRef]
7. Santhanakrishnan, A.; Jacob, J. Characterization of linear plasma synthetic jet actuators. In Proceedings of the 46th AIAA Aerospace Sciences Meeting and Exhibit, Reno, NV, USA, 7–10 January 2008.
8. Santhanakrishnan, A.; Reasor, D.A.; LeBeau, R.P. Characterization of linear plasma synthetic jet actuators in an initially quiescent medium. *Phys. Fluids* **2009**, *21*, 043602. [CrossRef]
9. Santhanakrishnan, A.; Jacob, J. Effect of plasma morphology on flow control using plasma synthetic jet actuators. In Proceedings of the 45th AIAA Aerospace Sciences Meeting and Exhibit, Reno, NV, USA, 8–11 January 2007.
10. Cybyk, B.; Wilkerson, J.; Simon, D. Enabling high-fidelity modeling of a high-speed flow control actuator array. In Proceedings of the 14th AIAA/AHI Space Planes and Hypersonic Systems and Technologies Conference, Canberra, Australia, 6–9 November 2006.

11. Caruana, D.; BARRICAU, P.; Hardy, P. The "Plasma Synthetic Jet" Actuator. Aero-thermodynamic characterization and first flow control applications. In Proceedings of the 47th AIAA Aerospace Sciences Meeting including The New Horizons Forum and Aerospace Exposition, Orlando, FL, USA, 5–8 January 2009.

12. Caruana, D.; Barricau, P.; Gleyzes, C. Separation control with plasma synthetic jet actuators. *Int. J. Aerodyn.* **2013**, *3*, 71. [CrossRef]

13. Caruana, D.; Rogier, F.; Dufour, G.; Gleyzes, C. The plasma synthetic jet actuator, physics, modeling and flow control application on separation. *AerospaceLab* **2013**, 1–13.

14. Raizer, Y.P. *Gas Discharge Physics*; Springer: Berlin, Germany, 1991; pp. 1–449.

15. Schavemaker, P.H.; Van der Slui, L. An improved mayr-type arc model based on current-zero measurements [circuit breakers]. *IEEE Trans. Power Delivery* **2000**, *15*, 580–584. [CrossRef]

16. Samimy, M.; Bridges, J. Flow and noise control in high speed and high reynolds number jets using plasma actuators. In Proceedings of the 3rd AIAA Flow Control Conference, San Francisco, CA, USA, 5–8 June 2006.

17. Zhang, Z.; Wu, Y.; Jia, M.; Song, H.; Sun, Z.; Zong, H.; Li, Y. The multichannel discharge plasma synthetic jet actuator. *Sens. Actuators A Phys.* **2017**, *253*, 112–117. [CrossRef]

18. Zhang, Z.; Wu, Y.; Jia, M.; Song, H.; Sun, Z.; Li, Y. Mhd-rlc discharge model and the efficiency characteristics of plasma synthetic jet actuator. *Sens. Actuators A* **2017**, *261*, 75–84. [CrossRef]

19. Huang, S.; Wu, Y.; Song, H.; Zhu, J.; Zhang, Z.; Song, X.; Li, Y. Experimental investigation of multichannel plasma igniter in a supersonic model combustor. *Exp. Therm Fluid Sci.* **2018**, *99*, 315–323. [CrossRef]

20. Grossman, K.R.; Cybyk, B.Z.; VanWie, D.M. Sparkjet actuators for flow control. In Proceedings of the 41st Aerospace Sciences Meeting and Exhibit, Reno, NV, USA, 6–9 January 2003.

21. Haack, S.; Taylor, T.; Emhoff, J.; Cybyk, B. Development of an analytical sparkjet model. In Proceedings of the 5th Flow Control Conference, Chicago, IL, USA, 28 June–1 July 2010.

22. Zong, H.; Wu, Y.; Li, Y.; Song, H.; Zhang, Z.; Jia, M. Analytic model and frequency characteristics of plasma synthetic jet actuator. *Phys. Fluids* **2015**, *27*, 027105. [CrossRef]

23. Zhang, Z.; Wu, Y.; Jia, M.; Song, H.; Sun, Z.Z.; Li, Y.H. Modeling and optimization of the multichannel spark discharge. *Chin. Phys. B* **2017**, *26*, 244–253. [CrossRef]

24. Shin, J. Characteristics of high speed electro-thermal jet activated by pulsed dc discharge. *Chin. J. Aeronaut.* **2010**, *23*, 518–522. [CrossRef]

25. Sary, G.; Dufour, G.; Rogier, F.; Kourtzanidis, K. Modeling and parametric study of a plasma synthetic jet for flow control. *AIAA J.* **2014**, *52*, 1591–1603. [CrossRef]

26. Zong, H.; Wu, Y.; Song, H.; Jia, M. Efficiency characteristic of plasma synthetic jet actuator driven by pulsed direct-current discharge. *AIAA J.* **2016**, *54*, 3409–3420. [CrossRef]

27. Martin, T.H. An empirical formula for gas switch breakdown delay. In Proceedings of the 7th Pulsed Power Conference, Monterey, CA, USA, 11–14 June 1989.

28. Dufour, G.; Hardy, P.; Quint, G.; Rogier, F. Physics and models for plasma synthetic jets. *Int. J. Aerodyn.* **2013**, *3*, 47. [CrossRef]

29. Greene, B.; Clemens, N.; Micka, D. Control of shock boundary layer interaction using pulsed plasma jets. In Proceedings of the 51st AIAA Aerospace Sciences Meeting including the New Horizons Forum and Aerospace Exposition, Grapevine, TX, USA, 7–10 January 2013.

30. Narayanaswamy, V.; Raja, L.L.; Clemens, N.T. Control of a shock/boundary-layer interaction by using a pulsed-plasma jet actuator. *AIAA J.* **2012**, *50*, 246–249. [CrossRef]

31. Narayanaswamy, V.; Clemens, N.; Raja, L. Investigation of a pulsed-plasma jet for shock/boundary layer cntrol. In Proceedings of the 48th AIAA Aerospace Sciences Meeting Including the New Horizons Forum and Aerospace Exposition, Orlando, FL, USA, 4–7 January 2010.

Multibody Simulation for the Vibration Analysis of a Turbocharged Diesel Engine

Enrico Armentani [1,*], Francesco Caputo [2], Luca Esposito [3], Venanzio Giannella [4] and Roberto Citarella [4]

1 Department of Chemical, Materials and Production Engineering, University of Naples Federico II, P.le V. Tecchio, 80, 80125 Napoli, Italy
2 Department of Engineering, University of Campania "Luigi Vanvitelli", Via Roma, 29, 81031 Aversa (CE), Italy; francesco.caputo@unicampania.it
3 Department of Industrial Engineering, University of Naples Federico II, P.le V. Tecchio, 80, 80125 Napoli, Italy; luca.esposito2@unina.it
4 Department of Industrial Engineering, University of Salerno, Via Giovanni Paolo II, 132, 84084 Fisciano (SA), Italy; vgiannella@unisa.it (V.G.); rcitarella@unisa.it (R.C.)
* Correspondence: enrico.armentani@unina.it; Tel.: +39-081-768-2450

Abstract: In this paper, a multibody calculation methodology has been applied to the vibration analysis of a 4-cylinder, 4-stroke, turbocharged diesel engine, with a simulation driven study of the angular speed variation of a crankshaft under consideration of different modeling assumptions. Moreover, time dependent simulation results, evaluated at the engine supports, are condensed to a vibration index and compared with experimental results, obtaining satisfactory outcomes. The modal analysis also considers the damping aspects and has been conducted using a multibody model created with the software AVL/EXCITE. The influence of crankshaft torsional frequencies on the rotational speed behavior has been evaluated in order to reduce the vibration phenomena. The focus of this work is related to industrial aspects since, for an existing and commercialized engine, a numerical and experimental complex study has been performed to enable design improvements aimed at reducing noise and vibrations. Existing procedures and algorithms are combined here to reach the abovementioned objectives in the most efficient way.

Keywords: vibration analysis; FEM; multibody simulations

1. Introduction

Structural and acoustic modeling methods [1], used to predict the vibroacoustics and aeroacoustics performance of aerospace [2] and automotive systems, have become a key tool in the design process.

Car engine dynamics are explored especially in the low frequency range and at low engine speeds, where the direct vibration transmission by the engine mounts is a critical excitation mechanism, but raising the maximum analyzed frequency constitutes an important industrial challenge for automotive and aerospace industry.

There are several examples in the literature describing a combination of multi-body simulation, including flexible FE subsystems, to perform dynamics and acoustic simulation of mechanical components.

In [3], a multibody model of a valve train system for a car engine was developed in order to analyze its resonant vibrational behavior. The dynamics of the valve train system were analyzed, applying a ramp to the crankshaft with a variable engine speed and considering the motion unsmoothness deriving from the inertia and combustion pressure loads.

In [4] the development of a numerical model to predict the noise radiating from manual gearboxes due to gear rattle is provided. The measured data are used to identify and reproduce the input excitation that is primarily generated from engine combustion forces. The dynamic interaction of the gearbox components, including flywheel, input/output shafts, contacting gear-pairs, bearings, and flexible housing is modeled using flexible multibody techniques. The acoustic response to the vibration of the gearbox housing is then predicted using vibroacoustic techniques.

In [5,6] the numerical modeling of noise radiated by an engine and by a car body, respectively, using the so-called Acoustic Transfer Vectors and Modal Acoustic Transfer Vectors concepts is presented. The dynamics of the engine are described using a finite element model loaded with an RPM-dependent excitation.

In [7], a technique to compute the noise radiated by a large truck engine is presented: the vibration is computed using a commercial FEM code, whose results are subsequently used in an acoustic radiation computation.

In [8], a vibroacoustic numerical and experimental analysis was carried out for the chain cover of a low powered four-cylinder four-stroke diesel engine. A Boundary Element (BE) model of the chain cover was realized to determine the chain cover noise emission, starting from the previously calculated structural vibrations. The numerical vibroacoustic outcomes were compared with those observed experimentally, obtaining a good correlation.

In [9,10], a novel and effective mathematical model and advanced analytical approaches to achieve a more accurate prediction of the spiral bevel gear dynamic response were developed to investigate the underlying physics affecting gear mesh and gear dynamic response generation and transmissibility.

In [11], an in-depth investigation of the dynamical load sharing behaviors of a four-planetary gear system with multi-floating components was provided.

In [12], the impact of coupling engine structure with rotating components on the engine noise and vibrations across all rpm and frequency range is illustrated.

The need for accurate models forms a major obstacle to the implementation of cylinder balancing methods for engines with a high number of cylinders [13]. This is due to closely spaced cylinder firings and the fact that the crankshaft dynamics cannot be ignored, partly due to the increased length of the crankshaft, and partly because analysis of higher frequency components is required to obtain sufficient information for balancing the cylinder-wise torque contributions. This deformation can assume significant values depending on the engine-load configuration (load change, crankshaft stiffness, kind of aspiration of the engine), and as such it is of great importance for safe engine operation.

In [14], an experimentally validated diesel engine simulation code is used to study and evaluate the importance of a notable engine dynamic issue, i.e., the crankshaft torsional (angular) deformations during turbocharged diesel engine operation, owing to the difference between instantaneous engine and load (resistance) torques. The analysis aims ultimately in studying the phenomena under the very demanding, and often critical, transient operating conditions. Details are provided concerning the underlying mechanism of the crankshaft torsional deformations during steady state and transient operation.

In [15], a methodology for predicting the piston to liner contact in running engines by means of MBD (Multi-Body Dynamics) and FEM is presented. In addition to the mathematical modeling of the excitation, the paper describes the transfer mechanisms of the piston slap phenomenon. Thus, the model is extended in order to analyze vibration transfer via engine structure. Results of simulation work show structure surface velocity levels and their contribution to integral levels in different frequency bands.

In [16], the mathematical modeling of body structures and the calculation of the non-linear connecting forces resulting from elastohydrodynamic contacts between piston-liner and shaft-bearing is described. Results of parametric studies, e.g., the influence of piston surface profile on the contact mechanism between piston and liner, are shown. In [17], the coupling of elastic multibody simulations (including elastohydrodynamic interactions) with finite element based vibration and acoustic analysis

is presented. In [18], the emphasis is on the integration of the kinetic reactions arising from the tribological conjunction of the dynamics of engine subsystems, piston, and crankshaft.

In [19], the CAE capabilities in the simulation of the dynamic and acoustic behavior of an engine, with a focus on the relative merits of modification and full-scale structural/acoustic optimization of engine, are presented.

In [20], an investigation of the diesel engine combustion-related fault detection capability of crankshaft torsional vibrations is presented: the torsional vibration amplitudes are used to superimpose the mass and gas torque; further mass and gas torque analysis is used to detect fault in the operating engine. The engine dynamics are analyzed with a focus on the low frequency range and low engine speeds, when vibration transmission through engine mounts becomes critical.

In [21,22], a detailed multi-body numerical model of an engine prototype is used to characterize the whole engine dynamic behavior in terms of forces and velocities. A combined usage of FEM and multi body methodologies is adopted for the dynamic analysis: both crankshaft and cylinder block are considered as flexible bodies, whereas all the other components are considered as rigid elements.

The focus of this work is related to industrial aspects because, for an existing and commercialized engine, a numerical and experimental complex study has been performed to enable design improvements aimed at reducing noise emission and vibrations. Existing procedures and algorithms are combined here to reach the abovementioned objectives in the most efficient way.

2. Problem Description and Modeling Approach

The analyzed problem concerns a numerical study of the vibrations of an in-line 4-cylinder, 4-strokes, internal combustion turbocharged diesel engine, to be used as a first step for future vibroacoustic analyses. Instead of a complex numerical analysis of the system through a direct FEM, which could involve prohibitive number of degrees of freedom, the authors present a modeling approach exhibiting a gradually increasing complexity. Starting from rigid body analysis and introducing progressively the elastic behavior of the various subsystems, using then a modal FEM analysis, the impact on accuracy of such modeling refinements comes out. The originality of the overall approach is related to the combination of various numerical approaches with an experimental analysis, for a very complex system.

The analyses are focused on the 2nd, 4th, 6th, and 8th order of motion irregularities that are analyzed at the flywheel and pulley. In addition, the time-dependent simulation results at the engine support brackets (engine bracket, gearbox bracket and differential bracket) are evaluated, condensed to a vibration index and finally compared with the experimental results.

A Multi-Body Dynamic Simulation (MBDS) of the crank train was used to characterize its dynamic behavior, starting from engine geometrical data and the available combustion loads, with both mechanical and combustion forces acting simultaneously on the crankshaft.

In order to examine the vibration behavior of the considered internal combustion engine, the behavior of the crankshaft was specifically analyzed with a focus on its torsional vibrations, namely calculating the motion irregularities of the crankshaft itself.

For the issue at hand, the modeled components were: crankshaft, pistons, connecting rods, main and connecting rod bearings, engine mounts (also named "support brackets"), contact stiffness between piston and cylinder.

The first realized model assumed rigid bodies, allowing assessing the course of the motion irregularities of the crankshaft at low frequencies. With a maximum regime for the engine established at 4500 rpm, we considered 0–300 Hz a low frequency range: component resonances in this range can be activated by the 2nd and 4th engine order. The considered mid-frequency range was 300–700 Hz: resonances in this range can mainly be activated by the 6th and 8th engine order. High frequencies, higher than 700 Hz, can only be activated by aeroacoustics phenomena.

The next step was the introduction of a crankshaft flexible model, leveraging on a FEM approach, in order to evaluate more accurately its dynamic behavior at higher frequencies. The frequency range of

interest was anyway limited to the low-medium frequencies because the whole engine was modeled as rigid with the only exception of the crankshaft. Focusing on the low-medium frequency range, it was reasonable to assume a negligible influence from the modal behavior of other components than the crankshaft.

Subsequently, the crankshaft FE model was further refined taking into consideration the presence of another component, the clutch: this allowed obtaining more accurate support brackets vibrations.

Finally, a numerical-experimental correlation for the validation of the numerical model was carried out.

Hypermesh and Abaqus [23] codes were respectively used for the FE modeling and modal analysis, whereas the realization of the multibody (MB) model and the forced vibrations analysis was demanded to AVL/Excite code [24].

The MB code considered the behavior of individual bodies as linear elastic; such bodies can be subject to both large rigid body motions and small deformations.

The applied external forces come from the pressure cycle of the combustion gases [25]: from Figure 1 it is possible to appreciate the cycle variations at different regimes. All the forces of an inertial nature are calculated internally by the code according to the actual speeds and accelerations of the bodies. Calculations performed for each operating regime and in the time domain provided the displacement, speed, and acceleration time histories of all the points of the system.
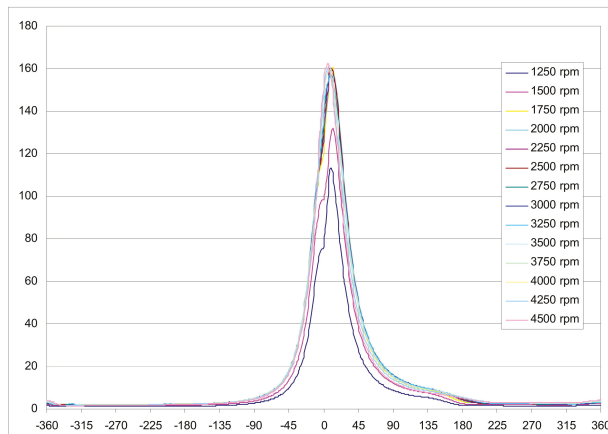

Figure 1. Experimental pressure cycles at different regimes for the engine under analysis.

2.1. System Dynamic Reduction

The adopted flexible MB approach is 'floating-frame-of-reference component-mode-synthesis (FFR-CMS)', whose theoretical description can be found in the MB books by Shabana [26,27]. The Craig Bampton dynamic condensation [28] was adopted. The first 50 eigenforms are used for the modal reduction (such number is judged sufficient for the scope).

The free-free natural frequencies of the reduced model are calculated and provided as input to the MB analysis: when the flexible body is connected, through the various joints, to the other bodies included in the overall model, the constrained natural frequencies are calculated and used to solve the forced analysis by a modal response approach.

The concept underlying the creation of a MB model is to subdivide a mechanical system, having an overall nonlinear elastic behavior, into linear elastic sub-systems and to concentrate nonlinearities in the connections between them. The elastic bodies are represented by the condensed matrices of the corresponding FE model. A number of nodes, usually those chosen in condensation, having a mass and connected to each other by massless springs and dampers, discretizes each elastic body.

In Figure 2a,b the schematization of the constraints and components making up the engine are shown, with highlight of engine mounts ("FTAB" body) and corresponding location with respect to the

engine (modeled as a rigid body "RI3D"). The condensation nodes of the flexible crankshaft ("CON6") are shown in Figure 2c.

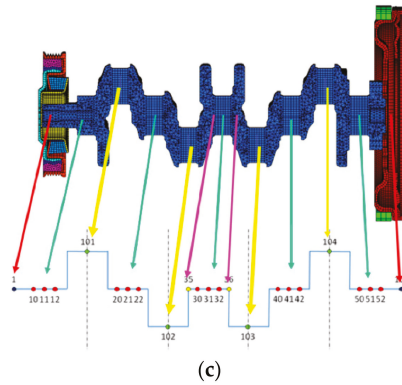(**a**)

(**b**)

Figure 2. *Cont.*

(**c**)
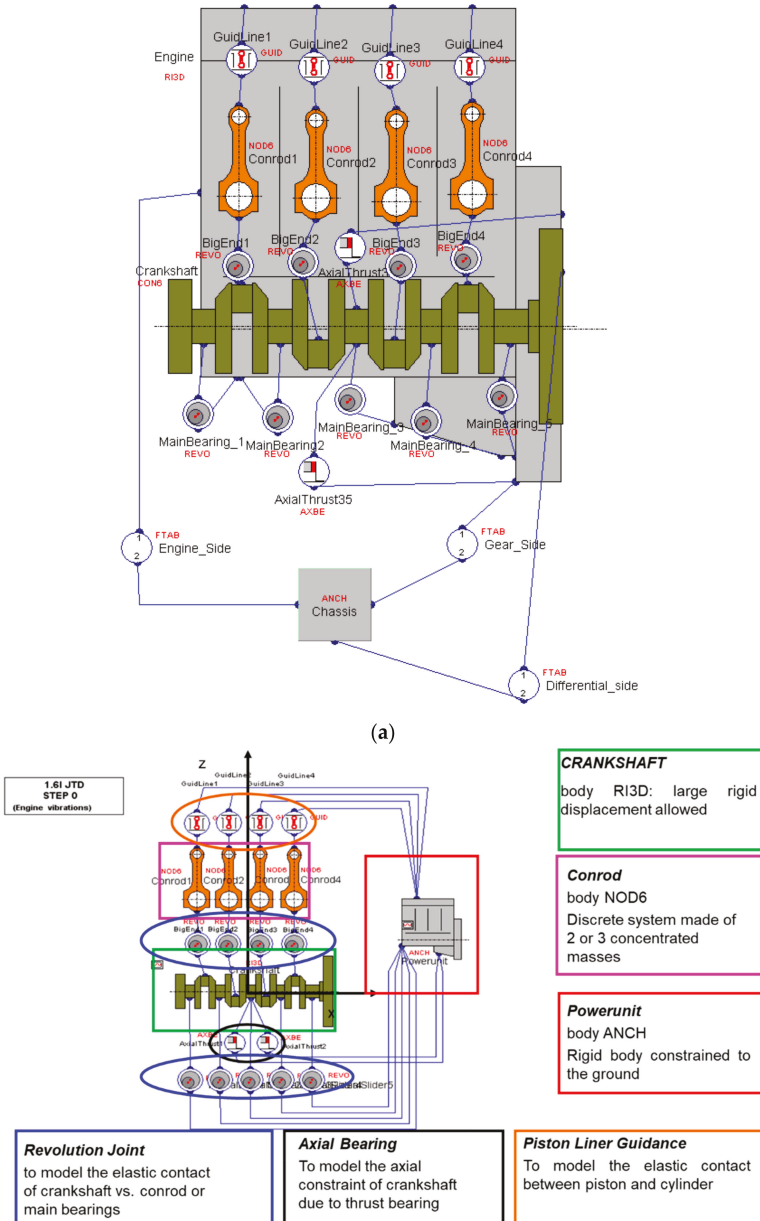
Figure 2. Graphic representation of bodies and connections (**a**,**b**) and highlight of crankshaft points used as master nodes for the reduction process (**c**).

For the damping matrix, the MB software refers to the so-called 'proportional damping', known as "Rayleigh damping" (Figure 3). This can be defined by using two frequencies and the damping ratio at these frequencies. The function of the damping ratio ε is as follows:

$$\xi_i = (a + b\ \omega_i^2)/(2\ \omega_i) \text{ with } \omega_i = 2\ \pi f_i,$$

where

- a and b are the calculated multiplication factors for the mass and stiffness matrix
- the recommended value for f_1 is the first crankshaft eigenfrequency
- the recommended value for f_2 is 1000 Hz
- the recommended value for d_1 at frequency f_1 is 0.03
- the recommended value for d_2 at frequency f_2 is 0.05
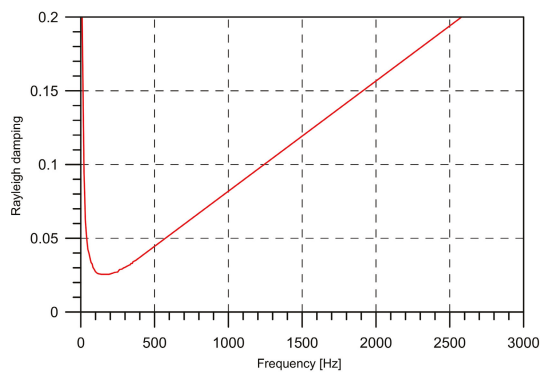
Figure 3. Rayleigh damping vs. frequency (Hz) for the crankshaft.

2.2. Models of Increasing Complexity

For the analysis of the vibration behavior of the internal combustion engine under examination, three models of increasing complexity were realized:

- The first approach, termed SOL1, realizes the simulation of the engine behavior using a rigid body model (Figure 4) and provides for the trend of the motion irregularities at low frequencies, with a first evaluation of the vibrations of the power train support brackets. The powertrain suspension brackets in the engine compartment are three: engine bracket, differential bracket, gearbox bracket (Figure 5a–d). These components are usually simulated in AVL/Excite as joints and treated as massless material points. The joints simulating the brackets were of Table Force/Moment type. This constraint allowed introducing the nonlinear behavior of the dowels stiffness's; stiffness and damping values were assigned (retrieved from the car company database) in the three directions x, y, z for each bracket and for different relative displacement values. The stiffness and damping values for the power train mounts were provided by the supplier and consist in a nonlinear relation between stiffness/damping and mount deformation.

- The second model, termed SOL2, is based on FE modeling of the crankshaft, with pulley and flywheel, in order to consider the flexibility of the crankshaft that, once appropriately condensed, is introduced into the MB calculation code. The aim is to obtain the values of the motion irregularities in addition to the support brackets vibrations. Comparing Figures 6 and 2b, it is possible to see an added condensation node (number 2) as requested by the splitting of pulley in two independent parts (capable of relative motion), the first (node number 1) referring to the shaft end and the second (node number 2) referring to the seismic mass. Now it is possible to point out the impact of torsional modes (in case they are excited) on the motion irregularities and support bracket vibrations. This will be analyzed in the next paragraph.

- The third model, termed SOL3, shows the FE modeling for both the previously considered crankshaft and the clutch unit.
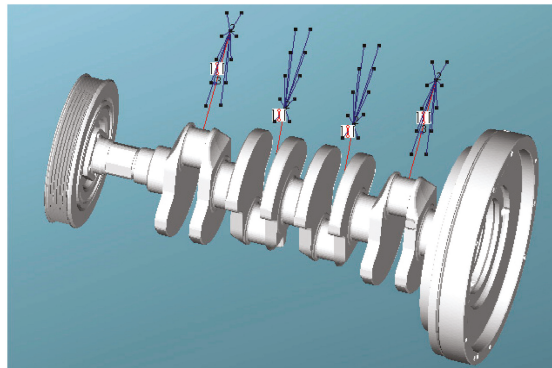

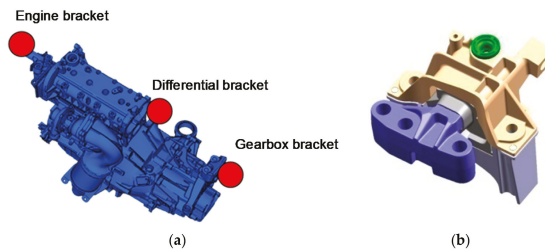**Figure 4.** Crank train with highlight of force introduction.

Figure 5. *Cont.*

151

(c)   (d)

Figure 5. (**a**) Powertrain with highlight of support positions: (**b**) engine bracket; (**c**) gearbox bracket; (**d**) differential bracket.
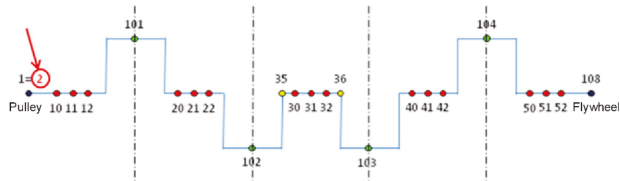

Figure 6. Highlight of added point N.2, geometrically coincident with the N.1 but rigidly connected to the seismic mass.

For all the models, the remaining powertrain components were considered as rigid, with assigned characteristics such as weight, mass center position and inertia. The gearbox was not modeled, neither was present in the experimental bench test (an engine brake was adopted).

Therefore, the purpose of model SOL1 is purely methodological, while models SOL2 and SOL3 are those on which the analyses of interest and outcomes comparison were carried out.

2.2.1. Model SOL1

For model SOL1, some components were schematized by an appropriate rigid body, such as a crankshaft, pulley, flywheel, clutch, connecting rods, pistons, piston pins and rings, or power unit (base, head, oil pan, distribution components, and accessories). In these cases, the specifications of geometric characteristics, values of inertia, mass, and position of the centers of gravity were sufficient.

Moreover, the chassis was schematized by means of a "Generic Body" that represents the car chassis and can be considered as a constraint on the ground to which the powertrain must be clamped by three brackets: the engine, gearbox, and differential brackets (Figure 2a,b). In particular, "Generic Body" is a tool of EXCITE customized for the specific application by introducing the proper parameter settings.

In order to represent the constraints between adjacent bodies, appropriate joints were used (Figure 2a,b). In the case of bearings, they were modeled by a revolution joint, with a given spring stiffness (related to the bearing stiffness) and damping value (related to the oil film characteristics). The stiffness values of the bearings were available from AVL database and selected for this specific engine version based on the following default values:

- Stiffness at zero displacement 1e + 008 N/m
- Damping at zero displacement 10,000 Ns/m
- Stiffness at radial clearance 1e + 008 N/m
- Damping at radial clearance 20,000 Ns/m
- Radial clearance 0.0001 m.

The joint force in radial direction is determined in the plane perpendicular to the main rotational axis as a function of the previously described parameters.

The crankshaft was connected to the crankcase by means of "Revolute Joints" that simulate the presence of the main bearings; this type of constraint allows us to recreate a linear contact between the

two bodies connected by a spring-damper modeling. In particular, the value of the clearance between shaft and crankcase and the stiffness and damping of the spring-damper system were inserted: these values depend on the maximum pressure in the combustion chamber, the bore, and the maximum force discharged on the single main bearings.

No modeling of the oil film was provided, namely, hydrodynamics of the fluid in the main bearings (e.g., between piston and cylinder liner and the connecting rod) was not considered. Actually, in the literature it is proposed to take into account even the elastohydrodynamic interactions for some applications, because, for vibroacoustic analysis, some local modes, like those in correspondence of the bearings, can play an important role especially when considering the crankshaft bending behavior. Anyway, the focus of this work was solely on the shaft torsional behavior. In fact, the elastohydrodynamic interactions generally do not influence the torsional behavior because, due to a sufficiently high crankshaft stiffness, there is no coupling between the bending modes affected by elastohydrodynamic interactions and the torsional modes. Moreover, elastohydrodynamic allowance would cause a huge increment (three times) of run times.

The bearings used in the engines to counteract the axial thrusts generated during motion were schematized with the constraint "Axial Thrust Bearing"; also for this case, clearance, stiffness, and damping values were provided. However, axial thrusts are considerably lower than those deriving from the vertical thrust, generated in the combustion chamber and acting on the main bearings (with this constraint, it was possible to connect a node of the shaft to more nodes of the crankcase).

The connecting rods were connected to the power unit through two constraints: the first component was a prismatic guide schematized through the Piston-Liner Guidance constraint and used to simulate the constraint between rods and plungers; the second component simulated the connecting rod bearing, for which the joint used for main bearings was taken into consideration.

The presented modeling does not calculate the torsional critical speeds, since the motion of this calculation model is rigid, and therefore it is a zero-pulse model. Therefore, the elements making up the system do not deform and rotate at the same speed.

2.2.2. Model SOL2

Model SOL2 introduces the flexibility of the crankshaft, getting a different dynamic behavior of the system and allowing the evaluation of those critical torsional speeds non-visible from model SOL1. This element of flexibility was introduced into the analysis through an FE modeling of the body crankshaft. The crankshaft comprised 150,000 nodes, 6 degrees of freedom (DOFs) per node, whereas the reduced condensed model comprised 50 nodes and 300 DOFs.

The free-free natural frequencies of the reduced model were calculated and provided as input for the MB analysis. When the flexible body was connected through the various joints to the other bodies included in the model, the constrained natural frequencies were calculated and used to solve the modal frequency response analysis.

In such a model (Figure 7), the clutch unit was modeled as a concentrated mass. Figure 8 shows the FE models of the flywheel and pulley.

The adopted mesh utilizes tetrahedral elements with an average size equal to 0.5 mm.
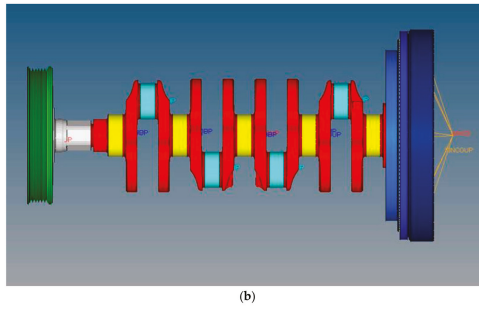

(a)

Figure 7. *Cont.*

(**b**)
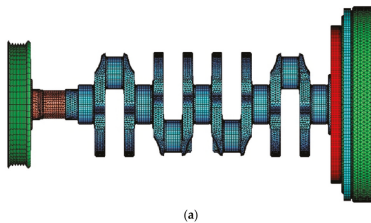
Figure 7. FE model of the shaft (**a**) with clutch mechanism modeled as a concentrated mass (**b**).

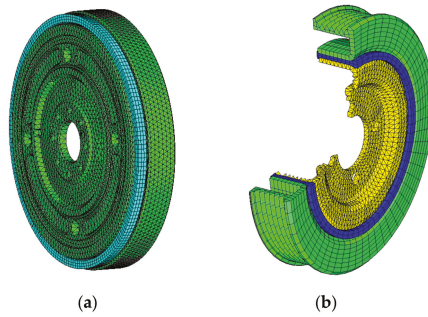(**a**)   (**b**)

Figure 8. FE model of the flywheel (**a**) and pulley (a cutout is shown) (**b**).

2.2.3. Model SOL3

Model SOL3 comprises the FE modeling of the clutch mechanism (Figure 9) in addition to the crankshaft already present in the SOL2 model.

Crankshaft and clutch mechanism meshes comprised nearly 450,000 tetrahedral and hexahedral elements and nearly 140,000 nodes. The salient features of the three models, SOL1, SOL2 and SOL3, are also condensed in Table 1.
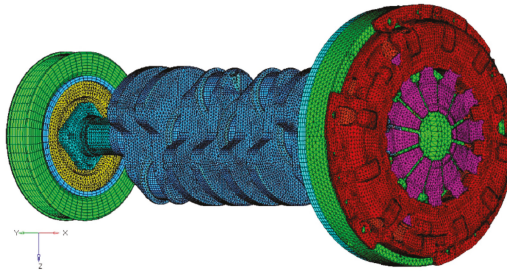
Figure 9. FE model of the shaft with discretized clutch mechanism.

Table 1. Characteristics of the calculation models.

Model	AVL/Excite Elements Used for the Schematization	Modeled FE Elements	Purpose
SOL1	crankshaft, connecting rod, power unit, generic body, revolute joint, axial thrust bearing, piston-liner guidance, table force/moment	-	Procedural—for the verification of the next steps
SOL2	connecting rod, power unit, generic body, revolute joint, axial thrust bearing, piston-liner guidance, table force/moment	crankshaft, pulley, flywheel	analysis and comparison
SOL3	connecting rod, power unit, generic body, revolute joint, axial thrust bearing, piston-liner guidance, table force/moment	crankshaft, pulley, flywheel, clutch mechanism	analysis and comparison

2.3. Experimental Setup

The experimental measurements were performed on a test bench (Figure 10), considering in particular a measurement point located on the powertrain flywheel. Therefore, in order to have a reliable comparison, the experimental motion irregularities were compared with the numerical ones in a reference node located in the mass center of the flywheel (node 108 shown in Figure 6). Calibration between numerical and experimental tests was based on the measured torque.

A preliminary check on the correlation of free-free numerical and experimental crankshaft eigenmodes was performed with satisfactory outcomes.
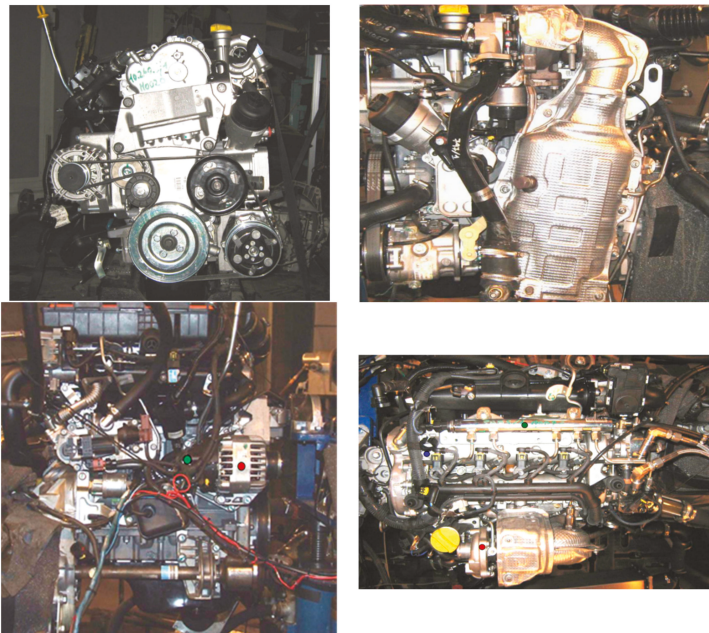

Figure 10. Test bench for the engine under analysis.

3. Results

3.1. Model SOL1

Although not leading to useful outcomes regarding the determination of the critical torsional speeds, Model SOL1 allowed us to obtain important outcomes for the model verification purposes, i.e., motion irregularity of crankshaft and global vibration index for the brackets.

It is well known that in an internal combustion engine, the engine torque generated by gas and inertia forces is periodic and subject to breakdown into a Fourier series as a sum of harmonics that can be more or less relevant to the engine dynamics according to the associated amplitude, phase, and order value.

3.1.1. Motion Irregularities

The outcomes of the simulation obtained with a rigid crankshaft (SOL1), focus on the study of the motion irregularities detected in the center of gravity of flywheel (node 108), hub (node 1), and seismic mass (node 2), as in Figure 6.

The even orders are the most relevant for the engine torque of a 4-stroke, 4-cylinder engine; therefore, their influence should be considered for motion irregularities assessment. Consequently, an evaluation of the magnitude of the 2nd engine order of crankshaft motion irregularity vs. speed was primarily carried out for the engine under test (Figure 11a).

The Campbell diagram represents the frequency spectrum of a non-stationary signal, in which the frequency is on the abscissa and the average angular velocity is on the ordinate, whereas the plotted data indicate the oscillation amplitude of the variable under test (in this case Δrpm). Campbell diagram for the motion irregularity evaluated on the flywheel (Figure 11b) clearly shows the prevalence of the 2nd engine order. It is interesting to observe that the 6th order seems to play a negligible role in the motion irregularities; however, this will be invalidated when the allowance for modal behavior is included in the analysis, triggering resonance with a torsional mode.
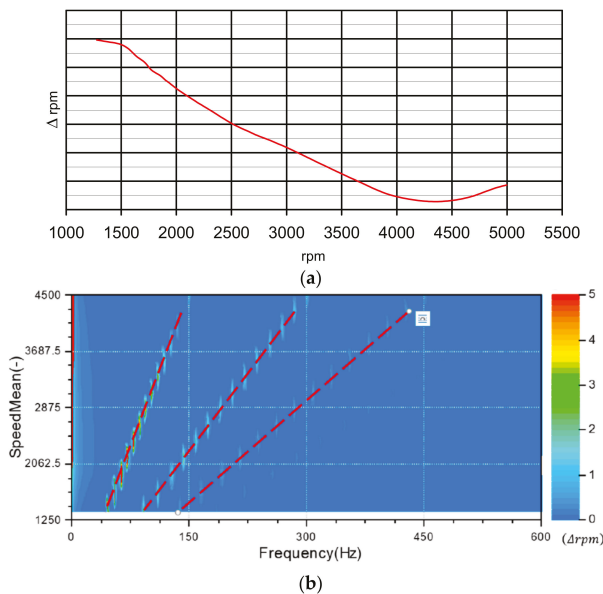

Figure 11. Motion irregularities—model SOL1: (**a**) 2nd engine order with highlight of Δrpm vs. speed (rpm) and (**b**) Campbell diagram of the motion irregularities with highlight of 2nd, 4th and 6th engine orders.

3.1.2. Global Vibration Index

A global vibration index, named as weighted sum, was also calculated for the brackets and defined as follows:

$$X(f) = \sqrt{\sum_{i=1}^{n} w_i^2(f) \cdot x_i^2(f)},$$ (1)

where:

$w_i(f)$ is the weighting factor for a given direction and position,

$x_i(f)$ is the rms acceleration for a given direction and position,

n is the total number of positions and directions (x, y and z) = number of brackets $\times$ 3.

The weighting factors used in Equation (1) depend on the vehicle in which the powertrain has to be installed and are generally provided by the vehicle platform unit. Without such information, as in the present case, the coefficients are all set to 1 (uniform weighing of the structural transmission paths).

The second order of the global vibration index of each bracket (engine, gearbox and differential brackets) is shown in Figure 12, with a contribution that is nearly frequency independent for gearbox and differential brackets, but increasing with frequency when considering the engine bracket. The corresponding global vibration index is shown in Figure 13 with reference to the amplitudes of numerical and experimental acceleration irregularities, and therefore to the amount of the transmitted vibration. Such a good numerical–experimental agreement can be explained by observing that the 2° engine order cannot trigger a torsional mode and consequently, when considering the second order effect, there is no loss of accuracy by neglecting the crankshaft flexibility.
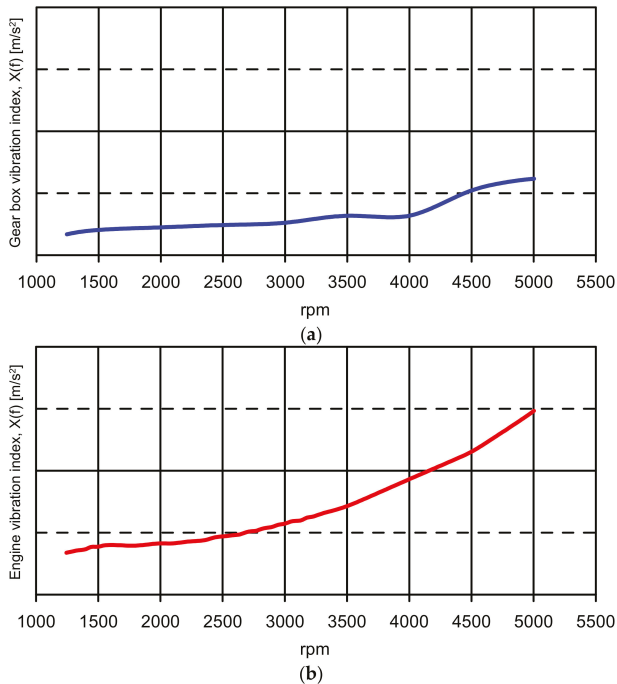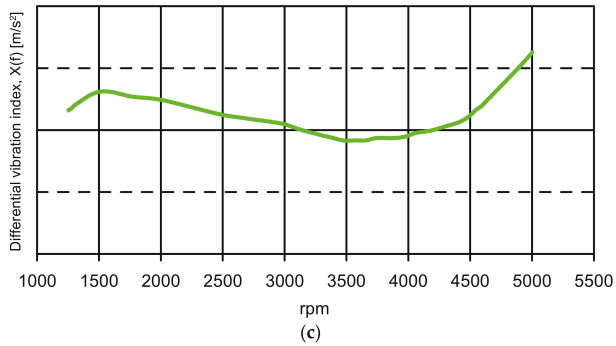

(a)

(b)

Figure 12. *Cont.*

(c)

Figure 12. Numerical bracket vibration indexes $X(f)$ [m/s^2] for the second engine order: (**a**) gear box; (**b**) engine; (**c**) differential.
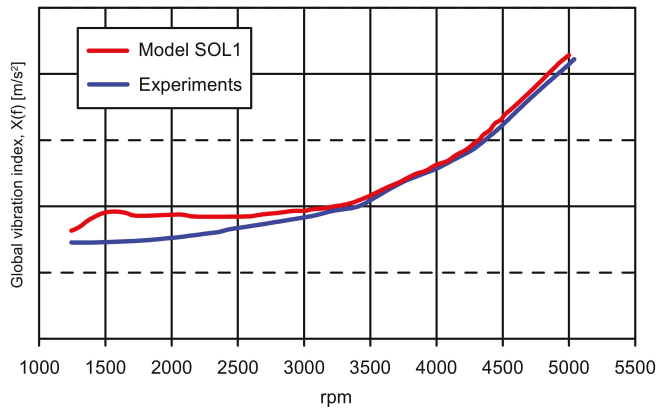

Figure 13. Numerical–experimental comparison of the brackets global vibration index for the second engine order.

Model SOL1 allowed us to verify some operating parameters, such as the motion irregularities and the global vibration index for the brackets; it also allowed us to highlight that, as expected, the second engine order harmonic force is predominant when neglecting the flexibility of any component.

3.2. Model SOL2

3.2.1. Motion Irregularities

From the modal analysis, it is possible to observe that, for the engine under testing in its operating frequency range, considering the real constraints (as enabled by the multibody analysis), the first two torsional modes are at 305 and 545 Hz, respectively (Figure 14). In the former, the hub and the seismic mass oscillate in phase, whereas their oscillation is out of phase for the latter. Anyway, the differences between free-free and constrained torsional eigenfrequencies are very low (nearly 15 Hz considering the first torsional mode with vertical and transversal springs at the bearings' locations); on the contrary, a relevant difference exists between the free-free and constrained bending modes.
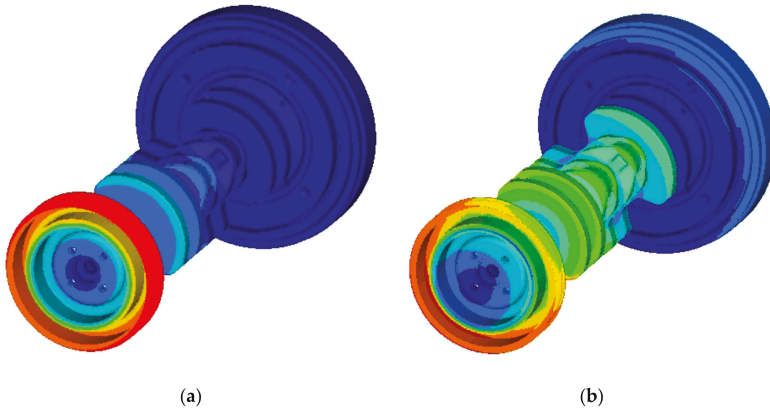
<div align="center">(a)   (b)</div>

Figure 14. 1st (**a**) and 2nd (**b**) torsional eigenmodes at 305 and 545 Hz, respectively.

The primary objective here is to detect how the amplitude of the motion irregularities is affected by the shaft torsional eigenfrequencies: in fact, in correspondence of resonances, the irregularities may have values so high as to make them critical to the vibroacoustic behavior of the whole powertrain.

The outcomes of model SOL2 are compared with the test data to assess the accuracy of this modeling. Considering that the experimental measurements are only available on the flywheel center, the numerical–experimental comparison can only involve node 108 (Figure 6).

The 2nd order of motion irregularity does not display any peak in the range 1250–5000 rpm (Figure 15); this is expected since the maximum involved excitation frequency,

$$f = 2 \times 5000/60 = 166.7 \text{ Hz,}$$

is not sufficiently high to trigger the first torsional eigenmode at 305 Hz; consequently, SOL2 provided the same results of SOL1 and a satisfactory correlation with experimental measurements made at flywheel (node 108), as in Figure 16. The minimum of the motion irregularities is at nearly 4250 rpm: in correspondence with such a regime, the combustion forces and inertia forces are almost in equilibrium.
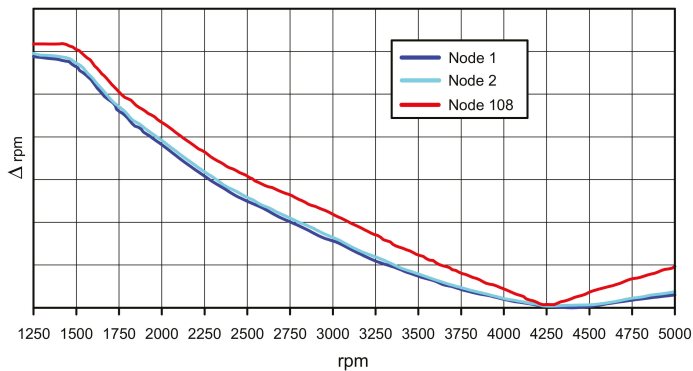

Figure 15. Numerical motion irregularities for the 2nd engine order at nodes 1, 2, and 108, as provided by model SOL2.
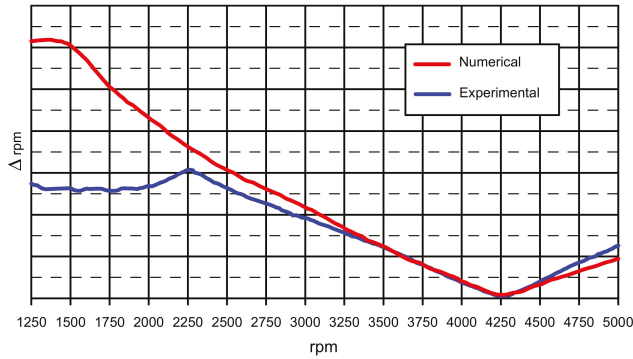
Figure 16. Numerical-experimental comparison of the motion irregularities for the 2nd engine order at node 108.

On the contrary, the 4th order of motion irregularity does display a peak in the range 1250–5000 rpm at nearly 4500 rpm (Figure 16), corresponding with the frequency

$$f = 4 \times 4500/60 = 300 \text{ Hz},$$

which is sufficiently close to the 1st torsional eigenfrequency (305 Hz) to confirm the hypothesis of a resonant behavior for the crankshaft. Such a peak only manifests with reference to nodes 1 and 2, but is negligible for node 108 (Figure 17).

A good correspondence between the numerical and experimental results is provided by SOL2 (Figure 18) for regimes higher than 2000 rpm, even if a slight underestimation of the irregularities is obtained. The lack of numerical vs. experimental correlation at low regimes is expected due to the turbolag phenomenon. In fact, during the bench test based on an acceleration from the min to the max regime, the turbo did not properly work at low regime (lower than 2000 rpm), whereas the simulation cannot allow for such behavior since it is based on a quasi-stationary variation of loading conditions.

It is worth noting that, as expected, the amplitude of oscillation for node 2 is higher than that of node 1: in fact, hub and seismic mass oscillate in phase, with the latter being more peripheral and consequently having larger oscillations.
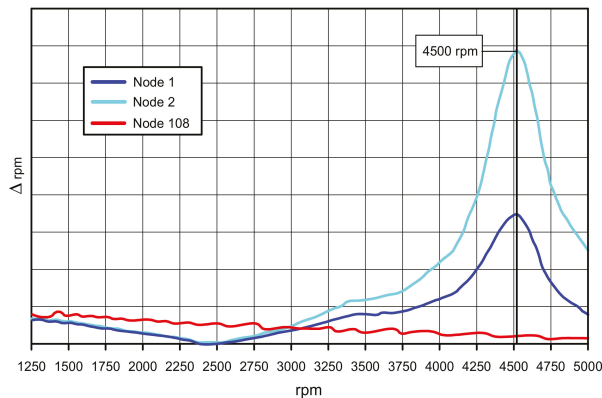

Figure 17. Numerical motion irregularities for the 4th engine order at nodes 1, 2, and 108, as provided by model SOL2.
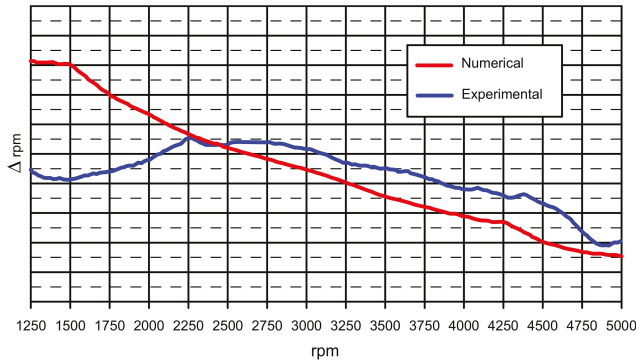
Figure 18. Numerical-experimental comparison of the motion irregularities for the 4th engine order at node 108, as provided by model SOL2.

Exploring the 6th order, a numerical peak at nearly 3050 rpm can be observed [18], corresponding with the frequency

$$f = 6 \times 3050/60 = 305 \text{ Hz},$$

which, again, is coincident with the 1st torsional eigenfrequency (305 Hz), confirming the hypothesis of resonant behavior for the crankshaft.

The experimental peak is at 3100 rpm, whereas the numerical peak is at 3050 rpm (Figure 19): this discrepancy can be attributed to the "discrete" acquisition procedure adopted in the test.

The discrepancies of motion irregularities at the low regimes can be surely explained by the turbolag phenomena, whereas the non-negligible underestimation provided by the simulation at high regimes (Figure 20) might be caused by the fact that the only crankshaft is modeled as flexible.
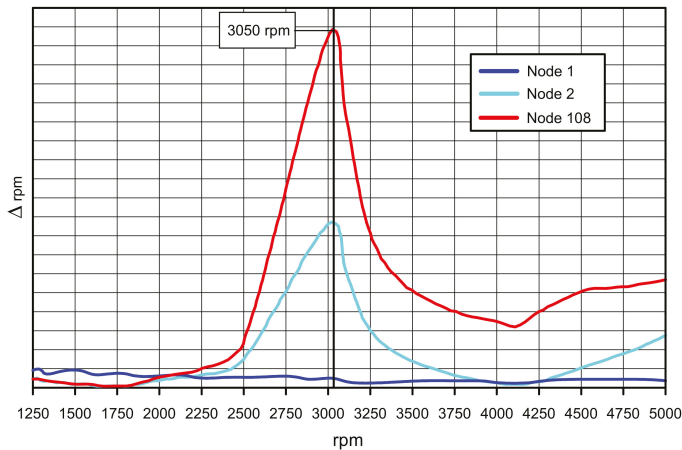

Figure 19. Numerical motion irregularities for the 6th engine order at nodes 1, 2, and 108, as provided by model SOL2.
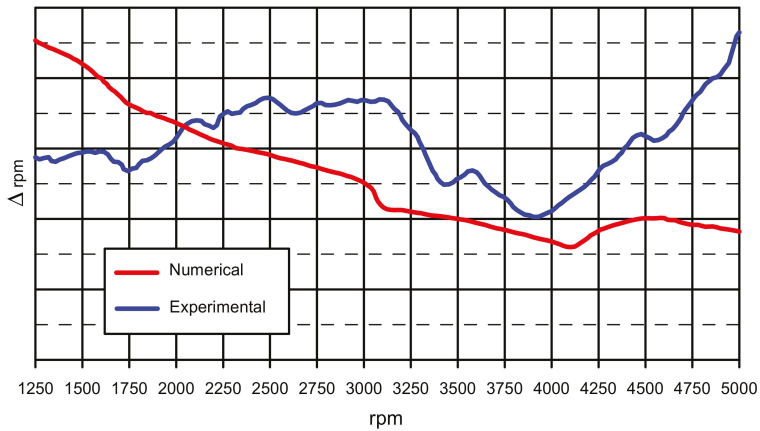
Figure 20. Numerical-experimental comparison of the motion irregularities for the 6th engine order at node 108, as provided by model SOL2.

Regarding the 8th order, two peaks at nearly 2250 and 4250 rpm can be found (Figure 22), corresponding with the frequencies

$$f_1 = 8 \times 2250/60 = 300 \text{ Hz},$$

$$f_2 = 8 \times 4250/60 = 567 \text{ Hz}.$$

These frequencies are sufficiently close to the 1st (305 Hz) and 2nd (545 Hz) torsional eigenfrequencies, confirming the hypothesis of resonant behavior for the crankshaft.

Again, a slight underestimation of motion irregularities provided by the simulation is evident (Figure 21).

In conclusion, the 2nd torsional eigenfrequency cannot be triggered by orders lower than the 8th; moreover, orders higher than the 8th are neglected because their amplitude is sufficiently low to prevent a relevant impact when triggering the torsional eigenfrequencies.
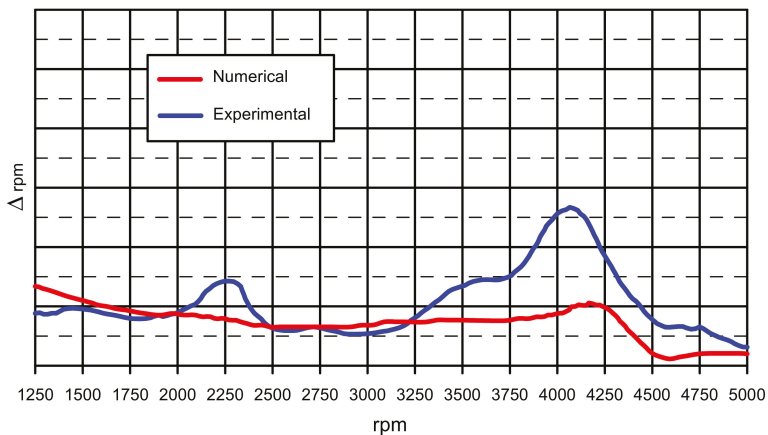

Figure 21. Numerical-experimental comparison of the motion irregularities for the 8th engine order at node 108, as provided by model SOL2.
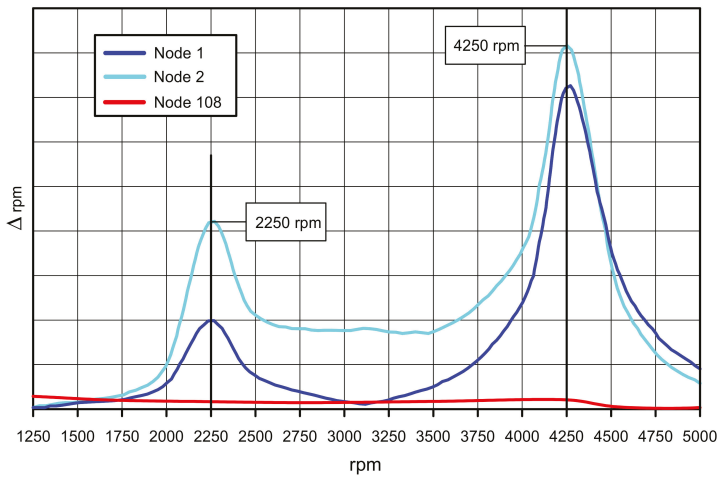
Figure 22. Numerical motion irregularities for the 8th engine order at nodes 1, 2, and 108, as provided by model SOL2.

3.3. Model SOL3

Regarding model SOL3, the outcomes of the 2nd engine orders motion irregularities do not significantly differ from those observed for model SOL2. In contrast, different results between the two models are obtained for the 4th engine order (Figure 23). In particular, a different trend of the brackets vibrations due to the explicit FE modeling of the clutch mechanism is observed.
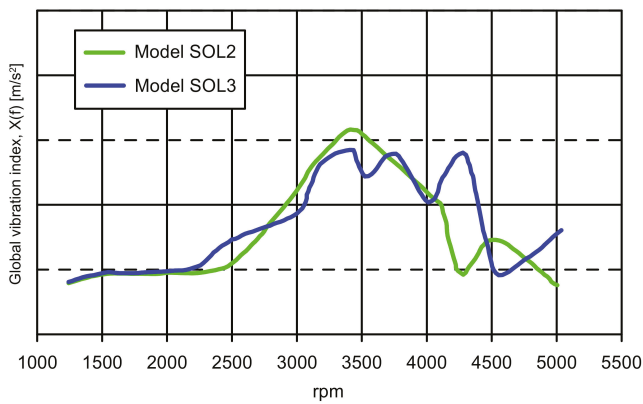

Figure 23. Global vibration index for the 4th engine order brackets: comparison between models SOL2 and SOL3.

4. Conclusions

In this work, three internal combustion turbocharged diesel engine multibody models of increasing complexity were developed and their vibration behavior observed.

The development of these multibody models allowed us to analyze the support brackets vibrations and crankshaft motion irregularities in order to proceed to a design optimization solution in production and/or the development phase.

The choice of adding the only flexibility of crankshaft, flywheel, and pulley is related to the range of frequencies of interest (up to 650 Hz) and to the exclusive focus on the impact of the crankshaft torsional behavior (the flexibility of other powertrain components comes out at higher frequencies). Consequently, in the frequency range of interest, it was not necessary to adopt complex models for the calculation of both the vibrational index at the engine brackets and the irregularity motion of crankshaft, with a substantial reduction in the computational burden.

The obtained outcomes of the three analyzed models can be summarized as follows:

- for what concerns the 2nd engine order motion irregularities and global vibration index, the rigid body model showed a good correlation with the experimental outcomes;
- the model with just the flexible shaft showed an adequate degree of correlation for the 2nd and 4th engine order motion irregularities; such a model represented the best compromise between the required computational effort and expected accuracy, also providing results that can be used for analyses requiring more in-depth study;
- the addition of explicit FE modeling for the clutch mechanism allowed us to improve the accuracy for the 4th engine order support brackets' vibrations.

The next steps for this work would be allowance for the flexibility of engine block and engine subsystems in order to calculate the impact of its resonances on the monitored vibrational parameters at higher frequencies. Clearly, such improvements would also require further considerations of the damping factors to be used in the calculations, to be fine-tuned by numerical experimental correlations performed on the single components.

Conflicts of Interest: The authors declare no conflicts of interest.

References

1. Citarella, R.; Federico, L. Advances in Vibroacoustics and Aeroacustics of Aerospace and Automotive Systems. *Appl. Sci.* **2018**, *8*, 366. [CrossRef]
2. Bianco, D.; Adamo, F.P.; Barbarino, M.; Vitiello, P.; Bartoccini, D.; Federico, L.; Citarella, R. Integrated Aero–Vibroacoustics: The Design Verification Process of Vega-C Launcher. *Appl. Sci.* **2018**, *8*, 88. [CrossRef]
3. Armentani, E.; Sbarbati, F.; Perrella, M.; Citarella, R. Dynamic analysis of a car engine valve train system. *Int. J. Veh. Noise Vib.* **2016**, *12*, 229–240. [CrossRef]
4. Yakoub, R.Y.; Corrado, M.; Forcelli, A.; Pappalardo, T.; Dutre, S. Prediction of System-Level Gear Rattle Using Multibody and Vibro-Acoustic Techniques. *SAE Tech. Pap.* **2004**. [CrossRef]
5. Gérard, F.; Tournour, M.; El Masri, N.; Cremers, L.; Felice, M.; Selmane, A. Acoustic Transfer Vectors for Numerical Modeling of Engine Noise. *Sound Vib. Mag.* **2002**, *36*, 20–25.
6. Citarella, R.; Federico, L.; Cicatiello, A. Modal acoustic transfer vector approach in a FEM–BEM vibro-acoustic analysis. *Eng. Anal. Bound. Elem.* **2007**, *31*, 248–258. [CrossRef]
7. Gustafsson, M.; Jacqmot, J.; Caro, S. Experimental Validation of an Efficient Procedure for Large Acoustic Radiation Problems. In Proceedings of the ISMA2010 Including USD2010, Leuven, Belgium, 20–22 September 2010; pp. 4557–4566, ISBN 978-907380287-2.
8. Armentani, E.; Sepe, R.; Parente, A.; Pirelli, M. Vibro-Acoustic Numerical Analysis for the Chain Cover of a Car Engine. *Appl. Sci.* **2017**, *7*, 610. [CrossRef]
9. Hua, X.; Lim, T.C.; Peng, T.; Wali, W.E. Dynamic Analysis of Spiral Bevel Geared Rotor Systems Applying Finite Elements and Enhanced Lumped Parameters. *Int. J. Automot. Technol.* **2012**, *13*, 97–107. [CrossRef]

10. Hua, X.; Lim, T.; Peng, T. Effect of Shaft-bearing Configurations on Spiral Bevel Gear Mesh and Dynamics. *SAE Tech. Pap.* **2011**. [CrossRef]

11. Xu, X.; Luo, T.; Luo, J.; Hua, X.; Langari, R. Dynamical load sharing behaviors of heavy load planetary gear system with multi-floating components. *Int. J. Model. Simul. Sci. Comput.* **2018**, *9*, 1850005. [CrossRef]

12. Hanim, S.; Zouani, A.; Felice, M. Integrated dynamic engine simulation for automotive noise & vibration predictions. In Proceedings of the NAFEMS Americas Conference, Seattle, WA, USA, 7–9 June 2016.

13. Östman, F.; Toivonen, H.T. Adaptive Cylinder Balancing of Internal Combustion Engines. *IEEE Trans. Control Syst. Technol.* **2011**, *19*, 782–791. [CrossRef]

14. Giakoumis, E.G.; Rakopoulos, C.D.; Dimaratos, A.M. Study of crankshaft torsional deformation under steady-state and transient operation of turbocharged diesel engines. *Proc. Inst. Mech. Eng. Part K J. Multi-Body Dyn.* **2008**, *222*, 17–30. [CrossRef]

15. Offner, G.; Priebsch, H. Elastic body contact simulation for predicting piston slap induced noise in an IC engine. In *Multi-Body Dynamics: Monitoring and Simulation Techniques-II*; Rahnejat, H., Ebrahimi, M., Whalley, R., Eds.; Professional Engineering Publishing: London, UK, 2000; pp. 191–206. ISBN 978-1-860-58258-5.

16. Offner, G.; Krasser, J.; Laback, O.; Priebsch, H. Simulation of multi-body dynamics and elasto-hydrodynamic excitation in engines especially considering piston-liner contact. *Proc. Inst. Mech. Eng. Part K J. Multi-Body Dyn.* **2001**, *215*, 93–102. [CrossRef]

17. Duvigneau, F.; Nitzschke, S.; Woschke, E.; Gabbert, U. A holistic approach for the vibration and acoustic analysis of combustion engines including hydrodynamic interactions. *Arch. Appl. Mech.* **2016**, *86*, 1887–1900. [CrossRef]

18. Perera, M.S.; Theodossiades, S.; Rahnejat, H. Elasto-multi-body dynamics of internal combustion engines with tribological conjunctions. *Proc. Inst. Mech. Eng. Part K J. Multi-Body Dyn.* **2010**, *224*, 261–277. [CrossRef]

19. Junhong, Z.; Jun, H. CAE process to simulate and optimise engine noise and vibration. *Mech. Syst. Signal Process.* **2006**, *20*, 1400–1409. [CrossRef]

20. Gawande, S.H.; Navale, L.G.; Nandgaonkar, M.R.; Butala, D.S.; Kunamalla, S. Fault Detection of Inline Reciprocating Diesel Engine: A Mass and Gas-Torque Approach. *Adv. Acoust. Vib.* **2012**, 1–6. [CrossRef]

21. Siano, D.; Citarella, R. Elastic Multi Body Simulation of a Multi-Cylinder Engine. *Open Mech. Eng. J.* **2014**, *8*, 157–169. [CrossRef]

22. Siano, D.; Citarella, R.; Armentani, E. Simulation of a multi-cylinder engine vibrational behavior. *Int. J. Veh. Noise Vib.* **2018**, in press.

23. Dassault Systems Simulia Corp. *Abaqus Analysis User's Manual*; Version 6.12.1; Dassault Systems Simulia Corp.: Providence, RI, USA, 2011.

24. *AVL EXCITE Base Module Reference Manual*.

25. Kim, S.J.; Kim, S.G.; Oh, K.S.; Lee, S.K. Excitation Force Analysis of a Powertrain Based on CAE Technology. *Int. J. Automot. Technol.* **2008**, *9*, 703–711. [CrossRef]

26. Shabana, A.A.; Ahmed, A. *Theory of Vibration—An Introduction*; Mechanical Engineering Series; Springer: New York, NY, USA, 1996; ISBN 978-1-4612-3976-5.

27. Shabana, A.A.; Ahmed, A. *Vibration of Discrete and Continuous Systems*; Mechanical Engineering Series; Springer: New York, NY, USA, 1997; ISBN 978-1-4612-4036-5.

28. Craig, R.; Bampton, M. Coupling of Substructures for Dynamic Analyses. *AIAA J.* **1968**, *6*, 1313–1319. [CrossRef]

A Study on Optimal Compensation Design for Meteorological Satellites in the Presence of Periodic Disturbance

Shijie Xu [1], Naigang Cui [2], Youhua Fan [1,*] and Yingzi Guan [2]

[1]   School of Science, Harbin Institute of Technology, Shenzhen 518055, China; xushijiehit@126.com
[2]   School of Astronautics, Harbin Institute of Technology, Harbin 150001, China; cui_naigang@163.com (N.C.);
    guanyz@hit.edu.cn (Y.G.)
*   Correspondence: yhfan@hit.edu.cn; Tel.: +86-0755-26033826

Featured Application: This work may be used to improve the accuracy of attitude stability of flexible meteorological satellites.

Abstract: Periodic disturbance may cause serious effects on the attitude of meteorological satellites, and the attenuation of periodic disturbance is required. In this paper, a fundamental study on the optimal design of constant compensations against known-law periodic disturbance for meteorological satellites is investigated. An analytical solution for the relationship between the frequency and amplitude ratios and the response of a typical second-order vibration system is firstly derived. The compensation and disturbance torques are determined according to practical engineering. The criteria for designing the optimal compensations are based on the analytical and simulation results. Then, the criteria are applied to a flexible spacecraft actuated by constant control torque in the presence of sustained periodic disturbance. The optimal compensation torque parameters for spacecraft are acquired based on former criteria. The compensate effectiveness of the optimal compensation torque is provided and compared with results of other selections in the frequency and amplitude ratio domain. Numerical simulation results and experimental results clearly demonstrate the good performance of proposed criteria. This work provides a significant reference for the vibration attenuation of meteorological satellites in the present of periodic disturbance.

Keywords: flexible spacecraft; periodic disturbance compensation; compensate torque design; vibration attenuation; reaction wheel.

1. Introduction

Meteorological satellites play a vital role in our daily life. To send back high-quality images, satellites have to meet stringent demands related to attitude accuracy [1–3]. However, periodic disturbances from spaceborne equipment result in difficulty in retaining stability in the attitude of spacecraft. The application of spaceborne microwave imaging instruments has substantially improved the image definition, but poor effects on attitude accuracy are also brought about by their known-law rotating imbalance [4–6]. Furthermore, characteristics like flexibility and low weight make spacecraft vulnerable to vibrations caused by numerous sources [7]. In this paper, we focus on the compensation of known-law long-lasting periodic disturbances and attenuation of vibrations to improve the attitude accuracy of meteorological satellites.

Many studies have been done on the attitude control of meteorological satellites. Mitigation of the periodic disturbances by compensating torques has been proposed by researchers over the course of the past years. Zhang et al. [8] presented a fault tolerant control for external disturbances and actuator

failures. This controller is the combination and application of the free weighting matrices method and LMI (linear matrix inequality) technique. However, this simply designed controller has not been well verified for flexible spacecraft. Cong et al. [9] presented an improved sliding mode attitude control algorithm with an exponential time-varying sliding surface. This controller enhanced the accuracy of maneuver in the presence of disturbances and parametric uncertainties. To reduce the dependence of estimate accuracy on a disturbance model, Hu et al. [10] designed a sliding mode disturbance observer for the attitude control of a rigid spacecraft in the presence of disturbance and actuator saturation. The adaptive controller has also been adopted. Unfortunately, the studies neglected the flexibility of the structure. The attitude control and disturbance rejection have been studied for flexible spacecraft during attitude maneuvering by Zhong et al. [11]. An improved compensator is developed to achieve asymptotic disturbance rejection. Then, a new robust state feedback controller is presented for the attitude maneuver. The proposed strategy achieved the maneuver process in the presence of small amplitude disturbances. Zhang et al. [12] proposed a generalized-disturbance rejection (GDR) control for vibration suppression of flexible structures in the presence of unknown continuous disturbances. The unknown disturbances are estimated by a generalized-disturbance rejection which is defined by a refined state space model. Chen et al. [13] focused on the disturbance observer-based control method to attenuate or reject disturbances for a spacecraft attitude control system. The disturbance observer is used to estimate the disturbances. Also, the feedforward compensation is given according to the corresponding results. Ma et al. [14] developed an adaptive failure compensation approach for the attitude control of satellites in the presence of disturbance and uncertain failures of actuators. This research mainly focuses on the disturbances from actuator failures; external disturbances have not been sufficiently considered. Lau et al. [15] improved the research on disturbance identification and rejection. The dipole-type disturbance rejection filter is adopted and applied in [15]. Subsequently, two simple close-loop system identification methods are introduced to improve the robustness of the rejection filter relative to frequency uncertainty. Chen et al. [16] made contributions to the rejection of general multi-periodic disturbances. The multi-periodic disturbances are estimated by a new presented method. Based on the estimation results, a new adaptive control method is applied for disturbance rejection. The residual vibration can be controlled in a specified range under the provided strategy. However, this approach assumes that all periods of disturbances should be known, which is difficult in practical engineering. Although the preceding strategies have made some achievements in disturbance rejection, parameter magnitudes considered in research, like the variation range of disturbance frequency and disturbance amplitudes, are not large enough. Furthermore, corresponding experiments verifying their effectiveness are absent in most literature, and it is unpractical to output complicated desired compensating torques by any actuators.

Maneuver actuators may also affect the attitude accuracy. Speaking of the actuators, jet thrusters are inappropriate for persistent disturbance. Reaction wheels are extensively used due to their advantage in generating continuous and precise torques without expending the propellant [17,18]. Although it is easy for torque mode reaction wheels to output a constant value torque, evident faults exist when tracking an expected time varying torque [19]. Most of the present papers failed to consider the capability of reaction wheels. These complex control output torques may be unfulfillable in common practical engineering. On the other hand, problems like time delay may be solved by the using of flywheel actuators. Sabatini et al. [20,21] tackled the problem of controlling time delayed systems. A prediction of state at the time of the control application has been performed to compensate for the time delay. A Kalman filter and the GNC loop were used to realize this purpose. Sabatini et al. also conducted research to test and improve the robustness of presented algorithm. Simulations and experiments were provided to confirm the effectiveness. Those works may cover the shortage caused by the time delay. Further, for meteorological satellites in the presence of known laws of periodic disturbances, those methods are inappropriate and superfluous. Based on those facts, for the compensation of periodic disturbed torques, constant reaction wheel torques may be the most practical and appropriate way. Unfortunately, work is limited on this issue in the literature.

Another way to improve the attitude accuracy of meteorological satellites is to actively suppress the residual vibrations of flexible appendages. This kind of strategy has been widely used in the attitude maneuver of spacecraft. Numerous studies have been presented for vibration suppression of flexible appendages. Smart materials, such as Magnetorheological Material (MR) [22], Piezoelectric Material (PM) [23,24], have been investigated and fabricated to eliminate the residual vibrations during the past decades. A wide range of control schemes has been proposed for the use of smart materials, such as positive position feedback (PPF) control [25], sliding mode control (SMC) [26], H-infinity control [27], and so on. However, these actuators and sensors have changed the structural property by mechanical interference, which is undesirable in many practical engineering applications. An active vibration suppression method called component synthesis vibration suppression (CSVS) can suppress vibration without additional structures attached to flexible structures. This method was first proposed by Liu et al. [28]. Then, Hu et al. [29] extended the application of the CSVS method in the attitude maneuver of spacecraft. However, as a feedforward control scheme, the application of the CSVS method is limited to the sensitivity to parameter uncertainties. Similar to the CSVS method, the input shaping technique is also used for vibration suppression. Kong et al. [30] extended the input shaping method by combining it with feedback control for the vibration control of flexible spacecraft during attitude maneuver. Their work remedied the shortcoming of input shaping as it is a feedforward control scheme. However, this technique is suitable for zero to zero maneuver. It is not appropriate for problems forced in this paper in which the disturbance is nonstop. All those tactics mentioned above have application in vibration attenuation of flexible appendages, but their application conditions are restrictive. They are not suitable for situations in which satellites are actuated by sustained disturbances. Motivated by the preceding discussion, finding an appropriate continuous compensating torque to attenuate the vibration of flexible appendages is the optimal option. However, direct studies about relationships between selection of compensate torques and vibration attenuation effectiveness for meteorological satellites are scarce.

In this paper, based on the requirement of meteorological satellites and practical limitations, step torques given by reaction wheels are adopted to compensate for the sinusoidal periodic disturbance. Two coefficients, frequency ratio and amplitude ratio, are introduced as parameters. A typical 2-order vibration system and a flexible spacecraft system are introduced. The optimal compensate torques and corresponding effect will be discussed by analytic methods. Residual vibrations are regarded as the standard of the disturbance compensate effect. To verify the effectiveness of the proposed strategy, simulation results are presented. We aim to determine the relationship between the selection of the two ratios and disturbance compensate effectiveness. Furthermore, an experimental study is provided to verify the effectiveness of the proposed strategy. It is hoped that the work will be helpful for solving practical engineering problems. In addition, preliminary investigations in this paper have limitations, and further discussions will be summarized in our next study.

The remaining part of this paper is organized as follows. Section 2 gives the mathematical modelling. Analytical relationships between ratios and residual vibration are given in Section 3. Numerical simulations, experiment results and discussions are presented in Section 3. Section 4 concludes the paper.

2. Materials and Methods

2.1. Modelling of the Flexible Spacrcraft

Three-axis spacecrafts with flexible appendages have a complex model. It is difficult for us to obtain the relationship between vibrations and control torques. To stress the key point of this paper, here we provided a simplified spacecraft model: A flywheel actuated single-axis gas suspending rotary table (SGSRT) is applied. The diagram of the SGSRT is shown in Figure 1.
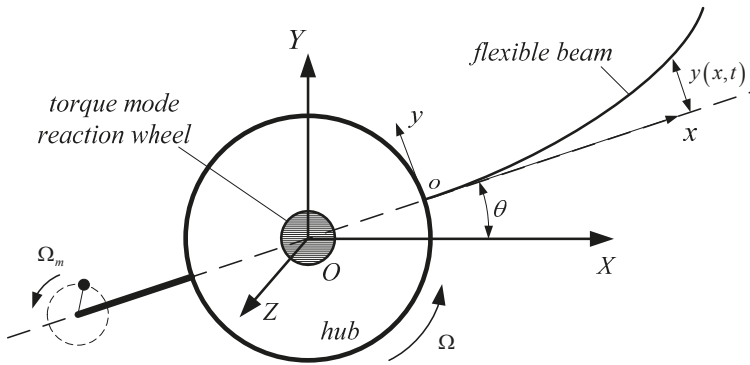
Figure 1. Diagram of SGSRT.

As is shown in Figure 1, this system is mainly consists of a rigid hub and a flexible beam. A rigid beam is fixed on the opposite side of flexible beam. An eccentric mass is rotating around the tip of the rigid beam at a constant angular velocity. A reaction wheel is placed at the centre of the hub. Define $OXYZ$ as the inertial frame and oxy as the frame fixed on the edge of rigid hub. $\theta(t)$ is the rotation angle of the hub. $y(x,t)$ is the displacement of place x in frame oxy. Ω and Ω_m are the angular velocity of rigid hub and eccentric mass, respectively. The flexible beam is assumed to be an Euler-Bernoulli beam. The Newton-Euler method is used to build the mathematical model of the system. The dynamic model of the flexible system shown in Figure 1 is

$$\begin{cases} J\dot{\Omega} + \int_0^L \mathbf{r_b} \times \mathbf{a_b} dx + \mathbf{r_m} \times \mathbf{a_m} m_m = \mathbf{T} \\ EI\frac{\partial^4 y}{\partial x^4} + \sigma\left[\frac{d^2 y}{dt^2} + (R_{hub} + x)\frac{d^2 \theta}{dt^2}\right] = 0 \end{cases} \tag{1}$$

where $\mathbf{J}$ is the rotational inertia matrix of the rigid hub. $\mathbf{r_b}$ is the vector from the centre of the hub to an arbitrary mass point in the flexible beam. $\mathbf{a_b}$ is the acceleration of mass points. $\mathbf{r_m}$ is the vector from the centre of the hub to the eccentric mass. $\mathbf{a_m}$ and m_m are the acceleration and mass of the eccentric mass, respectively. $\mathbf{T}$ is the actuator torque. R_{hub} is the radius of the rigid hub. EI is the flexural rigidity of the beam and σ is the surface density

As the SGSRT is adopted in this study, Equation (1) can be simplified because it is a single-axis rotation system. The simplified model can be expressed as:

$$\begin{cases} J\ddot{\theta} + \int_l (R_{hub} + x)\ddot{y}dm + W_m\Omega_m^2 = T \\ EI\frac{\partial^4 y}{\partial x^4} + \sigma\left[\frac{d^2 y}{dt^2} + (R_{hub} + x)\frac{d^2 \theta}{dt^2}\right] = 0 \end{cases} \tag{2}$$

where J is the rotation inertia of the system relative to the axis of rotation. W_m represents the influence on the system caused by eccentric mass. It can be expressed as $W_m = P_m\sigma_m\sin(\omega_m t)m_m$. P_m is a constant parameter about the position of the eccentric mass. σ_m is the horizontal distance from the eccentric mass to the tip of the rigid beam. $y = y(x,t)$ is the displacement of the flexible beam.

Using the assumed-mode method, the displacement of the flexible beam can be expressed as:

$$\mathbf{y} = [D]\boldsymbol{\eta} \tag{3}$$

where $[D]$ is a matrix consisting of modes of the flexible beam, η is the modal coordinate vector. In consideration of the orthogonality of the mode. Equation (2) can be shown as:

$$\begin{cases} J\ddot{\theta} + \delta\ddot{\eta} + W_m\Omega_m^2 = T \\ \delta^T\ddot{\theta} + \ddot{\eta} + C\dot{\eta} + K\eta = 0 \end{cases} \tag{4}$$

where δ is the coupling matrix of rotation and vibration. C and K are damping and stiffness matrices, respectively. It needs to be emphasized that the reaction wheel is assumed to be ideal equipment. That means it can generate ideal square torque. Furthermore, the influence on the system caused by eccentric mass is in sinusoidal law according to its expression. Hence, the two known-law kinds of torque will be adopted in the residual part.

2.2. Modelling of the Typical Second Order Vibration System

A typical second order vibration system is also used due to its advantage in distinct mathematical analytical solution. It can be shown as:

$$m\ddot{x} + c\dot{x} + kx = F \tag{5}$$

where m, c and k are the respective mass, damping and stiffness of the system. F is the mechanical load.

3. Results and Discussion

3.1. Analysis and Design of Optimal Compensate Criterion

For many studies about vibration suppression of flexible spacecraft, their simplified mathematical model can be expressed as a 2-order vibration system, for example, like the model used in [7]. This means the 2-order vibration system can be used to illustrate the vibration characters of flexible spacecraft. In this section, the typical second order vibration system will be used for analysis of the effectiveness of disturbance compensation and to confirm the optimal compensate criterion. Sinusoidal disturbance and square compensation are adopted based on practical engineering. It should be noted that the frequencies of two kinds of torques are assumed to be the same.

Assume there are two periodic exciting forces, F_1 and F_2, acting on the system. Then the system shown in Equation (5) can be expressed as:

$$m\ddot{x} + c\dot{x} + kx = F_1 + F_2 \tag{6}$$

where

$$F_1 = \begin{cases} B, & \frac{2j\pi}{\omega_f} \leq t < \frac{(2j+1)\pi}{\omega_f} \\ -B, & \frac{(2j+1)\pi}{\omega_f} \leq t < \frac{2(j+1)\pi}{\omega_f} \end{cases}, \; B \geq 0, \; j = 0,1,2,\dots$$

$$F_2 = -A\sin\left(\omega_f t\right), \; A \geq 0$$

ω_f is the natural frequency of both F_1 and F_2. B and A are the amplitudes of the square force and sinusoidal force, respectively. Periodic square force F_1 can be expressed by Fourier series as:

$$F_1 = \frac{a_0}{2} + \sum_{n=1}^{\infty}\left(a_n\cos n\omega_f t + b_n\sin n\omega_f t\right) \tag{7}$$

where the coefficients are:

$$a_0 = 0, \; a_n = 0, \; b_n = \begin{cases} \frac{4B}{n\pi}, & n = 1,3,5,\dots \\ 0 & n = 2,4,6,\dots \end{cases}$$

In this series, the fundamental harmonic has the maximal amplitude. Then, the right side of the equal sign in Equation (6) can be expressed as:

$$F_1 + F_2 = \left(\frac{4B}{\pi} - A\right)\sin \omega_f t + \frac{4B}{\pi}\left(\frac{1}{3}\sin 3\omega_f t + \frac{1}{5}\sin 5\omega_f t + \cdots\right) \tag{8}$$

Here, we introduce an auxiliary parameter called amplitude ratio, which can be expressed as $\beta = \frac{B}{A}$. Substitute Equation (8) into Equation (6), and replace B by β, we have:

$$m\ddot{x} + c\dot{x} + kx = \sum_{i=1}^{\infty} P_i \sin\left((2i-1)\omega_f t\right) \tag{9}$$

where

$$P_i = \begin{cases} \frac{(4\beta - \pi)A}{\pi}, & i = 1 \\ \frac{4A\beta}{(2i-1)\pi}, & i = 2, 3, 4, \ldots \end{cases}$$

Solving Equation (9), we obtain

$$x(t) = \sum_{i=1}^{\infty} \begin{Bmatrix} e^{-\zeta\omega_n t}\left(x_0 \cos \omega_d t + \frac{\dot{x}_0 + \zeta\omega_n x_0}{\omega_d}\sin \omega_d t\right) \\ +Q_i e^{-\zeta\omega_n t}\left[\sin\varphi_i \cos\omega_d t + \frac{\omega_n}{\omega_d}(\zeta\sin\varphi_i - \lambda(2i-1)\cos\varphi_i)\sin\omega_d t\right] \\ +Q_i \sin\left((2i-1)\omega_f t - \varphi_i\right) \end{Bmatrix} \tag{10}$$

where $x_0 = x(0)$, $\dot{x}_0 = \dot{x}(0)$ are the initial conditions. $\lambda = \frac{\omega_f}{\omega_n}$ is the frequency ratio.

$$Q_i = \frac{P_i/k}{\sqrt{\left(1 - (2i-1)^2\lambda^2\right)^2 + ((4i-2)\zeta\lambda)^2}}, \quad \varphi_i = \arctan\frac{(4i-2)\zeta\lambda}{1 - (2i-1)^2\lambda^2}$$

For zero initial conditions system, the solution shown in Equation (10) can be expressed as:

$$x(t) = \sum_{i=1}^{\infty} \begin{Bmatrix} Q_i e^{-\zeta\omega_n t}\left[\sin\varphi_i \cos\omega_d t + \frac{\omega_n}{\omega_d}(\zeta\sin\varphi_i - \lambda(2i-1)\cos\varphi_i)\sin\omega_d t\right] \\ +Q_i \sin\left((2i-1)\omega_f t - \varphi_i\right) \end{Bmatrix} \tag{11}$$

Equation (11) is the final displacement formula. The first line of Equation (11) will be decreased because of damping, and only the second line will remain when system becomes stable. We can find the displacement is strongly associated with the frequency and amplitude ratio, and the fundamental harmonic is vital in the compensated force design. Numerical simulations were provided to provide the laws.

'Simulation' in 'Matlab' was used here for exact residual vibration under different combinations of the frequency ratio and amplitude ratio. For the system of Equation (6), we set its natural frequency and damping ratio as $\omega_{sp} = \sqrt{0.9}$ and $\zeta_{sp} = 0.01/\omega_{sp}$, where the subscript 'sp' means mass-spring system. The amplitude value of sinusoidal disturbance A is set to be 1. In this way, only amplitude ratio and frequency ratio are required. It should be noted that the parameter used here is idealized. The detailed relevance of criterion design and damping will not be considered too much here. We may study those problems in the future. The compensation effect may not notable or excessive if the two ratios are too small or too big. The range of the amplitude ratio is selected from 0.3 to 1 while the range of the frequency ratio is selected from 0.3 to 3. The tip vibration is chosen to be the standard to show the effectiveness of disturbance torque suppression. Simulation results are exhibited in Figures 2–5.

Figure 2a,b are the total displacement results in two representations. The variation tendency is clear. At frequency ratio $\lambda = 0.3$ and $\lambda = 1$, residual vibrations sharply increased. These are resonances caused by different excitations. The system is mainly receiving two kinds of excitations. One is the composition of the fundamental harmonic of square force and another is the disturbance. Both of the two excitations have

the same frequency ω_f. Resonance appeared when $\lambda = 1$. Another kind of excitation is the remaining harmonics of square force. Frequency of the second order harmonic almost meets the fundamental natural frequency of system when $\lambda = 0.3$. As a result, resonance will appear again in the frequency ratio-domain. For each frequency ratio, there is always an amplitude ratio where the residual vibration reaches the minimum. For most frequency ratios, the best compensation effect appeared near the amplitude ratio $\beta = 0.7$. The result for frequency ratio $\lambda = 1$ is a typical case. For every frequency ratio, the fundamental harmonic of the square force compensates the sinusoidal force near $\beta = 0.7$. Those facts illustrated that $\beta = 0.7$ is the optimal option for most feasible frequency ratios.
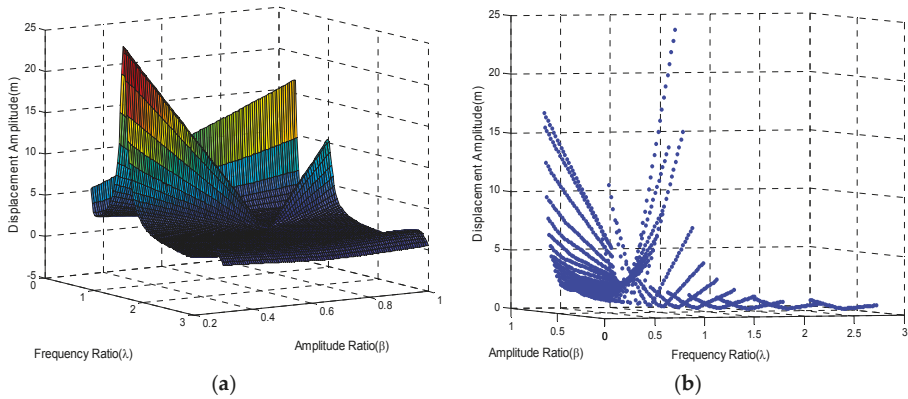
Figure 2. Displacement amplitude results in two forms: (**a**) In surface representation; (**b**) In marker representation.

Figure 3a,b provides the accelerations with different combinations of the amplitude and frequency ratio. From the results, we can find that the variation laws are the same as those for the displacement results. Resonances are obvious at $\lambda = 1$ and $\lambda = 0.3$. Beyond that, values vary homogeneously at different frequency ratios. The condition under which residual vibrations always have a minimum value for each frequency ratio is also distinct, especially for frequency ratios larger than 1. The minimum values are at about the centre of the amplitude ratio range. To show the results more clearly, Figures 4 and 5 show the comparisons between different ratios.
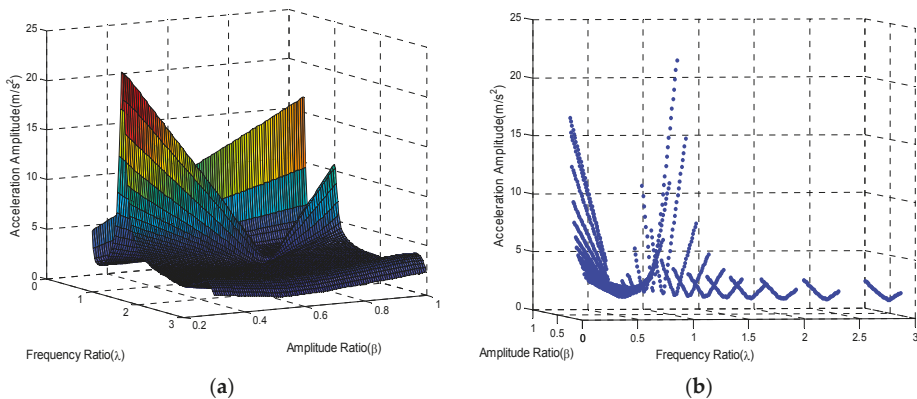

Figure 3. Acceleration amplitude results in two forms: (**a**) In surface representation; (**b**) In marker representation.

Figure 4a,b are parts of the results shown for the frequency ratio-domain. Four equally distributed amplitude ratios are selected. Data in two figures have the same variation laws. Situations when amplitude ratio $\beta = 0.7$ are the best as their vibrations are the smallest for almost all the frequency ratios. That is because the sinusoidal disturbance is properly counteracted by the fundamental harmonic of the step force. Resonance is conspicuous at frequency ratio $\lambda = 0.3$ and $\lambda = 1$.
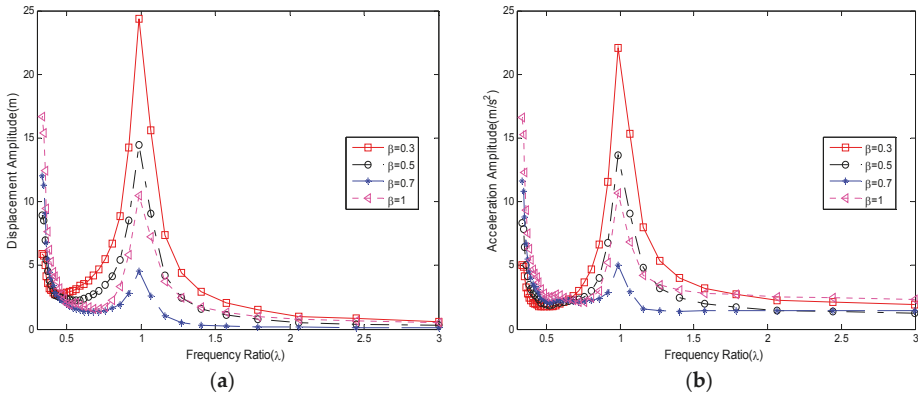
Figure 4. Results for the frequency ratio-domain: (**a**) Displacement amplitude results; (**b**) Acceleration amplitude results.
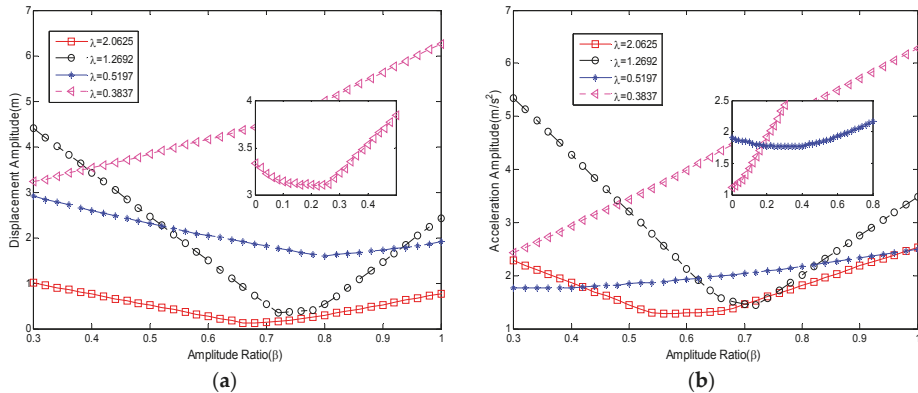
Figure 5. Results for the amplitude ratio-domain: (**a**) Displacement amplitude results; (**b**) Acceleration amplitude results.

Figure 5a,b are parts of the results shown for the amplitude ratio-domain. Each curve has its own minimum, but not all the minimums are located near $\beta = 0.7$. For frequency ratios greater than 1, the minimum appeared near $\beta = 0.7$. For frequency ratios less than 1, the minimum amplitude ratios are not fixed. Floating windows in Figure 5a,b illustrate that for some frequency ratios, their minimum may appear near $\beta = 0.2$. However, the corresponding frequency ratios do not frequently occur in practical engineering.

Results indicate that there is always an optimal combination of the amplitude and frequency ratio for disturbance compensation. In general, we can list the optimal compensate criterion: The optimal amplitude ratio is located within 0.6 to 0.7 for most of the frequency ratios. Besides, the frequency ratio should avoid 0.3 and 1, where it may cause resonance.

3.2. Simulations for Flexible Spacecraft

The former subsection demonstrated that the square compensation force can be used to mitigate the vibration caused by sinusoidal disturbance. To demonstrate the effectiveness of compensation in flexible spacecrafts, numerical simulations and experiments are implemented. In this subsection, the flexible spacecraft model in Equation (4) is adopted, and simulation results are presented.

The system is actuated by a sinusoidal disturbance and a square compensate torque produced by a periodic rotated eccentric mass and a reaction wheel, respectively. Residual vibrations with different combinations of frequency and amplitude ratios will be given to show the effectiveness.

Here, the torque T can be expressed as:

$$T = T_1 + T_2 \tag{12}$$

where T_1 and T_2 have the same expression as F_1 and F_2 in Equation (4), respectively. T_1 is given by the ideal reaction wheel. T_2 is from the periodic eccentric mass. T_1 and T_2 can be expressed as:

$$T_1 = \begin{cases} U, & \frac{2j\pi}{\omega_m} \leq t < \frac{(2j+1)\pi}{\omega_m} \\ -U, & \frac{(2j+1)\pi}{\omega_m} \leq t < \frac{2(j+1)\pi}{\omega_m} \end{cases}, \ U \geq 0, \ j = 0, 1, 2, \ldots$$
$$T_2 = -W_m \Omega_m^2$$

Equation (4) can be further expressed as:

$$\begin{cases} J\ddot{\theta} + \delta\ddot{\eta} = \sum_{i=1}^{\infty} P_i \sin((2i-1)\omega_m t) \\ \delta^T \ddot{\theta} + \ddot{\eta} + C\dot{\eta} + K\eta = 0 \end{cases} \tag{13}$$

where

$$P_i = \begin{cases} \frac{(4\beta - \pi)}{\pi} \Omega_m^2 P_m \sigma_m m_m, & i = 1 \\ \frac{4\Omega_m^2 P_m \sigma_m m_m \beta}{(2i-1)\pi}, & i = 2, 3, 4, \ldots \end{cases}$$
$$\beta = \frac{U}{\Omega_m^2 P_m \sigma_m m_m}$$

Substitute the first part of Equation (13) into the second formula of Equation (13), we will have:

$$\left(I_3 - \frac{\delta^T \delta}{J} \right) \ddot{\eta} + C\dot{\eta} + K\eta = -\frac{\delta^T}{J} \sum_{i=1}^{\infty} P_i \sin((2i-1)\omega_m t) \tag{14}$$

Modal solutions are complex to be predicted analytically, not to mention the multi-dimension modal. Thus, we will directly present the simulation results. Parts of parameters are measured values of experimental equipment used in our study. Others are calculated in a mathematical way. The moment of inertia of the rigid hub is $J = 15$ kg·m^2. The damping ratios of the vibration are $\zeta_1 = \zeta_2 = \zeta_3 = 0.05$, the natural frequencies are $\omega_{n1} = 2.11$ rad/s, $\omega_{n2} = 13.28$ rad/s, $\omega_{n3} = 37.15$ rad/s. The coupling matrix is $\delta = \begin{bmatrix} 2.65 & 0.54 & 0.21 \end{bmatrix}$ kg·m^2. In simulations, the mass of rotating eccentric mass is $m_m = 0.4$ kg, and its eccentric radius is $\sigma_m = 0.08$ m. The states of system are initialised to be zero.

The maximum of sinusoidal disturbance will vary in a certain range depending on each frequency ratio. Square compensation torques were assumed to be ideally outputted, which means it can perfectly fit the sinusoidal disturbance. The frequency ratio range is set from 0.3 to 3.2, and the amplitude ratio range is set from 0.3 to 1. Those settings are based on the results in the previous subsection. Amplitudes of flexible beam tip residual vibration under different combinations of frequency and amplitude ratios are calculated by 'Simulation' in 'Matlab' software. Simulation results are illustrated in Figures 6 and 7.

Figures 6a,b show the displacement of the flexible beam tip with all the combinations of frequency and amplitude ratio in this simulation. Similar to the results displayed in the former subsection,

when the amplitude ratio is near $\beta = 0.7$, the displacement of the flexible tip is minimal. This law is particularly obvious when the frequency ratio exceeds 0.5. Those results just proved the optimal criterion. Variation amplitudes are so weak that the trend is not so clear when the frequency ratio is smaller than 0.5.
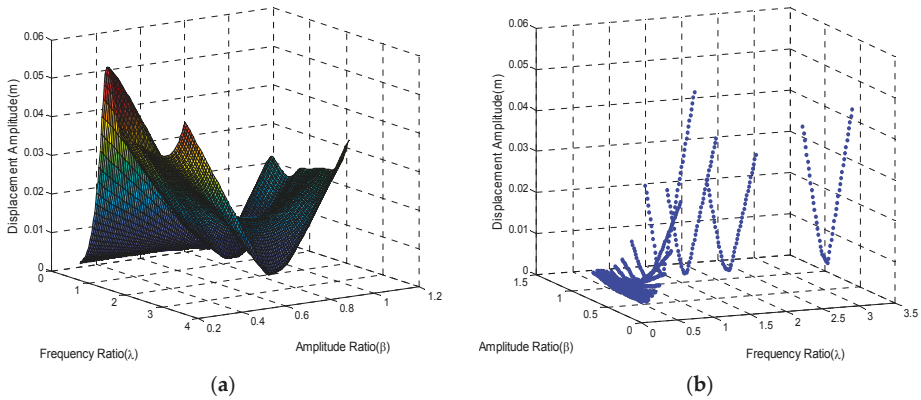

Figure 6. Displacement amplitude results in two forms: (**a**) In surface representation; (**b**) In marker representation.

Figure 7a,b are the amplitude history of the flexible beam tip acceleration. The tip acceleration is a real effect when the amplitude ratio is located near $\beta = 0.7$. The frequency of the system is fixed, so the increasing frequency ratio heightened the rotation velocity of the eccentric mass, and also the amplitude of torques. As a result, values of accelerations increase with increasing frequency ratio.
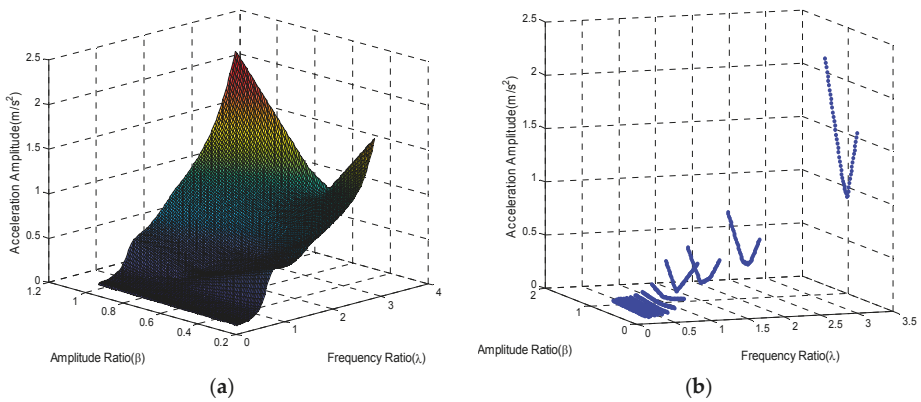

Figure 7. Acceleration amplitude results in two forms: (**a**) In surface representation; (**b**) In marker representation.

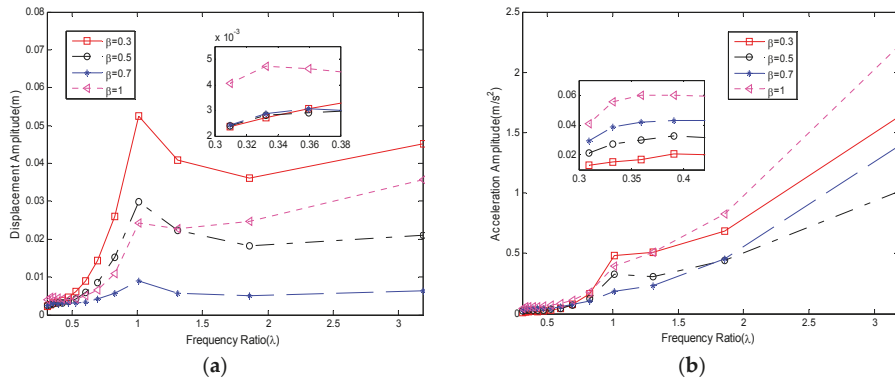Figure 8a,b show the amplitudes of residual vibration in the frequency ratio-domain with selected amplitude ratios.

Figure 8. Results in the frequency ratio-domain: (**a**) Displacement amplitude results; (**b**) Acceleration amplitude results.

The variation tendencies in Figure 8a,b are analogous to those in Figure 4a,b. Situations with $\beta = 0.7$ in the frequency ratio-domain are much smaller than those for the other three selected amplitude ratios. Resonance is obvious at $\lambda = 1$ for all the amplitude ratios even though the amplitude of the synthetic torque is small. The fundamental harmonic of square torque is adopted to compensate the sinusoidal disturbance while the other orders of the harmonic become the new disturbances. Frequency of the second order harmonic meets the fundamental natural frequency of the system precisely, but amplitudes of remaining orders of the harmonic are so small to cause evident vibrations. As a result, resonances at $\lambda = 0.3$, which are shown in floating windows, are not obvious. Although higher Fourier series result in new disturbances, the main effect is from the first order.

Figure 9a,b shows us how amplitudes vary in the amplitude ratio-domain under special frequency ratios.
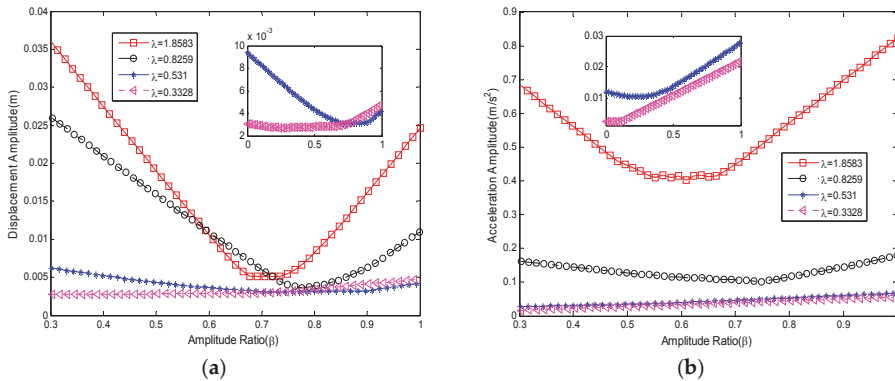

Figure 9. Results for the amplitude ratio-domain: (**a**) Displacement amplitude results; (**b**) Acceleration amplitude results.

Results revealed by Figure 9a,b demonstrated the relationship between the amplitude ratio and the level of residual vibration. The results all have the feature that the displacement amplitude always has a minimum in the amplitude ratio-domain. According to data in Figure 9a, $\beta = 0.7$ is an optimal region for the compensation of disturbances. The optimal amplitude ratio for tip acceleration, shown in Figure 9b, appears to be somewhat different, but the best combination of the amplitude and frequency

ratio does exist despite that the values are different for frequency ratios. All the simulation results demonstrated this for the most frequently occurring situations.

3.3. Experimental Results

Experiments were performed on an SGSRT to verify the proposed criterion and the simulation results. The equipment is shown in Figure 10. This systems mainly consists of a single-axis rotation hub, a flexible aluminium beam (2480 × 200 × 2.5 mm), a torque mode reaction wheel ($T_{max} = 0.065$ Nm) whose rotation axis is coincident with the hub, a periodic rotation dish with an eccentric mass to create the disturbance, and equipment on the hub for measuring, control and data exchange.
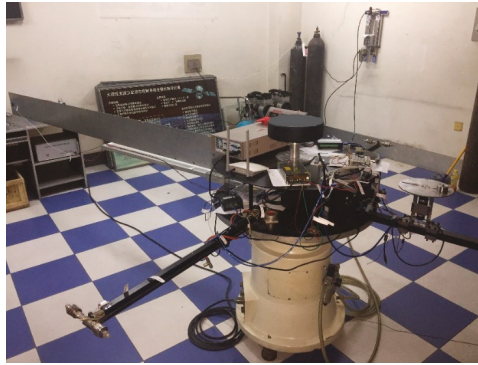

Figure 10. Experimental setup of a single-axis rotary table.

The hub is suspended by a gas bearing. A zero-gravity environment is required, and the table is limited to rotate on the horizontal plane. The residual vibration is measured by an accelerometer fixed on the tip of a flexible beam. The model of the accelerometer (± 2 *g*,$0 - 400$ *Hz*) is 2220-020, produced by Silicon Designe Inc. (Kirkland, WA, USA). Eccentric mass is chosen to be 0.4 kg and 0.25 kg for different frequency ratios, and the periodic rotation dish is placed 0.6 m from the rotation axis of the system. This is the best setting to generate sinusoidal disturbance whose amplitude is within the limits of the reaction wheel.

Frequencies of the experimental equipment have a close relationship with the experimental results. To identify the frequencies of the experimental equipment, free vibration tests were performed, and the fast Fourier transform (FFT) was applied. Figure 11a,b shows the measured tip acceleration data and the FFT result.
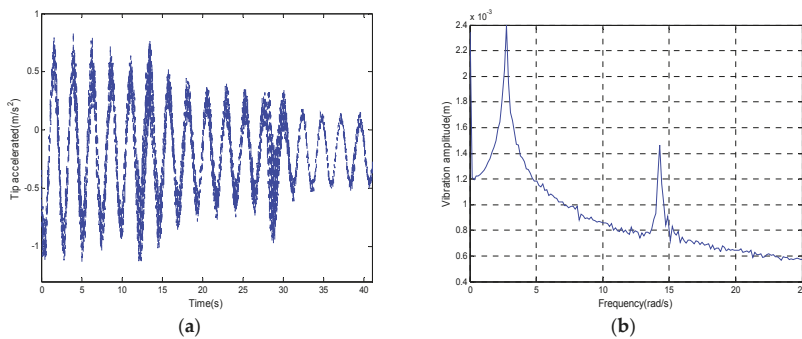

Figure 11. Tip free vibration and FFT analysis: (**a**) Measured tip free vibration; (**b**) FFT of tip free vibration.

Results show that the first two vibration orders are obvious. The measured and the calculated frequencies are shown in Table 1.

Table 1. The first and second frequencies (rad/s).

	1st Mode Frequency	2nd Mode Frequency
Measured	2.7382	13.9487
Calculated	2.8081	13.643
Error	2.781%	2.19%

The errors of the first two frequencies between measured and calculated results are 2.781% and 2.19%, respectively. In view of the difference between the experimental equipment and mathematical model, these errors are acceptable and negligible.

According to the previous results, there are 2 typical varying laws in the amplitude-ratio domain. For situations $\lambda < 0.5$, variation is not obvious. This is because the torques are too small for flexible systems. Similarly, the torques are too large when λ is too high. Considering those situations and the output ability of the experimental equipment, three frequency ratios 1.3, 0.9 and 0.6 were selected for the experiment. Thus, three cases of the experiment corresponding to three selected frequency ratios were provided. On the other hand, simulations illustrated that the optimal amplitude ratio for most frequency ratios is near 0.7. Thus, three amplitude ratios near 0.7 were also selected for experimental cases.

Simulations were performed with real parameters in the experiment. Zero initial conditions were provided for all the experiments. Square compensation torques from the reaction wheel and sinusoidal disturbance were started at the same time. The measured accelerations of the flexible beam tip are shown in Figures 12–14.

3.3.1. Case A

In this case, $\lambda = 0.6$, $\sigma_m = 0.08$ m, $m_m = 0.4$ kg. Three experiments were performed with $\beta = 0.6$, 0.8, 1, respectively. The tip residual accelerations are shown in Figure 12.

In case A, the frequency ratio is selected as 0.6. In this case, three typical experiments are conducted with three amplitude ratios. The measured tip accelerations are illustrated in Figure 12. The tip accelerations were recorded. It can be seen from Figure 12 that the vibration amplitude when $\beta = 0.6$ is the smallest. Vibration amplitude when $\beta = 0.8$ is slightly greater than that when $\beta = 0.6$. However, when the amplitude ratio is 1, the residual vibrations are much more obvious than before.
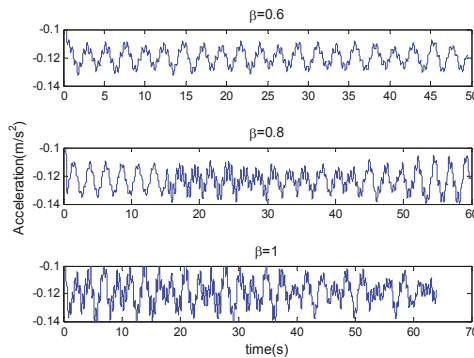

Figure 12. Measured accelerations of the flexible beam tip in Case A.

3.3.2. Case B

In this case, $\lambda = 0.9$, $\sigma_m = 0.04$ m, $m_m = 0.4$ kg. Three experiments were performed with $\beta = 0.6, 0.8, 1$, respectively. The tip residual accelerations are shown in Figure 13.
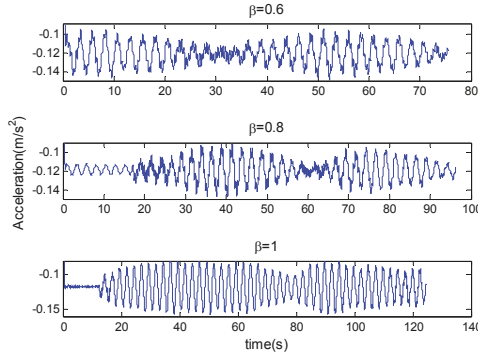

Figure 13. Measured accelerations of the flexible beam tip in Case B.

In case B, the envelope curves are obvious. That is because the frequency of torques is close to the natural frequency of the system. As the amplitude ratio increases, the maxima of the residual vibration increase.

3.3.3. Case C

In this case, $\lambda = 1.3$, $\sigma_m = 0.04$ m, $m_m = 0.25$ kg. Three experiments were performed with $\beta = 0.6, 0.8, 1$, respectively. The tip residual accelerations are shown in Figure 14.

In this case, the situations when $\beta = 0.6$ and $\beta = 0.8$ are almost the same, but when $\beta = 1$, the residual vibration amplitude increased evidently.

Experimental results illustrate the square torques are efficient to compensate sinusoidal disturbance, but the effects vary with different conditions. According to the results of experiments, for all the three cases, the compensation effects are almost the same when $\beta = 0.6$ and $\beta = 0.8$. Compared with that, situations when $\beta = 1$ are worse. The amplitudes of residual vibration during compensation are listed in Table 2.
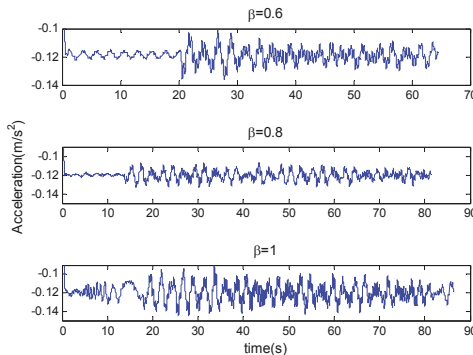

Figure 14. Measured accelerations of the flexible beam tip in Case C.

Table 2. Tip acceleration amplitude with different frequency and amplitude ratios m/s^2.

	β=0.6	fi = 0.8	fi = 1
$\lambda = 0.6$	0.020	0.025	0.041
$\lambda = 0.8$	0.043	0.046	0.072
$\lambda = 1.3$	0.018	0.023	0.037

Recall the added special simulation results which corresponded to the experiments. Figure 15 presents the results in the amplitude ratio-domain. The point marked 'ex' means the experimental data. The experimental results were largely in line with the simulation results. Simulation results show that the maximum amplitude of residual vibration always has a minimum point for each frequency ratio. Despite that the number of experiments is limited, the effectiveness and veracity of the proposed criterion are proved. Both experiments and simulations have verified the veracity of our study. However, it should be noted that all the experiment results are from the SGSRT, and the limitation of single axis rotation can be avoided. This limitation will be solved in future studies.
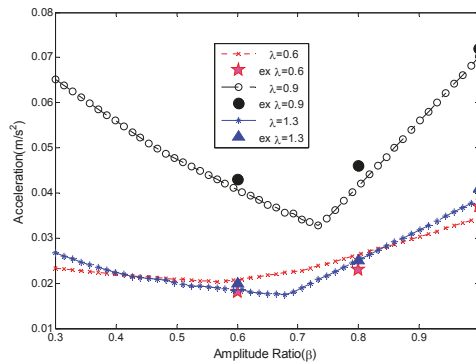

Figure 15. Experimental results and corresponding simulation results.

4. Conclusions

In this article, the optimal criterion of constant compensations has been investigated for flexible spacecraft in the presence of known-law sustained periodic disturbance and square torques. This criterion is mainly based on the mathematical analytical results of the typical vibration system. First, the constant square compensation torque is obtained using the Fourier expansion method, and the relationship between the response of the system and input torques is obtained. The optimal criterion is obtained according to the analysis and simulation results. The criterion exhibits advantages in a flexible spacecraft system in the presence of sustained periodic disturbance. In general, the optimal amplitude ratio is near 0.7 for most frequencies. The frequency ratio should avoid the points near 0.3 and 1. Both numerical simulations and experiments have been performed to verify the veracity of the obtained criterion. However, defects such as the disturbance being too simple and the SGSRT is equipment with only one axis rotation are obvious in our study, and extension studies will be investigated for those limitations in our future research.

References

1. Long, H.; Zhao, J. Robust constrained fault-tolerant attitude control for flexible spacecraft. *Proc. Inst. Mech. Eng. G-J. Aerosp. Eng.* **2017**, *1*, 1–13. [CrossRef]
2. Zhu, Z.; Guo, Y. Robust adaptive attitude tracking coordination control for spacecraft formation with unknown time-varying inertia. *Proc. Inst. Mech. Eng. G-J. Aerosp. Eng.* **2017**, 1–14. [CrossRef]
3. Fazlyab, A.R.; Saberi, F.F.; Kabganian, M. Adaptive attitude controller for a satellite based on neural network in the presence of unknown external disturbances and actuator faults. *Adv. Space Res.* **2016**, *57*, 367–377. [CrossRef]
4. Xiao, B.; Yin, S.; Wu, L. A Structure simple controller for satellite attitude tracking maneuver. *IEEE Trans. Ind. Electron.* **2017**, *64*, 1436–1446. [CrossRef]
5. Muramatsu, H.; Katsura, S. Adaptive periodic-disturbance observer for periodic-disturbance suppression. *IEEE Trans. Ind. Electron.* **2018**, 1–11. [CrossRef]
6. Fedele, G. A fractional-order repetitive controller for periodic disturbance rejection. *IEEE Trans. Autom. Control* **2017**, *63*, 1426–1433. [CrossRef]
7. Khushnood, M.A.; Xiaogang, W.; Naigang, C. Vibration attenuation of spacecraft in the presence of parametric and unmodeled dynamics uncertainties using collocated and noncollocated control: A comparative study. *J. Vib. Control* **2017**, 1–17. [CrossRef]
8. Zhang, R.; Qiao, J.; Li, T.; Guo, L. Robust fault-tolerant control for flexible spacecraft against partial actuator failures. *Nonlinear Dyn.* **2014**, *76*, 1753–1760. [CrossRef]
9. Cong, B.; Liu, X.; Chen, Z. Exponential Time-varying sliding mode control for large angle attitude eigenaxis maneuver of rigid spacecraft. *Chin. J. Aeronaut.* **2010**, *23*, 447–453. [CrossRef]
10. Hu, Q.; Li, B.; Qi, J. Disturbance observer based finite-time attitude control for rigid spacecraft under input saturation. *Aerosp. Sci. Technol.* **2014**, *39*, 13–21. [CrossRef]
11. Zhong, C.; Chen, Z.; Guo, Y. Attitude control for flexible spacecraft with disturbance rejection. *IEEE Trans. Aerosp. Electron. Syst.* **2017**, *53*, 101–110. [CrossRef]
12. Zhang, X.; Wang, R.; Zhang, S.; Wang, Z.; Qin, X.; Schmidt, R. Generalized-disturbance rejection control for vibration suppression of piezoelectric laminated flexible structures. *Shock Vib.* **2018**, *2018*, 1–17. [CrossRef]
13. Chen, W.; Yang, J.; Guo, L.; Li, S. Disturbance-observer-based control and related methods—An overview. *IEEE Trans. Ind. Electron.* **2016**, *63*, 1083–1095. [CrossRef]
14. Ma, Y.; Jiang, B.; Tao, G.; Cheng, Y. A direct adaptive actuator failure compensation scheme for satellite attitude control systems. *Proc. Inst. Mech. Eng. G-J. Aerosp. Eng.* **2014**, *228*, 542–556. [CrossRef]
15. Lau, J.; Joshi, S.S.; Agrawal, B.N.; Kim, J. Investigation of periodic-disturbance identification and rejection in spacecraft. *J. Guid. Control Dyn.* **2006**, *29*, 792–798. [CrossRef]
16. Chen, P.; Sun, M.; Yan, Q. Adaptive rejection of multi-periodic disturbances for a class of linear systems. *Int. J. Control* **2016**, *89*, 2250–2261. [CrossRef]
17. Hao, T.; Matunaga, S. New sliding mode control approach for rapid attitude maneuver using control moment gyros. *J. Aerosp. Eng.* **2016**, *29*, 06015001. [CrossRef]
18. Hu, Q.; Jia, Y.; Xu, S. Adaptive suppression of linear structural vibration using control moment gyroscopes. *J. Guid. Control Dyn.* **2014**, *37*, 990–996. [CrossRef]
19. Hu, Q.; Zhang, J. Attitude control and vibration suppression for flexible spacecraft using control moment gyroscopes. *J. Aerosp. Eng.* **2016**, *29*, 04015027. [CrossRef]
20. Sabatini, M.; Palmerini, G.B.; Leonangeli, N.; Gasbarri, P. Analysis and experiments for delay compensation in attitude control of flexible spacecraft. *Acta Astronaut.* **2014**, *104*, 276–292. [CrossRef]
21. Sabatini, M.; Gasbarri, P.; Palmerini, G.B. Delay compensation for controlling flexible space multibodies: Dynamic modeling and experiments. *Control Eng. Pract.* **2016**, *45*, 147–162. [CrossRef]
22. Azadi, M.; Fazelzadeh, S.A.; Eghtesad, M.; Azadi, E. Vibration suppression and adaptive-robust control of a smart flexible satellite with three axes maneuvering. *Acta Astronaut.* **2011**, *69*, 307–322. [CrossRef]
23. Zhang, Z.; Kan, J.; Wang, S.; Wang, H.; Yang, C.; Chen, S. Performance dependence on initial free-end levitation of a magnetically levitated piezoelectric vibration energy harvester with a composite cantilever beam. *IEEE Access* **2017**, *5*, 27563–27572. [CrossRef]

24. Arani, A.G.; Mosayyebi, M.; Kolahdouzan, F.; Kolahchi, R.; Jamali, M. Refined zigzag theory for vibration analysis of viscoelastic functionally graded carbon nanotube reinforced composite microplates integrated with piezoelectric layers. *Proc. Inst. Mech. Eng. G-J. Aerosp. Eng.* **2016**, *231*, 2464–2478. [CrossRef]
25. Wu, Y.; Zhang, W.; Meng, X.; Su, Y. Compensated positive position feedback for active control of piezoelectric structures. *J. Intell. Mater. Syst. Struct.* **2017**, *29*, 397–410. [CrossRef]
26. Lin, C.; Jheng, H. Active vibration suppression of a motor-driven piezoelectric smart structure using adaptive fuzzy sliding mode control and repetitive control. *Appl. Sci.* **2017**, *7*, 240. [CrossRef]
27. Khushnood, M.A.; Wang, X.; Cui, N. Active vibration control of a slewing spacecraft's panel using H∞ control. *J. Vibroeng.* **2016**, *18*, 2959–2973. [CrossRef]
28. Liu, D.; Yang, D.; Zhang, W. An optimal maneuver control method for the spacecraft with flexible appendages. In Proceedings of the Astrodynamics Conference, Minneapolis, MN, USA, 15–17 August 1988; pp. 294–300.
29. Hu, Q.; Ma, G. Flexible spacecraft vibration suppression using PWPF modulated input component command and sliding mode control. *Asian J. Control* **2007**, *9*, 20–29. [CrossRef]
30. Kong, X.; Yang, Z. Combined feedback control and input shaping for vibration suppression of flexible spacecraft. In Proceedings of the International Conference on Mechatronics & Automation, Changchun, China, 9–12 August 2009; pp. 3257–3262.

MDPI